Morphological Behavior of Linear ABC and ABAC Block Terpolymers

A DISSERTATION
SUBMITTED TO THE FACULTY OF THE GRADUATE SCHOOL
OF THE UNIVERSITY OF MINNESOTA
BY

Michael James Bluemle

IN PARTIAL FULFILLMENT OF THE REQUIREMENTS
FOR THE DEGREE OF
DOCTOR OF PHILOSOPHY

Frank S. Bates and Timothy P. Lodge, Advisors

April 2010

Acknowledgements

I would be remiss if I did not acknowledge the many, many people who have helped me reach this point in my academic career. First and foremost, I would like to thank my advisors, Frank Bates and Tim Lodge, for their support and guidance. They exhibited a nearly infinite amount of patience while gently (and sometimes not so gently) prodding me along. My growth as a scientist and as a person is in large part due to them.

I am also deeply indebted to many other members of the Bates and Lodge groups. Mahesh Mahanthappa, a great mentor, taught me anionic synthesis from a chemist's perspective in addition to the basics of scattering. I am grateful for all of the assistance that Alhad Phatak provided me with as I was learning the analytical techniques necessary for this work. I really, really appreciate all of the time Guillaume Fleury spent helping me synthesize and characterize many of the materials in this work. Additionally, Guillaume was a great person to discuss the many facets of my project and polymer science in general. I have also benefited greatly from discussions with many others: Kevin P. Davis, Adam Buckalew, Adam Meuler, Zach Thompson, Jian Qin, Lifeng Wu, Chris Ellison, Soo-Hyung Choi, Will Edmonds, Sangwoo Lee, Peter Simone, Louis Pitet, Liz Jackson, Ameara Mansour, Brad Jones, and Jingwen Zhang.

Finally, I would like to thank all of my family and friends. They have helped me get through these demanding times, while providing some laughs and a lot of fun along the way. I really enjoyed the Saturdays, whether it was tailgating or watching with the College Football crew. While I only actually played one summer, I always felt welcome

as part of the Bad News Beers softball team. It was certainly not my weak hitting and inept fielding that won us the championship that year. My parents have always been there to encourage and support me no matter what I was doing. Last, but not definitely not least, I need to thank my beautiful wife, Christi, for her love and support. I really appreciate her patience as I worked through these pressure-filled last few months.

To Christi, Jackson, Mom, and Dad

Abstract

An array of fascinating morphologies has been documented in ABC triblock terpolymers, including four distinct, triply periodic network phases. This thesis investigates the phase behavior of three terpolymer systems: poly(ethylene-*b*-cyclohexylethylene-*b*-dimethylsiloxane) (ECD) triblocks, CECD tetrablocks, and poly(styrene-*b*-isoprene-*b*-styrene-*b*-ethylene oxide) (SISO) tetrablocks. CECD and SISO are examples of a previously unexamined block polymer chain architecture: the ABAC tetrablock. The ABAC architecture provides an additional synthesis strategy for producing new ordered phases, or expanding the range of stability for a given microstructure.

A series of ECD triblocks with varying D block length and equal E and C content was prepared by sequential anionic polymerization and catalytic hydrogenation. Two samples exhibited order-order transitions from hexagonally arranged spheres of D in C/E lamellae to O^{70} (orthorhombic network structure with *Fddd* space group symmetry) with increasing temperature. The observation of O^{70} in the ECD system provides further evidence of the "universality" of this orthorhombic network structure in triblock terpolymers. However, the smaller window of stability for O^{70} in ECD as compared to the previously-studied ISO system suggests that differences in block statistical segment lengths can greatly affect the equilibrium morphology.

Characterization of CECD and SISO tetrablocks revealed the remarkable effects that molecular architecture can have on phase behavior. An orthorhombic network structure with *Pnna* symmetry (O^{52}) was identified on the basis of small-angle X-ray scattering and

transmission electron microscopy between hexagonally packed cylinder and core-shell cylinder morphologies in a series of CECD terpolymers. Microphase separation of the D blocks created spherical domains at the junctions of the trivalent connectors that make up the O^{52} network topology, while this intriguing morphology was stabilized by the terminal C chains in the CECD chain architecture. Formation of D spheres could also be confined within a C/E LAM_2 microstructure to create a structure-in-structure morphology by tuning the CECD composition. In the SISO system, inverted (minority I chains constituted the matrix) core-shell spheres and cylinders were identified. ISO triblocks with similar compositions formed LAM_2, O^{70}, and three-domain lamellae. These results again suggested that the ABAC molecular architecture was responsible for a striking morphological change.

Table of Contents

List of Tables

List of Figures

1

Block Polymer Phase Behavior

1.1 Introduction

We do not have to look far to see the impact that synthetic polymers have had on the modern world. Polymeric materials include tough plastics, like the poly(vinyl chloride) used in piping, the deformable, elastic rubbers used in car tires, and Kevlar®, the lightweight, strong aramid fiber used in bulletproof vests. The large molecular weights of polymers set them apart from small molecule compounds, and are responsible for their high melt viscosities and elasticities. The basic properties of a polymer are determined by the molecular weight and the monomer repeat unit. Thus, poly(styrene) (PS) is a rigid, transparent solid that softens into a viscous liquid above approximately 100 °C, while poly(butadiene) (PB) is a viscous liquid at room temperature. PS has a high elastic modulus, but is a brittle material. Conversely, PB can be extended to high strains without brittle failure, but has a low elastic modulus. An alloy of the two would create a material that utilizes the positive characteristics of both homopolymers and extends the range of possible applications. However, there have been very few instances of complete miscibility of different polymers to create a superior material, as most polymers

macrophase separate, even when their monomers readily mix. The large macromolecule chains greatly diminish the entropy of mixing compared to an identical mass of small molecules, such as the monomers. With miniscule entropy of mixing, the enthalpic incompatibilities of unlike macromolecules drive blended polymers to phase separate on the macroscopic length scale. Extensive research has focused on overcoming this limitation via processing or chemical compatibilization of the homopolymers, while controlling the critical parameters of dispersion, morphology, and adhesion between the immiscible phases.[1,2]

Synthesis of block polymers prevents the problem of macrophase separation that plagues blends of homopolymers, while exploiting the positive traits of dissimilar homopolymers. Block polymers are formed by the covalent attachment of two or more distinct homopolymers (blocks) together. Preparation of well-defined block polymers was spurred by the development of living anionic polymerization over 50 years ago.[3] If two monomers, A and B, are used to synthesize the block copolymer, a variety of architectures are possible with established chemical techniques, such as linear[4] diblock (AB), triblock (ABA), pentablock (ABABA) copolymers, and nonlinear[5] star diblocks $(AB)_nX$. With the addition of a third component, linear ABC triblocks and three-armed stars can be prepared. Chemical modification of all or some of the blocks, such as catalytic hydrogenation in this work, augments the range of possible copolymers and properties that are synthetically possible. In addition to the vast array of possible architectures, block polymers are especially appealing because they self-assemble into a wide range of microstructures below the order-disorder transition temperature (T_{ODT}).

These morphologies are caused by the incompatibility of the constituent blocks, which leads to local phase separation on the order of 5 to 50 nm.[6]

With the advent of living anionic polymerization, block copolymers were quickly commercialized as thermoplastic elastomers.[7] These materials act like cross-linked rubbers without vulcanization and can be processed at elevated temperatures. The triblock copolymers of poly(styrene-*b*-isoprene-*b*-styrene) (SIS) and poly(styrene-*b*-butadiene-*b*-styrene) (SBS) have been commonly used as thermoplastic elastomers because the glassy PS domains physically crosslink the rubbery polydiene domains, imparting strength and elasticity. Thermoplastic elastomers are typically used as additives in pressure sensitive adhesives, the rubber soles in footwear, asphalt, high-impact plastics, sealants, and automobile parts. These applications rely solely on the material properties of the constituent homopolymers without taking advantage of any particular morphology.[8] Future technologies are expected to utilize the long-range organization of a given microstructure, in addition to the properties of the component polymers. Research in the disparate areas of gas separation,[9] catalysis,[10] proton exchange fuel cell membranes,[11] and water purification[12] has already begun to exploit the mass transport properties of specific block polymer morphologies. Ordered block polymer phases have been used in conjunction with photolithography techniques to pattern substrates with features on the order of nanometers,[13-15] which has the possibility of revolutionizing the manufacturing of electronic devices. Control and prediction of these microstructures requires a thorough understanding of the principles that control block polymer phase behavior.

This thesis presents experimental research that contributes to the development of fundamental principles related to the morphological behavior of ABC triblock and ABAC tetrablock terpolymers. These results are an extension of the numerous experimental and theoretical studies conducted in the past few decades concerned with elucidating the phase behavior of AB diblock copolymers and ABC triblock terpolymers. The remainder of this chapter presents a review of the current understanding of block polymer thermodynamics.

1.2 Block Polymer Thermodynamics

1.2.1 AB Diblock Copolymers

The thermodynamics of polymer solutions and blends are often described by Flory-Huggins theory, which is a modified form of regular solution theory. The Flory-Huggins expression for the Gibbs free energy of mixing, ΔG_m, is given by

$$\frac{\Delta G_m}{kT} = \frac{f_A}{N_A}\ln f_A + \frac{f_B}{N_B}\ln f_B + f_A f_B \chi_{AB} \qquad (0.1)$$

where k is the Boltzmann constant, T is the temperature of the system, N_A and N_B are the repeat units of component A and B, f_A and f_B are the volume fractions of A and B and χ_{AB} is the segment-segment interaction parameter (also referred to as the Flory-Huggins interaction parameter).[16] For polymer blends (large N_A and N_B), the first two terms (entropic considerations) of Equation (0.1) are vanishingly small and the third term

(enthalpic interactions) dominates thermodynamic behavior. As a result, most homopolymer blends macroscopically phase separate. Block polymers, however, covalently link sequences of chemically distinct repeat units into a single macromolecule. This chemical structure prevents macroscopic phase separation in a block polymer, but does not eliminate the possibility of microphase separation. The fundamental microstructures in block polymers are controlled by the χ(s) between the constituent blocks and the overall degree of polymerization (N). Increasing χ favors a reduction in dissimilar block contacts, while increasing N causes losses of translational and configurational entropy. Alternatively, decreasing χ and/or N can lead to a disordered phase dominated by entropic interactions. Thus, for a given block composition, the product χN dictates the block polymer morphology. The degree of segregation due to χN has been divided into three regimes: the asymptotic weak and strong segregation limits (WSL and SSL) and the intermediate segregation region (ISR). WSL behavior (χN ~ 10 or less) is characterized by small local deviations in composition from the bulk volume fraction f. The other limit is SSL behavior (χN ? 10), where nearly pure blocks are formed with well-defined interfaces. In between these limits lies the ISR region, which only recently has been distinguished as a separate regime.[17]

The simplest and most widely studied class of block polymers is linear AB diblock copolymers. In the high temperature (low χ) disordered phase, the A and B blocks homogeneously blend, but as the temperature is decreased, the blocks microphase separate to form ordered morphologies. The classical microstructures are lamellae (L or LAM), hexagonally packed cylinders (C or Hex), and body-centered cubic spheres (BCC

or Q^{229}). More recently, a bicontinuous structure, the double gyroid (G or Q^{230}) phase has been identified[18,19] (Figure 1.1). The ordered bicontinuous double-diamond (OBDD) structure (see Figure 1.2), a previously reported bicontinuous phase in linear[20] and star[21] block copolymers, was reevaluated with additional scattering experiments and determined to be the G phase.[22] Another complex phase, the perforated lamellar (PL) structure shown in Figure 1.2, occurs when the minority-component layers of the lamellae develop a hexagonal arrangement of passages.[23-29] However, this phase was determined to be a long-lived metastable state.[30,31] Very recently, Takenaka and coworkers have identified an orthorhombic network structure (O^{70}) possessing *Fddd* symmetry over a very narrow region of composition space in weakly segregated poly(styrene-*b*-isoprene) diblock copolymers.[32,33] This fascinating network phase will be discussed in more depth with regard to ABC triblock terpolymer phase behavior.

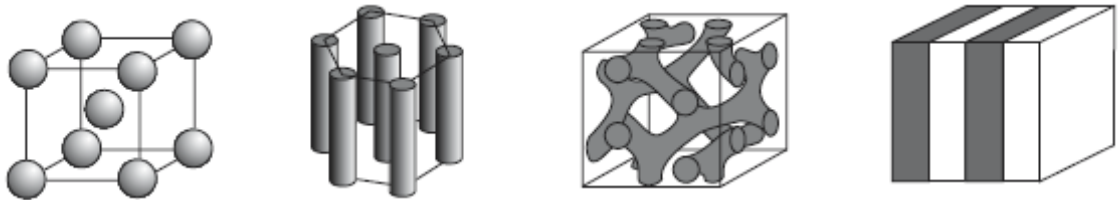

Figure 1.1: Stable morphologies present in AB copolymers with increasing volume fraction of minority component: body-centered cubic spheres (S), hexagonally-packed cylinders (C), bicontinuous double gyroid (G) and lamellae (L). Inverse phases are not shown. Reproduced from Abetz.[34]

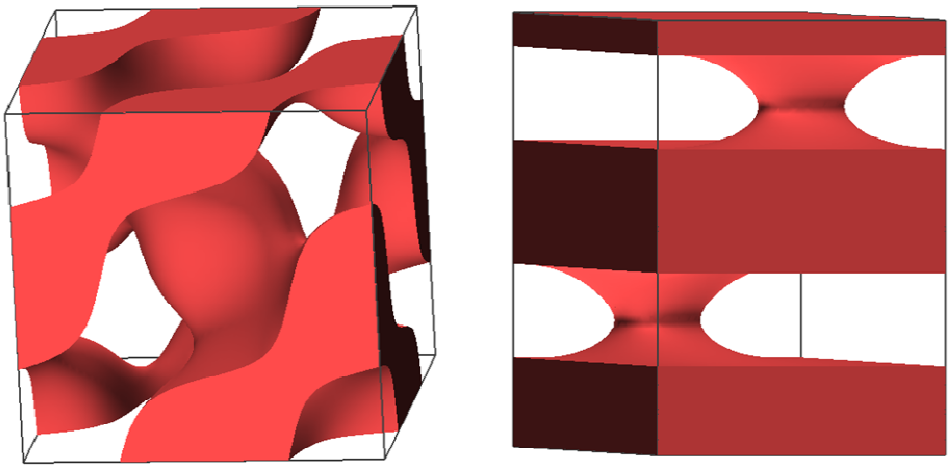

Figure 1.2: Space filling models of OBDD (left) and ABAB… stacking of HPL structure (right).

Based upon the work of Meier,[35] Krause,[36] Leary and Williams,[37] and Helfand,[38,39] Helfand and Wasserman were able to extend self-consistent field theory (SCFT) to permit quantitative calculations of free energies, composition profiles and chain conformations for narrow interfaces in the SSL.[40] Domain size was determined by minimization of an expression for free energy, which contained three principal contributions: interfacial tension between A and B domains, entropy loss due to localization of the A-B joints to the interphase, and the severe entropy loss associated with stretched chain conformations into the bulk of the microdomain. In the SSL the entropy loss due to chain stretching dominates the confinement entropy of the junction and balances the interfacial tension's drive towards larger domain sizes. The numerical solutions of the SCFT equations for the domain sizes of diblock and triblock copolymers compared favorably with experimental

results. Additionally, Helfand and Wasserman extended these numerical techniques to spherical[41] and cylindrical[42] domains in the SSL.

At the opposite end of the segregation spectrum is the WSL, which is crucial to the understanding of phase behavior near T_{ODT}. In this regime, Helfand's assumption of narrow interfaces is no longer valid. Modeling of block copolymers in the WSL was greatly advanced by the pioneering work of Leibler.[43] Leibler extended de Gennes' random phase approximation (RPA) for polymer melts[44] to the situation of a monodisperse AB diblock copolymer melt. A phase diagram of a diblock copolymer melt near T_{ODT} was mapped, which predicted a critical point at $(\chi N)_c = 10.495$, $f_c = 0.5$, where a compositionally symmetric melt was expected to undergo a second order phase transition from lamellae to the disordered phase. Fredrickson and Helfand[45] broadened Leibler's analysis to include the effects of composition fluctuations, which proved to be significant for realistic polymer molecular weights. Their work suggested a weak first-order phase transition for a symmetric diblock copolymer, at a larger χN than the second order phase transition determined by Leibler. The location of this order-disorder transition was predicted to be at $(\chi \bar{N})_{ODT} = 10.495 + 41.022\bar{N}^{-1/3}$, where $\bar{N}$ is proportional to the copolymer molecular weight and defined by the radius of gyration (R_g) and number density of copolymers (ρ_c), $\bar{N} = 6^3\left(R_g^3\rho_c\right)^2$. Additionally, unlike Leibler's analysis, direct transitions from the disordered state to cylinders and spheres were found by changes in temperature. In the limit of infinite molecular weight, Leibler's mean-field predictions were recovered. Subsequent experimental measurements of scattering from the ordered and disordered states of a poly(ethylene-*alt*-propylene-*b*-

ethylethylene) diblock copolymer showed qualitative agreement with Fredrickson and Helfand's fluctuation theory.[46]

Unification of the theories describing AB diblock copolymer phase behavior in the SSL and WSL was largely accomplished by Matsen and coworkers. With improvements in theoretical methods and computer technology, Matsen and Schick were able to solve the full SCFT equations for any periodic phase without making assumptions that had limited previous researchers.[47] These calculations determined that the HPL phase was unstable and predicted the G phase to be stable in the WSL and ISR. However, these calculations could not be extended to the SSL. This limitation was eliminated by the implementation of Matsen and Bates[48,49] and Cochran *et al*.[50] of additional Fourier terms in the representation of polymer segment profiles. This resulted in a phase diagram for diblock copolymer melts that compares even more favorably with experimental results (see Figure 1.3) in terms of observed phases and their locations along the abscissa. Both the theoretical and experimental phase diagrams revealed regions where the classical morphologies (BCC spheres, hexagonally packed cylinders, and lamellae) are stable in addition to channels between the lamellar and cylindrical microstructures where the gyroid microstructure is stable. The OBDD and HPL morphologies were determined to be unstable due high degrees of packing frustration.[30] The experimental phase portrait for poly(styrene-*b*-isoprene) (SI) copolymer melts generated by Khandpur *et al*.[51] and refined by Ryu *et al*.[52] (Figure 1.3) was the result of extensive morphological characterization experiments, including rheology, transmission electron microscopy and scattering measurements.

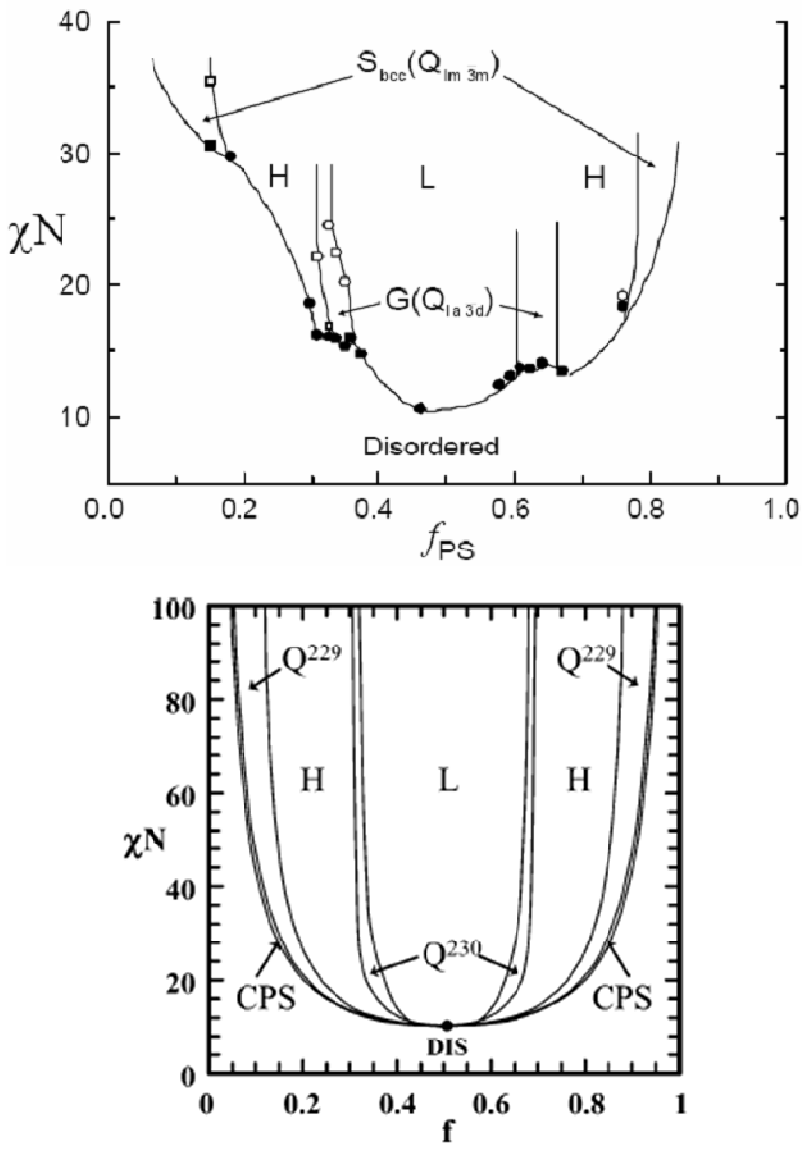

Figure 1.3: Comparison of experimental phase portrait of poly(styrene-*b*-isoprene) diblock copolymer obtained from data generated by Khandpur *et al.*[51] and Ryu *et al.*[52] and SCFT prediction by Cochran *et al.*[50] Images reproduced from Bailey[53] and Cochran *et al.*[50]

1.2.2 ABA Triblock Copolymers

The simplest extension of the AB diblock copolymer architecture is the symmetric ABA triblock copolymer. In the SSL, polymer chains in block polymers near domain interfaces are significantly stretched to minimize interfacial area. However, the middle portion of B chains in an ABA triblock are relatively far from domain interfaces, which results in unstretched, relaxed conformations. Thus, the free energy of a symmetric ABA triblock melt remains nearly unaffected by cutting polymer chains in half.[54] This was borne out by the predictions of nearly identical phase behavior for homologous AB and ABA melts by Helfand and Wasserman[40] and Matsen[55] with SCFT implementations. Mayes and Olvera de la Cruz investigated the phase behavior of symmetric and asymmetric triblock melts in the WSL[56] with Leibler's theory[43] and subsequently included fluctuation corrections.[57] Their work predicted that a symmetric ABA copolymer with $f = 0.5$ has a critical point at $\chi N = 17.9$, rather than 10.5 for a AB diblock. As in the previously discussed AB diblock copolymer case, the developments in SCFT made it possible to unify the theories governing ABA copolymer melts and map the entire phase diagram. Matsen and Thompson accomplished this with symmetric triblock copolymers[54] and Matsen extended this analysis to the asymmetric case.[58] A comparison of the theoretical phase diagrams for homologous AB and ABA copolymer melts ($N_{AB} = 2N_{ABA}$) is shown in Figure 1.4. The similarities in structure are immediately evident. As the asymmetry in blocks increases, there is a progression of lamellar, gyroid, cylindrical and spherical morphologies in an attempt to minimize to interfacial area. However, SCFT did predict several differences. As stated previously by Mayes and Olvera de la Cruz,[56]

triblock copolymers remain ordered down to lower χN than their diblock analogs due to the increased likelihood of penetration of B chains in an A domain in an AB copolymer as compared to the larger, "pinned" B block of an ABA triblock. The ABA phase diagram also becomes asymmetric along the abscissa because this effect is more pronounced at large volume fractions of A where disordering occurs due to the release of B chains from their domains. Experimentally measured T_{ODT}s of homologous pairs of SI and SIS[52] and poly(ethylene-*alt*-propylene-*b*-ethylethylene) (PEP-PE_E) and PEP-PE_E-PEP[59] compared favorably with the SCFT calculations. Additionally, domain spacings in homologous in diblock and triblock melts were found to be quite similar,[60,61] again in good agreement with theory. In addition to the classical phases, the gyroid microstructure has been identified in a number of triblock melts.[62-67]

A distinct difference between the AB and ABA architectures is that triblocks have both ends of their B blocks constrained to an interface with A. Thus, triblock copolymers can adopt two distinct configurations in morphologies with well-defined interfaces (Figure 1.5). In the looped configuration, both B block ends are located at the same domain boundary, but in the bridged conformation, the two ends are located at different interfaces. This has little effect on phase behavior, but the presence of bridges in ABA triblocks has been shown to greatly improve the mechanical properties of the block copolymer.[52,59] Theoretical calculations[55,68] have predicted the bridging fraction in the lamellar microstructure to be approximately 40%. Experimental measurements have confirmed the validity of this prediction.[69,70]

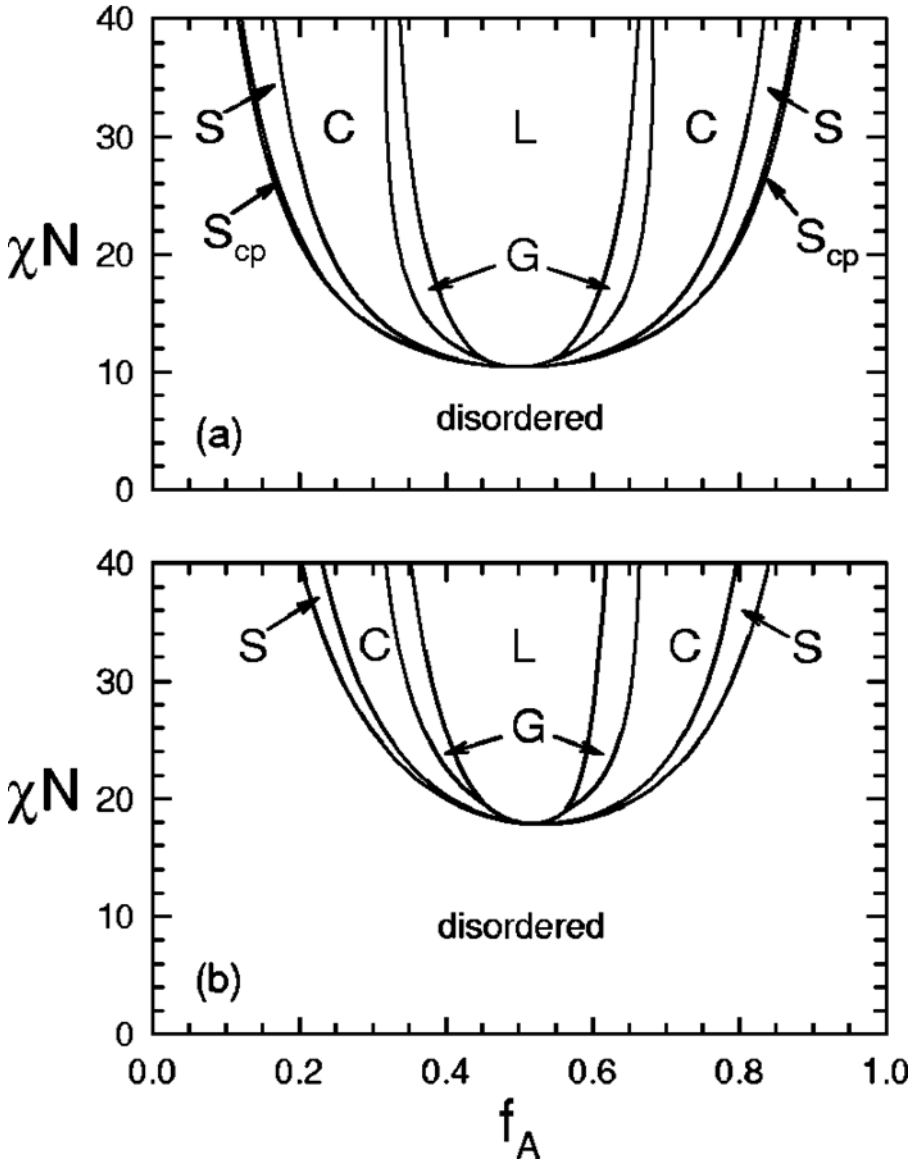

Figure 1.4: Phase portraits calculated with SCFT for melts of (a) AB diblock copolymers and (b) symmetric ABA triblock copolymers in terms of volume fraction f_A and segregation χN. Reproduced from Matsen.[58]

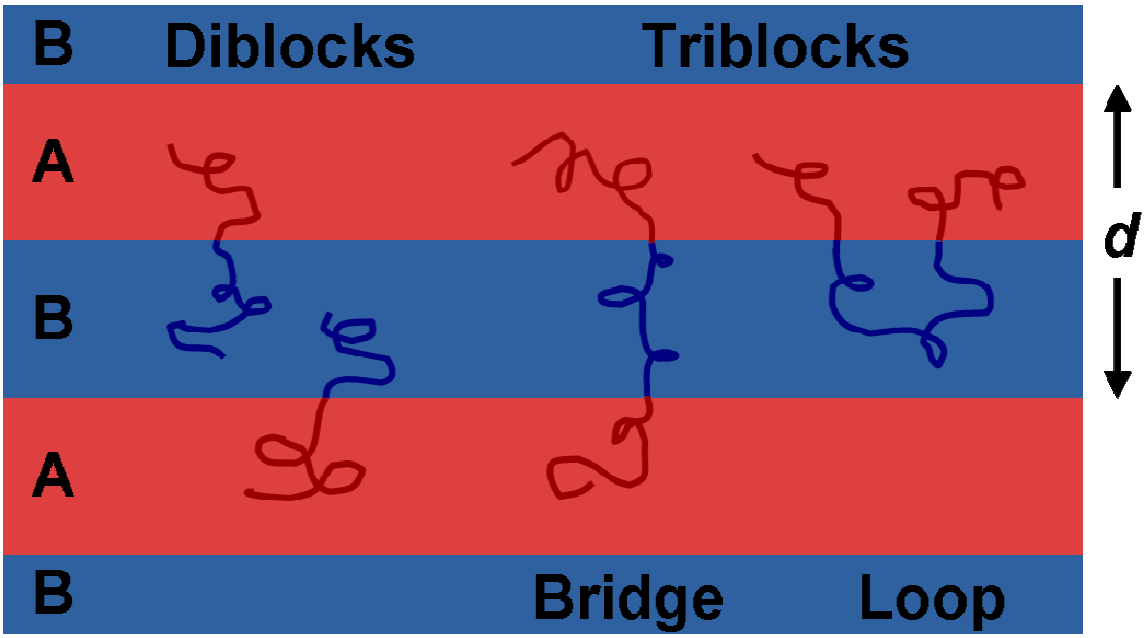

Figure 1.5: Possible configurations of AB diblock and ABA triblock copolymers in a lamellar morphology. Triblock chains can bridge domains, whereas diblocks can not. Adapted from Matsen and Thompson.[54]

1.2.3 ABC Triblock Terpolymers

Addition of a C chain to an AB diblock to form a terpolymer greatly complicates the thermodynamics of microphase separation. Two additional interaction parameters, χ_{AC} and χ_{BC}, and an extra composition variable are necessary to describe a given ABC triblock. Also, the sequence of blocks (ABC versus ACB or BAC) can have profound effects on terpolymer phase behavior. Intuitively, many more morphologies are possible for ABC triblocks than for AB and ABA copolymers. This wealth of self-assembled microstructures provides opportunities for the development of new applications, but also

greatly complicates the experimental and theoretical mapping of phase behavior in ABC triblocks. Investigation of the large parameter space of ABC terpolymer systems requires the laborious synthesis and characterization of many polymers, while making the theoretical descriptions of simpler copolymer systems inadequate. The universal χN versus f plane of AB diblocks does not have an ABC analog. Therefore, the approach of many researchers has been the systematic study of model ABC systems to discover new ABC microstructures and, more importantly, to determine fundamental information regarding the competition and balance between the three possible block interfaces (A/B, A/C, and B/C).

In this thesis, we adopt the classification scheme developed by Bailey to group ABC triblock terpolymers by the relative magnitudes of the binary interaction parameters in the system.[53] In ABC triblocks, two interfaces are required due to chain connectivity, A/B and B/C, whereas the A/C interface is not. Thus, A/C contacts will be generated only when they are energetically favorable. Bailey recognized that this led to three possible classes of ABC systems (see Table 1.1): (1) χ_{AC} is larger than χ_{AB} and χ_{BC}; thus, there is no preference to form A/C interfaces. This system is termed "nonfrustrated" and designated F^0. (2) χ_{AC} is intermediate to the other interaction parameters, which may lead to A/C interfaces. One interface in the system is most unfavorable (frustrated) and the class is termed F^1. (3) If χ_{AC} is smaller than χ_{AB} and χ_{BC}, A/C contacts are enthalpically favorable. Now two mandatory interfaces are frustrated and the system is termed F^2. Zheng and Wang[71] had previously proposed a similar categorization method, but

Table 1.1: Classification scheme for ABC triblock terpolymers based on relative segment-segment interaction parameters. Adapted from Bailey.[53]

Classification	χ_{ij} Relationship	Interfacial Description
F^0	$\chi_{AB} \cong \chi_{BC} \leq \chi_{AC}$	No A/C interfaces form, A/B and B/C interfaces are balanced without extreme curvature.
F^1	$\chi_{AB} \cong \chi_{AC} < \chi_{BC}$	Possible formation of A/C interfaces, B/C interfaces will have high degree of curvature.
F^2	$\chi_{AC} < \chi_{AB}, \chi_{BC}$	Possible formation of A/C interfaces, A/B and B/C interfaces will have high degree of curvature.

subdivided these three classes to account for special situations when two interaction parameters are equivalent.

The morphological behavior of ABC triblock terpolymers from each frustration class has been experimentally examined. Stadler, Abetz, and coworkers have investigated several F^2 systems, including poly(styrene-*b*-butadiene-*b*-methyl methacrylate),[72-77] poly(styrene-*b*-ethylenebutylene-*b*-methyl methacrylate),[74,75,78] and poly(styrene-*b*-ethylenebutylene-*b*-caprolactone)[79,80] Resulting microstructures depend on the proportions of A and C, but include "decorated" phases (B spheres, cylinders, rings, or helices on spheres or cylinders of A or C) for small values of f_B. These morphologies allow for increased AC interfacial area, while the discontinuous B microdomains decorate the AC interfaces. As the value of f_B is increased, the discrete B domains coalesce and the system forms three-domain lamellae (LAM_3). Additionally, Breiner *et al*. have reported an intricate "knitting pattern" phase intermediate to B cylinders at A/C lamellar interfaces and LAM_3 that is also a member of this class.[81,82]

Extensive research with F^1 type triblock systems, including poly(styrene-*b*-1,4-butadiene-*b*-4-vinylpyridine),[83] poly(styrene-*b*-isoprene-*b*-2-vinylpyridine),[84] poly(styrene-*b*-1,2-butadiene-*b*-2-vinylpyridine),[85,86] poly(isoprene-*b*-styrene-*b*-dimethylsiloxane),[87,88] poly(styrene-*b*-isoprene-*b*-ethylene oxide),[89] and poly(styrene-*b*-isoprene-*b*-lactide),[90] have identified core-shell analogs of the AB diblock morphologies (core-shell spheres,[83] core-shell cylinders,[85,88-90] and core-shell gyroid[85-87,89]) in addition to LAM_3, and perforated lamellar structures that maximize A/C contacts.[89] Identification of core-shell cylindrical and gyroid microstructures has generated interest in some of these materials as solid-state electrolytes[91] and nanoporous templates.[90]

The research of Bailey and coworkers with poly(styrene-*b*-isoprene-*b*-ethylene oxide) (SIO),[89] and later ISO,[92] is especially noteworthy. End-functionalization of SI or IS diblock copolymers with a hydroxyl group allowed re-initiation and growth of ethylene oxide from the parent diblock.[93] From a single batch of diblock copolymer, a series of triblock terpolymers that varied only O block length could be prepared. In this manner, systematic studies of phase behavior along the symmetric $f_S = f_I$ isopleth were conducted with both SIO and ISO triblocks. In the frustrated (F^1) SIO system, four ordered morphologies (pillared lamellae, core-shell cylinders, core-shell gyroid, and semi-perforated LAM_3) and multiple order-order transitions were identified at O compositions between LAM_2 ($f_O < 0.03$) and LAM_3 ($0.25 < f_O < 0.33$). This contrasts sharply with the nonfrustrated ISO system, as discussed below.

The third class of ABC terpolymers, F^0, are characterized by A/B and B/C interfaces, which resist extreme interfacial curvature and lack an A/C interface. A systematic study

of such a system was performed by Matsushita and coworkers with poly(isoprene-*b*-styrene-*b*-2-vinylpyridine) (ISV).[94-97] Samples of ISV with $f_I = f_V$ and $1/3 < f_S < 0.9$ were characterized by transmission electron microscopy and small-angle X-ray scattering. Increasing the size of the S block led to this sequence of morphologies: LAM_3, alternating gyroid (Q^{214}, $I4_132$ space group symmetry), alternating I and V cylinders on a tetragonal lattice, and alternating I and V spheres packed on a primitive cubic lattice analogous to crystalline CsCl. Besides LAM_3, these phases are fundamentally different from AB copolymer morphologies. The presence of two relatively balanced interfacial tensions ($\chi_{AB} \cong \chi_{BC}$) can cause F^0 terpolymers to break symmetry to accommodate the comparable A/B and B/C enthalpic contributions to the overall free energy of the system.[98] Thus, the double gyroid (Q^{230}, $Ia\bar{3}d$) observed in diblocks becomes the lower symmetry alternating gyroid (Q^{214}, $I4_132$) in ISV, hexagonally-packed cylinders become tetragonally-packed, and BCC spheres (Q^{229}, $Im\bar{3}m$) become simple cubic (Q^{221}, $Pm\bar{3}m$). More recent work by Bailey *et al*. with ISO identified an additional example of symmetry breaking in a series of samples with $f_I = f_S$ and $0 < f_S < 1/3$. Unlike the previously mentioned SIO,[89] only a single phase separated the LAM_2 and LAM_3 morphologies in ISO.[92]

On the basis of TEM, dynamic mechanical spectroscopy, static birefringence experiments, and SAXS, the intermediate phase in the ISO system was identified as a multiply continuous, three-dimensional network, tentatively assigned *Fddd* space group symmetry. While inorganic crystal systems with this lattice had been observed, this orthorhombic morphology had not been previously identified in any block polymer or

soft material system. Further research by Epps, Cochran and coworkers[98,99] refined the *Fddd* model and established a broad window of composition space over which O^{70} was stable. Like the cubic networks, Q^{230} and Q^{214}, O^{70} is composed of three-fold connectors, but the connectors are not equal lengths and the junctions are not three-fold symmetric. Bordering the O^{70} region of composition space, areas of stability for Q^{230} ($f_I > f_S$) and Q^{214} ($f_S < f_I$) were documented. Taken together, this represented an expansive window of network morphologies in the ISO triblock terpolymer system. Synthesis and structural characterization of additional ISO samples by Chatterjee *et al.*[100] identified another network region at high O content along with terpolymers with hexagonal and BCC symmetry. A computational study using SCFT of the ISO system by Tyler *et al.*[101] agreed reasonably well with the experimental results in terms of location of the network window.

The identification of O^{70} in poly(cyclohexylethylene-*b*-ethylethylene-*b*-ethylene), a fully saturated hydrocarbon system,[102] and poly(styrene-*b*-isoprene-*b*-dimethylsiloxane)[98] attests to the universal nature of this morphology in nonfrustrated ABC triblock terpolymers.

1.3 Thesis Overview

This thesis describes the synthesis and characterization of poly(ethylene-*b*-cyclohexylethylene-*b*-dimethylsiloxane) (ECD) triblocks, CECD tetrablocks, and poly(styrene-*b*-isoprene-*b*-styrene-*b*-ethylene oxide) (SISO) tetrablock terpolymers. ECD, like the well-studied ISO, is a nonfrustrated (F^0) system ($\chi_{EC} \cong \chi_{CD} < \chi_{ED}$). The

research concerning CECD and SISO represent the first investigations of phase behavior in ABAC tetrablock terpolymers. The morphological behavior of ECD, CECD, and SISO samples were identified using a combination of small-angle X-ray scattering (SAXS), transmission electron microscopy (TEM), dynamic mechanical spectroscopy (DMS), and differential scanning calorimetry (DSC). Descriptions of these analytical methods, the synthetic procedures, and the molecular characterization techniques necessary for this work are given in Chapter 2. The synthesis and observed phase behavior of a series of five ECD triblocks and five ECD binary blends with $f_E = f_C$ and $0 \leq f_D \leq 0.28$ are presented in Chapter 3. Like the ISO system, O^{70} is observed in these materials, but over a much smaller area of composition space. Two perforated lamellar structures are also identified. Chapters 4 ($f_C = f_E$) and 5 ($f_C/f_E = 3/7$) discuss the morphological behavior of CECD tetrablock terpolymers along two different isopleths. Chapter 5 includes the identification and characterization of an orthorhombic network structure with *Pnna* symmetry. The phase behavior of SISO, an extension of the extensive work done with ISO, is given in Chapter 6. Chapter 7 summarizes and compares the key results from Chapters 3 – 6.

1.4 References

(1) Koning, C.; Van Duin, M.; Pagnoulle, C.; Jerome, R. *Prog. Polym. Sci.* **1998**, *23*, 707-757.

(2) Jerome, R. *Macromol. Eng.* **2007**, *3*, 1753-1782.

(3) Szwarc, M.; Levy, M.; Milkovich, R. *J. Am. Chem. Soc.* **1956**, *78*, 2656-2657.

(4) Hadjichristidis, N.; Pitsikalis, M.; Iatrou, H. *Adv. Polym. Sci.* **2005**, *189*, 1-124.

(5) Hadjichristidis, N.; Pitsikalis, M.; Pispas, S.; Iatrou, H. *Chem. Rev.* **2001**, *101*, 3747-3792.

(6) Hamley, I. W. *J. Phys.: Condensed Matter* **2001**, *13*, R643-R671.

(7) Holden, G.; Milkovich, R. (Shell Internationale Research Maatschappij NV, Netherlands). Rubberlike block copolymers.US Patent 3265765, August 8, 1966.

(8) Lodge, T. P. *Macromol. Chem. and Phys.* **2003**, *204*, 265-273.

(9) Chen, J. C.; Feng, X.; Penlidis, A. *Sep. Sci. Technol.* **2004**, *39*, 149-164.

(10) Beletskaya, I. P.; Kashin, A. N.; Litvinov, A. E.; Tyurin, V. S.; Valetsky, P. M.; van Koten, G. *Organometallics* **2006**, *25*, 154-158.

(11) Harrison, W. L.; Hickner, M. A.; Kim, Y. S.; McGrath, J. E. *Fuel Cells* **2005**, *5*, 201-212.

(12) Choi, Y.; Lee, S.; Lee, D.; Ishigami, Y.; Kajiuchi, T. *J. Membr. Sci.* **1998**, *148*, 185-194.

(13) Stoykovich, M. P.; Mueller, M.; Kim, S. O.; Solak, H. H.; Edwards, E. W.; de Pablo, J. J.; Nealey, P. F. *Science* **2005**, *308*, 1442-1446.

(14) Edwards, E. W.; Stoykovich, M. P.; Muller, M.; Solak, H. H.; de Pablo, J. J.; Nealey, P. F. *J. Polym. Sci. Part B* **2005**, *43*, 3444-3459.

(15) Daoulas, K. C.; Muller, M.; Stoykovich, M. P.; Park, S.; Papakonstantopoulos, Y. J.; de Pablo, J. J.; Nealey, P. F.; Solak, H. H. *Phys. Rev. Lett.* **2006**, *96*, 036104/1-036104/4.

(16) Hiemenz, P. C.; Lodge, T. P. *Polymer Chemistry*, 2nd Edition; CRC Press: Boca Raton, FL, 2007.

(17) Fredrickson, G. H.; Bates, F. S. *Ann. Rev. of Mat. Sci.* **1996**, *26*, 501-550.

(18) Hajduk, D. A.; Harper, P. E.; Gruner, S. M.; Honeker, C. C.; Kim, G.; Thomas, E. L.; Fetters, L. J. *Macromolecules* **1994**, *27*, 4063-4075.

(19) Schulz, M. F.; Bates, F. S.; Almdal, K.; Mortensen, K. *Phys. Rev. Lett.* **1994**, *73*, 86-89.

(20) Hasegawa, H.; Tanaka, H.; Yamasaki, K.; Hashimoto, T. *Macromolecules* **1987**, *20*, 1651-1662.

(21) Thomas, E. L.; Alward, D. B.; Kinning, D. J.; Martin, D. C.; Handlin, D. L., Jr.; Fetters, L. J. *Macromolecules* **1986**, *19*, 2197-2202.

(22) Hajduk, D. A.; Harper, P. E.; Gruner, S. M.; Honeker, C. C.; Thomas, E. L.; Fetters, L. J. *Macromolecules* **1995**, *28*, 2570-2573.

(23) Hamley, I. W.; Koppi, K. A.; Rosedale, J. H.; Bates, F. S.; Almdal, K.; Mortensen, K. *Macromolecules* **1993**, *26*, 5959-5970.

(24) Hajduk, D. A.; Ho, R.; Hillmyer, M. A.; Bates, F. S.; Almdal, K. *J. Phys. Chem. B* **1998**, *102*, 1356-1363.

(25) Vigild, M. E.; Almdal, K.; Mortensen, K.; Hamley, I. W.; Fairclough, J. P. A.; Ryan, A. J. *Macromolecules* **1998**, *31*, 5702-5716.

(26) Ahn, J. H.; Zin, W. C. *Macromolecules* **2000**, *33*, 641-644.

(27) Zhu, L.; Huang, P.; Cheng, S. Z. D.; Ge, Q.; Quirk, R. P.; Thomas, E. L.; Lotz, B.; Wittmann, J. C.; Hsiao, B. S.; Yeh, F.; Liu, L. *Phys. Rev. Lett.* **2001**, *86*, 6030-6033.

(28) Zhu, L.; Huang, P.; Chen, W. Y.; Weng, X.; Cheng, S. Z. D.; Ge, Q.; Quirk, R. P.; Senador, T.; Shaw, M. T.; Thomas, E. L. *Macromolecules* **2003**, *36*, 3180-3188.

(29) Mortensen, K.; Vigild, M. E. *Macromolecules* **2009**, *42*, 1685-1690.

(30) Matsen, M. W.; Bates, F. S. *Macromolecules* **1996**, *29*, 7641-7644.

(31) Hajduk, D. A.; Takenouchi, H.; Hillmyer, M. A.; Bates, F. S.; Vigild, M. E.; Almdal, K. *Macromolecules* **1997**, *30*, 3788-3795.

(32) Takenaka, M.; Wakada, T.; Akasaka, S.; Nishitsuji, S.; Saijo, K.; Shimizu, H.; Kim, M. I.; Hasegawa, H. *Macromolecules* **2007**, *40*, 4399-4402.

(33) Kim, M. I.; Wakada, T.; Akasaka, S.; Nishitsuji, S.; Saijo, K.; Hasegawa, H.; Ito, K.; Takenaka, M. *Macromolecules* **2008**, *41*, 7667-7670.

(34) Abetz, V.; Simon, P. F. W. *Adv. Polym. Sci.* **2005**, *189*, 125-212.

(35) Meier, D. J. *J. Polym. Sci., Part C: Polym. Symp.* **1969**, *26*, 81-98.

(36) Krause, S. *J. Polym. Sci., Part B: Polym. Phys.* **1969**, *7*, 249-252.

(37) Leary, D. F.; Williams, M. C. *J. Polym. Sci., Polym. Lett. Ed.* **1970**, *8*, 335-340.

(38) Helfand, E. *Macromolecules* **1975**, *8*, 552-556.

(39) Helfand, E.; Tagami, Y. *J. Chem. Phys.* **1972**, *56*, 3592-3601.

(40) Helfand, E.; Wasserman, Z. R. *Macromolecules* **1976**, *9*, 879-888.

(41) Helfand, E.; Wasserman, Z. R. *Macromolecules* **1978**, *11*, 960-966.

(42) Helfand, E.; Wasserman, Z. R. *Macromolecules* **1980**, *13*, 994-998.

(43) Leibler, L. *Macromolecules* **1980**, *13*, 1602-1617.

(44) De Gennes, P. G. *Faraday Discuss. Royal Soc. Chem.* **1979**, *68*, 96-102.

(45) Fredrickson, G. H.; Helfand, E. *J. Chem. Phys.* **1987**, *87*, 697-705.

(46) Bates, F. S.; Rosedale, J. H.; Fredrickson, G. H. *J. Chem. Phys.* **1990**, *92*, 6255-6270.

(47) Matsen, M. W.; Schick, M. *Macromolecules* **1994**, *27*, 7157-7163.

(48) Matsen, M. W.; Bates, F. S. *Macromolecules* **1996**, *29*, 1091-1098.

(49) Matsen, M. W.; Bates, F. S. *J. Chem. Phys.* **1997**, *106*, 2436-2448.

(50) Cochran, E. W.; Garcia-Cervera, C. J.; Fredrickson, G. H. *Macromolecules* **2006**, *39*, 2449-2451.

(51) Khandpur, A. K.; Förster, S.; Bates, F. S.; Hamley, I. W.; Ryan, A. J.; Bras, W.; Almdal, K.; Mortensen, K. *Macromolecules* **1995**, *28*, 8796-8806.

(52) Ryu, C. Y.; Lee, M. S.; Hajduk, D. A.; Lodge, T. P. *J. Polym. Sci., Part B: Polym. Phys.* **1997**, *35*, 2811-2823.

(53) Bailey, T. S. *Ph.D. Dissertation*; University of Minnesota **2001**, 1-211.

(54) Matsen, M. W.; Thompson, R. B. *J. Chem. Phys.* **1999**, *111*, 7139-7146.

(55) Matsen, M. W. *J. Chem. Phys.* **1995**, *102*, 3884-3887.

(56) Mayes, A. M.; Olvera de la Cruz, M. *J. Chem. Phys.* **1989**, *91*, 7228-7235.

(57) Mayes, A. M.; Olvera de la Cruz, M. *J. Chem. Phys.* **1991**, *95*, 4670-4677.

(58) Matsen, M. W. *J. Chem. Phys.* **2000**, *113*, 5539-5544.

(59) Gehlsen, M. D.; Almdal, K.; Bates, F. S. *Macromolecules* **1992**, *25*, 939-943.

(60) Matsushita, Y.; Nomura, M.; Watanabe, J.; Mogi, Y.; Noda, I.; Imai, M. *Macromolecules* **1995**, *28*, 6007-6013.

(61) Mai, S.; Mingvanish, W.; Turner, S. C.; Chaibundit, C.; Fairclough, J. P. A.; Heatley, F.; Matsen, M. W.; Ryan, A. J.; Booth, C. *Macromolecules* **2000**, *33*, 5124-5130.

(62) Laurer, J. H.; Hajduk, D. A.; Fung, J. C.; Sedat, J. W.; Smith, S. D.; Gruner, S. M.; Agard, D. A.; Spontak, R. J. *Macromolecules* **1997**, *30*, 3938-3941.

(63) Avgeropoulos, A.; Dair, B. J.; Hadjichristidis, N.; Thomas, E. L. *Macromolecules* **1997**, *30*, 5634-5642.

(64) Dair, B. J.; Honeker, C. C.; Alward, D. B.; Avgeropoulos, A.; Hadjichristidis, N.; Fetters, L. J.; Capel, M.; Thomas, E. L. *Macromolecules* **1999**, *32*, 8145-8152.

(65) Kossuth, M. B.; Morse, D. C.; Bates, F. S. *J. Rheol.* **1999**, *43*, 167-196.

(66) Dair, B. J.; Avgeropoulos, A.; Hadjichristidis, N.; Thomas, E. L. *J. Mater. Sci.* **2000**, *35*, 5207-5213.

(67) Sakurai, S.; Isobe, D.; Okamoto, S.; Yao, T.; Nomura, S. *Phys. Rev. E: Stat., Nonlinear, and Soft Matter Phys.* **2001**, *63*, 061803/1-061803/5.

(68) Matsen, M. W.; Schick, M. *Macromolecules* **1994**, *27*, 187-192.

(69) Watanabe, H. *Macromolecules* **1995**, *28*, 5006-5011.

(70) Karatasos, K.; Anastasiadis, S. H.; Pakula, T.; Watanabe, H. *Macromolecules* **2000**, *33*, 523-541.

(71) Zheng, W.; Wang, Z. *Macromolecules* **1995**, *28*, 7215-7223.

(72) Beckmann, J.; Auschra, C.; Stadler, R. *Macromol. Rapid Commun.* **1994**, *15*, 67-72.

(73) Krappe, U.; Stadler, R.; Voigt-Martin, I. *Macromolecules* **1995**, *28*, 4558-4561.

(74) Stadler, R.; Auschra, C.; Beckmann, J.; Krappe, U.; Voight-Martin, I.; Leibler, L. *Macromolecules* **1995**, *28*, 3080-3097.

(75) Breiner, U.; Krappe, U.; Abetz, V.; Stadler, R. *Macromol. Chem. Phys.* **1997**, *198*, 1051-1083.

(76) Breiner, U.; Krappe, U.; Jakob, T.; Abetz, V.; Stadler, R. *Polym. Bull.* **1998**, *40*, 219-226.

(77) Brinkmann, S.; Stadler, R.; Thomas, E. L. *Macromolecules* **1998**, *31*, 6566-6572.

(78) Auschra, C.; Stadler, R. *Macromolecules* **1993**, *26*, 2171-2174.

(79) Balsamo, V.; von Gyldenfeldt, F.; Stadler, R. *Macromolecules* **1999**, *32*, 1226-1232.

(80) Balsamo, V.; Gil, G.; Urbina de Navarro, C.; Hamley, I. W.; Von Gyldenfeldt, F.; Abetz, V.; Canizales, E. *Macromolecules* **2003**, *36*, 4515-4525.

(81) Breiner, U.; Krappe, U.; Stadler, R. *Macromol. Rapid Commun.* **1996**, *17*, 567-575.

(82) Breiner, U.; Krappe, U.; Thomas, E. L.; Stadler, R. *Macromolecules* **1998**, *31*, 135-141.

(83) Kudose, I.; Kotaka, T. *Macromolecules* **1984**, *17*, 2325-2332.

(84) Matsushita, Y.; Tamura, M.; Noda, I. *Macromolecules* **1994**, *27*, 3680-3682.

(85) Hückstädt, H.; Göpfert, A.; Abetz, V. *Polymer* **2000**, *41*, 9089-9094.

(86) Hueckstaedt, H.; Goldacker, T.; Goepfert, A.; Abetz, V. *Macromolecules* **2000**, *33*, 3757-3761.

(87) Shefelbine, T. A.; Vigild, M. E.; Matsen, M. W.; Hajduk, D. A.; Hillmyer, M. A.; Cussler, E. L.; Bates, F. S. *J. Am. Chem. Soc.* **1999**, *121*, 8457-8465.

(88) Hardy, C. M.; Bates, F. S.; Kim, M.; Wignall, G. D. *Macromolecules* **2002**, *35*, 3189-3197.

(89) Bailey, T. S.; Pham, H. D.; Bates, F. S. *Macromolecules* **2001**, *34*, 6994-7008.

(90) Bailey, T. S.; Rzayev, J.; Hillmyer, M. A. *Macromolecules* **2006**, *39*, 8772-8781.

(91) Epps, T. H.,III; Bailey, T. S.; Pham, H. D.; Bates, F. S. *Chem. Mater.* **2002**, *14*, 1706-1714.

(92) Bailey, T. S.; Hardy, C. M.; Epps, T. H.,III; Bates, F. S. *Macromolecules* **2002**, *35*, 7007-7017.

(93) Hillmyer, M. A.; Bates, F. S. *Macromolecules* **1996**, *29*, 6994-7002.

(94) Mogi, Y.; Kotsuji, H.; Kaneko, Y.; Mori, K.; Matsushita, Y.; Noda, I. *Macromolecules* **1992**, *25*, 5408-5411.

(95) Mogi, Y.; Mori, K.; Matsushita, Y.; Noda, I. *Macromolecules* **1992**, *25*, 5412-5415.

(96) Mogi, Y.; Mori, K.; Kotsuji, H.; Matsushita, Y.; Noda, I.; Han, C. C. *Macromolecules* **1993**, *26*, 5169-5173.

(97) Mogi, Y.; Nomura, M.; Kotsuji, H.; Ohnishi, K.; Matsushita, Y.; Noda, I. *Macromolecules* **1994**, *27*, 6755-6760.

(98) Epps, T. H.,III; Cochran, E. W.; Bailey, T. S.; Waletzko, R. S.; Hardy, C. M.; Bates, F. S. *Macromolecules* **2004**, *37*, 8325-8341.

(99) Epps, T. H.,III; Cochran, E. W.; Hardy, C. M.; Bailey, T. S.; Waletzko, R. S.; Bates, F. S. *Macromolecules* **2004**, *37*, 7085-7088.

(100) Chatterjee, J.; Jain, S.; Bates, F. S. *Macromolecules* **2007**, *40*, 2882-2896.

(101) Tyler, C. A.; Qin, J.; Bates, F. S.; Morse, D. C. *Macromolecules* **2007***, 40,* 4654-4668.

(102) Cochran, E. W.; Bates, F. S. *Phys. Rev. Lett.* **2004***, 93,* 087802/1-087802/4.

2

Experimental Techniques

This chapter describes the experimental techniques used to synthesize and elucidate the phase behavior of the diblock, triblock, tetrablock polymers examined in this research. The aim has been to provide general concepts regarding each technique, while reserving detailed experimental procedures to Chapters 3 – 6.

2.1 Living Anionic Polymerization

Experimental measurements of the phase behavior of block polymers are greatly improved by the synthesis of model polymers with controllable molecular weight, composition, and narrow molecular weight distributions to minimize the effects of polydispersity (PDI). Additionally, theoretical polymer models often operate under the assumption that all polymer chains have the same molecular weight, i.e., a PDI of 1. These goals can be largely achieved via living anionic polymerization for a number of monomers. Living anionic polymerization is a chain-growth polymerization mechanism characterized by the lack of undesired transfer and termination steps.[1,2] The first successful application of this approach was by Szwarc *et al*., who polymerized styrene

and isoprene over 50 years ago via electron transfer of naphthalene anions to styrene.[3] Today living anionic synthesis is commonly employed with sequential monomer addition to produce block polymers, given that there is successful crossover between one monomer to the next.

Kinetics

The rate of initiation, R_i, of a polymer system is given by:

$$R_i = k_i [\mathrm{I}][\mathrm{M}] \tag{0.2}$$

where k_i is the initiation rate constant, [I] is the initiator concentration and [M] is the concentration of monomer. Similarly, the rate of polymerization, R_p, of nonterminating living anionic systems can be expressed as:

$$R_p = k_p [\mathrm{M}^-][\mathrm{M}] \tag{0.3}$$

where k_p is the apparent propagation rate constant and $[\mathrm{M}^-]$ is the total concentration of propagating anionic species.[4] If the rate of initiation is assumed to be instantaneous compared to propagation, the concentration of propagating anionic species is equal to the initial concentration of initiator, $[\mathrm{I}]_0$. Thus, Equation (0.3) can be rewritten as:

$$R_p = k_p [\mathrm{I}]_0 [\mathrm{M}] \tag{0.4}$$

With no modes of chain transfer or termination, the number-average degree of polymerization, $\overline{X}_n$, is the ratio of concentration of reacted monomer to the concentration of initial initiator, assuming that all of the initiator has been converted to propagating species. For polymerizations initiated by electron transfer agents, $\overline{X}_n$ is given by:

$$\bar{X}_n = \frac{2p[\mathrm{M}]_0}{[\mathrm{I}]_0} \tag{0.5}$$

where p is the fractional conversion of monomer at any time. Initiation by an alkyllithium, however, is given by:

$$\bar{X}_n = \frac{p[\mathrm{M}]_0}{[\mathrm{I}]_0} \tag{0.6}$$

because only one propagating species is formed by each initiator molecule. In addition to a lack of chain transfer and termination reactions, a well-mixed living anionic system must proceed with fast initiation in the absence of depropogation to have a distribution of chain lengths given by the Poisson distribution. The resulting PDI of such an ideal system is given by:

$$\mathrm{PDI} = 1 + \frac{\bar{X}_n}{\left(\bar{X}_n + 1\right)^2} \approx 1 + \frac{1}{\bar{X}_n} \tag{0.7}$$

and would generate a narrow molecular weight distribution for any reasonably large polymer.

Monomers

Dozens of different monomers have been successfully polymerized via living anionic polymerization routes, but most are of two distinct groups: monomers possessing one or more double bonds, and heterocyclic rings. Vinyl monomers contain the necessary double bond, but must also contain an electron withdrawing group to stabilize the carbanion after initiation. Additionally, substituent groups must not be susceptible to attack by the propagating anionic species. The stability of the resulting carbanions can be

estimated from the pK_a of the corresponding conjugate acid. The smaller the pK_a of the conjugate acid, the more stable the carbanion, and thus, the more reactive the monomer is during anionic polymerization. Many moieties can also interfere with anionic polymerization, especially those with acidic protons or electrophilic groups, but monomers with these functional groups may still be polymerized anionically if the problematic group can be protected.[5]

The research described in this thesis discusses the thermodynamic behavior of AB, ABA, ABC, and ABAC block polymers consisting of poly(cyclohexylethylene) (C), poly(ethylene) (E), poly(dimethylsiloxane) (D), poly(styrene) (S), poly(isoprene) (I), and poly(ethylene oxide) (O) blocks. From these six components, two polymer systems have been developed containing E/C/D and S/I/O. All of the corresponding monomers used to produce these materials were synthesized using living anionic procedures. Additionally, synthesis of the E and C blocks required anionic polymerization and heterogeneous catalytic hydrogenation of 1,4-poly(butadiene) ($B_{1,4}$) and S, respectively. The two diene monomers used in this work, 1,3-butadiene and isoprene, are amenable to anionic polymerization because the second vinyl bond provides resonance stabilization to the propagating carbanion. Similarly, the phenyl group provides stabilization of the propagating polystyryl anion during the anionic synthesis of poly(styrene). In both of these cases polymerization is thermodynamically favorable due to the breaking of vinylic bonds. In contrast, hexamethylcyclotrisiloxane (D_3), the monomer used to produce D, and ethylene oxide are heterocyclic rings, which propogate via a ring-opening mechanism.

These monomers initiate to produce stable oxanions, but do not propagate without addition of a polar modifier.

Initiation

Many different initiators have been used in anionic polymerizations, but the most versatile and useful are alkyllithium compounds. They are efficient as anionic initiators, commercially available, and soluble in a variety of solvents, including hydrocarbons.[6] Organolithium compounds are more soluble in hydrocarbons, as compared to other alkali metals as the counter ion, because of the covalent nature of the carbon-lithium bond and the strong association of the ion pairs. However, the aggregated species are generally inactive and only unassociated species participate in initiation and propagation reactions. Generally, aggregation can be minimized by decreasing concentration, using a strongly solvating solvent, such as benzene, or by increasing the temperature of the reaction. Alkyllithium initiators, such as *sec*-butyllithium used in this work, are commonly used for the synthesis of styrene and dienes into linear polymers, but multifunctional organometallic initiators have also been used to polymerize more complex architectures, such as star polymers.[7]

Solvent Effects

The choice of solvent in an anionic polymerization can have two very important effects: the rate at which the polymerization proceeds, and the resulting regiochemistry of the polymer. As alluded to earlier, anionic polymerization in an aliphatic solvent is considerably slower than in aromatic hydrocarbons because of increased association of the initiator and propagating species. Polymerization rates can be increased by the

addition of polar solvents like tetrahydrofuran (THF), but can affect the resulting microstructure of 1,3-dienes, such as isoprene and butadiene. This effect is illustrated in Table 2.1 for poly(butadiene) polymerized in mixtures of cyclohexane and THF. In this work, the synthesis of D blocks was conducted in a 50:50 mixture of THF and cyclohexane because D_3 will only add one unit without propagating in non-polar solvents.

Table 2.1: Effects of temperature and solvent polarity on the microstructure of poly(butadiene) in cyclohexane and THF.[8]

Temperature, °C	[THF]:[Li][a]	% 1,2 addition
40	45:1	46
30	85:1	62
20	85:1	73
-55	pure THF	90

[a]Ratio of THF concentration to *sec*-butyllithium concentration.

Sequential Anionic Polymerization

Sequential anionic polymerization works well in producing block copolymers with narrow molecular weight distributions and distinct blocks, if the carbanions of the preceding block can initiate the polymerization of the next monomer. This often presents a limit on the multiblock architectures that are synthetically possible. For instance, a poly(methyl methacrylate) carbanion will not initiate the polymerization of styrene, but a polystyryl carbanion will initiate polymerization of methyl methacrylate.[4] Thus, a

poly(styrene-*b*-methyl methacrylate) diblock copolymer requires polymerization of the styrene block first.

Purification of Solvents and Monomers

For an anionic polymerization to be truly "living", all materials involved in the anionic synthesis must be very pure. Propagating anionic centers are very reactive towards common impurities such as oxygen, water, carbon dioxide, and other electrophilic substances. Purification of solvents and monomers, along with high vacuum techniques and synthesis under inert atmospheres[9] were used to produce monodisperse block copolymers, as detailed below.

Solvent purification followed the column-based approach detailed by Pangborn *et al.*[10] Cyclohexane was sparged with argon and stored under 15 psi of argon pressure. The solvent passed through two catalyst packed columns; the first packed with an oxygen scavenging copper-alumina redox catalyst (CU-0226S, Engelhard), the second with activated alumina (A15 grade) to remove moisture. Purification of THF followed the same procedure, except that the copper-alumina catalyst was omitted due to its reactivity to ether compounds and substituted with a second column of activated alumina.

Purification of the monomers in this work consisted of a rigorous, multi-step approach, which was tailored to each monomer. Styrene, isoprene, ethylene oxide, and D_3 were subjected to three freeze-pump-thaw cycles (freezing the monomer in liquid nitrogen under dynamic vacuum (<100 millitorr)) to remove dissolved oxygen. At this temperature, the solubility of gases becomes vanishingly small. Monomers were then twice stirred over purification agents for at least 30 minutes to remove inhibitors and any

remaining oxygen. Dibutylmagnesium (styrene and D_3), *n*-butyllithium (butadiene and isoprene), butylmagnesiumchloride (ethylene oxide), and calcium hydride (D_3) were used as the purification agents. The choice of purification agent and reaction conditions was dependent upon the reactivity and volatility of the monomer. D_3 is a solid at room temperature (melting point of ~60 ºC) making an elevated temperature (90 ºC) necessary to dissolve the purification agents in the liquid D_3. Due to the low vapor pressure of styrene (boiling point of 145 ºC), its purification was conducted at 40 ºC. However, the less reactive dibutylmagnesium is necessary because *n*-butyllithium can initiate polymerization of styrene. Isoprene, 1,3-butadiene, and ethylene oxide, on the other hand, are much more volatile monomers with boiling points of 34 ºC, -4.4 ºC, and 10.7 ºC, respectively. [**IMPORTANT SAFETY NOTICE:** Butadiene and ethylene oxide are toxic gases at room temperature. Extreme care should be taken with the purification and handling of these materials.] Purification of these monomers was conducted in an ice water bath to remove heat generated during the purification reaction and reduce their volatility (sufficiently in the cases of 1,3-butadiene and ethylene oxide that they could be worked with in the liquid state). Purified monomers were then transferred into evacuated, flame treated burettes and stored for up to two days away from light, at room temperature (styrene and D_3) or in a dry ice/isopropanol bath (1,3-butadiene, isoprene, and ethylene oxide).

2.2 Size Exclusion Chromatography

Size exclusion chromatography (SEC) or gel permeation chromatography (GPC), as it is also widely known, is the commonly employed characterization technique used to determine the molecular weight distributions of macromolecules. To utilize SEC, a solution containing the polymer (mobile phase) is passed through a column packed with porous particles (stationary phase). The separation of different molecular weight polymers occurs because smaller molecules permeate the porous stationary packing to a greater extent than the larger molecules. A suitable detector monitors the eluting solution and records its concentration as a function of retention volume, V_R, the volume of solvent that passes through the column prior to a particular molecular weight. Refractive index (RI) or uv-visible absorption concentration detectors have been the most commonly utilized, but are often used in conjunction with light scattering and/or viscometric detectors.[5]

SEC columns are often calibrated with a solution of polymers, such as polystyrene, with known molecular weights. However, because separation is based not directly on molecular weight, but on hydrodynamic volume, V_h, accuracy of molecular weights requires use of standards matching the analyte. This difficulty can be mitigated by the use of universal calibration. This assumes that the retention volume of a polymer is directly related to its hydrodynamic volume, which is related to a solution's intrinsic viscosity, $[\eta]$, by:

$$[\eta] \sim \frac{V_h}{M} \sim \frac{V_R}{M} \tag{0.8}$$

Combining this relationship with the Mark-Houwink equation,

$$[\eta] = kM^{a} \tag{0.9}$$

where *k* and *a* are Mark-Houwink parameters for a given polymer, yields:

$$V_R \sim kM^{1+a} \tag{0.10}$$

which can be used to determine the absolute molecular weight of any polymer based on calibration of the column with a standard polymer, if the Mark-Houwink parameters of both polymers are known. This molecular weight distribution can be used to calculate the number-average molecular weight, M_n, weight-average molecular weight, M_w, and PDI (M_w/M_n) of the polymer.

2.3 Nuclear Magnetic Resonance Spectroscopy

Nuclear magnetic resonance (NMR) spectroscopy has several common uses in polymer chemistry. Namely, real-time monitoring of the disappearance of monomer and/or appearance of polymer during polymerization, quantitative analysis of the stereoregularity of newly synthesized polymers,[4] and quantitative analysis of the relative amounts of each polymer in a multiblock copolymer. This last application of NMR spectroscopy was used in this work as will be detailed below. Additionally, proton (^{1}H) NMR spectroscopy was used to determine extent of hydrogenation of unsaturated polymer precursors as illustrated in Figure 2.1.

This valuable characterization technique is based on the ability of a sample in a magnetic field to absorb electromagnetic radiation in the radio frequency (RF) region at

distinct, diagnostic frequencies. The absorption of nuclei of ^{1}H and ^{13}C are especially relevant to polymer chemists, but NMR spectroscopy of other nuclei, such as ^{19}F and ^{31}P, is also possible. These four nuclei all have quantum spin numbers of 1/2, meaning that in an external magnetic field there are two possible spin states (against and with the external field) with an excess of spins in the lower energy level.[11] Once placed in an NMR spectrometer, a sample is pulsed with a range of RF energy, which excites the protons. As the protons return to the ground state, they release the absorbed energy. This energy is collected by a detector as a free induction decay (FID) in the time domain, but is converted to a readable spectrum in the frequency domain via a Fourier transformation. The FID and frequency domain spectrum contain information about all of the protons in the sample affected by the RF pulse, but each proton has a resonance frequency (Larmor frequency) where maximum signal intensity is obtained. The Larmor frequency of each proton is dependent upon the magnetic field that it feels, which is not exactly the same as the applied field strength. The effective field strength that each proton experiences depends on the electronic environment of the proton and the presence of other, close protons.[12] Induced magnetic fields caused by the circulation of electrons about a proton have the effect of shielding the proton, if the induced magnetic field opposes the applied field, or deshielding the proton, if the induced magnetic field enhances the applied field. By convention, the chemical shifts of protons are usually compared to the protons in tetramethylsilane, which is taken to be 0.0 ppm on the delta (δ) scale. The chemical shifts of other protons are defined as

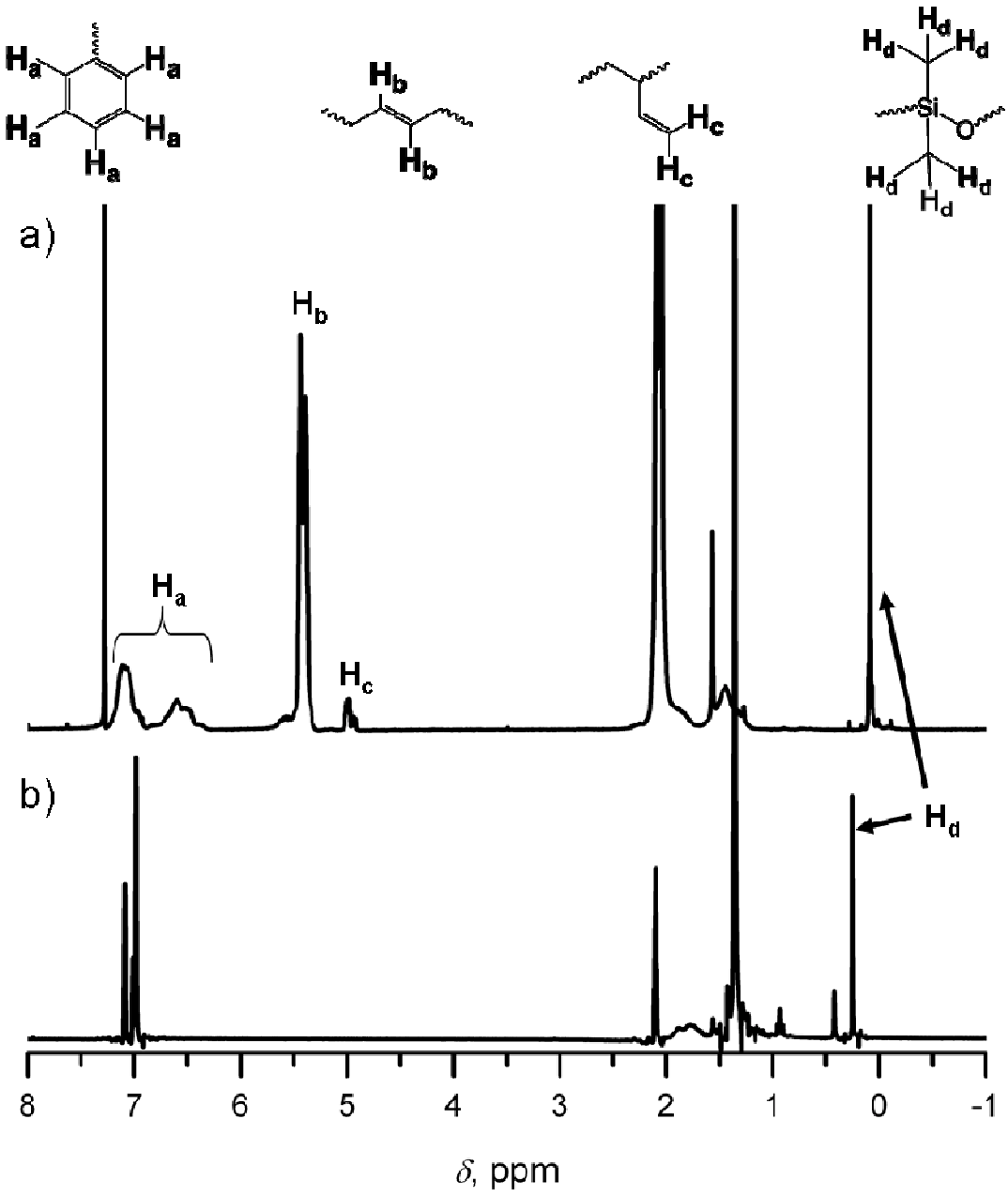

Figure 2.1: Representative ^{1}H NMR spectra for (a) $SB_{1,4}SD$ in deuterated chloroform at room temperature and b) the subsequent CECD polymer in deuterated toluene at 70 ºC. The lack of resonances between 4.5 and 7.5 ppm (besides those associated with the solvent) in (b) indicates that the polymer is completely saturated.

$$\delta = \frac{\nu^{\text{sample}} - \nu^{\text{spectrometer}}}{\nu^{\text{spectrometer}}} \qquad (0.11)$$

where ν^{sample} and $\nu^{\text{spectrometer}}$ refer to the observed frequency of the sample and the frequency at which the NMR spectrometer is operating, respectively. Thus, the chemical shift of a given proton is independent of the strength of the NMR spectrometer. The chemical shifts of distinctive chemical moieties in the polymers used in this work are shown in Table 2.2.

2.4 Differential Scanning Calorimetry

The glass transition and melting (for semicrystalline polymers) temperatures are important characteristics of a polymer, which have relevance to the processing and use temperatures of the material. Additionally, they may reveal some insights into the structure of the polymer. A common thermal analysis technique to determine these transition temperatures is differential scanning calorimetry (DSC).[5,15,16] A small amount of the polymer sample (typically, 5 – 10 mg) is placed in an aluminum pan and heated or cooled at a controlled rate. A reference material in an equivalent pan (or an empty pan) is also subjected to the same temperature variation. The differential scanning calorimeter monitors the temperature of both pans while adjusting the heat flow to the sample pan to maintain the same temperature in both pans. This is typically accomplished with a resistive heating element. If the sample undergoes a thermal transition which causes a change in the heat capacity, the magnitude of the heat flow and direction

Table 2.2: Characteristic ^{1}H NMR resonances (relative to tetramethylsilane) in deuterated chloroform at room temperature of polymers used in this research.[13,14]

Polymer	Structure	Chemical shift, ppm
poly(styrene)	-CH_2-CH(C_6**H_5**)-	6.4 - 7.2
	-CH_2-C**H**(C_6H_5)-	1.8
	-C**H_2**-CH(C_6H_5)-	1.5
poly(1,4-butadiene)	-CH_2-C**H**=C**H**-CH_2-	5.4
	-C**H_2**-CH=CH-C**H_2**-	2.0
poly(1,2-butadiene)	-CH_2-CH(C**H**=CH_2)-	5.4
	-CH_2-CH(CH=C**H_2**)-	4.9
	-CH_2-C**H**(CH=CH_2)-	2.0
	-C**H_2**-CH(CH=CH_2)-	1.2
poly(dimethylsiloxane)	-Si(C**H_3**)$_2$-O-	0.07
poly(1,4-isoprene)	-CH_2-C(CH_3)=C**H**-CH_2-	5.1
	-C**H_2**-C(CH_3)=CH-C**H_2**-	2.0
	-CH_2-C(C**H_3**)=CH-CH_2-	1.6
poly(3,4-isoprene)	-CH_2-CH(C(CH_3)=C**H_2**)-	4.7
	-CH_2-C**H**(C(CH_3)=CH_2)-	2.0
	-CH_2-CH(C(C**H_3**)=CH_2)-	1.6
	-C**H_2**-CH(C(CH_3)=CH_2)-	1.3
poly(ethylene oxide)	-CH_2-C**H_2**-O-	3.6

(exothermic or endothermic) are recorded by the DSC. Unlike low molecular weight crystalline solids, semicrystalline polymers have a broad melting range and are highly dependent on branching and side groups. For polymers the peak melting temperature is usually taken as the melting point. If the heat of fusion of the crystal phase, ΔH_m, is known, the crystallinity (X_c) of a semicrystalline block is determined by:

$$X_c = \frac{\Delta H_s}{\Delta H_m * w_c} \tag{0.12}$$

where ΔH_s is the experimentally measured heat of fusion of the sample and w_c is the weight fraction of the semicrystalline block. This is obtained by integrating the total area under the experimental melting curve obtained by DSC as shown in Figure 2.2.

2.5 Small Angle X-ray Scattering

A variety of scattering experiments are possible to determine relevant length scales, morphologies, and molecular weights of macromolecules, depending on the wavelength used for scattering. Light scattering experiments of polymer solutions can be used to yield the weight-average molecular weight and radius of gyration of the polymer and the solvent/polymer interaction parameter, χ.[5] However, smaller wavelength sources, X-rays, were used in this work to elucidate the morphology of bulk polymer samples. Though the physical principles of X-ray and light scattering are the same, the causes of scattering differ. X-rays interact with the electron clouds surrounding atomic nuclei and scatter due to differences in electron density. Light scattering, in contrast, occurs from refractive index fluctuations. An elastic (no exchange of energy between wave and medium)

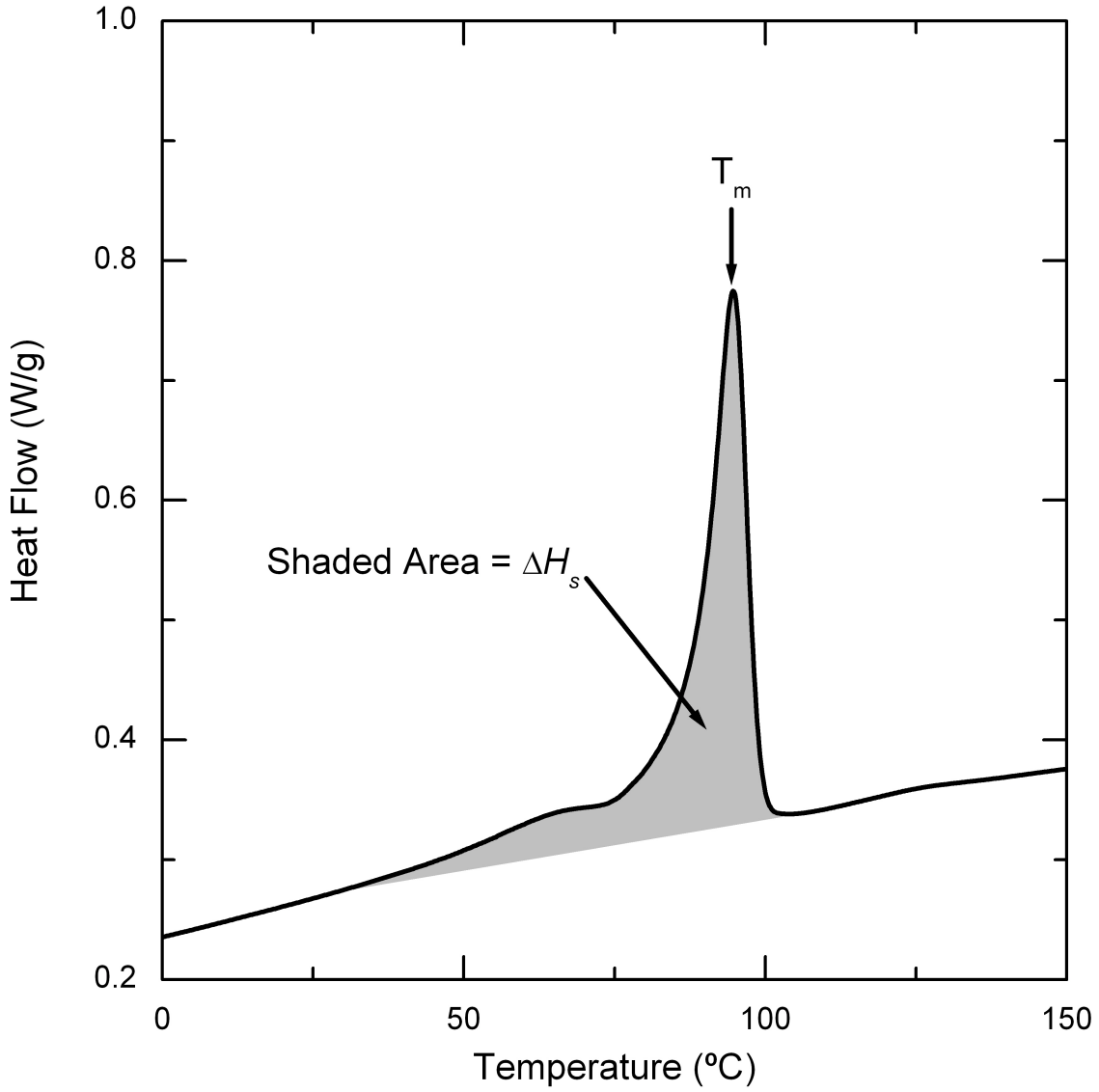

Figure 2.2: DSC trace near the melting temperature (T_m) of E for a CEC triblock copolymer collected at a heating rate of 10 ºC/min. The shaded area corresponds to the heat of fusion (ΔH_s) of the E block.

scattering event is illustrated in Figure 2.3 with relevant parameters. The incident and scattering wave vectors are denoted by $\boldsymbol{k}_i$ and $\boldsymbol{k}_s$, respectively, and their magnitudes ($\frac{2\pi}{\lambda}$, where λ is the wavelength) are equal because the scattering is elastic. The scattering vector, $\boldsymbol{q}$, is defined by the difference between the incident and scattered wave vectors:

$$\boldsymbol{q} = \boldsymbol{k}_i - \boldsymbol{k}_s \tag{0.13}$$

The scattering vector represents the amount of momentum that must be transferred into the medium along the direction of $\boldsymbol{q}$. The magnitude of $1/\boldsymbol{q}$ (units of length) is also important because it determines the structural information that can be determined by a given scattering experiment.[5] After some trigonometry, it is apparent that:

$$|\boldsymbol{q}| = \frac{4\pi}{\lambda}\sin\left(\frac{\theta}{2}\right) \tag{0.14}$$

where θ is the scattering angle.

Bulk samples, however, are composed of many scattering planes, not just isolated scattering objects. The superposition of scattering waves from the many centers in a sample yields diffraction patterns which give useful structural information concerning the arrangement of atoms in the material. The basis of the understanding scattering patterns obtained from ordered materials is Bragg's equation,[17] which will be briefly described here. Consider a wave incident on a series of parallel scattering planes (planes of high electron density for SAXS) with interplanar spacing *d* (Figure 2.4). The parallel incident rays ($\boldsymbol{k}_i$) make an angle of $\theta/2$ with these planes and the top plane is taken as the

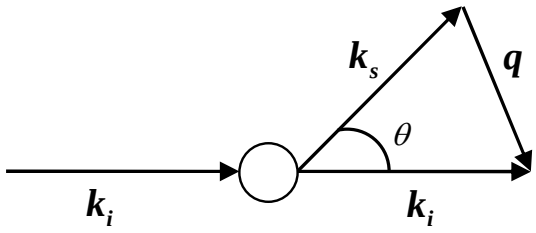

Figure 2.3: Schematic of elastic scattering from a single scattering object. $\boldsymbol{k}_i$ and $\boldsymbol{k}_s$ represent the incident and scattered wave vectors, respectively, $\boldsymbol{q}$ is the scattering vector and θ is the scattering angle.

reference. For the waves of one plane to be in phase with those of another plane and thus constructively interfere, the distance traveled by the next further plane must be $n\lambda$ larger, where n is an integer. This requirement is the basis of Bragg's law:

$$n\lambda = 2d\sin\left(\frac{\theta}{2}\right) \tag{0.15}$$

which states that a wave scattered from the $n = 1$ plane must travel an additional distance of $2d\sin(\theta/2)$ as compared to a wave scattered by the reference plane. Combining Bragg's equation with the magnitude of the scattering vector (Equation (0.14)) yields:

$$|\boldsymbol{q}| = \frac{2n\pi}{d} \tag{0.16}$$

It is clear that the length scales that can be probed by scattering experiments are limited by λ and the scattering angle θ. For a typical laboratory SAXS setup that uses Cu K_α X-rays (λ = 0.154 nm),[17] the scattering angle must be less than 5° to access the

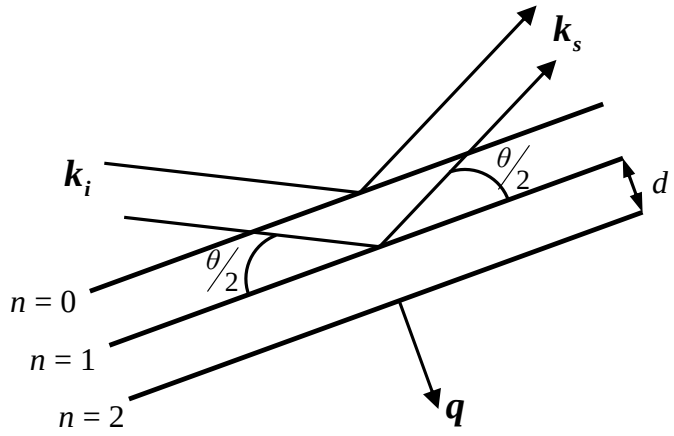

Figure 2.4: Schematic of Bragg's law. Interplanar spacing is distance *d*. The incident and scattering waves each make angle $\theta/2$ with the scattering planes. The direction of the scattering vector $\boldsymbol{q}$ is also noted.

relevant domain spacings (5 – 100 nm) of block polymers. In the laboratory, the scattering angle (and thus the range of accessible length scales) can be adjusted by modifying the sample-to-detector distance. However, the experimentally accessible range of θ is also limited by the size of the detector (determines the maximum measurable θ) and parasitic scattering surrounding the beam stop (minimum measurable θ). Conversely, wide angle X-ray scattering (WAXS) with angles of up to 90º are used to elucidate structural information on the Angstrom length scale, which is relevant to the crystallization of macromolecules.

Revisiting Bragg's Law (Equation (0.15)), it is apparent that $\sin\left(\frac{\theta}{2}\right)$ and thus the magnitude of the scattering vector, $|\boldsymbol{q}|$, are inversely proportional to *d*, the interplanar spacing in a crystal lattice. Hence, materials with large *d* yield diffraction maxima at small values of $|\boldsymbol{q}|$, whereas samples with small *d* produce reflections at large $|\boldsymbol{q}|$. Due to this inverse relationship between *d* and $|\boldsymbol{q}|$, it is convenient to introduce a reciprocal lattice based on 1/*d*. This reciprocal lattice can be defined by considering a direct (real space) lattice with the lattice parameters *a*, *b*, *c*, α, β, γ, and the volume *V* for the unit cell (Figure 2.5) and a reciprocal lattice with the lattice parameters *a**, *b**, *c**, α^*, β^*, γ^*, and the volume *V** with the same origin. This second lattice is constructed such that:

$$\begin{aligned} \boldsymbol{a}\cdot\boldsymbol{b}^* &= \boldsymbol{a}\cdot\boldsymbol{c}^* = \boldsymbol{b}\cdot\boldsymbol{c}^* = \boldsymbol{a}^*\cdot\boldsymbol{b} = \boldsymbol{a}^*\cdot\boldsymbol{c} = \boldsymbol{b}^*\cdot\boldsymbol{c} = 0 \\ \boldsymbol{a}\cdot\boldsymbol{a}^* &= \boldsymbol{b}\cdot\boldsymbol{b}^* = \boldsymbol{c}\cdot\boldsymbol{c}^* = 1 \end{aligned} \tag{0.17}$$

Additionally, the lengths of the reciprocal base vectors are defined by:

$$\boldsymbol{a}^* = \frac{\boldsymbol{b}\times\boldsymbol{c}}{V},\ \boldsymbol{b}^* = \frac{\boldsymbol{c}\times\boldsymbol{a}}{V},\ \boldsymbol{c}^* = \frac{\boldsymbol{a}\times\boldsymbol{b}}{V} \tag{0.18}$$

With these newly defined vectors, a reciprocal lattice vector $\boldsymbol{d}^*$ can be constructed from the origin to a reciprocal lattice point:

$$\boldsymbol{d}^* = h\boldsymbol{a}^* + k\boldsymbol{b}^* + l\boldsymbol{c}^* \tag{0.19}$$

where *h*, *k*, and *l* are Miller indices describing planes in the direct lattice. $\boldsymbol{d}^*$ can be used to determine the spacing d_{hkl} between Bragg planes defined by *h*, *k*, and *l*. First the vector $\boldsymbol{d}_{hkl}$ is defined in terms of direct space basis vectors $\boldsymbol{a}$, $\boldsymbol{b}$, and $\boldsymbol{c}$. Referring to the lattice plane depicted in Figure 2.6, it can be defined that:

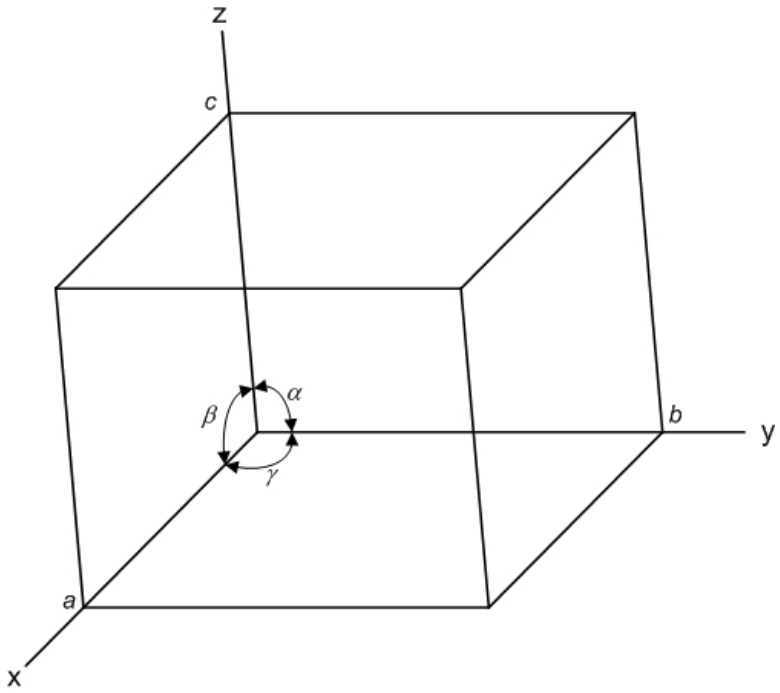

Figure 2.5: Generalized unit cell with axial lengths *a*, *b*, and *c* and interaxial angles α, β, and γ.

$$\boldsymbol{OA} = \frac{\boldsymbol{a}}{h},\ \boldsymbol{OB} = \frac{\boldsymbol{b}}{k},\ \boldsymbol{OC} = \frac{\boldsymbol{c}}{l} \tag{0.20}$$

where *h*, *k*, and *l* are again Miller indices, which provide a unique definition of the set of parallel planes. The line *BA* is represented by the vector $\left(\frac{\boldsymbol{a}}{h} - \frac{\boldsymbol{b}}{k}\right)$ and $\left(\frac{\boldsymbol{a}}{h} - \frac{\boldsymbol{c}}{l}\right)$ represents the line *CA* in the same plane. If $\boldsymbol{d}^*$ is orthogonal to the plane *ABC*, it must be normal to the non-parallel lines *BA* and *CA*. Taking the dot product of the reciprocal lattice vector and these two vectors proves this orthogonality:

$$\begin{aligned}\boldsymbol{d}^*\cdot\left(\frac{\boldsymbol{a}}{h}-\frac{\boldsymbol{b}}{k}\right)&=\left(h\boldsymbol{a}^*+k\boldsymbol{b}^*+l\boldsymbol{c}^*\right)\cdot\left(\frac{\boldsymbol{a}}{h}-\frac{\boldsymbol{b}}{k}\right)=\frac{h}{h}\boldsymbol{a}\cdot\boldsymbol{a}^*-\frac{k}{k}\boldsymbol{b}\cdot\boldsymbol{b}^*=0\\ \boldsymbol{d}^*\cdot\left(\frac{\boldsymbol{a}}{h}-\frac{\boldsymbol{c}}{l}\right)&=\left(h\boldsymbol{a}^*+k\boldsymbol{b}^*+l\boldsymbol{c}^*\right)\cdot\left(\frac{\boldsymbol{a}}{h}-\frac{\boldsymbol{c}}{l}\right)=\frac{h}{h}\boldsymbol{a}\cdot\boldsymbol{a}^*-\frac{l}{l}\boldsymbol{c}\cdot\boldsymbol{c}^*=0\end{aligned} \tag{0.21}$$

where Equation (0.19) and the definitions for the direct and reciprocal basis vectors (Equation (0.17)) are used to simplify the result. Lastly, d_{hkl} is found by projecting one of the vectors $\frac{\boldsymbol{a}}{h}$, $\frac{\boldsymbol{b}}{k}$, or $\frac{\boldsymbol{c}}{l}$ onto its normal unit vector, $\frac{\boldsymbol{d}^*}{|\boldsymbol{d}^*|}$. Combining this for $\frac{\boldsymbol{a}}{h}$ yields:

$$d_{hkl}=\frac{\boldsymbol{a}}{h}\cdot\frac{\boldsymbol{d}^*}{|\boldsymbol{d}^*|}=\frac{h\boldsymbol{a}\cdot\boldsymbol{a}^*}{h|\boldsymbol{d}^*|}=\frac{1}{|\boldsymbol{d}^*|} \tag{0.22}$$

where $|\boldsymbol{d}^*|$ can be calculated as:

$$\begin{aligned}|\boldsymbol{d}^*| &= \sqrt{\left(h\boldsymbol{a}^*+k\boldsymbol{b}^*+l\boldsymbol{c}^*\right)\cdot\left(h\boldsymbol{a}^*+k\boldsymbol{b}^*+l\boldsymbol{c}^*\right)}\\ &= \sqrt{\left(h\boldsymbol{a}^*\right)^2+\left(k\boldsymbol{b}^*\right)^2+\left(l\boldsymbol{c}^*\right)^2+2kl\boldsymbol{b}^*\cdot\boldsymbol{c}^*+2hl\boldsymbol{c}^*\cdot\boldsymbol{a}^*+2hk\boldsymbol{a}^*\cdot\boldsymbol{b}^*}\\ &= \sqrt{\left(ha^*\right)^2+\left(kb^*\right)^2+\left(lc^*\right)^2+2hka^*b^*\cos\gamma^*+2hla^*c^*\cos\beta^*+2klb^*c^*\cos\alpha^*}\end{aligned} \tag{0.23}$$

where α^*, β^*, and γ^* are the angles between and a^*, b^*, and c^* are the magnitudes of the reciprocal lattice vectors. The relationships between the direct and reciprocal space parameters have been summarized in Table 2.3.[17] Substituting the result in Equation (0.22) into Equation (0.16), which was derived from Bragg's Law yields:

$$|\boldsymbol{q}_{hkl}| = q_{hkl} = 2\pi|\boldsymbol{d}^*| = \frac{2\pi}{d_{hkl}} \tag{0.24}$$

This powerful result is the form factor ($F(\boldsymbol{q})$) and implies that diffraction may occur only when the scattering vector $|\boldsymbol{q}_{hkl}|$ equals a reciprocal lattice vector. This can be visualized in the Ewald construction, as described below.

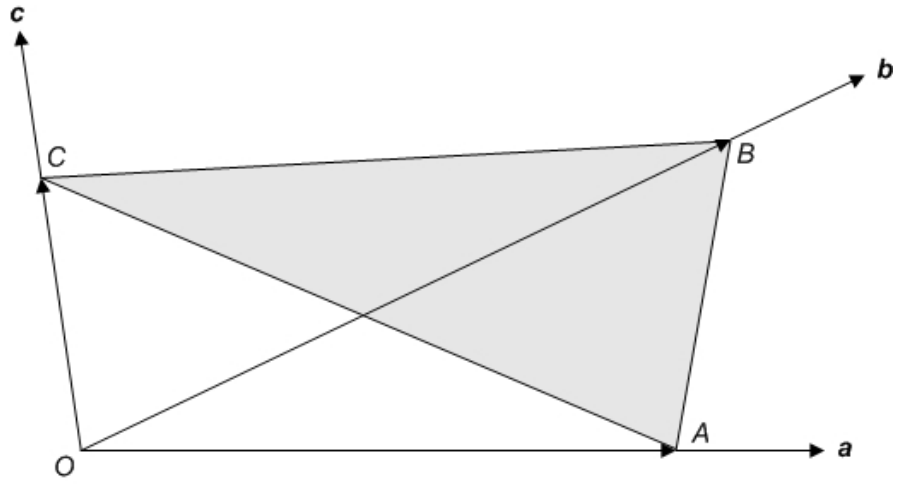

Figure 2.6: Geometrical representation of a lattice plane in terms of direct lattice basis vectors.

Table 2.3: Relationships between direct and reciprocal lattice parameters.

$a^* = \frac{bc}{V}\sin\alpha$	$\cos\alpha^* = \frac{\cos\beta\cos\gamma - \cos\alpha}{\sin\beta\sin\gamma}$
$b^* = \frac{ac}{V}\sin\beta$	$\cos\beta^* = \frac{\cos\alpha\cos\gamma - \cos\beta}{\sin\alpha\sin\gamma}$
$c^* = \frac{bc}{V}\sin\gamma$	$\cos\gamma^* = \frac{\cos\alpha\cos\beta - \cos\gamma}{\sin\alpha\sin\beta}$
$V = \frac{1}{V^*} = abc\sqrt{1-\cos^2\alpha-\cos^2\beta-\cos^2\gamma+2\cos\alpha\cos\beta\cos\gamma}$	

As shown by Equation (0.24), scattering may occur when $|\boldsymbol{q}_{hkl}|$, which is a function of the geometry of the experiment, equals a reciprocal lattice vector, which is dependent upon on the orientation and lattice parameters of the crystalline material under investigation. These two concepts can be visually combined in construction of Ewald's

sphere (Figure 2.7).[18] A sphere of radius $2\pi/\lambda$ is drawn and positioned in such a way that Bragg's Law is satisfied, and diffraction may occur, whenever a reciprocal lattice point intersects with the surface of the Ewald sphere. (The nomenclature for the vectors in Figure 2.7 is the same as those in Figure 2.3). Additionally, the Ewald sphere reveals which reflections are experimentally accessible given the experimental setup. The diameter of the Ewald sphere, $4\pi/\lambda$, dictates the lowest reflections that are detectable with a given λ. By decreasing λ, one can increase the population of experimentally accessible scattering events. The reciprocal lattice, on the other hand, can be rotated by reorienting the sample with respect to the X-ray source. An ideal polycrystalline sample contains a large number of randomly oriented crystallites, which leads to isotropic Debye-Scherrer rings.

While $F(\boldsymbol{q})$ determines allowable values of q_{hkl} that satisfy Bragg's Law for a given unit cell, the arrangement of atoms within the unit cell must also be taken into account. The repetition of atom positions may be described with one or more symmetry operations. These symmetry elements include mirror planes (*m*), inversion operations ($\bar{1}$), rotation axes (e.g., 2, a two-fold rotation), and screw axes (e.g., 2_1, a two-fold rotation with a translation of 1/2). These periodic arrangements of atoms may lead to systematic extinctions in reflections allowed by $F(\boldsymbol{q})$ due to destructive interference. The structure factor $S(\boldsymbol{q})$ accounts for these systematic cancellations and can be represented by summation over all of the atoms in the unit cell:

$$S(\boldsymbol{q}) = \sum_n f_n e^{-2\pi i(\boldsymbol{q}\cdot\boldsymbol{r}_n)} \tag{0.25}$$

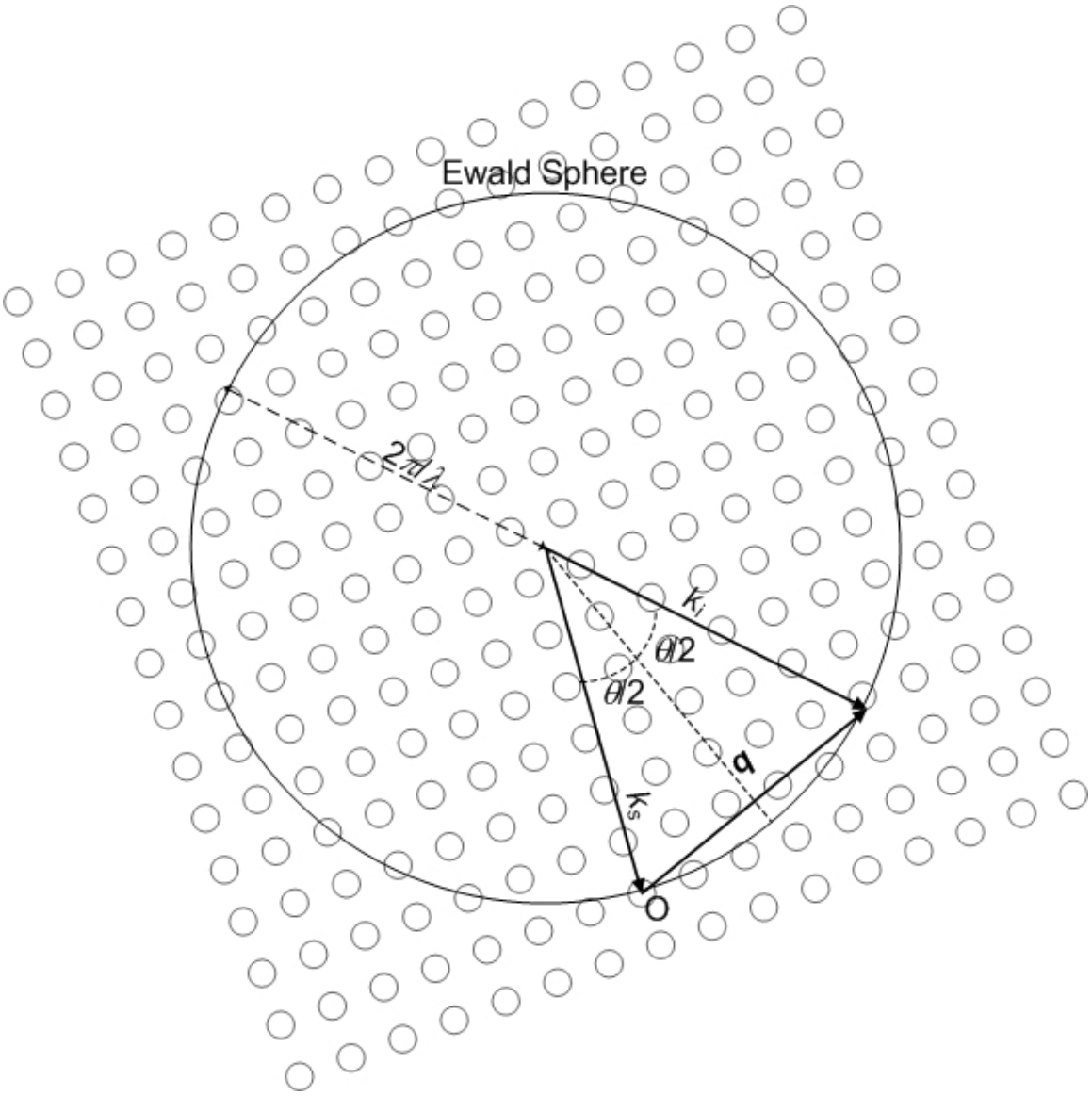

Figure 2.7: Geometrical representation of the Ewald circle in reciprocal space. The origin is marked with the *O*.

where f_n is the atomic form factor and $\boldsymbol{r_n}$ is the position of atom n in the unit cell. This equation can be rewritten for a given crystal plane with Miller indices (*hkl*):

$$S_{hkl} = \sum_n f_n e^{-2\pi i\left(hx_n + ky_n + lz_n\right)} \tag{0.26}$$

where x_n, y_n, and z_n are the fractional coordinates of atom n in the unit cell. As an example of how the structure factor affects the diffraction intensity from a specific lattice, consider the body-centered cubic system. The positions of the atoms within this unit cell can be reduced to:

$$\begin{matrix}\left(0,0,0\right) \\ \left(1/2, 1/2, 1/2\right)\end{matrix} \tag{0.27}$$

Substituting these two positions into Equation (0.26) gives:

$$\begin{aligned} S_{hkl} &= f\left(e^{-2\pi i\left(h(0)+k(0)+l(0)\right)} + e^{-2\pi i\left(h\left(1/2\right)+k\left(1/2\right)+l\left(1/2\right)\right)}\right) \\ &= f\left(1+e^{-\pi i\left(h+k+l\right)}\right) \\ &= f\left(1+\left(-1\right)^{\left(h+k+l\right)}\right) \end{aligned} \tag{0.28}$$

Thus, when $h+k+l$ is odd, S_{hkl} is zero and a reflection will not appear from a scattering plane with these Miller indices even if it satisfies Bragg's Law. Identification of systematic absences in experimental diffraction data can greatly aid in the determination of a unique space group.

In addition to $F(\boldsymbol{q})$ and $S(\boldsymbol{q})$, the scattering intensity from a sample is dependent upon the contrast within the material. As mentioned previously, X-rays diffract due to differences in electron density (κ_i). More specifically for block polymers, contrast is

derived from the square of the difference in electron densities between domains. Incorporating this factor into a relationship for scattering intensity yields:

$$\text{Intensity} \propto \left(\kappa_i - \kappa_j\right)^2 F\left(\boldsymbol{q}\right) S\left(\boldsymbol{q}\right) \tag{0.29}$$

Thus, block copolymers with constituent species that have very similar electron densities, as is the case for some polyolefins, would have very weak scattering intensities for all $\boldsymbol{q}$, even those allowed by the form and structure factors. To overcome this limitation, many researchers have relied upon small-angle neutron scattering (SANS) to characterize the morphologies of these materials.[19-21] While the physical principles of SANS are the same as SAXS, contrast in a SANS experiment is derived from differences in the scattering length densities of the nuclei in the sample.

Under certain conditions, external fields can be used to induce macroscopic alignment in a bulk block copolymer specimen, generating a "single crystal" specimen. Numerous experiments have demonstrated that shear fields are effective at reducing the number of grains in lamellae- and cylinder-forming block copolymer melts.[22-25] Additionally, reciprocating shear has been used extensively in this work to produce long-range order in block copolymer samples, which facilitated in the identification of the bulk morphology of these materials. A thorough discussion of this topic for CECD materials is presented in Chapters 4 and 5.

More frequently, ordered block copolymer samples consist of a large number of randomly oriented grains. This situation is illustrated in Figure 2.8 for a polydomain block copolymer specimen. The diffraction pattern that is generated from this "powder" sample consists of concentric Debye-Scherrer rings with isotropic intensity and radii

$|\boldsymbol{q}_{hkl}|$. These two-dimensional scattering data are typically integrated to yield a one-dimensional plot of diffraction intensity versus $|\boldsymbol{q}|$. Maxima in this plot correspond to the Bragg reflections allowed by the form factor. The intensity of each peak is a function of contrast, the structure factor, and the long-range order of the sample. The peak positions can be compared to the allowed positions of various morphologies. Thus, lattice parameters and space group symmetry can be determined from the scattering pattern generated by a powder sample.

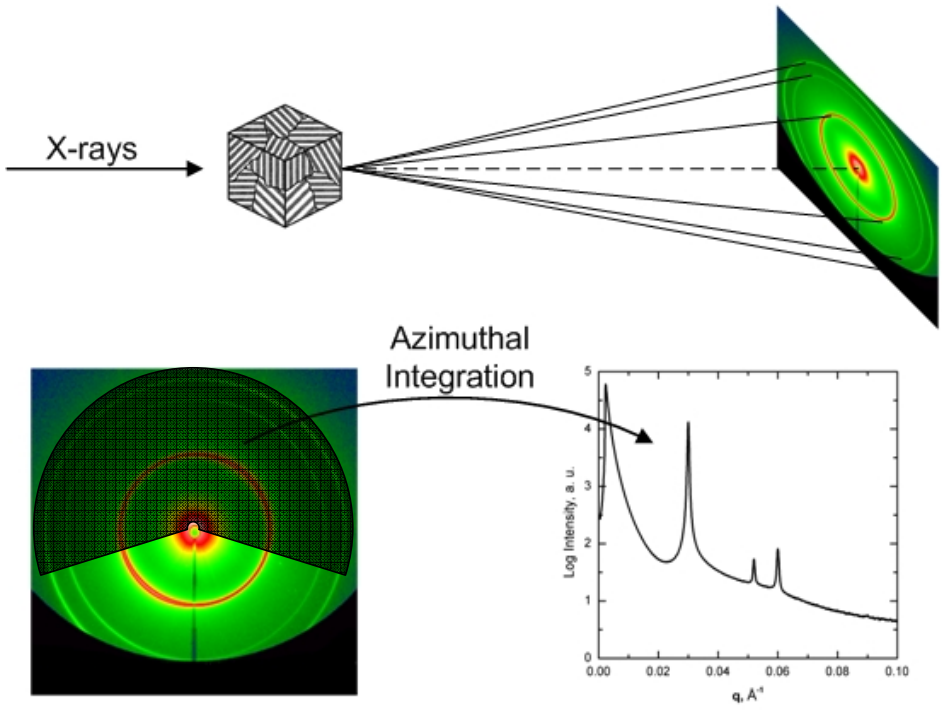

Figure 2.8: Example of a SAXS experiment on a polydomain sample depicting collection of 2D scattering data and azimuthal integration to yield 1D plot.

The general expression for q_{hkl} or d_{hkl} in terms of lattice constants and Miller indices is given by:

$$q_{hkl} = \frac{2\pi}{d_{hkl}} = 2\pi\sqrt{\left(\frac{h}{a}\right)^2 + \left(\frac{k}{b}\right)^2 + \left(\frac{l}{c}\right)^2 + 2\frac{hk}{ab}\cos\gamma^* + 2\frac{hl}{ac}\cos\beta^* + 2\frac{kl}{bc}\cos\alpha^*} \quad (0.30)$$

which was found by substituting Equation (0.23) into Equation (0.24). Equation (0.30) can be greatly simplified for the common morphologies encountered in block copolymers. For example, in the cubic crystal system (see Table 2.4) only a single unit cell length a is necessary because $a = b = c$ and $\alpha^* = \beta^* = \gamma^* = 90^\circ$. Thus, the possible reflections and d-spacing between planes are given by:

$$q_{hkl} = \frac{2\pi}{d_{hkl}} = \frac{2\pi}{a}\sqrt{h^2 + k^2 + l^2} \quad (0.31)$$

For two-dimensional hexagonally packed cylinders, $a = b$, $c = \infty$, and $\gamma^* = 60^\circ$, and Equation (0.30) reduces to:

$$q_{hkl} = \frac{2\pi}{d_{hkl}} = \frac{2\pi}{a}\sqrt{h^2 + k^2 + hk} \quad (0.32)$$

For a one-dimensional lamellar array, $b = c = \infty$ and the values of q_{hkl} and d_{hkl} are given by:

$$q_{hkl} = \frac{2\pi}{d_{hkl}} = \frac{2\pi}{a}h \quad (0.33)$$

For these three crystal systems the relative peaks positions (q_{hkl}/q_{001}) are a function of a single parameter a making fitting of SAXS data to these unit cells straightforward. The orthorhombic system, however, is a function of three lattice parameters a, b, and c (Table

2.4). The possible peak positions and d-spacing between planes for this unit cell are given by:

$$q_{hkl} = \frac{2\pi}{d_{hkl}} = 2\pi\sqrt{\left(\frac{h}{a}\right)^2 + \left(\frac{k}{b}\right)^2 + \left(\frac{l}{c}\right)^2} \tag{0.34}$$

Table 2.4: Properties of the seven crystal systems.

Crystal System	Parameters	Lattice Symmetry
Triclinic	$a \neq b \neq c;\ \alpha \neq \beta \neq \gamma$	$\bar{1}$
Monoclinic	$a \neq b \neq c;\ \alpha = \gamma = 90^o;\ \beta > 90^o$	$2/m$
Orthorhombic	$a \neq b \neq c;\ \alpha = \beta = \gamma = 90^o$	mmm
Tetragonal	$a = b \neq c;\ \alpha = \beta = \gamma = 90^o$	$4/mmm$
Trigonal		
rhombohedral lattice	$a = b = c;\ \alpha = \beta = \gamma \neq 90^o$	$\bar{3}m$
hexagonal lattice	$a = b = c;\ \alpha = \beta = 90^o;\ \gamma = 120^o$	$6/mmm$
Hexagonal	$a = b = c;\ \alpha = \beta = 90^o;\ \gamma = 120^o$	$6/mmm$
Cubic	$a = b = c;\ \alpha = \beta = \gamma = 90^o$	$m3m$

Two morphologies found in block copolymer materials possess orthorhombic symmetry.[26-30] These structures have been termed O^{70} and O^{52}, where O signifies an orthorhombic unit cell and the number represents the appropriate space group in the crystallographic tables.[31] A description of the process of fitting lattice parameters to a block copolymer sample with O^{52} symmetry is detailed in Chapter 5. The allowed reflections for several block copolymer morphologies have been listed in Table 2.5.

Table 2.5: Allowed reflections for certain block copolymer morphologies.

Morphology	Space Group	q_{hkl}	q_{hkl}/q_{001}
Lamellae ($LAM_{2,3}$)	$\bar{1}$ (1D)	$\frac{2\pi}{d}h$	1, 2, 3, 4, 5, …
BCC (S), Q^{229}	$Im\bar{3}m$	$\frac{2\pi}{d_{001}}\sqrt{h^2+k^2+l^2}$	$\sqrt{2},\ \sqrt{4},\ \sqrt{6},\ \sqrt{8},\ \sqrt{10},$ ...
Hexagonal cylinders (C)	$P6$ (2D)	$\frac{2\pi}{d_{01}}\sqrt{h^2+k^2+hk}$	$\sqrt{1}, \sqrt{3}, \sqrt{4}, \sqrt{7}, \sqrt{9},$ ...
Gyroid (G), Q^{230}	$Ia\bar{3}d$	$\frac{2\pi}{d_{001}}\sqrt{h^2+k^2+l^2}$	$\sqrt{6},\ \sqrt{8},\ \sqrt{14},\ \sqrt{16},\ \sqrt{20},$ ...
O^{52}	$Pnna$	$\frac{2\pi}{d_{001}}\sqrt{\left(\frac{c}{a}h\right)^2+\left(\frac{c}{b}k\right)^2+l^2}$	variable

2.6 Transmission Electron Microscopy

Microscopy has long been a useful tool for the generation of real space images of small structures, with the resolution of the microscope determined by the wavelength of the illumination source. Optical microscopes are limited by the wavelength of visible light (350 – 700 nm), making them impractical for materials with features on the nanometer length scale. Electron microscopy greatly extends this lower limit of resolution to the sub-nanometer realm. This has led to transmission electron microscopy (TEM) becoming the primary tool for the microstructural characterization of many block copolymer systems. However, reconstructing the spatial distribution of block copolymer domains from the two-dimensional projections generated by TEM can be difficult and sometimes misleading. Despite differences in symmetry among different phases, similar projections are possible, especially among network morphologies.[32,33] An overreliance on

TEM led to a misidentification of the gyroid phase as the ordered bicontinuous double diamond (OBDD) mesostructure in star,[34-36] linear AB,[37] and linear ABA[38] block copolymers. Thorough analysis with SAXS showed that the equilibrium morphology of some of the star block copolymers was more consistent with gyroid than OBDD.[32] Additionally, TEM only provides information on the local state of order over a very small region of the sample. Due to these potential pitfalls, complementary characterization techniques such as SAXS, which probes a much larger sample volume, should be used in conjunction with TEM to definitively determine bulk block polymer morphologies.

A simplified schematic of a TEM depicting the relevant electromagnetic lenses and apertures is shown in Figure 2.9. In a TEM instrument employing a thermionic source, electrons are generated under vacuum (~10^{-3} Pa) by resistively heating a material (traditionally tungsten, but lanthanum hexaboride is also used) to overcome its work function. An accelerating voltage (typically 50 to 400 kV) directs the high velocity electrons towards the sample. Modifying the magnetic field of the condenser lenses regulates the spread of the electron beam (the “spot size”), while the objective lens controls the magnification of the sample image. Apertures after the second condenser lens and objective lens are used to eliminate off-axis electrons leading to a better collimated beam and improved image contrast. Those electrons that do reach the sample may scatter, be absorbed, or travel unaffected through the sample. The principles are

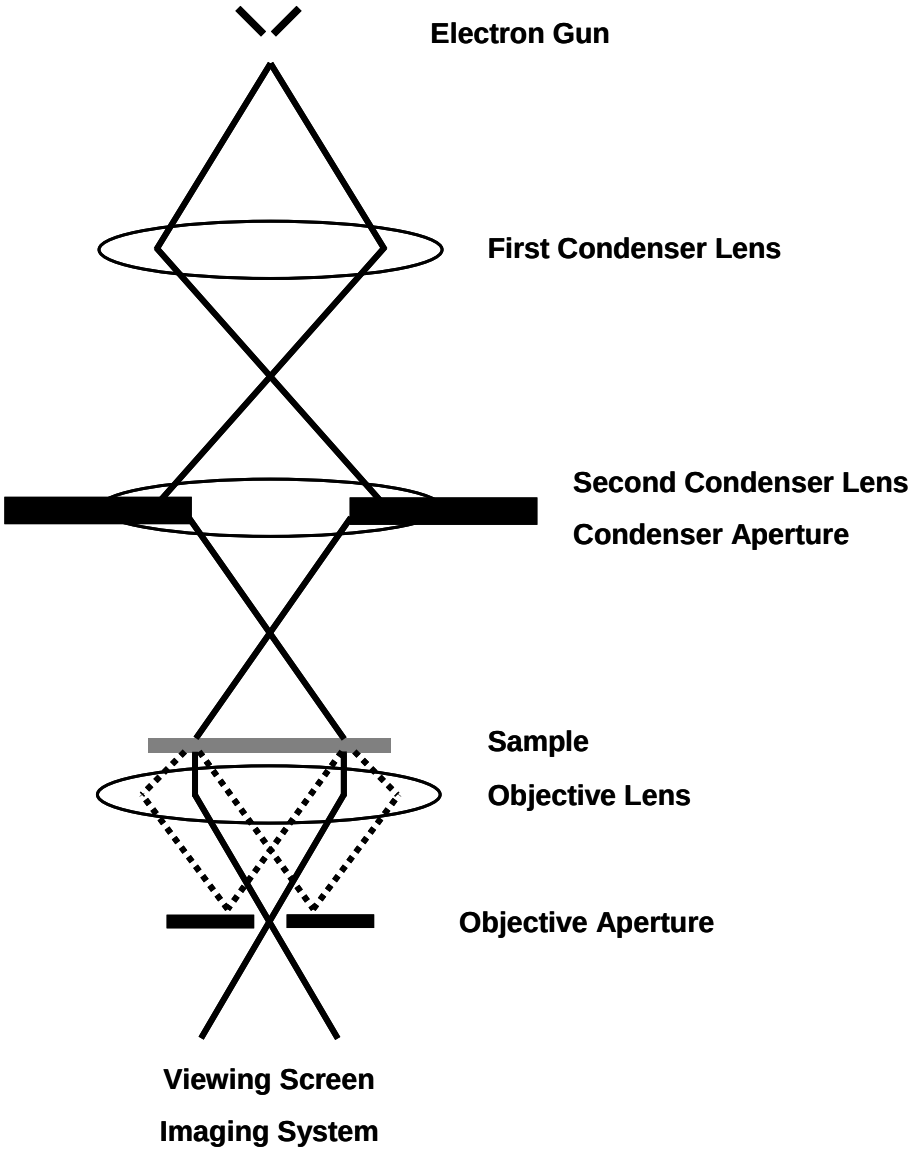

Figure 2.9: Schematic of the relevant lenses and apertures in a TEM instrument.

analogous to X-ray scattering, except that electrons interact with the entire atoms, while X-rays interact with the individual electrons surrounding atomic nuclei. The strength of this interaction is related to the differential cross section $\frac{d\sigma}{d\Omega}$, assuming only elastic scattering:

$$\frac{d\sigma(2\theta)}{d\Omega} = \frac{e^4 Z^2}{16(E_0)^2 \sin^4 \theta} \tag{0.35}$$

where 2θ is the scattering angle, e is the charge of an electron, Z is the atomic number, and E_0 is the beam energy.[39] It is apparent from this equation that heavier atoms (higher Z) scatter more intensely at higher angles. By inserting the objective aperture between the sample and the viewing screen (Figure 2.9), these high angle electrons are cut off, resulting in dark areas in TEM images.

Imaging of the D-containing block copolymers (ECD and CECD) characterized in this research was aided by the natural contrast between the D domains, which contain silicon (Z = 14), and the hydrocarbon blocks that are comprised entirely of carbon (Z = 6) and hydrogen (Z = 1) atoms. However, most block copolymers do not contain this natural contrast between domains. In these cases image contrast between blocks is typically augmented with selective stains containing heavy atoms. Two common staining agents used in TEM characterization of polymer systems, osmium tetroxide, OsO_4, and ruthenium tetroxide, RuO_4, were utilized in this work. The choice of stain is dependent upon the material under study. RuO_4 is a far stronger oxidant than OsO_4; RuO_4 will stain polymers that contain an ether, alcohol, aromatic, amine, or unsaturated moiety.[40] Conversely, OsO_4 reacts with vinylic bonds, but not aromatic moieties or ether linkages

making, it an ideal selective stain for the I block in ISO,[26,27,41] OSISO,[30] or the SISO block polymers employed in this work. TEM samples of SISO were prepared by cryo-microtoming bulk samples with a diamond knife at –70 ºC (~10 ºC below the T_g of the I block) to create thin slices (60 – 90 nm thickness). These thin sections were collected on a copper grid and exposed to a 4 wt% aqueous solution of OsO_4 for 10 minutes. This exposure time was found to provide sufficient contrast between the darkened I domains and the bright S and O domains.

A second staining technique was also employed to provide contrast between saturated hydrocarbon blocks, which lack the reactive chemical moieties to use OsO_4 or RuO_4 in the manner described above. Khandpur *et al.*[42] and Brown and Butler[43] reported similar methods of differential staining with RuO_4 vapors that could distinguish domains in fully saturated block polymers or among polyolefin blend components. RuO_4 diffuses more rapidly into amorphous domains, where the RuO_4 likely reacts with the polymer by chemical oxidation, making these areas darker compared to glassy and semicrystalline regions. To facilitate this differential diffusion process, a polished, flat surface was first created on bulk polymer samples via cryo-microtoming. These specimens were then exposed to RuO_4 vapors created by reacting 0.2 mg of ruthenium chloride with 1 mL of sodium hypochlorite in a 5 mL scintillation vial for 1 – 4 hours. [**IMPORTANT SAFETY NOTICE:** RuO_4 is highly reactive and poisonous and should be handled and disposed with extreme care.] Thin sections of stained samples were then microtomed and collected on copper grids for subsequent TEM analysis. A gradient in RuO_4 concentration

is created perpendicular to the polished face. Hence, slices with different levels of contrast could be collected from the same specimen by varying the cutting depth.

2.7 Dynamic Mechanical Spectroscopy

The subject of rheology is devoted to the study of flow and deformation of matter under the application of stress or strain. Of interest to this work is the response of a viscoelastic block polymer to an oscillatory shear field. This relationship is not only dependent upon the characteristics of the constituent blocks, but also the morphology of the polymer. Dynamic mechanical spectroscopy (DMS), or dynamic mechanical analysis (DMA) as it is also known, is a rheology experiment that utilizes sinusoidal shear to probe the viscoelastic response of polymers over a wide range of frequencies. The origin and governing equations for the viscoelastic response of materials to oscillatory shear will be described below. Readers interested in a much broader and comprehensive treatment of rheological theory and measurement techniques are directed to the text by C. W. Macosko.[44]

The two limiting cases for the response of a material to strain are viscous and elastic responses. For fluids of small molecules, energy is dissipated by friction generated by the motion of the molecules. This relationship is defined by the material's viscosity, η, which for a Newtonian fluid is independent of the shear rate ($\dot{\gamma}$):

$$\sigma = \eta\dot{\gamma} \tag{0.36}$$

where σ is the stress. In contrast, a solid under a small strain is primarily elastic, in that it will store energy and remain deformed as long as the strain is applied. The simplest relationship incorporating this relationship between force and deformation is Hooke's law:

$$\sigma = G\gamma \tag{0.37}$$

where G is the shear modulus of the material. In general, G is a function of time, temperature and strain, though for sufficiently small strains G is independent of strain. When this is the case, the system is in the linear viscoelastic regime. It is important for the modulus to be independent of strain in dynamic, oscillating experiments for the strain is constantly changing.

Polymers, however, combine the responses of both small molecule fluids and solids. When subjected to a deformation, individual polymer molecules adopt non-equilibrium conformations, which result in the loss of entropy. If allowed, the molecules will relax to their isotropic, equilibrium distribution of conformations, but this motion causes dissipation of stored elastic energy.[5] These phenomena of viscous dissipation and elasticity are what make the viscoelastic properties of polymers so unique. The simplest model to describe this viscoelastic behavior is Maxwell's model. A Maxwell element consists of a Hookean spring with spring constant $\hat{G}$ connected in series with a Newtonian dashpot with viscosity $\hat{\eta}$ (see Figure 2.10).[44] Application of an oscillatory strain to this system is represented by the function:

$$\gamma = \gamma_0 \sin(\omega t) \tag{0.38}$$

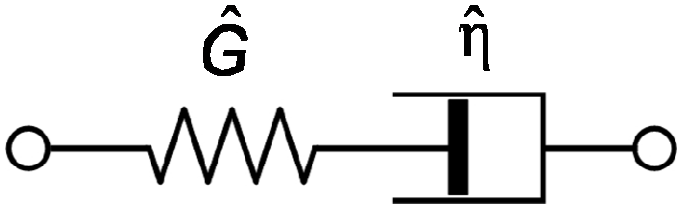

Figure 2.10: The Maxwell model for a viscoelastic material, which incorporates a Hookean spring and Newtonian dashpot with spring constant $\hat{G}$ and viscosity $\hat{\eta}$, respectively.

where ω is the frequency. The time dependent response of this system is the solution to the first order differential equation:

$$\frac{d\gamma}{dt} = \frac{1}{\hat{\eta}}\sigma + \frac{1}{\hat{G}}\frac{d\sigma}{dt} \tag{0.39}$$

Insertion of Equation (0.38) yields the solution:

$$G(\omega,\ t) = \hat{G}\frac{\omega^2\lambda^2}{1+\omega^2\lambda^2}\sin(\omega t) + \hat{G}\frac{\omega\lambda}{1+\omega^2\lambda^2}\cos(\omega t) \text{ where } \lambda \equiv \frac{\hat{\eta}}{\hat{G}} \tag{0.40}$$

The shear modulus can also be decomposed into two waves with the same frequency, one in phase with the strain (elastic or storage, G') and one 90º out of phase (viscous or loss, G''). This decomposition leads to two dynamic moduli, which together define the complex modulus, G^*:

$$\begin{aligned} G'(\omega) &= \hat{G}\frac{\omega^2\lambda^2}{1+\omega^2\lambda^2} \\ G''(\omega) &= \hat{G}\frac{\omega\lambda}{1+\omega^2\lambda^2} \\ G^* &= G' + iG'' \end{aligned} \tag{0.41}$$

Though the Maxwell model is a poor representation of any real polymer, its natural development of elastic and viscous moduli are important for these parameters are ubiquitous in the characterization of block copolymers. Additionally, λ is the characteristic relaxation time of the system. Real polymeric systems have multiple modes of relaxation (λ_i), which have been more accurately described by the Rouse model,[45]which partitions polymer chains into "submolecules" long enough to obey Gaussian statistics. Higher and higher order λ_i's correspond to smaller and smaller collections of submolecules, whereas λ_1 is the relaxation time of the entire polymer chain. Thus, in a DMS experiment there is a direct relationship between the applied frequency and the length scale that is probed. At high frequencies, G' and G'' are dominated by the shortest relaxations corresponding to the smallest length scales of the polymer chains. To interrogate the viscoelastic response at larger length scales, such as those associated with ordered block copolymers, lower frequencies (below a critical frequency ω_c) are required.

Below ω_c, block copolymer melts exhibit characteristic low-frequency linear viscoelastic properties, which are governed by the state of order.[46] In the disordered state, block copolymers demonstrate liquid-like terminal behavior ($G' \sim \omega^2, G'' \sim \omega$), indicating that the entire chain can relax to return to equilibrium conformations. However, in the ordered state, a complicated response dependent upon microstructure is observed. Zhao and coworkers demonstrated that both the gyroid and body-centered cubic sphere phases exhibit a solid-like response ($G' \sim \omega^0$) extending to low frequencies.[47] Kossuth *et al*. later reaffirmed these results for a large number of diblock and triblock copolymers and suggested that this phenomenon resulted from the three-

dimensional nature of these morphologies.[48] More recent DMS experiments on triply continuous network phases in block terpolymers have reinforced this idea.[26,27,30] However, unoriented lamellae and hexagonal cylinders display behavior intermediate to a Newtonian fluid and a solid. Experiments with lamellar samples have yielded the scaling $G' \sim G'' \sim \omega^{1/2}$,[24,47,49-51] which has also been supported by theoretical calculations.[52] In contrast, rheological measurements with polydomain hexagonal cylinders typically display the scaling relationship $G' \sim G'' \sim \omega^{1/3}$.[53,54]

Due to differences in the viscoelastic response of the block copolymer phases and the disordered state at frequencies below ω_c, DMS experiments are commonly employed to identify order-disorder (T_{ODT}) and order-order (T_{OOT}) transition temperatures. In an isochronal temperature ramp experiment, G' and G'' are measured while heating or cooling the polymer sample. A precipitous drop in G' of several orders of magnitude upon heating is characteristic of the transition from an ordered morphology to the disordered phase.[19,51,55-57] The T_{ODT} of a block copolymer is typically determined upon heating because disordering is nearly barrier-free, whereas the ordering transition is dictated by nucleation and growth kinetics.[58,59] Transitions from one ordered phase to another are also associated with discontinuous changes (may be increasing or decreasing depending on the morphologies) in G' upon heating or cooling.[60,61] Unlike order-disorder transitions, order-order transition measurements may be complicated by slow kinetics. Alternatively, the viscoelastic response of a block copolymer can be characterized with isothermal frequency scans. A typical procedure is to measure G' and G'' as a function of ω across a broad range of temperatures. The moduli collected at the various

temperatures are superimposed to make master curves of $G'(\omega)$ and $G''(\omega)$ at a reference temperature, which is referred to as time-temperature superposition (TTS).[62] While some have questioned the validity of applying TTS to block copolymer viscoelastic data because of differences in the temperature dependence of the relaxation processes of the constituent blocks,[63] it has proven useful in corroborating transition temperatures. DMS experiments can be quite useful in providing viscoelastic data which may be suggestive of certain ordered phases, but care should be taken to support presumed morphologies with additional experiments, such as SAXS and TEM.

2.8 References

(1) Lodge, T. P. *Macromol. Chem. and Phys.* **2003**, *204*, 265-273.

(2) Hadjichristidis, N.; Pitsikalis, M.; Iatrou, H. *Adv. Polym. Sci.* **2005**, *189*, 1-124.

(3) Szwarc, M.; Levy, M.; Milkovich, R. *J. Am. Chem. Soc.* **1956**, *78*, 2656-2657.

(4) Odian, G. *Principles of Polymerization*; Wiley-Interscience: Hoboken, NJ, 2004.

(5) Hiemenz, P. C.; Lodge, T. P. *Polymer Chemistry*, 2nd Edition; CRC Press: Boca Raton, FL, 2007.

(6) Hadjichristidis, N.; Iatrou, H.; Pispas, S.; Pitsikalis, M. *J. Polym. Sci. Part A* **2000**, *38*, 3211-3234.

(7) Hadjichristidis, N.; Pitsikalis, M.; Pispas, S.; Iatrou, H. *Chem. Rev.* **2001**, *101*, 3747-3792.

(8) Weimann, P. A.; Jones, T. D.; Hillmyer, M. A.; Bates, F. S.; Londono, J. D.; Melnichenko, Y.; Wignall, G. D.; Almdal, K. *Macromolecules* **1997**, *30*, 3650-3657.

(9) Ndoni, S.; Papadakis, C. M.; Bates, F. S.; Almdal, K. *Rev. Sci. Instrum.* **1995**, *66*, 1090-1095.

(10) Pangborn, A. B.; Giardello, M. A.; Grubbs, R. H.; Rosen, R. K.; Timmers, F. J. *Organometallics* **1996**, *15*, 1518-1520.

(11) Silverstein, R. M.; Webster, F. X.; Kiemle, D. J. *Spectrometric Identification of Organic Compounds;* John Wiley & Sons, Inc.: Hoboken, NJ, 2005.

(12) Morrison, R. T.; Boyd, R. N. *Organic Chemistry*; Prentice Hall: Englewood Cliffs, NJ, 1992.

(13) Hillmyer, M. A.; Bates, F. S. *Macromolecules* **1996**, *29*, 6994-7002.

(14) Gottlieb, H. E.; Kotlyar, V.; Nudelman, A. *J. Org. Chem.* **1997**, *62*, 7512-7515.

(15) Wetton, R. E. *Polymer Characterisation;* Hunt, B. J., James, M. I., Eds.; Blackie Academic & Professional: New York, 1993.

(16) Campbell, D.; White, J. R. *Polymer Characterization: Physical Techniques;* Chapman and Hall: New York, 1989.

(17) Stout, G. H.; Jensen, L. H. *X-Ray Structure Determination;* John Wiley & Sons: New York, 1989.

(18) Dinnebier, R. E.; Billinge, S. J. L., Eds.; *Powder Diffraction: Theory and Practice;* The Royal Society of Chemistry: Cambridge, UK, 2008.

(19) Almdal, K.; Bates, F. S.; Mortensen, K. *J. Chem. Phys.* **1992**, *96*, 9122-9132.

(20) Almdal, K.; Mortensen, K.; Koppi, K. A.; Tirrell, M.; Bates, F. S. *J. Phys. II* **1996**, *6*, 617-637.

(21) Papadakis, C. M.; Almdal, K.; Mortensen, K.; Vigild, M. E.; Stepanek, P. *J. Chem. Phys.* **1999**, *111*, 4319-4326.

(22) Keller, A.; Pedemonte, E.; Willmouth, F. M. *Nature* **1970**, *225*, 538-539.

(23) Hadziioannou, G.; Mathis, A.; Skoulios, A. *Colloid Polym. Sci.* **1979**, *257*, 136-139.

(24) Koppi, K. A.; Tirrell, M.; Bates, F. S.; Almdal, K.; Colby, R. H. *J. Phys. II* **1992**, *2*, 1941-1959.

(25) Tepe, T.; Schulz, M. F.; Zhao, J.; Tirrell, M.; Bates, F. S.; Mortensen, K.; Almdal, K. *Macromolecules* **1995**, *28*, 3008-3011.

(26) Bailey, T. S.; Hardy, C. M.; Epps, T. H.,III; Bates, F. S. *Macromolecules* **2002**, *35*, 7007-7017.

(27) Epps, T. H.,III; Cochran, E. W.; Bailey, T. S.; Waletzko, R. S.; Hardy, C. M.; Bates, F. S. *Macromolecules* **2004**, *37*, 8325-8341.

(28) Cochran, E. W.; Bates, F. S. *Phys. Rev. Lett.* **2004**, *93*, 087802/1-087802/4.

(29) Takenaka, M.; Wakada, T.; Akasaka, S.; Nishitsuji, S.; Saijo, K.; Shimizu, H.; Kim, M. I.; Hasegawa, H. *Macromolecules* **2007**, *40*, 4399-4402.

(30) Meuler, A. J.; Fleury, G.; Hillmyer, M. A.; Bates, F. S. *Macromolecules* **2008**, *41*, 5809-5817.

(31) Hahn, T., Ed.; *International Tables for X-ray Crystallography;* Kluwer Academic Publishers: Boston, MA, 1992.

(32) Hajduk, D. A.; Harper, P. E.; Gruner, S. M.; Honeker, C. C.; Thomas, E. L.; Fetters, L. J. *Macromolecules* **1995**, *28*, 2570-2573.

(33) Cochran, E. W. *Ph.D. Dissertation*; University of Minnesota **2004**, 1-316.

(34) Thomas, E. L.; Alward, D. B.; Kinning, D. J.; Martin, D. C.; Handlin, D. L., Jr.; Fetters, L. J. *Macromolecules* **1986**, *19*, 2197-2202.

(35) Alward, D. B.; Kinning, D. J.; Thomas, E. L.; Fetters, L. J. *Macromolecules* **1986**, *19*, 215-224.

(36) Herman, D. S.; Kinning, D. J.; Thomas, E. L.; Fetters, L. J. *Macromolecules* **1987**, *20*, 2940-2942.

(37) Hasegawa, H.; Tanaka, H.; Yamasaki, K.; Hashimoto, T. *Macromolecules* **1987**, *20*, 1651-1662.

(38) Xie, R.; Yang, B.; Jiang, B. *Macromolecules* **1993**, *26*, 7097-7099.

(39) Williams, D. B.; Carter, C. B. *Transmission Electron Microscopy: A Textbook for Materials Science;* Plenum Press: New York, 1996.

(40) Trent, J. S.; Scheinbeim, J. I.; Couchman, P. R. *Macromolecules* **1983**, *16*, 589-598.

(41) Chatterjee, J.; Jain, S.; Bates, F. S. *Macromolecules* **2007**, *40*, 2882-2896.

(42) Khandpur, A. K.; Macosko, C. W.; Bates, F. S. *J. Polym. Sci. Part B* **1995**, *33*, 247-252.

(43) Brown, G. M.; Butler, J. H. *Polymer* **1997**, *38*, 3937-3945.

(44) Macosko, C. W. *Rheology: Principles, Measurements and Applications;* Advances in Interfacial Engineering; Wiley-VCH: New York, 1994.

(45) Rouse, P. E., Jr. *J. Chem. Phys.* **1953**, *21*, 1272-1280.

(46) Fredrickson, G. H.; Bates, F. S. *Ann. Rev. of Mat. Sci.* **1996**, *26*, 501-550.

(47) Zhao, J.; Majumdar, B.; Schulz, M. F.; Bates, F. S.; Almdal, K.; Mortensen, K.; Hajduk, D. A.; Gruner, S. M. *Macromolecules* **1996**, *29*, 1204-1215.

(48) Kossuth, M. B.; Morse, D. C.; Bates, F. S. *J. Rheol.* **1999**, *43*, 167-196.

(49) Bates, F. S.; Rosedale, J. H.; Fredrickson, G. H. *J. Chem. Phys.* **1990**, *92*, 6255-6270.

(50) Rosedale, J. H.; Bates, F. S. *Macromolecules* **1990**, *23*, 2329-2338.

(51) Patel, S. S.; Larson, R. G.; Winey, K. I.; Watanabe, H. *Macromolecules* **1995**, *28*, 4313-4318.

(52) Kawasaki, K.; Onuki, A. *Phys. Rev. A: At., Mol., and Opt. Phys.* **1990**, *42*, 3664-3666.

(53) Morrison, F. A.; Winter, H. H.; Gronski, W.; Barnes, J. D. *Macromolecules* **1990**, *23*, 4200-4205.

(54) Ryu, C. Y.; Lee, M. S.; Hajduk, D. A.; Lodge, T. P. *J. Polym. Sci. Part B* **1997**, *35*, 2811-2823.

(55) Almdal, K.; Rosedale, J. H.; Bates, F. S. *Macromolecules* **1990**, *23*, 4336-4338.

(56) Winter, H. H.; Scott, D. B.; Gronski, W.; Okamoto, S.; Hashimoto, T. *Macromolecules* **1993**, *26*, 7236-7244.

(57) Foerster, S.; Khandpur, A. K.; Zhao, J.; Bates, F. S.; Hamley, I. W.; Ryan, A. J.; Bras, W. *Macromolecules* **1994**, *27*, 6922-6935.

(58) Kim, W. G.; Chang, M. Y.; Garetz, B. A.; Newstein, M. C.; Balsara, N. P.; Lee, J. H.; Hahn, H.; Patel, S. S. *J. Chem. Phys.* **2001**, *114*, 10196-10211.

(59) Cochran, E. W.; Bates, F. S. *Macromolecules* **2002**, *35*, 7368-7374.

(60) Hillmyer, M. A.; Bates, F. S.; Almdal, K.; Mortensen, K.; Ryan, A. J.; Fairclough, J. P. A. *Science* **1996**, *271*, 976.

(61) Sakamoto, N.; Hashimoto, T.; Han, C. D.; Kim, D.; Vaidya, N. Y. *Macromolecules* **1997**, *30*, 1621-1632.

(62) Williams, M. L.; Landel, R. F.; Ferry, J. D. *J. Am. Chem. Soc.* **1955**, *77*, 3701-3707.

(63) Han, C. D.; Kim, J. K. *Polymer* **1993**, *34*, 2533-2539.

3

Morphological Behavior of Neat Triblocks and Binary Blends of Poly(ethylene-*b*-cyclohexylethylene-*b*-dimethylsiloxane) Terpolymers

3.1 Introduction

ABC triblock terpolymers have proven especially interesting due to their ability to produce a multitude of periodic microstructures with a wide variety of mechanical, chemical, and physical characteristics. However, the large parameter space presented by ABC triblocks has been daunting for both experimentalists and theoreticians. Systematic experimental investigation of block polymer phase behavior requires the laborious synthesis and characterization of many samples. As documented in Chapter 1, early investigations were typically limited in terms of the effects that composition, molecular weight, block sequence, and temperature have on ABC morphological behavior (an exception to this are the extensive studies done by Mogi and coworkers[1-3]). Additionally, many reports have dealt with strongly-segregated polymer systems that relied on solvent-

casting as a means of inducing microstructural ordering.[1,3-19] In some cases the choice of solvent clearly affected the observed morphology,[8,12,15] making realization of the equilibrium phase uncertain. To mitigate these problems, Bates and coworkers have typically studied ABC triblock systems in the weak or intermediate segregation strength regimes where the disordered state is experimentally accessible. This approach was previously utilized to map the phase behavior of an AB diblock copolymer system.[20,21] Additionally, a new synthetic strategy, the growth of ethylene oxide from a hydroxyl-terminated macromolecule,[22] has allowed the creation of sequences of ABC triblocks that differed only in C chain length. This technique was used to characterize the phase behavior of poly(styrene-*b*-isoprene-*b*-ethylene oxide) (SIO) along the $f_S = f_I$ isopleth,[23] where f_S and f_I are the volume fractions of the S and I blocks, respectively, and ISO over a wide range of composition space.[24-26] Comparison of SIO and ISO with similar compositions demonstrated that changes in block sequencing can cause strikingly different phase behavior.

This chapter focuses on the morphological behavior of a series of poly(ethylene-*b*-cyclohexylethylene-*b*-dimethylsiloxane) (ECD) terpolymers with $f_E \cong f_C$ and $0 \leq f_D \leq 0.28$. These ECD triblocks were synthesized from a single batch of diblock copolymer to ensure that there was no difference in the size and distribution of the E and C blocks. Additional binary blends of consecutive ECD triblocks were prepared to create samples with intermediate compositions. These approaches greatly reduced the synthetic demands required for a systematic investigation of phase behavior. ECD triblocks are an example of a "nonfrustrated" terpolymer system[27] because $\chi_{EC} \cong \chi_{CD} < \chi_{ED}$, where χ is the

segment-segment interaction parameter. (See Chapter 1 for a detailed discussion of the classifications of ABC triblocks). We anticipated qualitatively similar morphological behavior as other nonfrustrated triblock terpolymers with comparable compositions. This includes the well-investigated ISO system in which O^{70}, an orthorhombic network morphology possessing *Fddd* symmetry, was documented along the $f_I = f_S$ isopleth.[24,25] Network structures are interesting due to their multiply continuous domains, which offer the opportunity to create semipermeable membranes and low-density optical materials. An additional consideration for the ECD system was the preparation of nanoporous monoliths via chemical etching of the D block.[28,29] These potential applications make the identification of network regions in ECD and other nonfrustrated terpolymer systems especially attractive.

In this chapter we present the phase assignments made for five ECD triblocks and five triblock blends on the basis of a combination of small-angle X-ray scattering (SAXS), transmission electron microscopy (TEM), and dynamic mechanical spectroscopy (DMS) experiments. Rheological measurements were used to locate morphological transitions (order-order and order-disorder) and establish the frequency-dependent behavior of the samples. In most samples, conclusive identification of the morphology was possible based on Bragg scattering generated during SAXS experiments. TEM provided complementary visual evidence to support microstructure assignments. Deviations in phase behavior between ECD and ISO are rationalized on the basis of the magnitudes of the χ parameters in the two systems.

3.2 Experimental Section

3.2.1 Block Polymer Synthesis

Synthesis of the polymers utilized in this chapter was accomplished through sequential anionic polymerization of 1,3-butadiene, styrene, and hexamethylcyclotrisiloxane (D_3), followed by catalytic hydrogenation to generate saturated block polymers as detailed in Figure 3.1. Styrene, 1,3-butadiene, D_3, cyclohexane, and tetrahydrofuran were rigorously purified as described elsewhere.[30,31] 1,3-butadiene was initiated by *sec*-butyllithium and polymerized (93% 1,4 addition) in cyclohexane at 40 ºC under an argon atmosphere. An aliquot of the first block was removed after 16 hours for analysis by size-exclusion chromatography before proceeding with the addition of styrene, also at 40 ºC. After 16 hours, the reaction media was divided into separate reactors via cannulation, prior to the polymerization of the dimethylsiloxane block. This ensures that the triblock terpolymers differ only in volume fraction of the third block. Measured amounts of D_3 were added to each reactor and allowed to stir for 12 hours at 20 ºC, resulting in the incorporation of one D_3 unit to each polymer chain. Propagation was then achieved by adding tetrahydrofuran (equivalent to the volume of cyclohexane) to the reaction media. The propagation step was stopped after 4 hours by adding excess chlorotrimethylsilane, resulting in a conversion of ~50% of D_3 monomer. The precursor terpolymer was recovered by precipitation into a 3:1 solution of methanol and 2-propanol, followed by filtration, and complete drying under dynamic vacuum. Hydrogenation of the

poly(butadiene-*b*-styrene-*b*-dimethylsiloxane) precursor triblocks in cyclohexane at 170 ºC over a silica-supported platinum/rhenium catalyst[32] (Dow Chemical Co.) resulted in the desired poly(ethylene-*b*-cyclohexylethylene-*b*-dimethylsiloxane) (ECD) triblock terpolymers. The ECD polymers were precipitated in methanol, filtered, and dried under dynamic vacuum. An EC diblock copolymer was made in an analogous manner except for the addition and polymerization of D_3. Instead, the SB precursor diblock copolymer was produced by cannulating the living reaction media into excess degassed methanol. This reaction scheme resulted in a series of homologous ECD triblock copolymers containing a common EC diblock core and varying D chain lengths.

3.2.2 Molecular Characterization

Molecular weight distributions of the initial butadiene block, the SB diblock, and the BSD triblock terpolymers were obtained by size exclusion chromatography (SEC) on a Waters 717 GPC equipped with three Polymer Labs Mixed-C columns and a Waters 410 differential refractometer. Samples were run at 30 ºC with a flow rate of 1.0 mL/min using tetrahydrofuran as the mobile phase. Polydispersities were estimated using ten poly(styrene) standards (Polymer Laboratories). SEC traces of the EC and ECD block polymers obtained at 135 ºC in 1,2,4-trichlorobenzene on a Polymer Laboratories PL-GPC-220 were monomodal, confirming that degradation does not occur during hydrogenation (see Figure 3.2 for representative SEC traces).

Quantitative compositions of the unsaturated SB and BSD block polymers were determined using ^{1}H NMR spectroscopy on a Varian UNITY 300 spectrometer at room

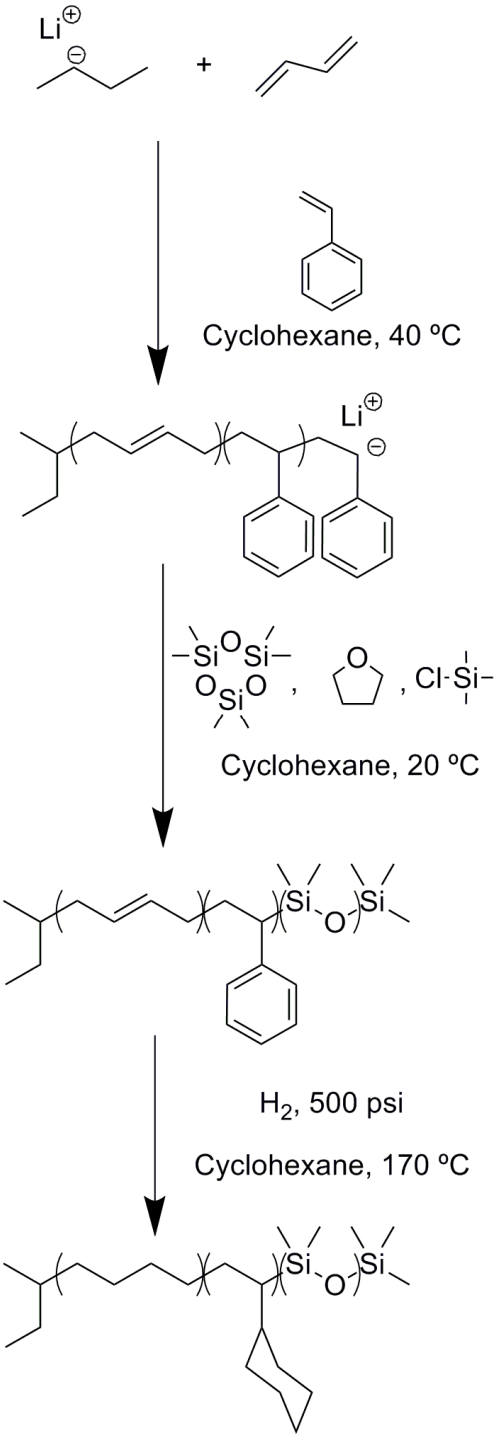

Figure 3.1: Two-step synthesis scheme employing sequential anionic polymerization and catalytic hydrogenation to produce ECD triblock terpolymers.

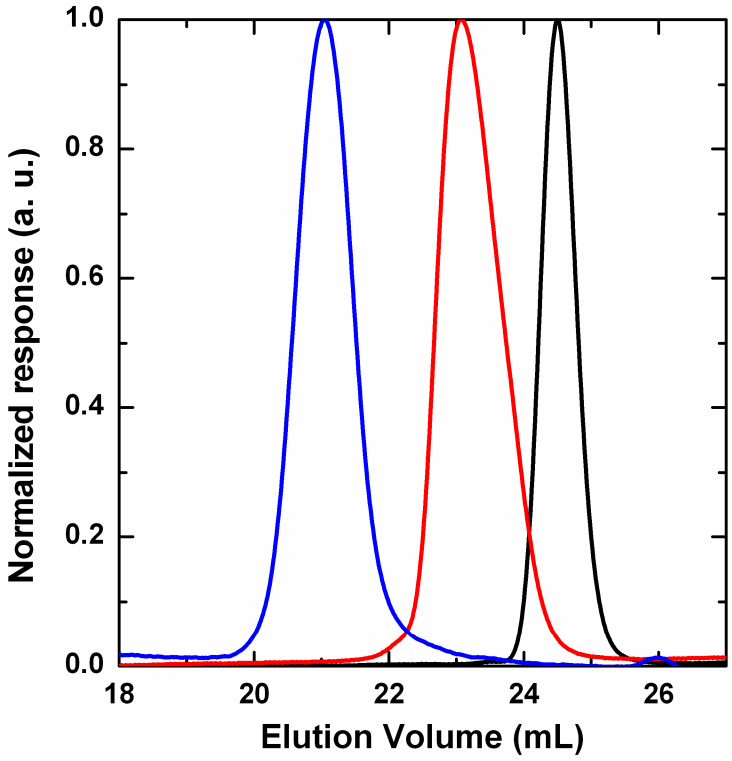

Figure 3.2: SEC traces for B aliquot (black curve), BSD triblock (red curve), and ECD triblock (blue curve). The B aliquot and BSD triblock data were collected at 30 ºC on a GPC using tetrahydrofuran as the eluent, whereas the ECD trace was obtained on a separate GPC with 1,2,4-trichlorobenzene at 135 ºC as the mobile phase.

temperature with a pulse repetition delay of 20 s. Samples were dissolved in deuterated chloroform. Volume fractions of poly(styrene), 1,4-poly(butadiene), and poly(dimethylsiloxane) were determined from measured mole fractions using homopolymer densities at 140 ºC.[33] ^{1}H-NMR spectroscopy at 70 ºC in deuterated toluene using a Varian INOVA 300 spectrometer confirmed the extent of hydrogenation for the

EC and ECD block polymers to be greater than 97%. The molecular characterization data for the block polymers utilized in this chapter are summarized in Table 3.1.

3.2.3 Blend Preparation

Binary mixtures of consecutive ECD triblocks were prepared by codissolution in benzene at 70 ºC followed by freeze-drying under dynamic vacuum in 20 mL vials.

3.2.4 Thermal Analysis

Calorimetry experiments were conducted with a TA Instruments Q1000 differential scanning calorimeter. A measured amount of polymer powder (5 – 10 mg) was heated to 170 ºC to erase the sample thermal history prior to cooling to –150 ºC at 10 ºC/min. Data were acquired upon second heating at a temperature ramp rate of 10 ºC/min. The degree of crystallinity within the E domains was determined by the integration of the melting peaks and referencing to the heat of fusion of bulk poly(ethylene) (277 J/g).[34]

3.2.5 Dynamic Mechanical Spectroscopy (DMS)

All DMS experiments were performed on a Rheometrics Scientific ARES rheometer configured with 25 mm diameter parallel plates. Measurements were made under a constant blanket of nitrogen to mitigate polymer degradation at elevated temperatures. Powder polymer samples were loaded onto the plates and melted at 150 ºC prior to heating to 10 ºC above the T_{ODT} at a rate of 10 ºC/min. The specimen was then held at this temperature for 10 minutes and quickly cooled well below the T_{ODT} to erase the thermal history of the sample. Isochronal (ω = 1 rad/s) measurements of the dynamic

elastic (G') and loss (G'') moduli were collected at a heating rate of 2 ºC/min with a strain amplitude of 1%, which was determined to be within the linear viscoelastic regime. Isothermal frequency sweeps ($100 \leq \omega \leq 0.1$ rad/s) were conducted on heating over a range of temperatures in 10 or 20 ºC increments to characterize the linear viscoelastic response of the polymer.

3.2.6 Small-angle X-ray Scattering (SAXS)

SAXS experiments were conducted at the Advanced Photon Source at Argonne National Laboratory using the instruments maintained by the DuPont-Northwestern-Dow Collaborative Access Team (DND-CAT). An X-ray wavelength (λ) of 0.729 Å and a sample-to-detector distance of 5.504 m were utilized in these measurements. Two-dimensional data were acquired with a Mar CCD area detector. A DSC chamber with a helium purge was employed to control the sample temperature. Two-dimensional diffraction patterns were azimuthally averaged and are reported in this chapter as plots of intensity as a function of the magnitude of the scattering wave vector $|\boldsymbol{q}| = q = 4\pi\lambda^{-1}\sin(\theta/2)$, where θ is the scattering angle.

Samples were prepared as 1 mm thick films for investigation by SAXS. The films were formed by compression-molding polymer powder between Teflon sheets at 2000 psi for 5 – 6 min at temperatures approximately 10 ºC above the ODT. The molded samples were then annealed under vacuum for 18 hours below the ODT before quenching into liquid nitrogen to crystallize the E block and fix the ordered phase. Once loaded into the

DSC chamber of the synchrotron SAXS line, specimens were heated from room temperature to target temperatures and held there for 2 – 5 min prior to data collection.

3.2.7 Transmission Electron Microscopy (TEM)

TEM micrographs of select samples were collected on two microscopes: a JEOL 1210 and a JEOL 1200 EXII. Both instruments were operated at an accelerating voltage of 120 kV. The compression-molded, annealed samples investigated by SAXS were also used for TEM. Bulk specimens were initially cryo-microtomed at –120 ºC on a Reichart ultramicrotome fitted with a Microstar diamond knife to create a flat surface. Some samples were stained with ruthenium tetroxide vapors for 1.5 hours to obtain sufficient electron mass density contrast between the different blocks.[35-37] Stained pieces were microtomed at room temperature to create thin sections (70 – 90 nm thickness), which were collected on copper grids (Ted Pella) for subsequent TEM analysis. This method produced films that were typically not uniform in thickness with many defects (i.e., holes), as discussed in the Results and Analysis section. Thin sections of unstained samples generated by cryo-microtoming at –120 ºC proved to be more uniform. Unstained ECD specimens have natural contrast between D and the other polymer domains due to the higher electron density of silicon.

3.3 Results and Analysis

The parent EC diblock, five ECD triblocks, and five binary blends of consecutive ECD triblocks (Table 3.1) were used to examine the phase behavior of ECD along the

Table 3.1: Characterization data for ECD triblock terpolymers and binary blends.

Polymer[a]	M_n, kDa	M_w/M_n	f_E[b]	f_C[b]	f_D[b]	Phase[c]	T_{OOT}, ºC[d]	T_{ODT}, ºC[d]	Lattice dimensions, nm[e,f]
EC	11.0	1.12	0.50	0.50	0	LAM		161	18.4
ECD-1	11.3	1.11	0.49	0.48	0.03	LAM		154	18.1
Blend A	11.6	1.11	0.48	0.47	0.05	LAM		150	17.8
Blend B	11.9	1.10	0.47	0.46	0.07	LAM		144	17.8
ECD-2	12.2	1.10	0.46	0.45	0.09	LAM		140	17.5
ECD-3	12.9	1.09	0.43	0.43	0.14	LAM		150	17.3
ECD-4	13.4	1.08	0.41	0.42	0.17	LAM		158	17.3
Blend C	14.1	1.08	0.40	0.39	0.21	LAM		168	18.1
Blend D	14.6	1.08	0.38	0.38	0.24	S-LAM		179	1.06, 18.0 (160)
Blend E	15.1	1.08	0.37	0.37	0.26	S-LAM → O^{70}	182	225	0.274, 0.555, 77.9 (200)
ECD-5	15.4	1.08	0.36	0.36	0.28	S-LAM → O^{70}	204	266	0.269, 0.544, 80.8 (220)

[a]ECD triblocks were synthesized from single EC diblock.

[b]Volume fractions were calculated from published melt density data at 140 ºC (ρ_C = 0.920 g/cm^3, ρ_E = 0.784 g/cm^3, and ρ_D = 0.895 g/cm^3).[33]

[c]LAM: lamellae; S-LAM: spheres in lamellae; O^{70}: orthorhombic network.

[d]Order-order and order-disorder transition temperatures determined by DMS.

[e]Temperature is 120 ºC unless otherwise listed in parentheses (ºC).

[f]Lattice dimensions listed for Blend D and O^{70} specimens correspond to *a*/*c* and *c* and *a*/*c*, *b*/*c*, and *c*, respectively.

symmetric $f_E = f_C$ isopleth. We have employed blending to avoid additional synthetic efforts and to characterize morphological behavior at compositions between synthesized polymers. This approach has been utilized before by Bailey *et al*. to investigate the phase behavior of poly(styrene-*b*-isoprene-*b*-ethylene oxide).[23] Due to the synthetic scheme utilized in this work, the effect of blending only increases the polydispersity of the D chains. We anticipate that the phase behavior exhibited by binary blends of ECD triblocks to be reasonably similar to neat ECD terpolymers. However, we do note that a subtle shift in the double gyroid phase window has been observed when binary diblock blends were compared to single-component samples.[38] Four ordered morphologies have been identified in this system: lamellae (LAM), tetragonally and hexagonally arranged spheres of D in C/E lamellae (S-LAM), and the orthorhombic network structure O^{70}. A majority of the samples were identified as LAM. (Here we note that the distinction between two- and three-domain lamellae, LAM_2 and LAM_3, respectively, is somewhat arbitrary due to their common symmetry.) Two samples displayed an order-order transition from hexagonally packed S-LAM at lower temperatures to O^{70} at higher temperatures. In the following sections, we present detailed descriptions of the characterization results that led to these morphology assignments.

3.3.1 Lamellae (LAM)

Lamellae phase assignments have been made on the basis of SAXS and TEM for the EC diblock, four ECD triblocks, and three binary blends, which span the range of f_D from 0 to 0.21. The SAXS patterns for these samples collected at 120 ºC are shown in Figure 3.3. Diffraction reflections at $q/q^* = 1$, 2, and 3, where q^* is the position of the first peak,

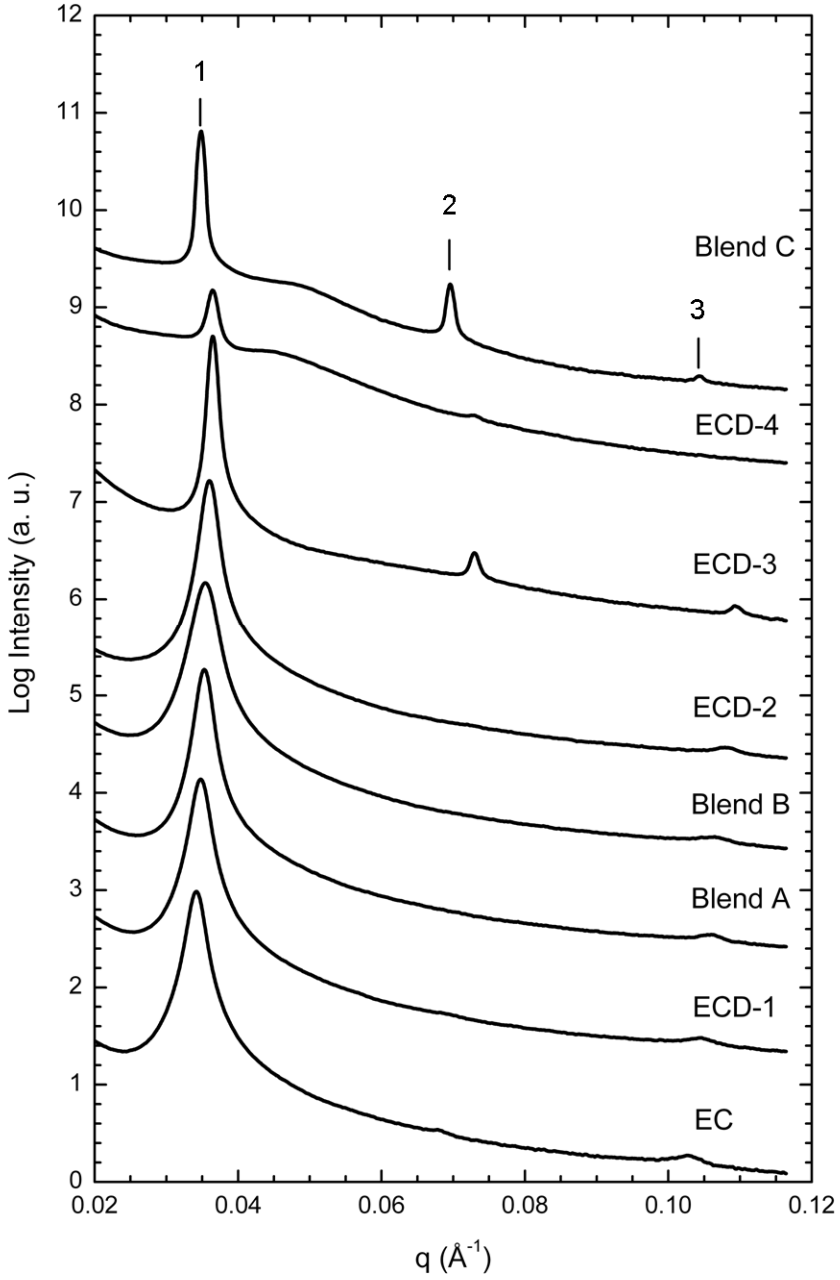

Figure 3.3: Synchrotron SAXS patterns collected at 120 ºC for samples possessing lamellar symmetry. The specimens were annealed for 18 hours at 120 ºC (160 ºC for Blend C) and quenched in liquid nitrogen prior to annealing and data collection at 120 ºC.

are apparent for the EC diblock and ECD-1 triblock, though the 2q^* reflections are very weak. These ratios are consistent with a lamellar morphology. With an increase in D block length ($0.05 \leq f_D \leq 0.09$, Blend A, Blend B, and ECD-2), 3q^* reflections are visible, but the 2q^* peaks are absent. At higher D content ($0.14 \leq f_D \leq 0.21$, ECD-3, ECD-4, and Blend C), the primary reflections narrow, and pronounced 2q^* peaks are apparent. These three samples also correspond to an increase in T_{ODT} with increasing f_D (see following paragraph concerning DMS results). The very weak or absent 2q^* diffraction reflections in the samples with $f_D \leq 0.09$ are consistent with alternating lamellae of nearly equal volume fractions, i.e., the LAM_2 structure.[25,39] ECD-4 and Blend C exhibit an additional broad maximum centered at approximately $\sqrt{2}q^*$ that is not associated with the lamellar structure factor. Hardy *et al*.[40] have reported similar broad maxima in the SAXS data obtained from ordered poly(isoprene-*b*-styrene-*b*-dimethylsiloxane) (ISD) triblock melts. These results were likened to the correlation hole effect observed in isotropic block polymer melts,[41-43] and attributed to partial miscibility of the I and S blocks. We suggest that the higher order maxima in ECD-4 and Blend C arise from block-block correlations within the mixed C + D domain. Observation of midblock-end block correlations in ECD triblocks with SAXS is possible due to sufficient levels of electron density contrast between all binary block pairs, as discussed by Cochran *et al*.[43] The electron density contrast between C and D is calculated as

$$\left[\rho_e^C - \rho_e^D\right]^2 = \left[0.515 - 0.484\right]^2 = 0.0010 \left[\frac{\text{mol e}^-}{\text{cm}^3}\right]^2 \qquad (0.42)$$

where ρ_e^C and ρ_e^D correspond to the electron densities of C and D, respectively, and have units of $\frac{\text{mol e}^-}{\text{cm}^3}$. This value is comparable to the contrast between E and D:

$$\left[\rho_e^E - \rho_e^D\right]^2 = \left[0.448 - 0.484\right]^2 = 0.0013 \left[\frac{\text{mol e}^-}{\text{cm}^3}\right]^2 \quad (0.43)$$

and is the same order of magnitude as the electron density contrast between E and C:

$$\left[\rho_e^E - \rho_e^C\right]^2 = \left[0.448 - 0.515\right]^2 = 0.0045 \left[\frac{\text{mol e}^-}{\text{cm}^3}\right]^2 \quad (0.44)$$

Figure 3.4 displays the dynamic elastic (G') and loss (G'') moduli for the LAM samples while heating (2 ºC/min) at a constant frequency of 1 rad/s to determine T_{ODT}. For all samples, G' and G'' nearly overlap at temperatures below T_{ODT} before abruptly decreasing at T_{ODT}. As noted previously,[44] G'' is typically not as sensitive as G' to the order–disorder transition; thus, the sudden decrease in G' is larger and more apparent than G''. As listed in Table 3.1 and shown in Figure 3.5, there is an initial decrease in T_{ODT} with increasing f_D before increasing with ECD-3 (14% D). This trend follows an initial decrease in domain spacing (as measured by SAXS, see Table 3.1) with the addition of longer D chains. We address these unanticipated results in greater detail in the Discussion. No order-order transitions (abrupt changes in G' or G'' below T_{ODT}) were observed in these samples.

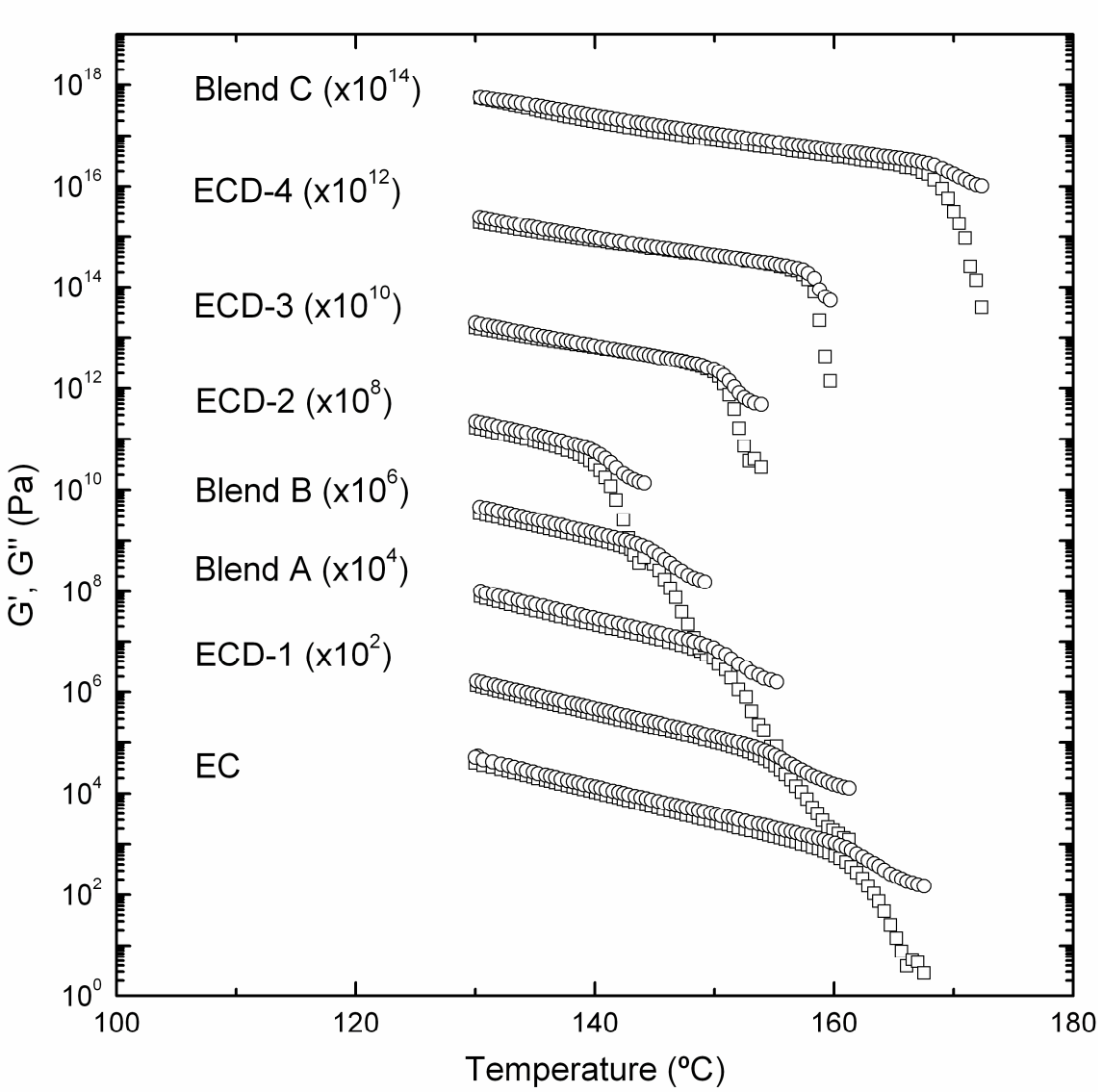

Figure 3.4: Isochronal temperature scans of dynamic elastic (□) and loss (○) moduli for the EC diblock, four ECD triblocks, and three blends in the LAM region measured while heating at 2 ºC/min with a strain amplitude of 1% and a frequency of 1 rad/s. The discontinuous drop in both moduli indicates the LAM to disorder transition. The data are shifted vertically by the specified factors for clarity.

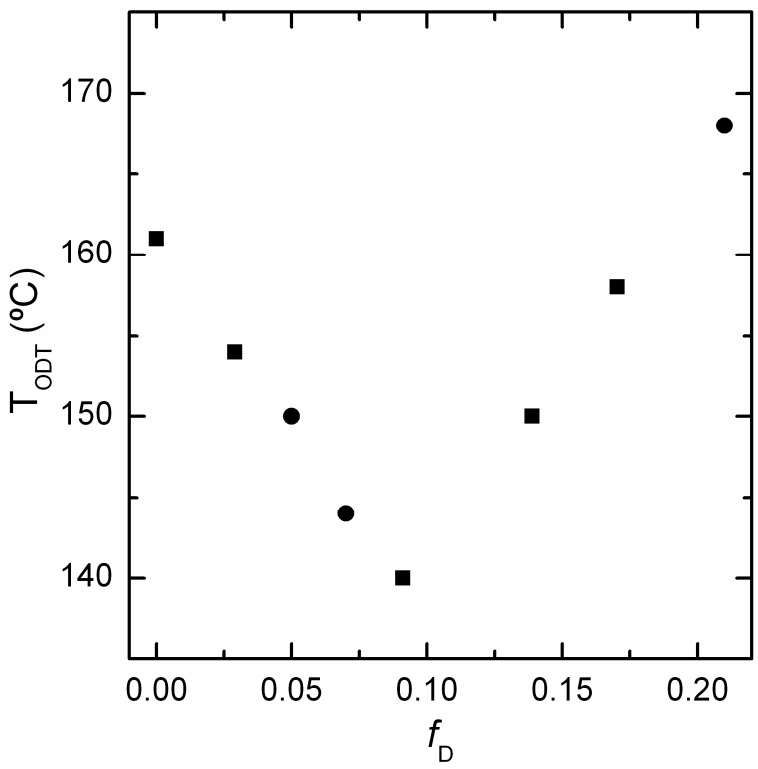

Figure 3.5: Summary of order-disorder transition temperatures (T_{ODT}) as a function of D composition for the LAM samples. Values of T_{ODT} were determined by DMS as shown in Figure 3.4. Solid squares and circles denote neat block polymers and binary blends, respectively.

TEM was also utilized to characterize the LAM microstructures. However, microtoming uniform and mechanically intact thin slices after staining with RuO_4 proved difficult, resulting in poor TEM images. In Figure 3.6, TEM micrographs of stained samples of the EC diblock and ECD-4 triblock are presented. In both micrographs alternating light and dark stripes are apparent. For EC, these light and dark layers correspond to unstained E and stained C lamellae, respectively. In the image generated

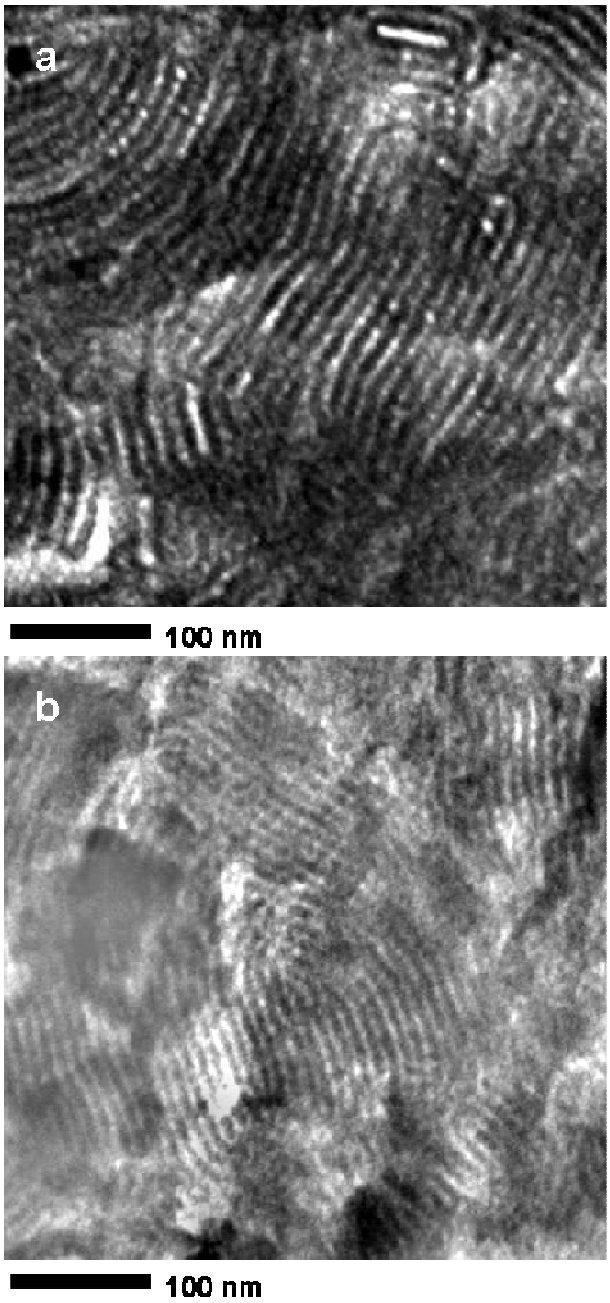

Figure 3.6: TEM micrographs of (a) EC and (b) ECD-4 after staining with RuO_4. Lighter regions correspond to semicrystalline E domains, while darker areas are the (a) C and (b) mixed C + D domains. The alternating layers of light and dark regions are consistent with the lamellar phase assignments made on the basis of SAXS.

from ECD-4 (Figure 3.6b), light areas again correspond to unstained E domains, while darker regions are due preferential staining of the mixed C + D domains. These micrographs, while not of the highest quality, support the LAM assignment made on the basis of the SAXS results.

3.3.2 Spheres-in-Lamellae (S-LAM)

Three samples were determined to have a spheres-in-lamellae (S-LAM) morphology on the basis of SAXS, TEM, and DMS results. This phase consists of alternating layers of E and C + D components. Within the C lamellae are microphase-separated D spheres, which are either arranged tetragonally (Blend D, 24% D) or hexagonally (Blend E, 26% D and ECD-5, 28% D). This section will detail the experimental results which led to these phase assignments.

Blend E and ECD-5, undergo OOTs with increasing temperature; this transition from a low-temperature morphology to a distinct high-temperature phase will be presented in Section 3.3.3. Conversely, an OOT is not apparent in the shear moduli data collected during heating for Blend D (24% D) (see Figure 3.7a). Upon cooling (Figure 3.7b), G' and G'' recover their original values, suggesting that the ordered phase is regained. Both heating and cooling scans exhibit a crossover in G' and G'' corresponding to a "rubbery plateau", where $G' > G''$ below the crossover temperature.[45] These differences in mechanical response are also apparent in the frequency-dependent data presented in Figure 3.8. Time-temperature superposition (TTS) largely fails for both G' and G'', except for the highest reduced frequency data. (We note that for rheologically complex materials, like ECD, TTS is not strictly valid.[46] However, the TTS principle is useful for

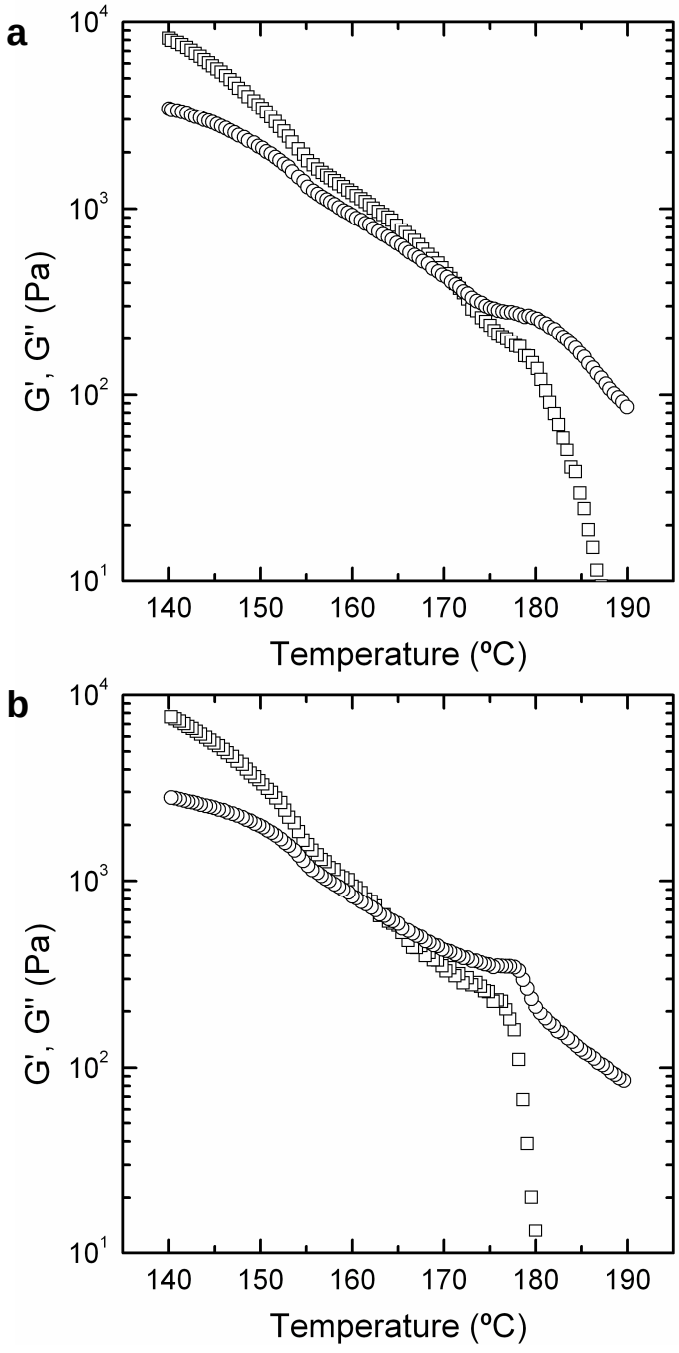

Figure 3.7: G' (□) and G'' (○) for Blend D obtained upon isochronal (ω = 1 rad/s) (a) heating and (b) cooling at a rate of 2 ºC/min. The ODT is apparent at 179 ºC.

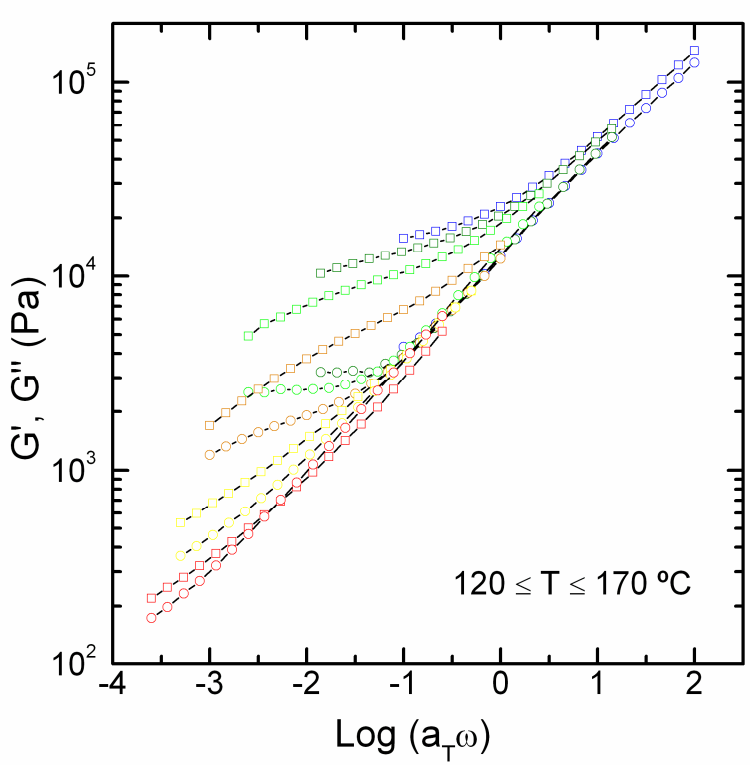

Figure 3.8: Master curves generated for Blend D using time-temperature superposition with T_{ref} = 120 ºC. Open squares (□) and circles (○) denote *G'* and *G"*, respectively. Data were collected at 120 (blue), 130 (dark green), 140 (light green), 150 (orange), 160 (yellow), and 170 ºC (red).

the identification of different frequency-dependent regimes in ordered and disordered block polymers.) The shift factors a_T used to generate the master curves in Figure 3.8 are monotonic and could be closely approximated with the WLF equation[47] (see Figure 3.9). At 170 ºC (red data in Figure 3.8), $G' : G'' : \omega^{1/2}$; this behavior has been documented in unoriented lamellar block copolymers.[45,48-50] With decreasing temperature, the low-frequency response of G' and G'' become less sensitive to ω ($G' : \omega^n$ and $G'' : \omega^m$,

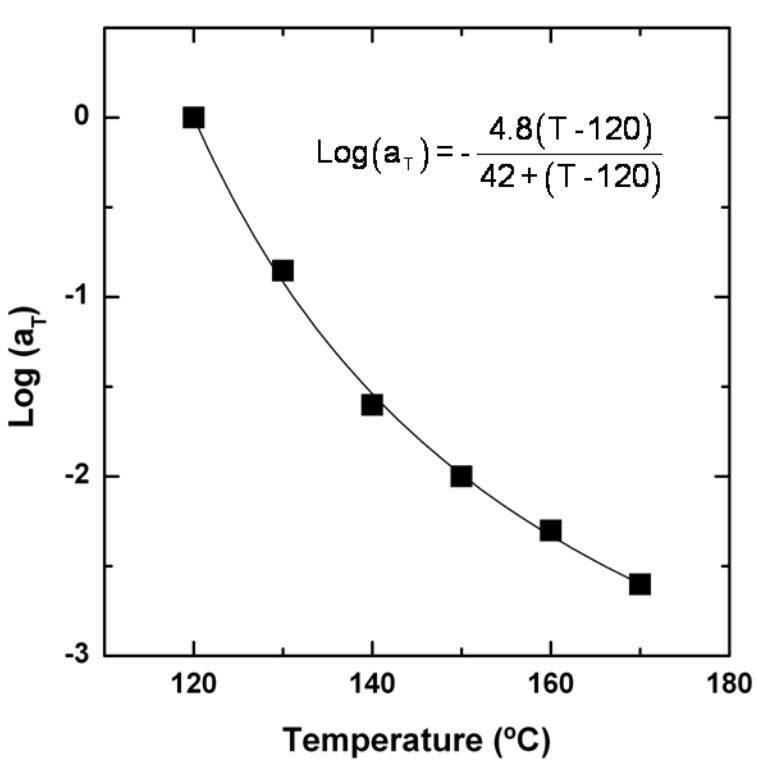

Figure 3.9: Temperature dependence of the shift factors used to generate Figure 3.8, and the corresponding fit to the WLF equation (solid line).

where n and $m < 1/2$). At 120 and 130 ºC, G': $\omega^{0.15}$ and $G' > G''$. These rheological results are consistent with a complex, temperature-dependent layered structure.

Figure 3.10 displays a SAXS pattern for Blend D obtained at 160 ºC, which differs greatly from the previously discussed LAM samples. The peak positions and their ratios to the primary reflection have been summarized in Table 3.2. The first two peaks are located at nearly coincident wavevectors ($q \cong 0.0330$ and 0.0350 Å^{-1}), and can not be accounted for by a cubic lattice. Higher order reflections at $q/q^* \cong 1$, $\sqrt{2}$, $\sqrt{4}$, $\sqrt{5}$, and $\sqrt{8}$ are consistent with the first five allowed peaks of a structure with two-dimensional

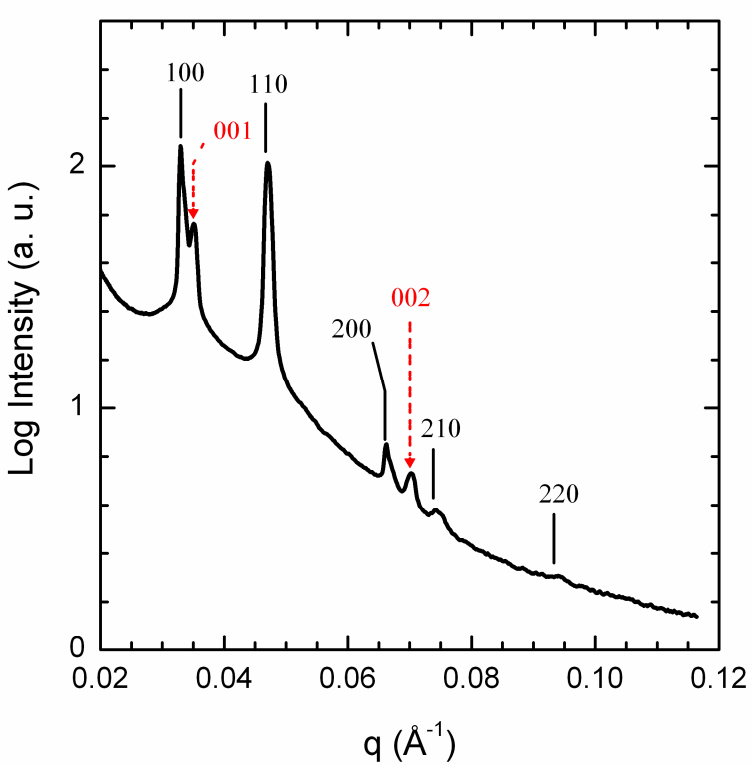

Figure 3.10: Azimuthally integrated synchrotron SAXS data for Blend D collected at 160 ºC. The sample was prepared by annealing for 18 hours at 160 ºC prior to annealing and data collection. The peaks have been indexed to a two-dimensional tetragonal lattice (solid black lines) embedded in a layered structure (red dashed lines).

Table 3.2: Comparison of observed and predicted peak positions for Blend D.

Observed		2D Tetragonal Lattice in Lamellae[a]	
Peak Location ($Å^{-1}$)	Ratio	Index	Ratio
0.0330	1.00	100	1.00 (= √1)
0.0350	1.06	001	1.06
0.0470	1.42	110	1.41 (= √2)
0.0663	2.01	200	2.00 (= √4)
0.0701	2.12	002	2.12
0.0743	2.25	210	2.24 (= √5)
0.0941	2.85	220	2.83 (= √8)

[a]Calculated using the lattice parameters a = 19.0 and c = 18.0 nm (a/c = 1.06).

tetragonal symmetry, and do not conform to a two-dimensional hexagonal lattice. The remaining reflections at $q \cong 0.0350$ and 0.0701 $Å^{-1}$ have the approximate ratio 1:2, which is consistent with a one-dimensional layered structure. Taken together, the seven peaks identified in the scattering profile of Blend D (Figure 3.10, Table 3.2) can be attributed to a two-dimensional tetragonal lattice superimposed on a one dimensional structure. TEM provides further evidence for this complex morphology (see below). The lattice parameters $a/c = 1.06$ and $c = 18.0$ nm yield the indexing scheme presented in Figure 3.10. The interlayer spacing for Blend D ($c = 18.0$ nm at 160 ºC) compares favorably to the domain spacing measured for the LAM Blend C sample (17.5 nm at 140 ºC).

TEM provides further support for a complex layered structure. In the micrograph presented in Figure 3.11a of an unstained Blend D sample, the D domains appear black, while the E and C are much lighter and indistinguishable. Isolated, circular regions of D are arranged on a rectangular lattice (pmm symmetry). We interpret these results as spherical domains of D periodically distributed within C lamellae. The fast Fourier transformation (FFT) of the image (see inset of Figure 3.11a) yields a characteristic length scale for the layer-to-layer thickness of 15.1 nm. Comparing this value to the SAXS results (c lattice parameter) yields, $d_{TEM} \cong 0.85 d_{SAXS}$. We attribute this discrepancy in length scales, which has been previously noted in other triblock terpolymer systems,[24,25] to E block crystallization (38% crystallinity as measured by DSC). The TEM provides direct visual evidence that the tetragonal lattice observed in the SAXS results consists of spherical D domains. A similar morphology has been observed by Shibayama and coworkers in a poly(styrene-*b*-(4-vinylbenzyl)dimethylamine-*b*-isoprene) (SAI)

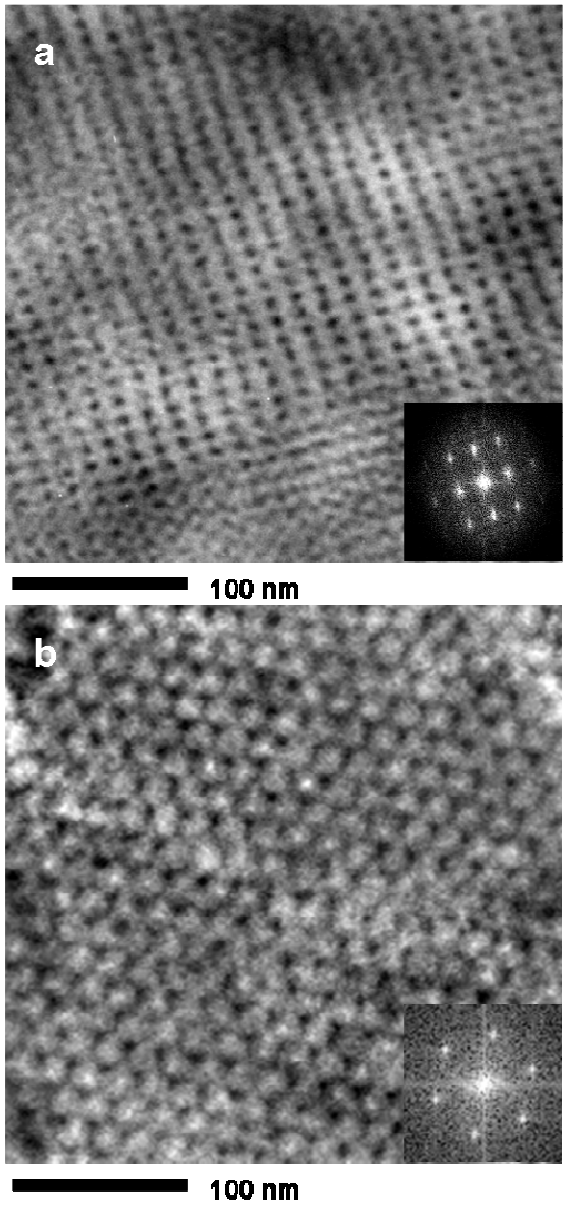

Figure 3.11: TEM micrographs and corresponding FFTs (shown in insets) generated from (a) unstained Blend D and (b) RuO_4-stained ECD-5 (annealed at 160 ºC, below T_{OOT}). In both micrographs discrete, dark regions are consistent with microphase-separated spheres of D.

triblock terpolymer with 35% S, 39% A, and 26% I by volume.[51] The authors identified a two-dimensional lattice of spherical I domains dispersed in A lamellae via TEM. Additional SAXS measurements were consistent with the secondary structure, but the authors could not determine the symmetry of the two-dimensional lattice due to a lack of higher order reflections.

Returning to Blend E (26% D) and ECD-5 (28% D), the DMS results presented in Figure 3.12 provide clear evidence of OOTs in these materials. In the heating scan (Figure 3.12a), increases in G' and G'' prior to the T_{ODT} are consistent with an OOT. The microstructural transformation is also apparent upon cooling (Figure 3.12b), with a small hysteresis in moduli. G' remains relatively constant with increasing temperature for both samples, except for the uptick at T_{OOT}, whereas G'' steadily rises with increasing temperature (there also appears to be a small, abrupt increase in G'' at T_{OOT}). Between $140 \leq T \leq 160$ ºC, G' is approximately an order of magnitude larger than G'', but the moduli are nearly equivalent just below T_{ODT}. These results are markedly different than those presented for the LAM and tetragonally packed spheres-in-lamellae samples (see Figures 3.4 and 3.7).

SAXS powder patterns obtained for Blend E (180 ºC) and ECD-5 (200 ºC) below their respective T_{OOT}s are given in Figure 3.13. The scattering results are qualitatively similar, with a large number of diffraction peaks of varying intensity (summarized in Tables 3.3 and 3.4). Like the SAXS data generated from Blend D (Figure 3.10), a second, strong reflection is present at nearly the same position as the primary peak ($q \cong 0.0326$ and 0.0348 $Å^{-1}$ for Blend E). However, a low q shoulder on the primary peak is also

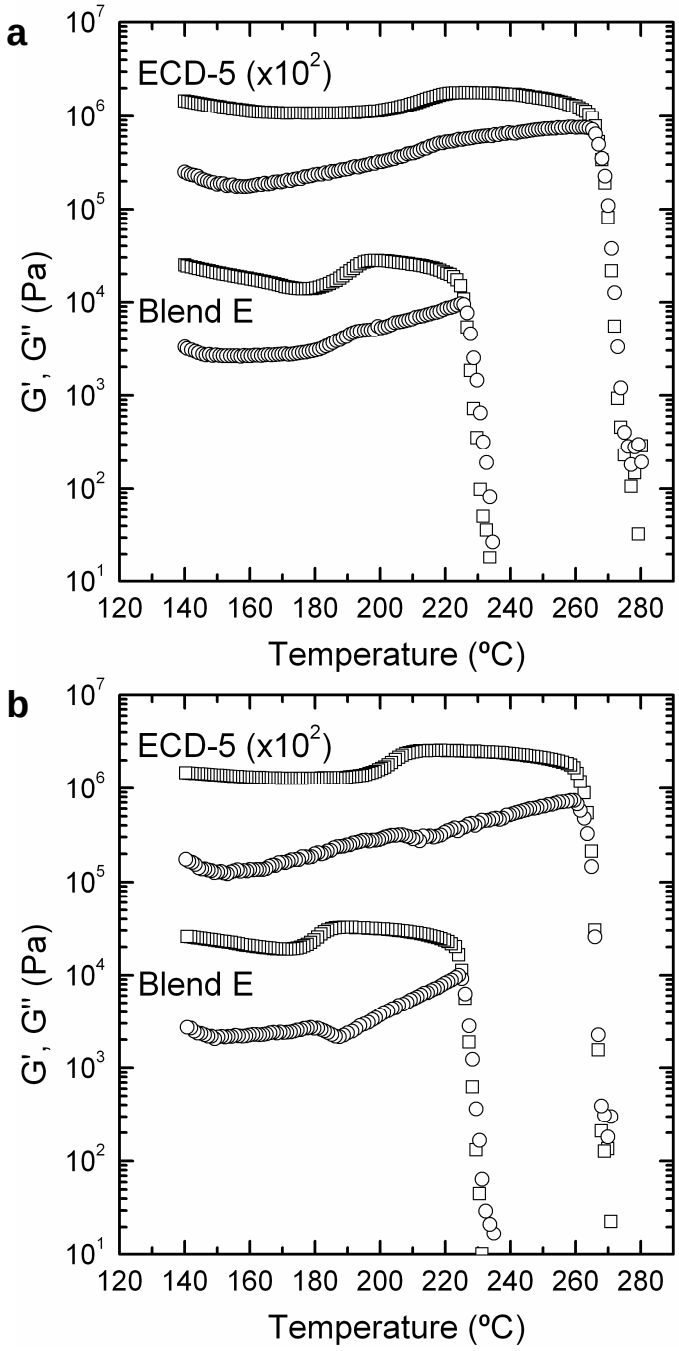

Figure 3.12: Isochronal (ω = 1 rad/s) elastic (□) and loss (○) moduli for Blend E and ECD-5 collected upon (a) heating and (b) cooling at a rate of 2 ºC/min. The ECD-5 data have been shifted vertically for clarity.

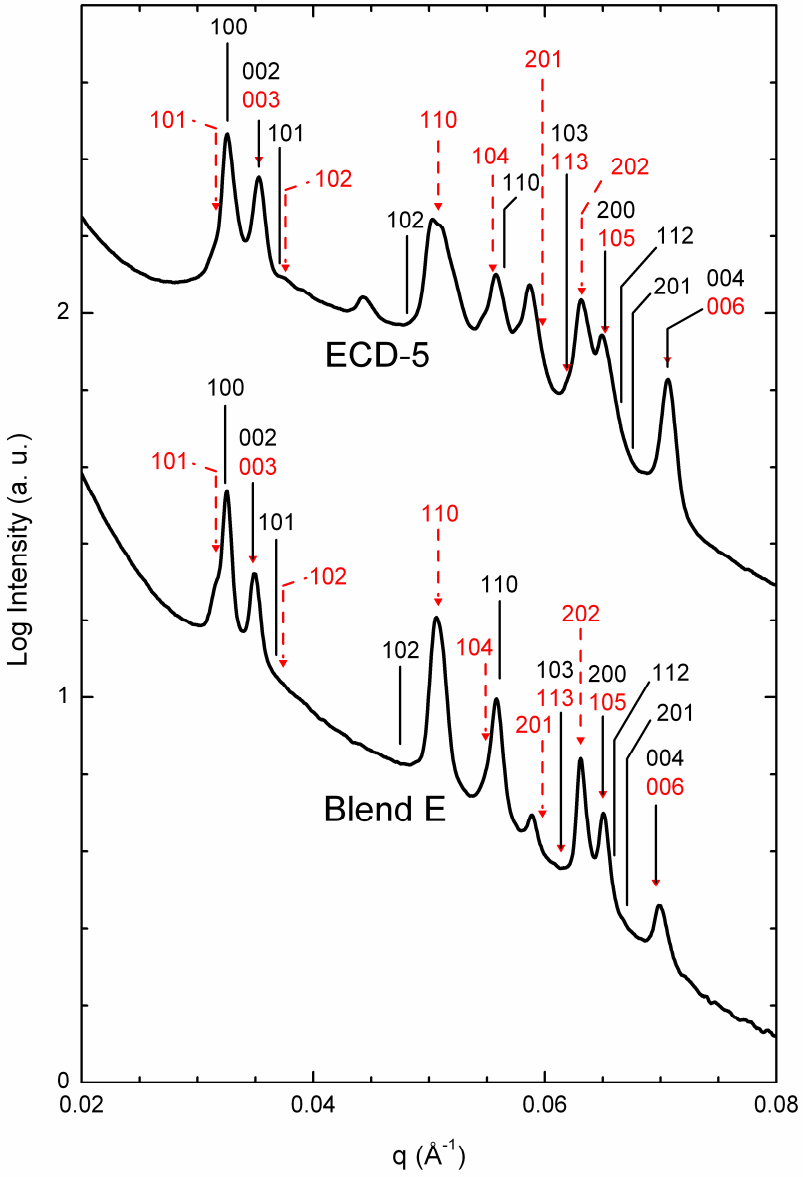

Figure 3.13: Synchrotron SAXS patterns for Blend E and ECD-5 collected at 180 and 200 ºC, respectively. The samples were annealed for 18 hours prior to annealing and data collection at the specified temperatures. The data are indexed according to $P6_3/mmc$ (solid black lines) and $R\bar{3}m$ (red dashed arrows) symmetry. The upper curve is shifted vertically for clarity.

Table 3.3: Comparison of observed (SAXS data in Figure 3.13) and predicted peak positions for Blend E.

Observed		ABCABC… stacking[a]		ABAB… stacking[b]	
Peak Location ($Å^{-1}$)	Ratio	Index	Peak Location ($Å^{-1}$)	Index	Peak Location ($Å^{-1}$)
0.0316	1.00	101	0.0316		
0.0326	1.03			100	0.0324
0.0348	1.10	003	0.0348	002	0.0348
				101	0.0368
		102	0.0374		
				102	0.0475
0.0508	1.61	110	0.0508		
		104	0.0549		
0.0558	1.77			110	0.0561
0.0589	1.86				
		201	0.0598		
		113	0.0616	103	0.0614
0.0631	2.00	202	0.0631		
0.0651	2.06	105	0.0650	200	0.0648
				112	0.0660
				201	0.0671
0.0698	2.21	006	0.0696	004	0.0696

[a]Calculated using the lattice parameters $a/c = 0.458$ and $c = 54.0$ nm.

[b]Calculated using the lattice parameters $a/c = 0.620$ and $c = 36.1$ nm.

apparent (more evident in Blend E), which was not observed in the Blend D sample. These results are inconsistent with cubic and two-dimensional (tetragonal or hexagonal) space groups, which only possess one characteristic length scale. Attempted fits of the observed scattering reflections with *Fddd* (O^{70}) and *Pnna* (O^{52}) symmetries proved to be quite unsatisfactory. Additionally, a TEM micrograph generated from ECD-5 (Figure 3.11b), displays six-fold symmetry, which is characteristic of either a hexagonal, trigonal,

Table 3.4: Comparison of observed (SAXS results in Figure 3.13) and predicted peak positions for ECD-5.

Observed		ABCABC… stacking[a]		ABAB… stacking[b]	
Peak Location ($Å^{-1}$)	Ratio	Index	Peak Location ($Å^{-1}$)	Index	Peak Location ($Å^{-1}$)
0.0316	1.00	101	0.0316		
0.0326	1.03			100	0.0326
0.0353	1.12	003	0.0353	002	0.0353
0.0374	1.18	102	0.0376	101	0.0371
0.0444	1.41				
				102	0.0481
0.0507	1.60	110	0.0508		
0.0558	1.77	104	0.0555	110	0.0565
0.0587	1.86				
		201	0.0598		
		113	0.0619	103	0.0622
0.0631	2.00	202	0.0632		
0.0649	2.05			200	0.0652
		105	0.0657		
				112	0.0666
				201	0.0676
0.0707	2.24	006	0.0706	004	0.0706

[a]Calculated using the lattice parameters $a/c = 0.463$ and $c = 53.4$ nm.

[b]Calculated using the lattice parameters $a/c = 0.625$ and $c = 35.6$ nm.

or cubic structure, though we note that certain projections of O^{70} and O^{52} appear pseudo-hexagonal.[25,52]

If we again compare the scattering results from Blend E and ECD-5 to Blend D (Figure 3.10), we notice a similarity in wavevectors for the second prominent peak in all of the samples. For Blend D, this reflection ($q \cong 0.0350$ $Å^{-1}$, see Table 3.2) was attributed to the inter-layer spacing in the lamellar structure. Strong reflections at peak ratios of approximately 1:2 in Blend E ($q \cong 0.0348$ and 0.0698 $Å^{-1}$, see Table 3.3) and ECD-5 ($q \cong$

0.0353 and 0.0707 $Å^{-1}$, see Table 3.4) are evidence of a layered structure in these samples. Taking the TEM results as evidence of hexagonal packing of D spheres, we can visualize two sphere packing arrangements: ABAB… stacking (Figure 3.14a) and ABCABC… stacking (Figure 3.14b). The space groups associated with these structures are $P6_3/mmc$ and $R\bar{3}m$, respectively. If we associate the suspected inter-layer peaks to the 002 and 003 reflections of $P6_3/mmc$ and $R\bar{3}m$, we directly obtain the c lattice parameters, which are related as $c_{AB...}/2 = c_{ABC...}/3$. Additionally, correlating the first prominent reflection in the SAXS data ($q \cong 0.0326$ $Å^{-1}$ for Blend E and ECD-5) to the 100 reflection of the $P6_3/mmc$ lattice yields the second lattice parameter (a) for this structure. The allowed reflections for this symmetry with the deduced lattice parameters have been noted in Figure 3.13 (solid black lines). Good agreement is observed for the 100, 002, 110, 200, and 004 reflections and experimentally observed peak positions (there is also weak peak in the ECD-5 scattering data that may correspond to the 101 reflection). However, there are still a number of experimentally observed peaks not accounted for by this single space group. If we consider the low q shoulder of the 100 $P6_3/mmc$ peak to be the first allowed reflection of the $R\bar{3}m$ space group (101), we can directly determine a for this second structure. However, there is uncertainty in the exact peak location due to the stronger 100 $P6_3/mmc$ reflection. This uncertainty can be diminished by fitting a prominent, higher-order peak. Taking the strong peak at $q \cong 0.051$ $Å^{-1}$ evident in both Blend E and ECD-5 as the 110 reflection of the $R\bar{3}m$ space group, yields lattice parameters that correctly place the 101 reflection on the low q side of the 100 $P6_3/mmc$ reflection (see Figure 3.13). The fitted lattice parameters yield the indexing

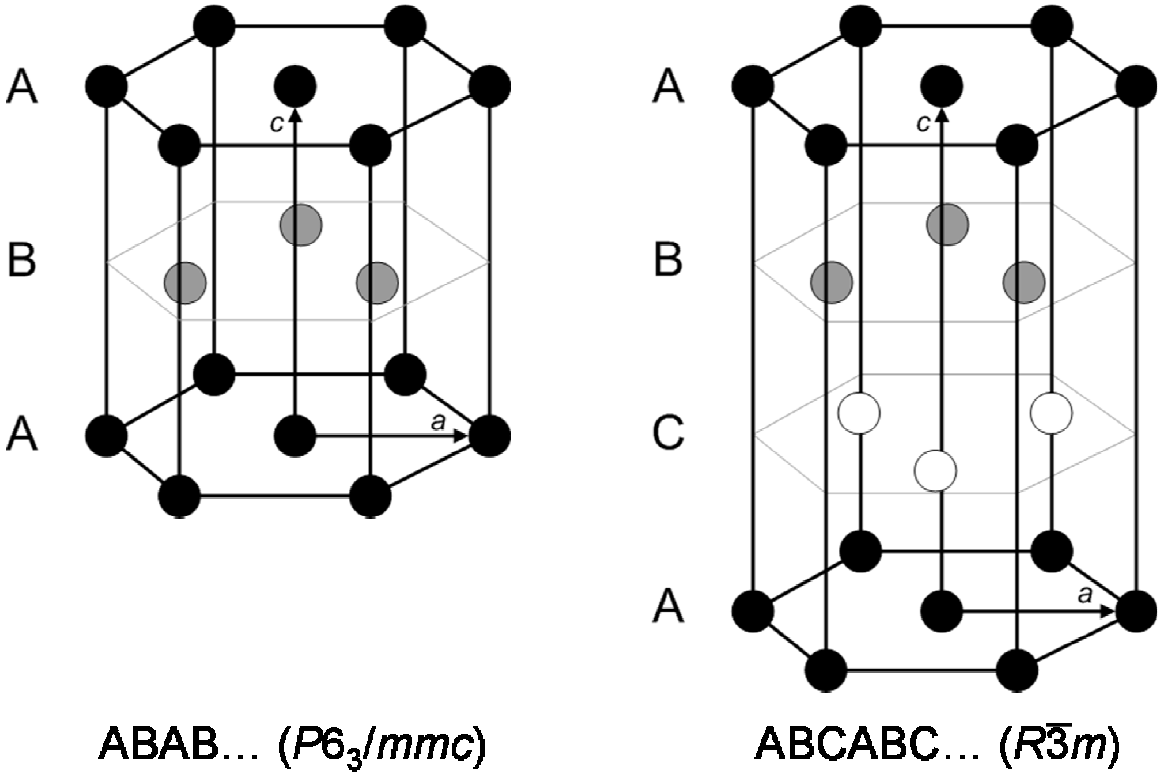

Figure 3.14: Schematic representation of hexagonal lattice models of ABAB… and ABCABC… stacking arrangements. The lattice parameters are represented by *a* and *c*.

scheme presented in Figure 3.13 for the ABCABC… stacking model (red dashed lines). Experimentally observed peaks can be attributed to the 101, 003, 110, 202, and 006 reflections of the $R\bar{3}m$ symmetry (the peak located at the 105 reflection is more likely due to overlapping of the 200 $P6_3/mmc$ reflection). With these two space groups, we can account for 8 of the 9 observed peaks in Blend E and 9 of the 11 reflections in ECD-5. The prominent peak in ECD-5 at $q \cong 0.0444$ Å^{-1} has a position ratio of approximately $\sqrt{2}q^*$, suggesting that it may be consistent with a tetragonal or cubic structure. However, the lack of other, higher order reflections that are clearly correlated to this peak makes

this hypothesis purely speculative. The other unaccounted reflection is located at $q \cong 0.059$ Å^{-1} in both samples. We do not have an explanation for this shortcoming, making this morphological analysis plausible, but not definitive.

3.3.3 Spheres-in-Lamellae to O^{70} Transition

As shown in Figure 3.12, DMS results suggest that Blend E (26% D) and ECD-5 (28% D), undergo order-order transitions from the previously described spheres-in-lamellae structure to a higher modulus morphology with increasing temperature. Additionally, the cooling and heating traces nearly superimpose with little hysteresis, indicating that the transition is reversible. The frequency-dependent viscoelastic response of these materials was also probed below and above T_{OOT}. Figures 3.15 and 3.16 display these results for Blend E and ECD-5, respectively, constructed using TTS (T_{ref} = 140 ºC for both samples, see Figure 3.17 for the shift factors used to generate Figures 3.15 and 3.16). Again, TTS fails for a significant fraction of the data, especially in the low-temperature regime for Blend E (Figure 3.15a). The frequency results are qualitatively different for the sample below and above T_{OOT}. In the low-temperature regime, G' decreases with decreasing ω, whereas the high-temperature phase exhibits a solid-like response with $G' \sim \omega^0$ and $G' > G''$. The rheological behavior below T_{OOT} is qualitatively similar to the low-temperature ($T \leq 140$ ºC) viscoelastic response of Blend D (Figure 3.8). Solid-like behavior has been attributed to three-dimensional morphologies, such as BCC spheres, double gyroid, or O^{70}.[25,38,53]

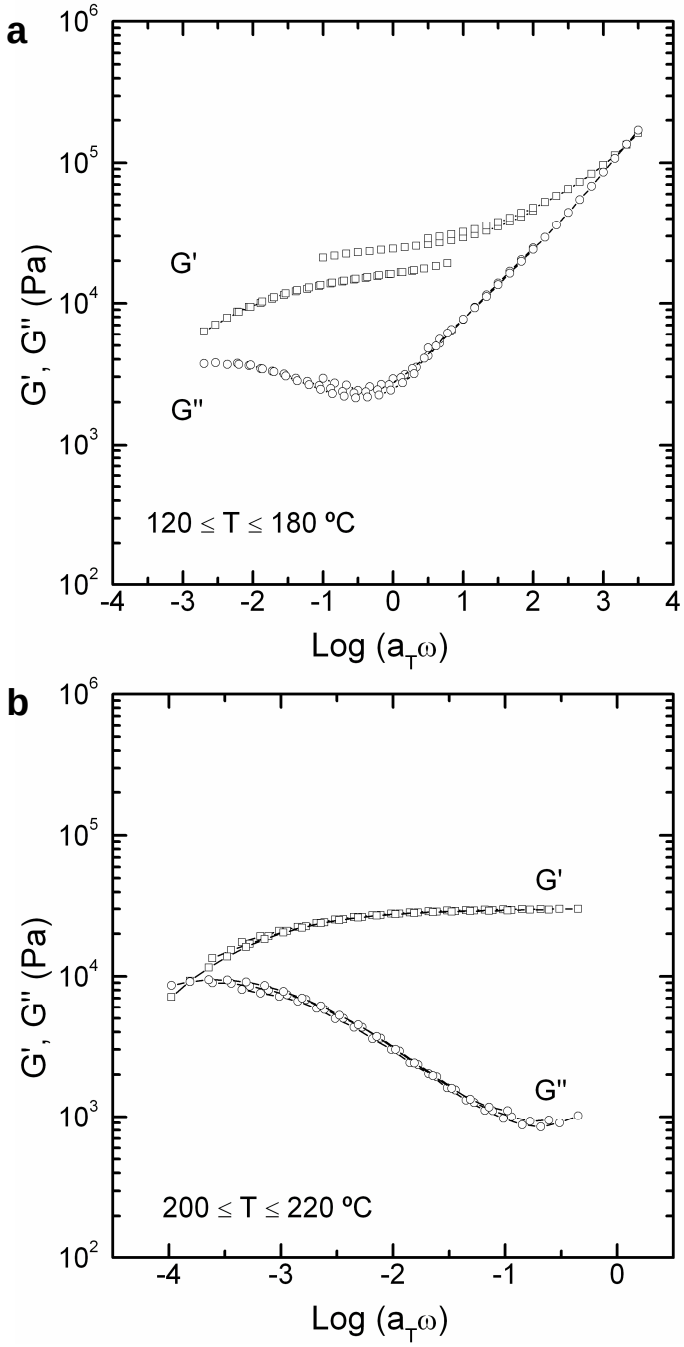

Figure 3.15: Frequency-dependent moduli for Blend E at temperatures between (a) 120 and 180 ºC and (b) 200 and 220 ºC shifted according to time-temperature superposition. The reference temperature for both (a) and (b) is 140 ºC.

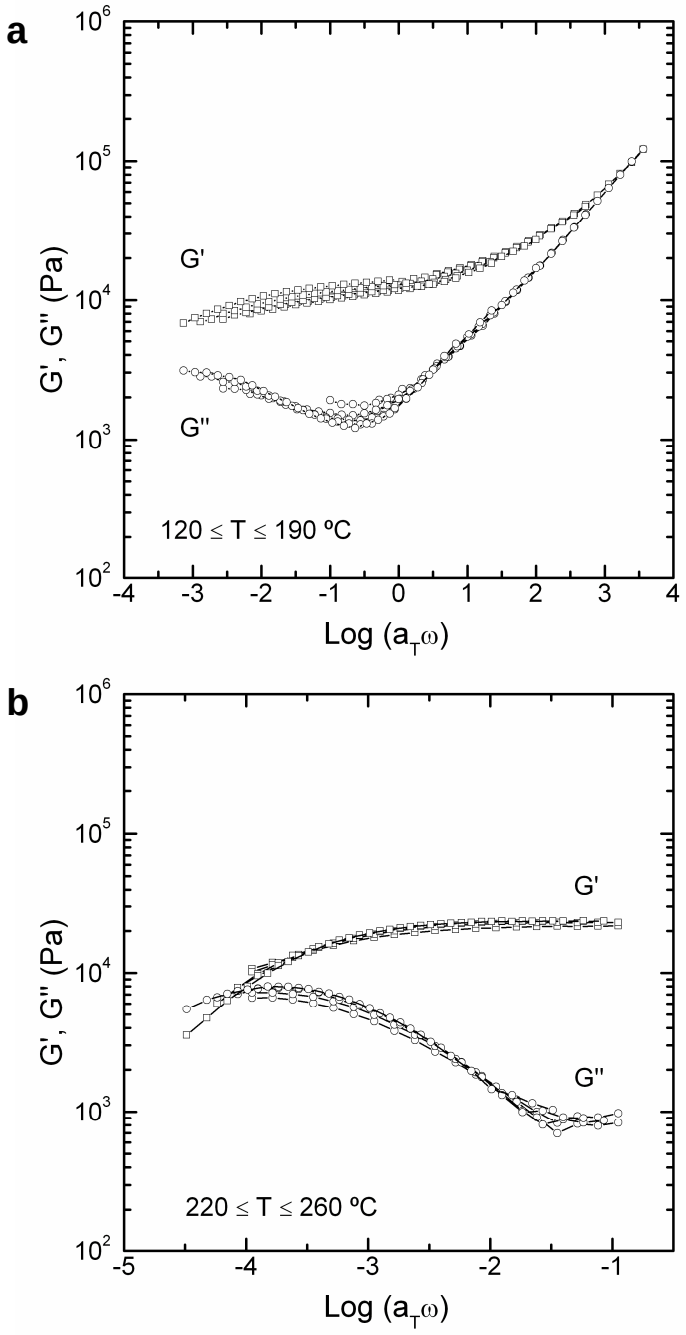

Figure 3.16: Isothermal frequency results for ECD-5 at temperatures between (a) 120 and 190 ºC and (b) 220 and 260 ºC shifted according to time-temperature superposition. The reference temperature for both (a) and (b) is 140 ºC.

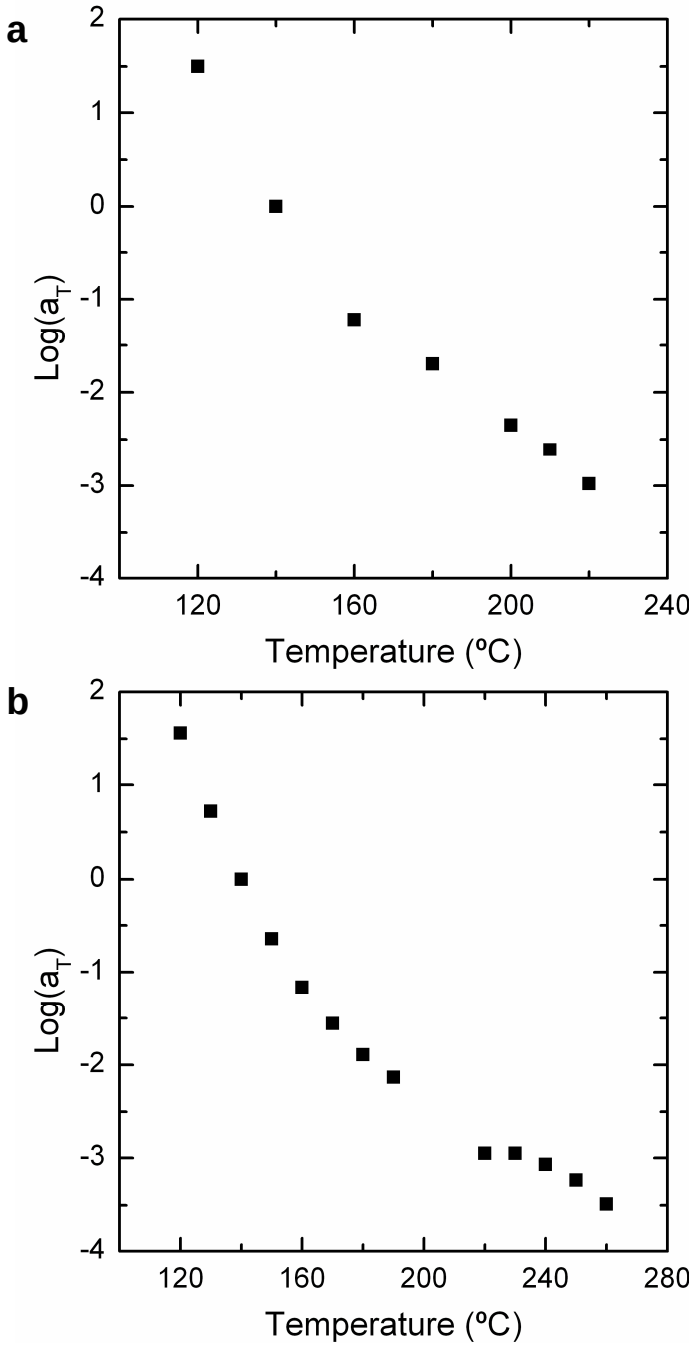

Figure 3.17: Horizontal shift factors used in (a) Figure 3.15 and (b) Figure 3.16 to generate low- and high-temperature master curves for Blend E and ECD-5, respectively.

Figure 3.18 displays SAXS data obtained from Blend E and ECD-5 above their T_{OOT}s at 200 and 220 ºC, respectively. The similarity in peak positions for these two patterns suggests a common morphology. (ECD-5 also possesses two low intensity peaks marked with ▼ at $q \cong 0.0349$ and 0.0698 Å^{-1}. These reflection positions have the ratio 1:2, and correspond well to peaks associated with the low-temperature phase. At 200 ºC (see Figure 3.13), the 002/003 and 004/006 reflections of the $P6_3/mmc$ and $R\bar{3}m$ lattices were observed at $q \cong 0.0353$ and 0.0706 Å^{-1}, respectively. These two inter-layer peaks do not persist when the sample is heated to 240 ºC). The rich array of reflections does not correspond to a cubic, tetragonal, or hexagonal lattice, but an orthorhombic lattice can account for these peak locations. (For example, the reflections for Blend E are at q/q^* = 1, 1.20, 1.54, 1.57, 1.71, 1.81, 1.95, and 2.00.) Orthorhombic unit cells have three independent lattice dimensions, *a*, *b*, and *c*, which generate reflections at $q_{hkl} = 2\pi\left[h^2/a^2 + k^2/b^2 + l^2/c^2\right]^{1/2}$, where *h*, *k*, and *l* are the associated Miller indices. A least-squares fitting procedure previously described by Meuler[54] yielded the lattice parameters listed in Table 3.1 for the O^{70} phase. These lattice dimensions lead to the indexing presented in Figure 3.18. We note that small changes in lattice parameters can produce large deviations in the locations of higher order reflections. The unit cell dimensions *a*/*c* and *b*/*c* for Blend E and ECD-5 are slightly smaller than those reported earlier for the O^{70} morphology in a SI diblock (*a*/*c* = 0.285 and *b*/*c* = 0.570),[55] ISO triblocks (*a*/*c* = 0.280 – 0.297 and *b*/*c* = 0.554 – 0.591),[24-26] a saturated poly(cyclohexylethylene-*b*-ethylethylene-*b*-ethylene) triblock (*a*/*c* = 0.30 and *b*/*c* = 0.60),[56] and an OSISO pentablock (*a*/*c* = 0.293 and *b*/*c* = 0.577).[57] TEM micrographs

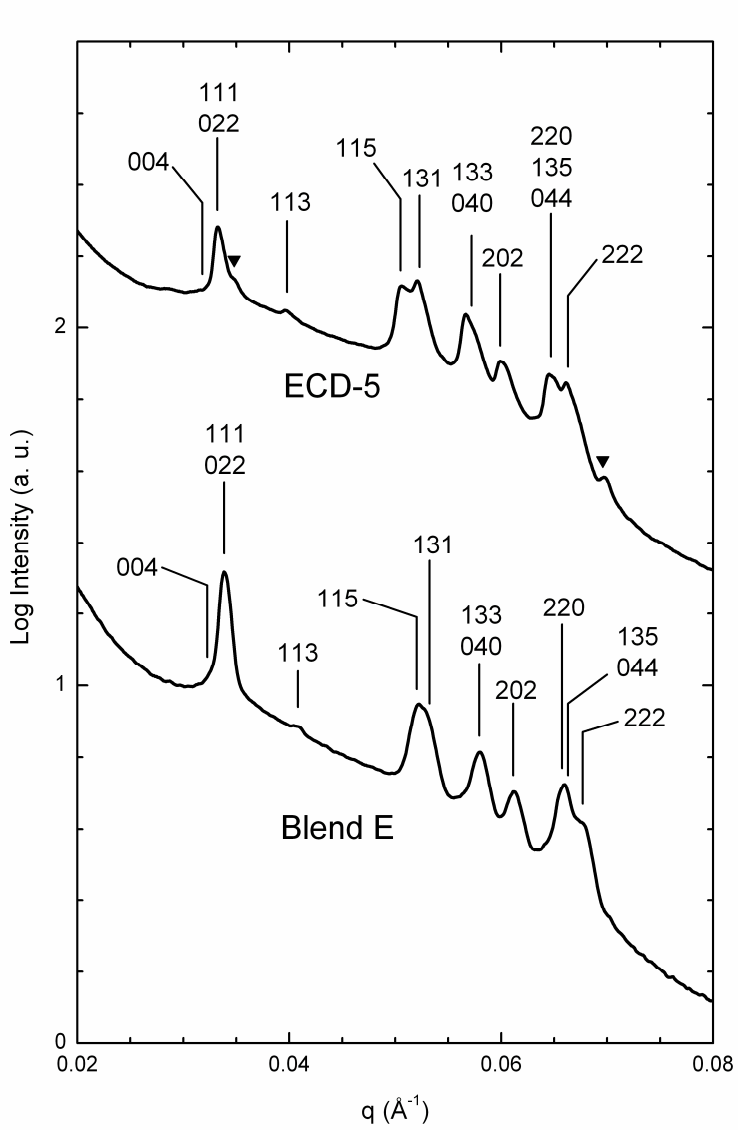

Figure 3.18: Integrated SAXS data for Blend E and ECD-5 samples after heating to the O^{70} phase. These patterns were collected at 200 and 220 ºC for Blend E and ECD-5, respectively. The diffraction data are indexed with the *Fddd* space group according to the lattice parameters listed in Table 3.1. The low intensity peaks denoted with ▼ in ECD-5 correspond to the 002/003 and 004/006 reflections of the low-temperature morphology. The upper trace is shifted vertically for visual clarity.

were not obtained for the O^{70} phase due to difficulty in trapping the high-temperature phase at a temperature suitable for analysis by TEM.

3.4 Discussion

In the series of ECD terpolymers and binary blends presented in this chapter, four ordered phases were identified along the symmetric $f_E = f_C$ isopleth: lamellae, tetragonally and hexagonally packed spheres of D in lamellae, and O^{70} (see Figures 3.19 and 3.20). SAXS was used as the primary technique for morphological characterization, with TEM and DMS utilized as complementary tools. We believe that these results provide additional insights into the principles that govern the complex phase behavior of triblock terpolymers.

As discussed in Chapter 1, it is useful to categorize ABC triblock systems based on the relative magnitudes of the segment-segment interaction parameters. The following binary interaction parameters have been reported:[31,58,59]

$$\begin{aligned} \chi_{EC} &= 29.4T^{-1} - 0.017 \\ \chi_{CD} &= 28.1T^{-1} + 0.01 \\ \chi_{ED} &= 90.7T^{-1} - 0.0946 \end{aligned} \tag{0.45}$$

which are based on a common segment volume of 118 $Å^3$. At 150 ºC, $\chi_{EC} = 0.052$, $\chi_{CD} = 0.076$, and $\chi_{ED} = 0.120$ (see Figure 3.21 for the temperature dependence of interaction parameters). Thus, ECD is an example of a "nonfrustrated" triblock terpolymer because it satisfies the inequality[27]

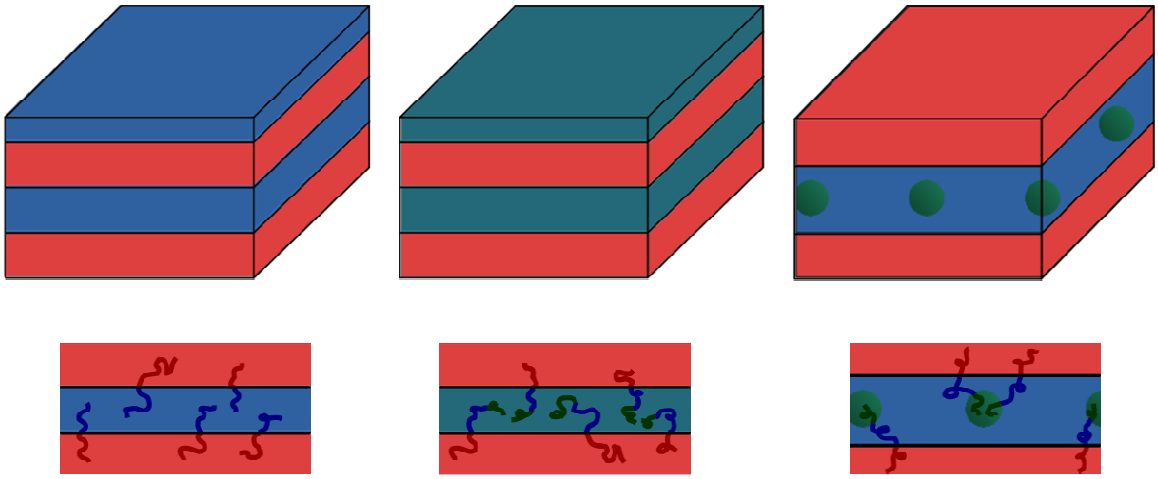

Figure 3.19: Top row: Illustrations of layered morphologies identified in EC diblock and ECD triblocks. Red, blue, and green correspond to E, C, and D, respectively. Bottom row: Sketches of ECD chains depict molecular packing within each structure.

$$\chi_{EC} < \chi_{CD} < \chi_{ED} \tag{0.46}$$

However, as shown in Figure 3.21, Equation (0.46) does not hold for all temperatures. With increasing temperature, χ_{ED} approaches χ_{CD} until they are equal at 325 ºC. While experiments were not conducted at this elevated temperature, the strong temperature-dependence of χ_{ED} must be considered when discussing the morphological behavior of ECD triblocks. Additionally, the assumption that the binary interaction parameters do not change when placed in a ternary system is questionable. Despite this caveat, the formation of E/C and C/D interfaces appears to be preferred over E/D contacts, and no unfavorable interfaces are dictated by chain connectivity in the ECD molecule. One reason for choosing the ECD system was an enhanced likelihood in discovering network morphologies, which have been found in other nonfrustrated triblock terpolymer systems.

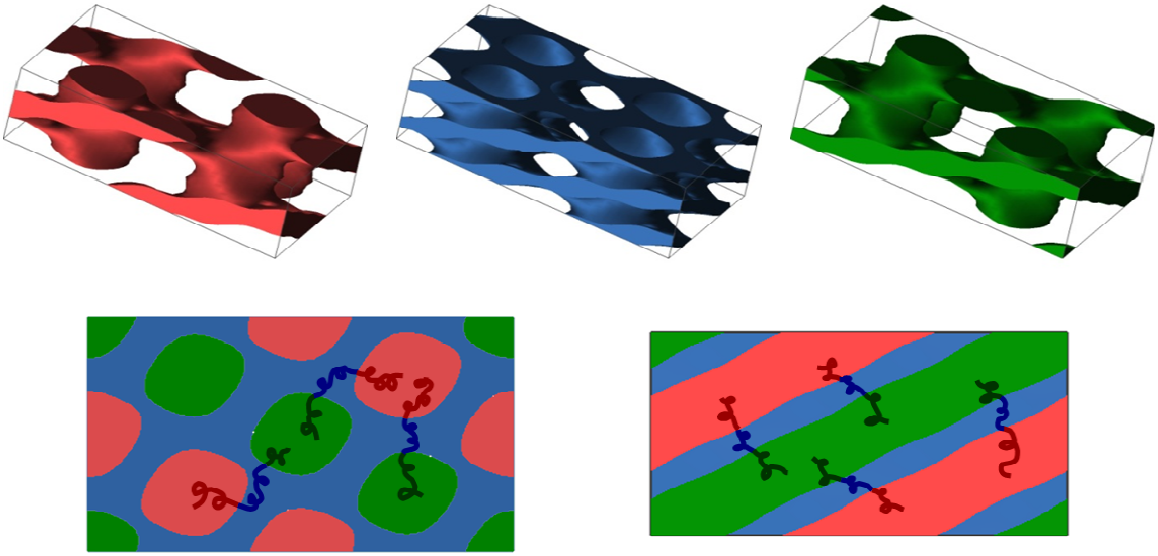

Figure 3.20: Top row: Space-filling models of O^{70} corresponding to E (red), C (blue), and D (green) domains generated by a Fourier synthesis technique. The depicted volume fractions represent the experimental composition of ECD-5. Bottom row: The [100] (left) and [001] (right) projections of the O^{70} unit cell. Sketches of ECD chains illustrate the assembly of the O^{70} morphology.

We attribute the large LAM region (0 to 21% D) documented in these ECD triblocks to the magnitudes and sequencing of χ parameters. Mixing (at least partial) of D chains within the C domain is preferred compared to formation of a fully microphase separated, three-domain morphology. The latter case would cause large chain stretching penalties in the D domains due to the compositional asymmetry of the polymer. With increasing D composition, the mixed C/D state becomes less energetically favorable and spheres of fully segregated D are formed (Blend D, 24% D). For ECD-4 (17% D) and Blend C (21%

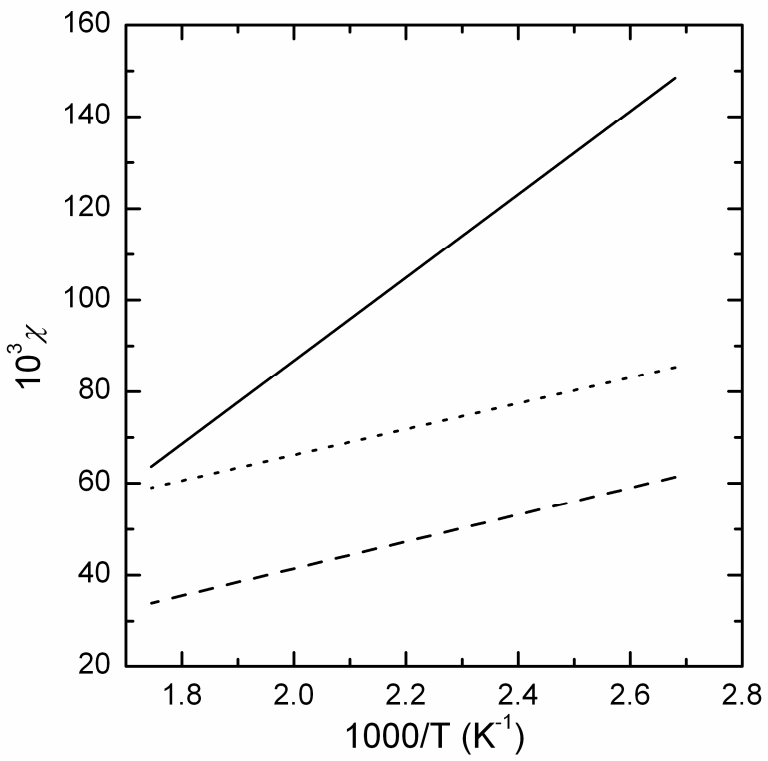

Figure 3.21: Temperature dependence of χ_{EC} (dashed line), χ_{CD} (dotted line), and χ_{ED} (solid line) calculated from Equation (0.45).

D), $\chi_{CD}N_{CD} \cong 10$ and 11 (at 140 ºC), respectively, where N_{CD} is the degree of polymerization for the C and D blocks. This simple calculation suggests that the D segments are nearly microphase separated within the C domain, which is consistent with the scattering results documented for these samples (see Figure 3.3).

Additionally, we speculate that the initial decrease in T_{ODT} with addition of D to the parent diblock is the result of the values of χ in this system. This explanation is supported by random-phase approximation (RPA) calculations by Werner and Fredrickson on the effects of χ sequencing in triblock terpolymer melts.[60] The authors were surprised to find

that under certain conditions, addition of a more incompatible block led to less segregation, i.e., a decrease in T_{ODT}. However, this effect had a limit and at significant segregation strengths an ordered phase was energetically favorable. This unexpected behavior is analogous to the decline and eventual increase in T_{ODT} for the ECD polymers in this study (see Figure 3.5). We might expect that the most effective means of screening unfavorable E/D contacts would be remaining in the ordered state (leading to a higher T_{ODT} with increasing D as the overall molecular weight increased). This is the behavior that was documented in ISO, also a nonfrustrated triblock system, at comparable compositions.[24,25] However, the χ parameters in the ECD system are relatively balanced with $\chi_{ED} \cong 1.6\chi_{CD}$ (at 150 ºC and decreases with increasing temperature) compared to $\chi_{IO} \cong 3.3\chi_{SO}$ (at 150 ºC[61]) for the ISO system. D is, therefore, only slightly selective to C compared to E. As D is added to the parent diblock, it can dilute E/C contacts, making the ordered LAM phase less energetically favorable compared to the disordered state. This result causes the disordering process to be preferred at lower temperatures (similar phenomena are also well-documented in block copolymer/solvent systems[62]). Prior to segregation into a three-domain structure, this dilution effect weakens and T_{ODT} begins to increase as the length of the D chains increase. The large differences in the ISO χ parameters likely lead to the observed monotonic increase in T_{ODT} in that system.

When the D blocks segregate (Blend D, 24% D), they form spheres (supported by the TEM micrograph in Figure 3.11), which remain embedded in C layers (see illustrations in Figure 3.19). Based on SAXS results these D spheres are tetragonally or hexagonally packed. However, for Blend E and ECD-5, there is clear evidence of a phase transition to

the multiply continuous O^{70} morphology with increasing temperature. This network phase is characterized by saddle surfaces with negative interfacial Gauss curvature (see Figure 3.20).[25] These complex microstructures are induced by two competing effects: the equal composition E and C domains favor flat interfaces, whereas the smaller D block prefers a curved interface with C. Evidently, the spheres-in-lamellae structure best accomplishes this at a lower temperature, while the hyperbolic surfaces present in the O^{70} network are favored at higher temperatures.

As stated previously, one of the goals of this study was to identify and test the universality of network formation in triblock terpolymer systems. A natural comparison to these ECD triblocks is the ISO system, which has been extensively studied by Bates and coworkers.[24-26] Over a broad range of O, $0.13 \leq f_O \leq 0.24$, O^{70} was identified as the equilibrium morphology. At lower and higher f_O, two- and three-domain lamellar (LAM_3) structures were stable, respectively. Epps *et al*.[25] suggested that this wide window of network stability was a result of the orthorhombic lattice (three adjustable unit cell parameters), which has two additional degrees of freedom compared to cubic structures (one lattice parameter). While we have identified O^{70} in two ECD samples, the O^{70} network region is shifted to larger end block compositions (f_D) compared to ISO (f_O). Additionally, O^{70} was only stable as a high-temperature phase in the ECD triblocks, whereas most O^{70} ISO samples did not exhibit OOTs. Equilibrium self-consistent field theory (SCFT) calculations by Tyler *et al*. demonstrated that the statistical segment lengths and χ parameters associated with an ABC triblock terpolymer system can have dramatic effects on the size and location of the O^{70} phase window.[63] As discussed

previously, the LAM phase is able to accommodate rather large D chains before segregation into three-domain structures. This pushes the formation of complex morphologies (spheres-in-lamellae and O^{70}) to relatively high D content (Blend D, 24% D). Synthesis and morphological characterization of ECD polymers along this isopleth with higher D content and along other, asymmetric isopleths would provide additional insights into the breadth and depth of the O^{70} window in ECD terpolymers.

3.5 Conclusions

We detail the morphological behavior of a series of ECD triblocks along the symmetric $f_E = f_C$ isopleth that vary only in D content. Four ordered structures were identified in this work using SAXS, TEM, and DMS. At low D content, the D blocks mix with C, and the lamellar phase of the parent diblock is maintained. With increased D chain length, microphase separation occurs; the D domains consist of spheres tetragonally or hexagonally arranged in the C layers. Increasing temperature drives order-order transitions in two samples to the multiply continuous O^{70} network. The limited O^{70} region identified in ECD contrasts sharply with the previously studied ISO system, which we have attributed to differences in the magnitudes of the χ parameters. The results from this work provide further understanding of the subtle effects that influence phase behavior in nonfrustrated ABC triblock terpolymers.

Acknowledgement. The synthesis of the polymers in this chapter was greatly improved by the assistance and general cheerfulness of Lynn Wolf. I also thank Dr. Steven Weigand and Dr. Denis Keane at the DuPont-Northwestern-Dow Synchrotron Research Center at the Advanced Photon Source for setting up the experimental equipment used to acquire the SAXS data presented in this chapter. I thank Professor Eric Cochran for the use of his modeling program to generate Figure 3.20.

3.6 References

(1) Mogi, Y.; Kotsuji, H.; Kaneko, Y.; Mori, K.; Matsushita, Y.; Noda, I. *Macromolecules* **1992**, *25*, 5408-5411.

(2) Mogi, Y.; Mori, K.; Kotsuji, H.; Matsushita, Y.; Noda, I.; Han, C. C. *Macromolecules* **1993**, *26*, 5169-5173.

(3) Mogi, Y.; Nomura, M.; Kotsuji, H.; Ohnishi, K.; Matsushita, Y.; Noda, I. *Macromolecules* **1994**, *27*, 6755-6760.

(4) Fielding-Russell, G. S.; Pillai, P. S. *Polymer* **1974**, *15*, 97-100.

(5) Price, C.; Lally, T. P.; Stubbersfield, R. *Polymer* **1974**, *15*, 541-543.

(6) Arai, K.; Kotaka, T.; Kitano, Y.; Yoshimura, K. *Macromolecules* **1980**, *13*, 455-457.

(7) Matsushita, Y.; Yamada, K.; Hattori, T.; Fujimoto, T.; Sawada, Y.; Nagasawa, M.; Matsui, C. *Macromolecules* **1983**, *16*, 10-13.

(8) Arai, K.; Ueda-Mashima, C.; Kotaka, T.; Yoshimura, K.; Murayama, K. *Polymer* **1984**, *25*, 230-238.

(9) Kudose, I.; Kotaka, T. *Macromolecules* **1984**, *17*, 2325-2332.

(10) Beckmann, J.; Auschra, C.; Stadler, R. *Macromol. Rapid Commun.* **1994**, *15*, 67-72.

(11) Stadler, R.; Auschra, C.; Beckmann, J.; Krappe, U.; Voight-Martin, I.; Leibler, L. *Macromolecules* **1995**, *28*, 3080-3097.

(12) Breiner, U.; Krappe, U.; Stadler, R. *Macromol. Rapid Commun.* **1996**, *17*, 567-575.

(13) Breiner, U.; Krappe, U.; Jakob, T.; Abetz, V.; Stadler, R. *Polym. Bull.* **1998**, *40*, 219-226.

(14) Breiner, U.; Krappe, U.; Thomas, E. L.; Stadler, R. *Macromolecules* **1998**, *31*, 135-141.

(15) Brinkmann, S.; Stadler, R.; Thomas, E. L. *Macromolecules* **1998**, *31*, 6566-6572.

(16) Hückstädt, H.; Göpfert, A.; Abetz, V. *Polymer* **2000**, *41*, 9089-9094.

(17) Hueckstaedt, H.; Goldacker, T.; Goepfert, A.; Abetz, V. *Macromolecules* **2000**, *33*, 3757-3761.

(18) Avgeropoulos, A.; Paraskeva, S.; Hadjichristidis, N.; Thomas, E. L. *Macromolecules* **2002**, *35*, 4030-4035.

(19) Ludwigs, S.; Boker, A.; Abetz, V.; Muller, A. H. E.; Krausch, G. *Polymer* **2003**, *44*, 6815-6823.

(20) Förster, S.; Khandpur, A. K.; Zhao, J.; Bates, F. S.; Hamley, I. W.; Ryan, A. J.; Bras, W. *Macromolecules* **1994**, *27*, 6922-6935.

(21) Khandpur, A. K.; Förster, S.; Bates, F. S.; Hamley, I. W.; Ryan, A. J.; Bras, W.; Almdal, K.; Mortensen, K. *Macromolecules* **1995**, *28*, 8796-8806.

(22) Hillmyer, M. A.; Bates, F. S. *Macromolecules* **1996**, *29*, 6994-7002.

(23) Bailey, T. S.; Pham, H. D.; Bates, F. S. *Macromolecules* **2001**, *34*, 6994-7008.

(24) Bailey, T. S.; Hardy, C. M.; Epps, T. H.,III; Bates, F. S. *Macromolecules* **2002**, *35*, 7007-7017.

(25) Epps, T. H.,III; Cochran, E. W.; Bailey, T. S.; Waletzko, R. S.; Hardy, C. M.; Bates, F. S. *Macromolecules* **2004**, *37*, 8325-8341.

(26) Chatterjee, J.; Jain, S.; Bates, F. S. *Macromolecules* **2007**, *40*, 2882-2896.

(27) Bailey, T. S. *Ph.D. Dissertation*; University of Minnesota **2001**, 1-211.

(28) Ndoni, S.; Vigild, M. E.; Berg, R. H. *J. Am. Chem. Soc.* **2003**, *125*, 13366-13367.

(29) Cavicchi, K. A.; Zalusky, A. S.; Hillmyer, M. A.; Lodge, T. P. *Macromol. Rapid Commun.* **2004**, *25*, 704-709.

(30) Ndoni, S.; Papadakis, C. M.; Bates, F. S.; Almdal, K. *Rev. Sci. Instrum.* **1995**, *66*, 1090-1095.

(31) Maheshwari, S.; Tsapatsis, M.; Bates, F. S. *Macromolecules* **2007**, *40*, 6638-6646.

(32) Hucul, D. A.; Hahn, S. F. *Adv. Mater.* **2000**, *12*, 1855-1858.

(33) Fetters, L. J.; Lohse, D. J.; Richter, D.; Witten, T. A.; Zirkel, A. *Macromolecules* **1994**, *27*, 4639-4647.

(34) Brandrup, J.; Immergut, E. H. *Polymer Handbook*, Wiley: New York, 1989.

(35) Brown, G. M.; Butler, J. H. *Polymer* **1997**, *38*, 3937-3945.

(36) Khandpur, A. K.; Macosko, C. W.; Bates, F. S. *J. Polym. Sci. Part B* **1995**, *33*, 247-252.

(37) Hermel, T. J.; Hahn, S. F.; Chaffin, K. A.; Gerberich, W. W.; Bates, F. S. *Macromolecules* **2003**, *36*, 2190-2193.

(38) Zhao, J.; Majumdar, B.; Schulz, M. F.; Bates, F. S.; Almdal, K.; Mortensen, K.; Hajduk, D. A.; Gruner, S. M. *Macromolecules* **1996**, *29*, 1204-1215.

(39) Hasegawa, H.; Hashimoto, T.; Kawai, H.; Lodge, T. P.; Amis, E. J.; Glinka, C. J.; Han, C. C. *Macromolecules* **1985**, *18*, 67-78.

(40) Hardy, C. M.; Bates, F. S.; Kim, M.; Wignall, G. D. *Macromolecules* **2002**, *35*, 3189-3197.

(41) Leibler, L. *Macromolecules* **1980**, *13*, 1602-1617.

(42) Bates, F. S. *Macromolecules* **1985**, *18*, 525-528.

(43) Cochran, E. W.; Morse, D. C.; Bates, F. S. *Macromolecules* **2003**, *36*, 782-792.

(44) Fredrickson, G. H.; Bates, F. S. *Annu. Rev. Mater. Sci.* **1996**, *26*, 501-550.

(45) Wu, L.; Cochran, E. W.; Lodge, T. P.; Bates, F. S. *Macromolecules* **2004**, *37*, 3360-3368.

(46) Han, C. D.; Kim, J. K. *Polymer* **1993**, *34*, 2533-2539.

(47) Williams, M. L.; Landel, R. F.; Ferry, J. D. *J. Am. Chem. Soc.* **1955**, *77*, 3701-3707.

(48) Rosedale, J. H.; Bates, F. S. *Macromolecules* **1990**, *23*, 2329-2338.

(49) Riise, B. L.; Fredrickson, G. H.; Larson, R. G.; Pearson, D. S. *Macromolecules* **1995**, *28*, 7653-7659.

(50) Vigild, M. E.; Chu, C.; Sugiyama, M.; Chaffin, K. A.; Bates, F. S. *Macromolecules* **2001**, *34*, 951-964.

(51) Shibayama, M.; Hasegawa, H.; Hashimoto, T.; Kawai, H. *Macromolecules* **1982**, *15*, 274-280.

(52) Cochran, E. W. *Ph.D. Dissertation*; University of Minnesota **2004**, 1-316.

(53) Kossuth, M. B.; Morse, D. C.; Bates, F. S. *J. Rheol.* **1999**, *43*, 167-196.

(54) Meuler, A. J. *Ph.D. Dissertation*; University of Minnesota **2009**, 1-328.

(55) Takenaka, M.; Wakada, T.; Akasaka, S.; Nishitsuji, S.; Saijo, K.; Shimizu, H.; Kim, M. I.; Hasegawa, H. *Macromolecules* **2007**, *40*, 4399-4402.

(56) Cochran, E. W.; Bates, F. S. *Phys. Rev. Lett.* **2004**, *93*, 087802/1-087802/4.

(57) Meuler, A. J.; Fleury, G.; Hillmyer, M. A.; Bates, F. S. *Macromolecules* **2008**, *41*, 5809-5817.

(58) Almdal, K.; Hillmyer, M. A.; Bates, F. S. *Macromolecules* **2002**, *35*, 7685-7691.

(59) Cochran, E. W.; Bates, F. S. *Macromolecules* **2002**, *35*, 7368-7374.

(60) Werner, A.; Fredrickson, G. H. *J. Polym. Sci. Part B* **1997**, *35*, 849-864.

(61) Frielinghaus, H.; Hermsdorf, N.; Almdal, K.; Mortensen, K.; Messe, L.; Corvazier, L.; Fairclough, J. P. A.; Ryan, A. J.; Olmsted, P. D.; Hamley, I. W. *Europhys. Lett.* **2001**, *53*, 680-686.

(62) Lodge, T. P.; Pudil, B.; Hanley, K. J. *Macromolecules* **2002**, *35*, 4707-4717.

(63) Tyler, C. A.; Qin, J.; Bates, F. S.; Morse, D. C. *Macromolecules* **2007**, *40*, 4654-4668.

4

Formation of a Structure-in-Structure Morphology in Poly(cyclohexylethylene-*b*-ethylene-*b*-cyclohexylethylene-*b*-dimethylsiloxane) Tetrablocks

4.1 Introduction

In the previous chapter, the phase behavior of a sequence of poly(ethylene-*b*-cyclohexylethylene-*b*-dimethylsiloxane) (ECD) triblock terpolymers was presented. These triblocks had equal E and C content and D varied from 0 to 28% by volume. ECD terpolymers are an example of a "nonfrustrated" system like poly(isoprene-*b*-styrene-*b*-ethylene oxide) (ISO) triblocks. Extensive morphological characterization of ISO samples has revealed a rich variety of phases, including three triply-periodic network microstructures.[1-3] In this chapter we present the synthesis, characterization, and phase behavior of a series of CECD tetrablock terpolymers. Like the ECD triblocks discussed in Chapter 3, these CECD tetrablocks contain equal volume fractions of C and E, but the C is divided evenly between the first and third blocks. In Chapter 5, the self-assembly

behavior of CECD materials with an asymmetric C to E ratio of three to seven will be presented. The positioning of two separate C blocks in these tetrablocks creates a new molecular architecture, which adds an additional design parameter in the synthesis of block polymers and can produce qualitatively different morphological behavior.

Advances in macromolecular chemistry have led to controlled chain-growth polymerization methods that can incorporate a wide-range of monomers into linear (AB diblocks, ABA triblocks, ABC triblocks, ABABA pentablocks, etc.)[4,5] and complex (star, miktoarm, comb, graft, etc.)[4-6] block polymer architectures. Incorporation of additional chemically distinct blocks greatly expands the number and complexity of phases, but also dramatically increases the number of parameters that dictate self-assembly. This is readily apparent when we compare linear AB copolymer and ABC terpolymer phase behavior (see Chapter 1 for a more detailed discussion). Just four equilibrium phases have been found in AB diblocks: lamellae (LAM), hexagonally-packed cylinders, body-centered cubic spheres (BCC), and the bicontinuous double gyroid.[7-13] (A fifth morphology, an orthorhombic network with *Fddd* symmetry (O^{70}), has only very recently been documented in poly(styrene-*b*-isoprene) diblock copolymers by Takenaka and coworkers[14,15] after it was predicted to be stable over a very narrow region of phase space.[16-18]) Conversely, over thirty morphologies have been identified in linear ABC systems,[1,3,19-34] with more likely to be discovered. These ABC triblock phases include phases composed of "classical" structures (spheres, cylinders, and lamellae) in which a minority component either decorates another domain (spheres on spheres, spheres or cylinders on cylinders, and spheres or cylinders at a lamellar interface)[21-23,25,26,35] or is

fully embedded in the domain (spheres in lamellae and cylinders in lamellae).[32,36-38] These complex morphologies are the result of competing packing constraints induced by the addition of a block with asymmetric composition and a preference to minimize enthalpically unfavorable chain contacts. While the increased number of molecular variables has precluded the creation of a "universal" ABC terpolymer phase portrait, the rich self-assembly behavior of ABC triblocks continues to fascinate researchers and stimulate interest in their utility in applications as diverse as semipermeable membranes,[29] nanoporous templates,[39] and solid-state electrolytes.[40,41]

This chapter, along with the following two, discusses the phase behavior of a previously unstudied block polymer architecture: the ABAC tetrablock terpolymer. The number of independent parameters that affect phase behavior in ABAC tetrablocks are the same as ABC triblocks, with an additional A block composition variable. In this work, we chose to keep the volume fractions of the two A blocks equal, which reduces the parameter space greatly. The ABAC molecular architecture is a variation of the ABC triblock and its symmetric ABCBA (CBABC) analog. While ABCBA pentablocks adopt the same microstructures as homologous ABC triblocks,[42,43] the division of A chains into two blocks in the ABAC terpolymer architecture is anticipated to influence its self-assembly behavior. The number of possible interfaces does not vary among these systems (A/B, A/C, and B/C), but chain stretching within the central A block will be greatly affected. Additionally, the ABAC molecular architecture has the potential to produce mechanically robust materials compared to ABC triblocks. Placing hard (high T_g) A blocks adjacent to a soft (low T_g) B block, such as in CEC, mimics tough ABA

thermoplastic elastomers.[44] This strategy has been demonstrated previously in an ABCBA pentablock system to greatly improve mechanical toughness compared to homologous ABC triblocks.[43]

Evaluation of the phase behavior of one CEC triblock copolymer and six CECD tetrablock terpolymers containing equal C and E content was performed using a collection of complementary analytical techniques. Dynamic mechanical spectroscopy (DMS) experiments determined the thermal (order-disorder transitions) and viscoelastic behavior of the block polymers. Small-angle X-ray scattering (SAXS) on sheared and unoriented samples was used to obtain information regarding the symmetry of the polymer morphology as a function of temperature. Lastly, transmission electron microscopy (TEM) provided visual evidence of the microstructure and the spatial distribution of domains within a given morphology.

4.2 Experimental Section

The experimental techniques used to synthesize and characterize the morphological behavior of the materials presented in this chapter are similar to those described previously in Chapter 3 for ECD triblock terpolymers. However, for completeness, they are reviewed here as there are some differences.

4.2.1 CECD Tetrablock Synthesis

The polymers used in this study were synthesized and characterized using the experimental techniques detailed in Chapter 2. Six CECD tetrablock terpolymers with equal C and E content were synthesized using the two-step approach detailed in Figure 4.1. Poly(styrene-*b*-butadiene-*b*-styrene-*b*-dimethylsiloxane) (SBSD) block terpolymer precursors were produced through sequential anionic polymerization of styrene, butadiene, styrene, and hexamethylcyclotrisiloxane (D_3). Styrene, butadiene, D_3, cyclohexane, and tetrahydrofuran were rigorously purified as described elsewhere.[45,46] Polymerization of the first block was initiated by *sec*-butyllithium in cyclohexane at 40 ºC under an argon atmosphere. An aliquot of the styrene block was removed after 8 hours for analysis by size-exclusion chromatography (SEC) before proceeding with the sequential monomer addition sequence. Butadiene and styrene were sequentially added and polymerized at 40 ºC (~93% 1,4 addition for butadiene). Polymerization of the dimethylsiloxane block was conducted in two steps. D_3 was added to the reaction media and allowed to stir for 12 hours at 20 ºC, resulting in the incorporation of one D_3 unit to each polymer chain. Propagation was then achieved by adding tetrahydrofuran (equivalent to the volume of cyclohexane) to the reaction media. The propagation step was stopped after 4 hours by adding excess chlorotrimethylsilane, resulting in a conversion of ~50% of D_3 monomer. The precursor terpolymer was recovered by precipitation into a 3:1 solution of methanol and 2-propanol, followed by filtration and complete drying under dynamic vacuum. Saturation of the SBSD precursor terpolymers in cyclohexane at 170 ºC over a silica-supported platinum/rhenium catalyst[47] (Dow

Chemical Co.) resulted in the desired CECD tetrablock copolymers. The saturated polymers were precipitated in methanol, filtered, and dried completely under dynamic vacuum. A CEC triblock copolymer was made in an analogous manner except D_3 monomer was not added. Instead, the SBS precursor triblock copolymer was produced by termination of the living polystyryl anions with excess degassed methanol.

4.2.2 Molecular Characterization

Molecular weight distributions of the initial styrene blocks, the SBS triblock, and the SBSD block terpolymers were obtained by SEC on a Waters 717 GPC equipped with three Polymer Labs Mixed-C columns and a Waters 410 differential refractometer. Samples were run at 30 ºC with a flow rate of 1.0 mL/min using tetrahydrofuran as the mobile phase. Polydispersities were calculated using ten poly(styrene) standards (Polymer Laboratories). SEC traces of the CEC and CECD copolymers obtained at 135 ºC in 1,2,4-trichlorobenzene on a Polymer Laboratories PL-GPC-220 were monomodal, confirming that degradation does not occur during hydrogenation.

Quantitative compositions of the unsaturated SBS and SBSD block copolymers were determined using ^{1}H NMR spectroscopy on a Varian UNITY 300 spectrometer with a pulse repetition delay of 20 s using samples dissolved in deuterated chloroform at room temperature. Volume fractions of poly(styrene), 1,4-poly(butadiene), and poly(dimethylsiloxane) were determined from measured mole fractions using homopolymer densities at 140 ºC.[48] ^{1}H-NMR spectroscopy at 70 ºC in deuterated toluene using a Varian INOVA 300 spectrometer confirmed the extent of hydrogenation for the

CEC and CECD block polymers to be greater than 97%. The molecular characterization data for the block copolymers utilized in this chapter are summarized in Table 4.1.

4.2.3 Dynamic Mechanical Spectroscopy (DMS)

Samples used for DMS were prepared by compression-molding polymer powder into 25 mm ◈ 0.8 mm disks at 170 ºC using a pressure of 2000 psi for 5 – 6 min. A Rheometrics Scientific ARES strain-controlled rheometer fitted with 25 mm diameter parallel plates was used to perform all rheological experiments. The dynamic elastic (G') and loss (G'') moduli were measured as a function of temperature at a constant frequency to probe for the order-disorder transition temperature (T_{ODT}). All measurements to determine T_{ODT}s were made from 140 ºC until 10 ºC beyond the point of disorder (or to 300 ºC if there was not an apparent T_{ODT}), defined by a large, discontinuous decrease in G'. The sample was then held at this temperature for 10 minutes and quickly cooled (20 ºC/min) to well below T_{ODT} before a second isochronal heating ramp. Reported T_{ODT}s were measured on this second heating ramp. Isothermal frequency scans ($100 \leq \omega \leq 0.1$ rad/s) were also conducted to confirm the presence of the T_{ODT} and characterize the viscoelastic response of the sample. All measurements were made under a constant blanket of nitrogen to mitigate polymer degradation at elevated temperatures. Experiments were conducted with a strain amplitude of 1%, which was within the linear viscoelastic regime of the block polymers.

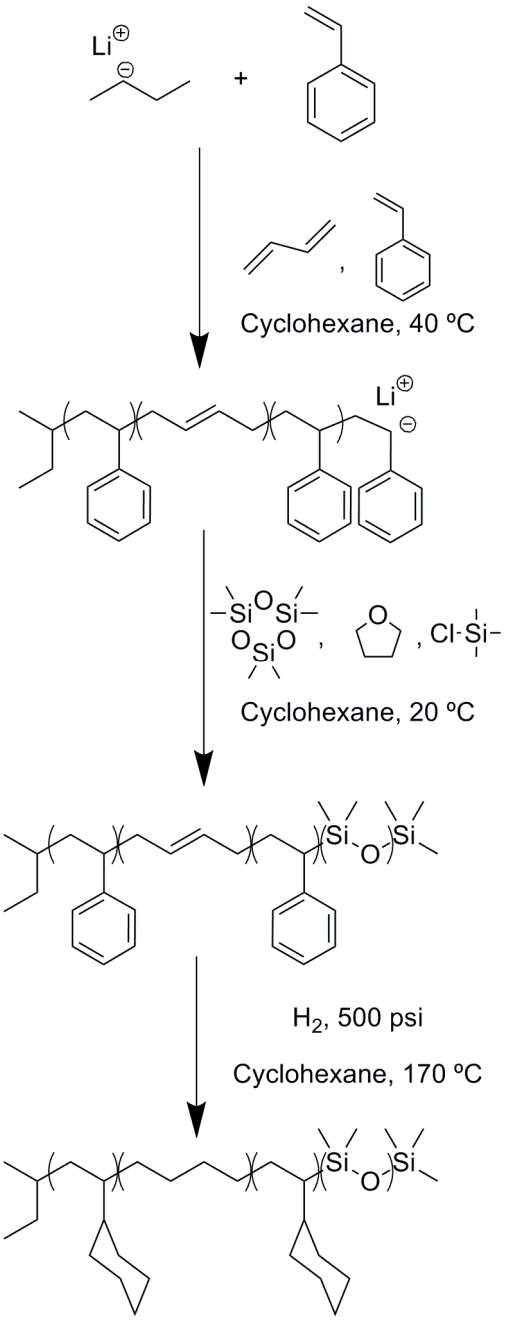

Figure 4.1: Two-step synthesis scheme employing sequential anionic polymerization followed by catalytic hydrogenation to produce poly(cyclohexylethylene-*b*-ethylene-*b*-cyclohexylethylene-*b*-dimethylsiloxane).

4.2.4 Small-angle X-ray Scattering (SAXS)

SAXS experiments were conducted at the Advanced Photon Source at Argonne National Laboratory using the instruments maintained by the DuPont-Northwestern-Dow Collaborative Access Team (DND-CAT). An x-ray wavelength (λ) of 0.729 Å and a sample-to-detector distance of 5.504 m were utilized in these measurements. Two-dimensional data were acquired with a Mar CCD area detector. A DSC hot-stage with a helium purge controlled the specimen temperature. Two-dimensional diffraction patterns were azimuthally averaged and are reported as plots of intensity versus the magnitude of the scattering wave vector $|\boldsymbol{q}| = q = 4\pi\lambda^{-1}\sin(\theta/2)$, where θ is the scattering angle.

Three sample preparation methods were employed in this work:

(1) Two samples were determined to have experimentally accessible T_{ODT}s. Powder patterns of these materials were taken at 140 ºC after annealing at 10 ºC above the ODT for 3 min.

(2) Samples with experimentally inaccessible T_{ODT}s (>300 ºC) were prepared as 1 mm thick films for extended annealing prior to investigation by SAXS. The films were formed by compression-molding polymer between Teflon sheets at 2000 psi for 5 – 6 min at 170 ºC. The molded samples were then annealed under vacuum for 7 days at 200 ºC. Once loaded into the DSC chamber of the synchrotron SAXS line, specimens were heated from room temperature to selected temperatures and held there for 2 – 5 min prior to data collection.

(3) Selected samples were shear-oriented using the reciprocating shear device described by Mortensen *et al.*[49] prior to SAXS experiments. 20 mm ◈ 20 mm ◈ 1 mm

compression-molded samples were subjected to large amplitude oscillatory shear ($|\gamma|$ = 200% and ω = 0.5 s^{-1}) under an argon atmosphere below T_{ODT} for 2 hours. After shearing, the specimen was cooled to room temperature over a two hour period leading to vitrification of the C domains ($T_{g,C} \cong 135$ °C) followed by partial crystallization of the E blocks ($T_m \cong 100$ °C), which locked in the morphology developed at the higher melt temperature. Small sections (3 mm x 2 mm) were cut from the macroscopically oriented specimen for investigation by SAXS along the vorticity direction (z) (see Figure 4.2 for deformation geometry). Two-dimensional SAXS results in this chapter are reported in the format $\boldsymbol{q}_x$-$\boldsymbol{q}_y$.

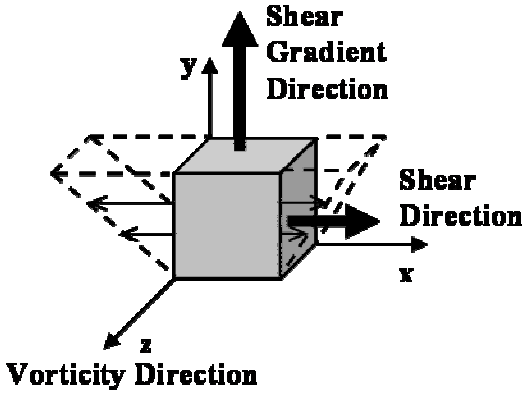

Figure 4.2: Diagram of reciprocating shear coordinate system with the shear (x), shear gradient (y), and vorticity (z) directions noted.

4.2.5 Transmission Electron Microscopy (TEM)

TEM micrographs were collected on a JEOL 1210 transmission electron microscope operating at 120 kV in the bright field mode at the University of Minnesota Institute of Technology Characterization Facility. Sections of the macroscopically oriented samples investigated by SAXS were also examined by TEM. Specimens were initially cryo-microtomed at –120 ºC on a Reichart ultramicrotome fitted with a Microstar diamond knife to create a flat surface. Some samples were stained with ruthenium tetroxide vapors for 1 – 4 hours to obtain sufficient electron mass density contrast between the different blocks.[50-52] Stained and unstained pieces were cryo-microtomed at –120 ºC to create thin sections (70 – 90 nm thickness), which were collected on copper grids (Ted Pella) for subsequent TEM analysis. Unstained CECD specimens have natural contrast between D and the other polymer domains due to the higher electron density of silicon.

4.3 Results and Analysis

Seven block polymers were synthesized with a fixed C to E ratio of approximately one to one ($f_C \cong f_E$ isopleth) and D content from 0 to 33% by volume. The molecular characteristics of these materials are summarized in Table 4.1. The molecular weights and compositions were determined from the aliquot taken from the first poly(styrene) block and the ^{1}H NMR spectra of the poly(styrene-*b*-butadiene-*b*-styrene-*b*-dimethylsiloxane) precursor polymer. The morphologies, lattice dimensions, and T_{ODT}s were obtained on the basis of SAXS, TEM, and DMS.

Table 4.1 Characterization data for CEC triblock and CECD tetrablock polymers.

Polymer	M_n, kDa	M_w/M_n	f_C[a]	f_E[a]	f_D[a]	Phase[b]	T_{ODT},°C[c]	d, nm[d,e]
CEC-2*	22.5	1.06	0.51	0.49	0	LAM_2	280	20.7
CECD-6	22.3	1.10	0.46	0.46	0.08	LAM_2	199	19.6
CECD-7	23.5	1.08	0.43	0.44	0.13	[S-LAM][f] → Cubic	285	21.3
CECD-8	20.3	1.08	0.42	0.42	0.16	S-LAM	>300	36.9, 25.5
CECD-9	25.0	1.07	0.40	0.41	0.19	S-LAM	>300	39.1, 27.7
CECD-10	22.5	1.07	0.38	0.38	0.24	LAM_3[g]	>300	37.0
CECD-11	24.1	1.09	0.33	0.34	0.33	LAM_3[g]	>280	38.4

*Synthesized by Guillaume Fleury.

[a]Volume fractions calculated from melt density data at 140 °C (ρ_C = 0.920 g/cm^3, ρ_E = 0.784 g/cm^3, and ρ_D = 0.895 g/cm^3).[48]

[b]LAM_2: two-domain lamellae; Cubic: unknown structure with likely cubic symmetry; S-LAM: spheres hexagonally-packed within two-domain lamellae; LAM_3: three-domain lamellae.

[c]Order-disorder transition temperature determined by DMS.

[d]Temperature is 140 °C.

[e]Lattice dimensions, d, where $d = 2\pi/q^* = d_{hkl}$, (hkl) = (100) for LAM, (110) for Cubic, (001) and (100) for S-LAM.

[f]Indicates tentative assignment of likely metastable morphology.

[g]Predominant morphology. SAXS and TEM suggest coexistence with S-LAM and cylinders.

We begin evaluation of the melt phase behavior of the block terpolymers listed in Table 4.1 by presenting SAXS profiles in Figure 4.3 from unaligned, annealed samples. All of the specimens generated isotropic, Debye-Scherrer scattering patterns indicating that the samples consisted of ordered, randomly oriented microstructures. The SAXS data were acquired at 140 ºC after disordering the sample (CEC-2 and CECD-6) or annealing for 7 days at 200 ºC (CECD-7, -8, -9, -10, and -11). The SAXS patterns can be divided into four different regions based on changes in the scattering profiles:

(1) A well-defined primary peak and higher order reflections are readily apparent in the scattering profiles for CEC-2 (0% D) and CECD-6 (8% D). CECD-6 also exhibits a broad maximum at $q \cong 0.055$ Å^{-1}.

(2) For CECD-7 (13% D), the primary peak and a scattering maximum at $q \cong 0.049$ Å^{-1} now appear to consist of multiple reflections. Other weak higher order reflections are also apparent.

(3) Further increasing the volume fraction of D to 16 and 19% (CECD-8 and CECD-9) dramatically shifts the primary peak position to a lower value of q and numerous well-defined, higher-order peaks are visible.

(4) For CECD-10 (24% D) and CECD-11 (33% D), the relative peak positions have not changed, but some of the reflections broaden and weaken in intensity compared to the previous region.

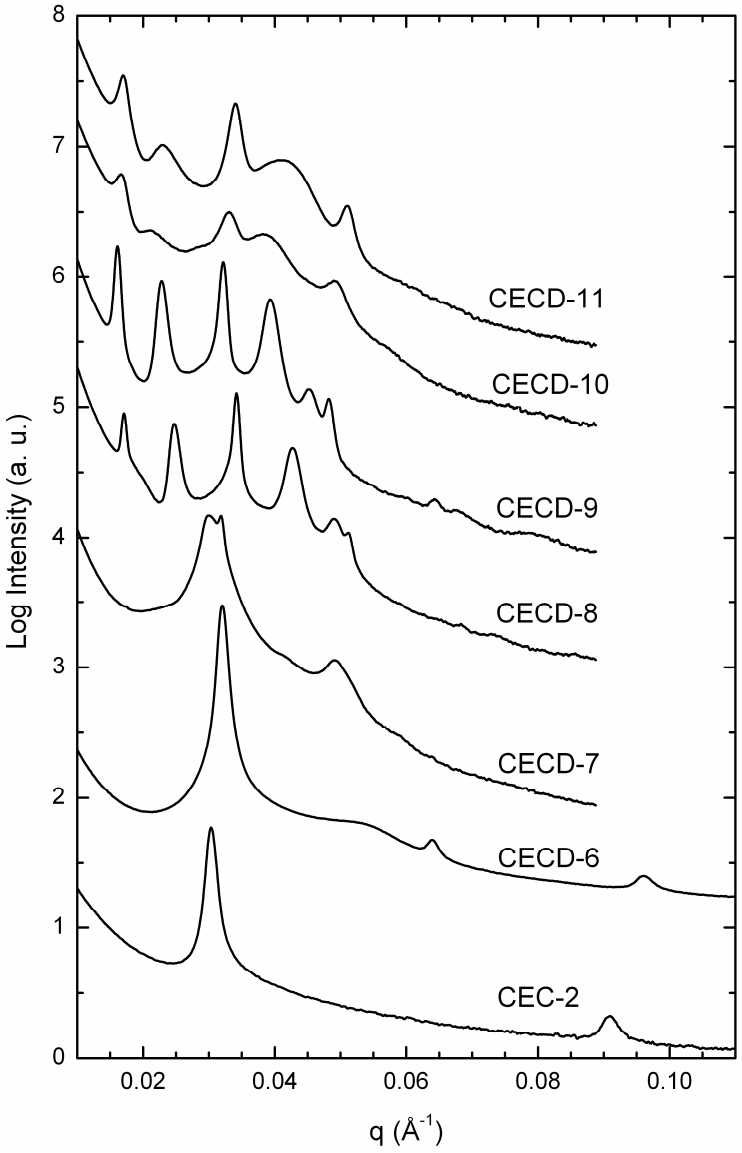

Figure 4.3: Azimuthally integrated SAXS profiles of CEC-2 triblock and CECD tetrablocks. CEC-2 and CECD-6 were annealed 10 ºC above T_{ODT} for 3 min prior to annealing and data collection at 140 ºC. CECD-7, -8, -9, -10, and -11 were annealed at 200 ºC for 7 days prior to annealing and acquisition of data at 140 ºC. Scattering peaks of varying intensity and breadth are apparent in all of the profiles indicative of ordered morphologies. The data are shifted vertically for clarity.

4.3.1 Region 1 – Two-domain Lamellae (LAM_2)

A LAM_2 phase has been assigned on the basis of SAXS and TEM results for CEC-2 (0% D) and CECD-6 (8% D). The synchrotron SAXS powder patterns for these samples are presented in Figure 4.4. Diffraction peaks at q^*, $2q^*$, and $3q^*$, where q^* is the primary Bragg reflection, are evident for CECD-6. Reflections for CEC-2 appear at q^* and $3q^*$; the absence of the $2q^*$ peak is consistent with a symmetric LAM_2 structure factor extinction.[2] The domain spacings, $d = 2\pi/q^*$, are reported in Table 4.1 for these lamellar samples. Unlike CEC-2, CECD-6 displays a broad bump at $q \cong 0.055$ $Å^{-1}$. This result is qualitatively similar to the scattering profiles observed for two lamellar ECD triblocks (ECD-4 and Blend C, Chapter 3). As discussed previously in Chapter 3, this broad maximum likely stems from C block-D block correlations within the mixed C + D domain, and corroborates the two-domain phase assignment.

A TEM micrograph of CECD-6, presented in Figure 4.5, supports the assignment of LAM_2. The dark stripes correspond to RuO_4-stained, mixed C + D domains, while the semicrystalline E domains appear white. Periodic undulations along the lamellar interfaces are likely a consequence of crystallization in the E block. Comparison of the results presented in Figures 4.4 and 4.5 yields $d_{TEM} \cong 0.8 d_{SAXS}$ for CECD-6. The reasons for this discrepancy in measured domain spacings are not completely understood,[1,2] though E crystallization (20% crystallinity as measured by DSC) and shrinkage of the sample in the electron beam would lead to this effect. Attempts at

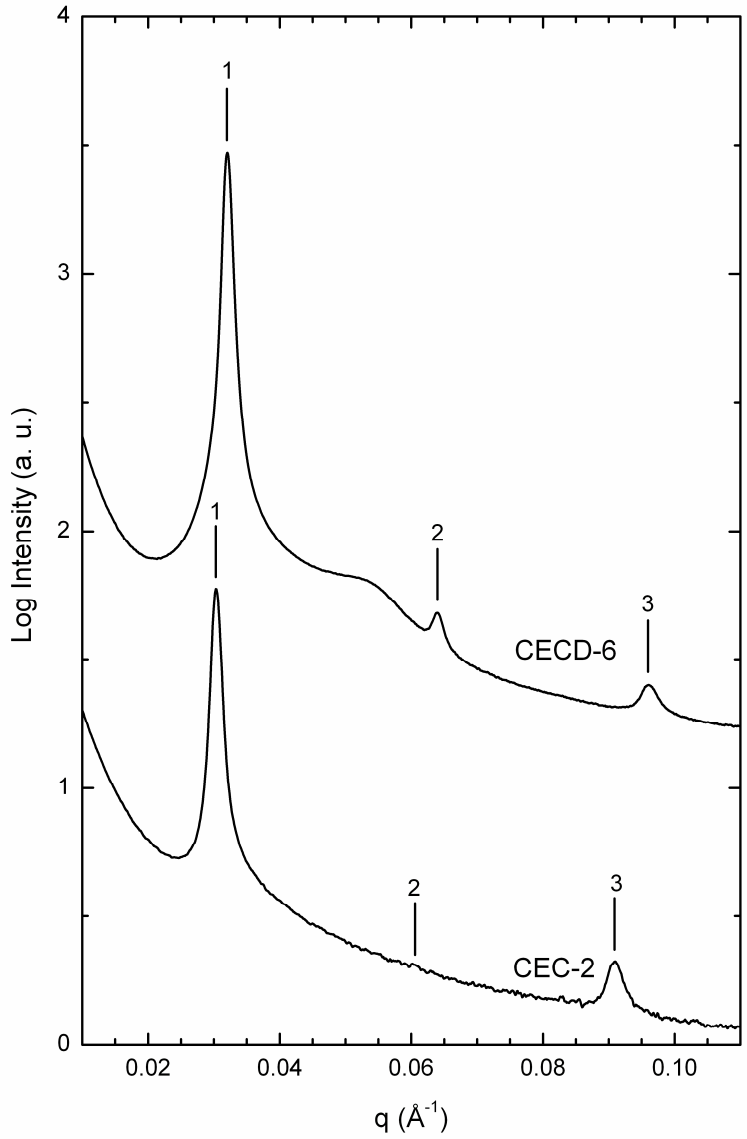

Figure 4.4: SAXS data for CEC-2 (0% D) and CECD-6 (8% D) collected at 140 ºC (identical results as given in Figure 4.3). The diffraction data are indexed to a lamellar morphology. The absence of the 2*q** reflection in CEC-2 is consistent with a structure factor extinction for symmetric LAM_2.[2] The upper curve is shifted vertically for clarity.

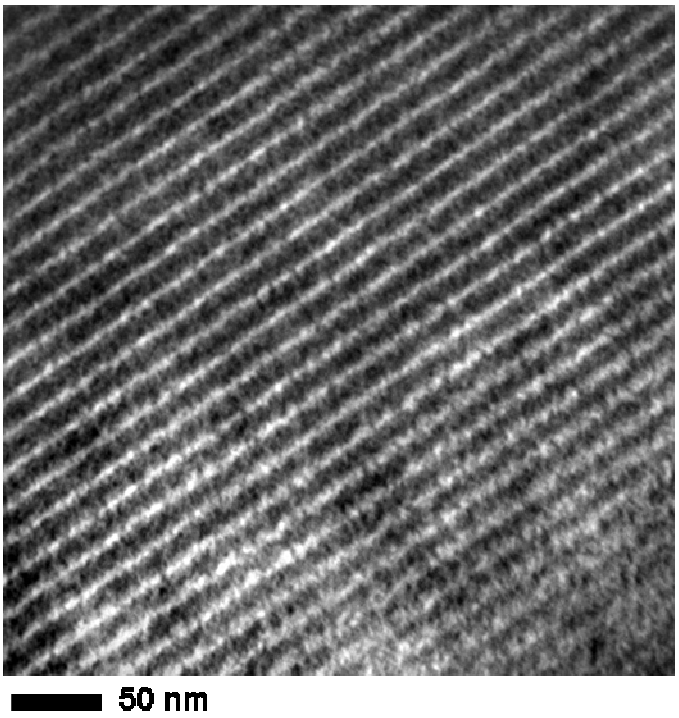

Figure 4.5: TEM micrograph generated from RuO_4-stained CECD-6 from the LAM_2 region. The sample was sheared (γ = 200%, $\dot{\gamma}$ = 0.5 s^{-1}, T = 170 ºC) to facilitate imaging. The RuO_4 preferentially interacts with the C and D domains making them darker.

visualizing the lamellar structure without RuO_4 staining were unsuccessful, suggesting that D is mixed within the C domains, i.e., a LAM_2 structure.

The location of the order-to-disorder transition temperature (T_{ODT}) of CEC-2 and CECD-6 was identified upon heating by isochronal DMS measurements (shown in Figure 4.6). The dynamic elastic (G') and loss (G'') moduli gradually decrease with increasing temperature until declining precipitously at the T_{ODT}. Interestingly, despite similar molecular weights (see Table 4.1), the T_{ODT} of CEC-2 is over 80 ºC higher

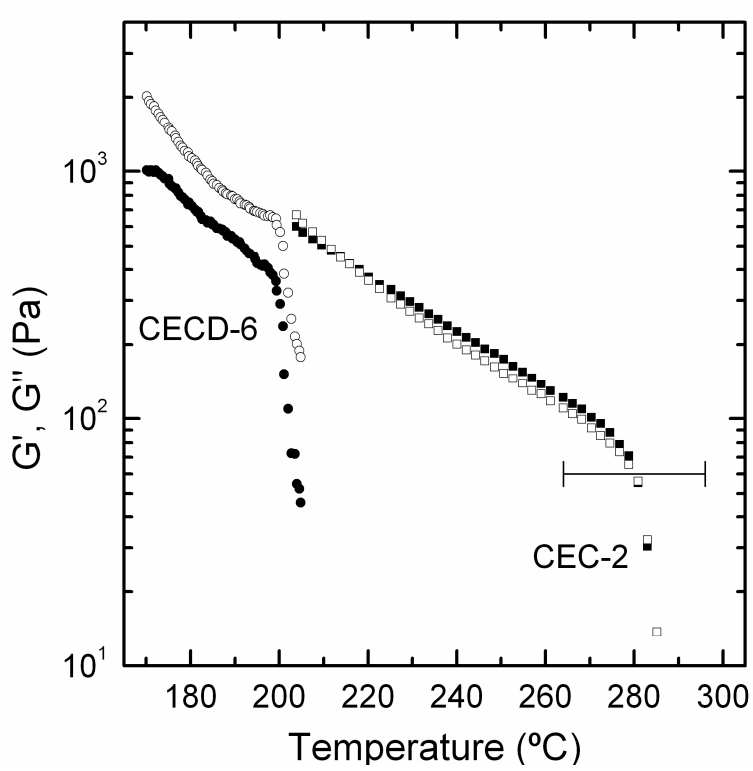

Figure 4.6: Isochronal (0.1 and 0.05 rad/s for CEC-2 and CECD-6, respectively) elastic (solid symbols) and loss (open symbols) moduli collected from lamellar CEC-2 (■, □) and CECD-6 (●, ○) block polymers. Samples were annealed 10 ºC above the T_{ODT} for 10 min prior to cooling back to the ordered state and collecting these data upon heating. The moduli of both samples exhibit discontinuous decreases at T_{ODT} indicative of a transition from an ordered to a disordered phase. The uncertainty in T_{ODT} for CEC-2 due to error associated with the measured molecular weight is also indicated.

than the T_{ODT} of CECD-6. The uncertainty in T_{ODT} for CEC-2 has been estimated using the experimentally determined correlation for $\chi(T)${{8 Cochran,Eric W. 2002; }} and a 5% error in the measured degree of polymerization (N). This uncertainty is

indicated by the horizontal error bar in Figure 4.6 and is considerably smaller than the difference in T_{ODT}s between the two polymers. A decline in T_{ODT} with increasing D content was also documented in the series of ECD triblocks discussed in Chapter 3. However, the T_{ODT} depression in the ECD system was much more modest (~20 ºC), suggesting that block architecture can have a dramatic effect on the energetically preferred morphological state, i.e., ordered or disordered. Neither sample exhibited sharp decreases or increases in G' or G'' upon heating from 140 ºC to the T_{ODT}. We interpret this as a lack of order-order transitions (OOTs).

4.3.2 Region 2 – Suspected Spheres-in-Lamellae to Cubic Phase Transition

Returning to Figure 4.3, one sample, CECD-7 (13% D), generated a SAXS powder pattern with several broad peaks that appear to consist of multiple reflections. Prior to presenting additional structural characterization data for CECD-7, its linear viscoelastic properties will be discussed. Isochronal DMS measurements obtained while heating and cooling are given in Figure 4.7a. Upon heating there is evidence of a morphological transition in G'' beginning at 210 ºC, which is less apparent in G'. Both G' and G'' decline precipitously at T_{ODT}. Upon cooling, G' and G'' do not track the heating curves, suggesting that the low-temperature phase is not regained and the order-order transition observed on heating has not been reversed. The linear viscoelastic response of the high-temperature phase between 210 and 270 ºC is presented in Figure 4.7b using time-temperature superposition (TTS). The low-frequency plateau in G' is suggestive, but not definitive, of a three-dimensional morphology, such as network structures or BCC spheres.[53]

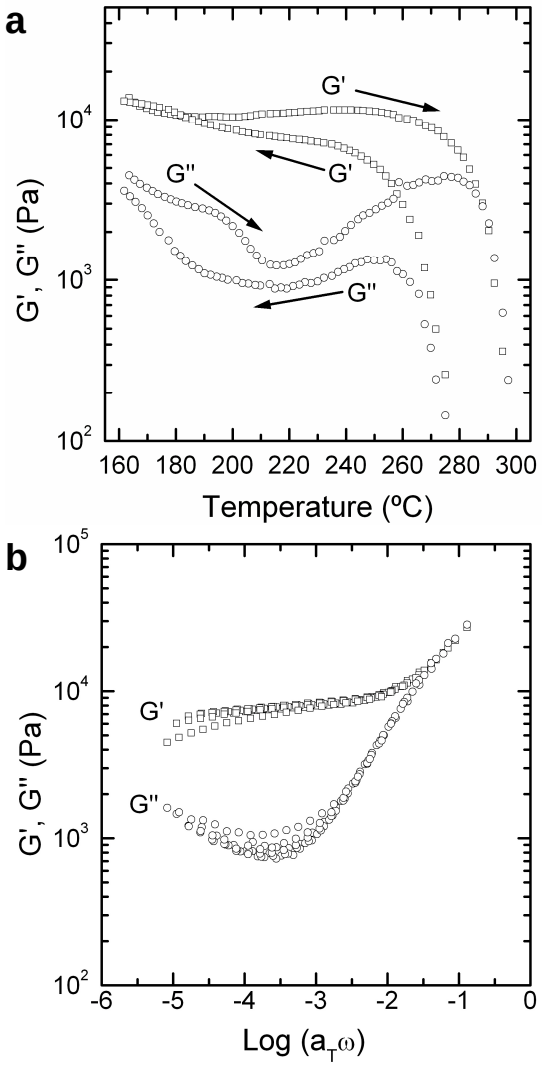

Figure 4.7: (a) Isochronal (ω = 0.05 rad/s) elastic (□) and loss (○) moduli for CECD-7 collected upon heating and cooling at 0.1 ºC/min. The sample was annealed for 10 minutes at 300 ºC and quickly cooled (20 ºC/min) to 160 ºC prior to data collection. (b) Frequency sweep data, G' (□) and G'' (○), for CECD-7 collected at 10 ºC increments from 210 to 270 ºC, shifted according to time-temperature superposition with T_{ref} = 140 ºC. This solid-like viscoelastic response is consistent with a morphology with three-dimensional translational order.

To further aid in the assignment of the low- and high-temperature phases in CECD-7, a sample was shear-oriented prior to SAXS measurements using a previously described, custom built device[49] at 180 ºC (below the T_{OOT} identified in Figure 4.7a) with a strain amplitude and shear rate of $|\gamma|$ = 200% and $\dot{\gamma}$ = 0.5 s^{-1}, respectively. In Figure 4.8, two-dimensional SAXS data from the $\boldsymbol{q_x}$-$\boldsymbol{q_y}$ plane collected at (a) 140 and (b) 200 ºC after heating the sample from room temperature are presented. At 140 ºC, very strong reflections perpendicular to the shear (x) direction are apparent at $q \cong 0.032$ $Å^{-1}$. There is also weak, off-meridional scattering at $q \cong 0.028$ $Å^{-1}$. Upon heating to 200 ºC (annealed at this temperature for 5 min prior to data collection), four off-meridional reflections are evident at $q \cong 0.027$ $Å^{-1}$ at 53 ± 2º relative to the meridian. Higher-order reflections are also present at $2q^*$ along the meridian and at $1.62q^*$, which are 24 ± 3º relative to the meridian. The strong meridional reflections are indicative of a layered morphology with the layer normals aligned parallel to the shear gradient direction (y) (see morphological illustrations and shear coordinate system in Figure 4.8). The off-meridional diffraction spots are evidence of a secondary structure with a separate periodicity. Qualitatively similar two-dimensional scattering patterns have been observed for the hexagonally perforated layer (HPL) morphology in shear-oriented diblock copolymers.[54-59] However, these scattering results are also consistent with spheres of D embedded in the C/E lamellar structure. This is the how we interpret the scattering in conjunction with the results obtained by TEM. The same sheared CECD-7 sample used for SAXS (data presented in Figure 4.8) was used to generate the TEM image presented in

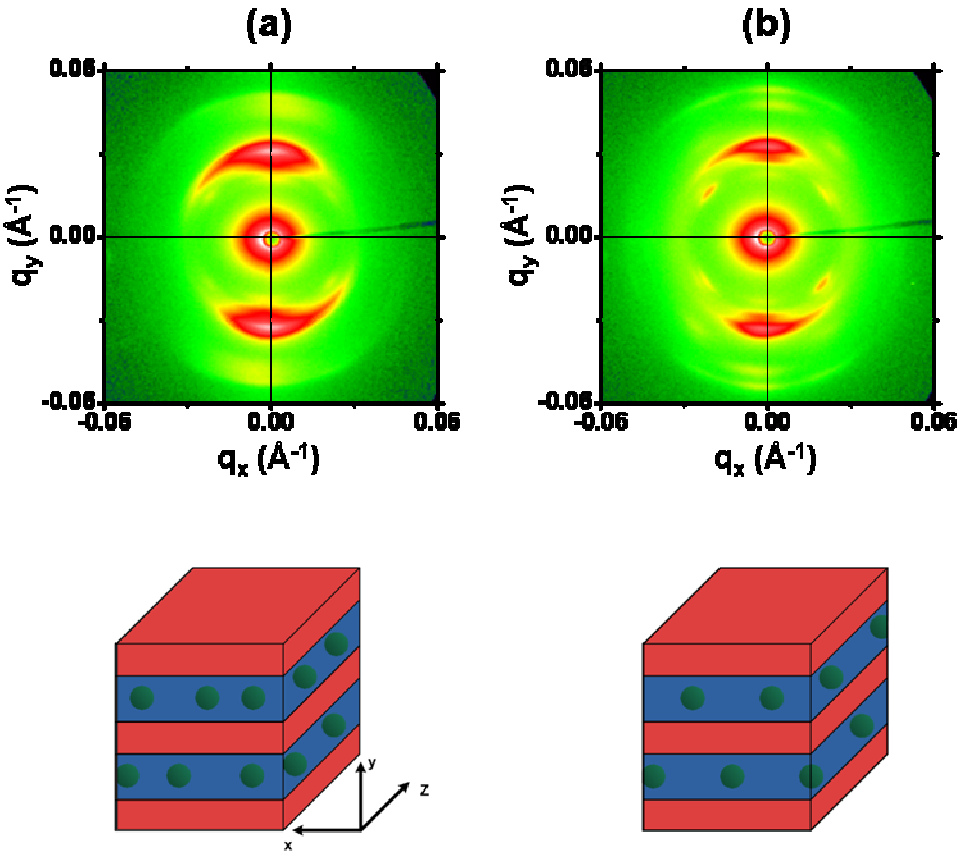

Figure 4.8: Two-dimensional SAXS results obtained from CECD-7 after shear-alignment ($|\gamma|$ = 200%, $\dot{\gamma}$ = 0.5 s^{-1}, T = 180 ºC, X-ray beam incident to z-direction). After processing, the sample was cooled to room temperature and sectioned. The oriented specimen was heated from room temperature to (a) 140 ºC and subsequently (b) 200 ºC on the SAXS line. The SAXS data were obtained after 5 min at each temperature. The scattering are consistent with a layered morphology, with "parallel" alignment, and a secondary structure. The secondary structure is drawn as spheres; the shape can not be determined from these data, but is consistent with the complementary TEM micrograph given in Figure 4.9.

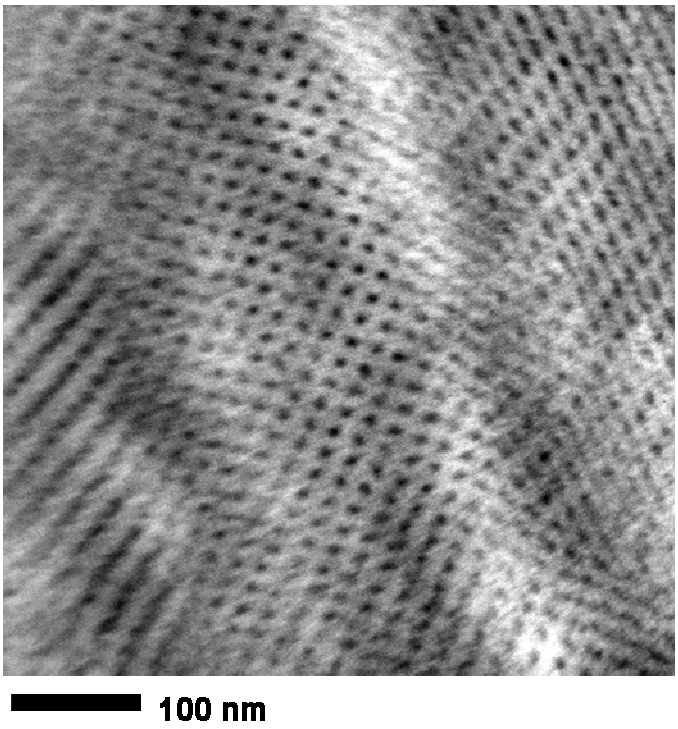

Figure 4.9: Unstained TEM micrograph generated from CECD-7 after shear orientation ($|\gamma|$ = 200%, $\dot{\gamma}$ = 0.5 s^{-1}, T = 180 ºC). The D domains appear dark, while the lighter areas correspond to C and E blocks. The discrete, circular D domains are consistent with spheres of D.

Figure 4.9. In this micrograph obtained without staining, discrete, circular D domains are readily apparent (dark areas). There is no clear evidence of continuity within the D domain, strongly suggesting that they consist of isolated, spherical particles. Thus, we attribute the scattering results in Figure 4.8 to spherical D domains embedded in C/E layers. At 140 ºC, the spheres lack little long-range order, and the secondary scattering is relatively weak. Heating to 200 ºC enhances the correlation between D

spheres, resulting in stronger and higher-order off-meridional reflections (see illustrations in Figure 4.8).

The CECD-7 sample presented in Figure 4.8 was heated further to 250 ºC on the SAXS beam line, which yielded a strikingly different scattering pattern (Figure 4.10a). The two strong meridional and four weaker off-meridional spots present at 200 ºC have collapsed to a common *q*, suggesting convergence to a single length scale. This supposition is consistent with a cubic or two-dimensional (hexagonal or tetragonal) lattice. Cooling the sample to 200 ºC and subsequently to 140 ºC (Figures 4.10b and 4.10c, respectively) does not change the symmetry of the scattering patterns. Additionally, the six-fold symmetry present after heating to 250 ºC is characteristic of either a hexagonal, trigonal, or cubic structure.

The SAXS patterns show diffraction spots at relative radial positions of 1, √2, √3, and 2 (see Figure 4.11 for one-dimensional profile of scattering data collected at 140 ºC). The reflections at position ratios of √2 and √3 are inconsistent with two-dimensional hexagonal and tetragonal space groups, respectively. We note that these reflections can be generated by incorporation of a second lattice parameter in a three-dimensional hexagonal or tetragonal structure, but the presence of a second length scale (or three in the case of orthorhombic space groups) is not suggested by any of the scattering data available at this time.

Considering cubic space groups, reflection (*hkl*) occurs at a radial location of mq^*, where *m* is the peak modulus ($h^2 + k^2 + l^2 = m^2$). A peak modulus of 1 eliminates 16 of the 17 possible cubic extinction symbols, leaving only *P*---, which includes

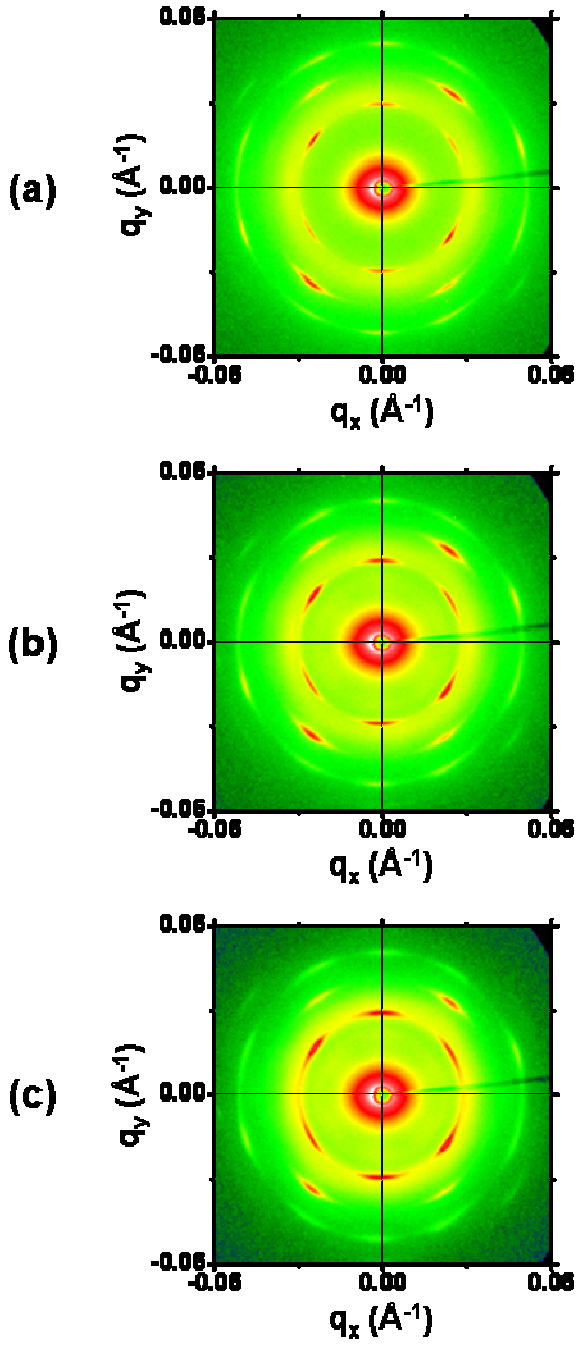

Figure 4.10: SAXS patterns collected at (a) 250, (b) 200, and (c) 140 ºC for the same CECD-7 sample presented in Figure 4.8. The specimen was held at each temperature for 5 min prior to data collection.

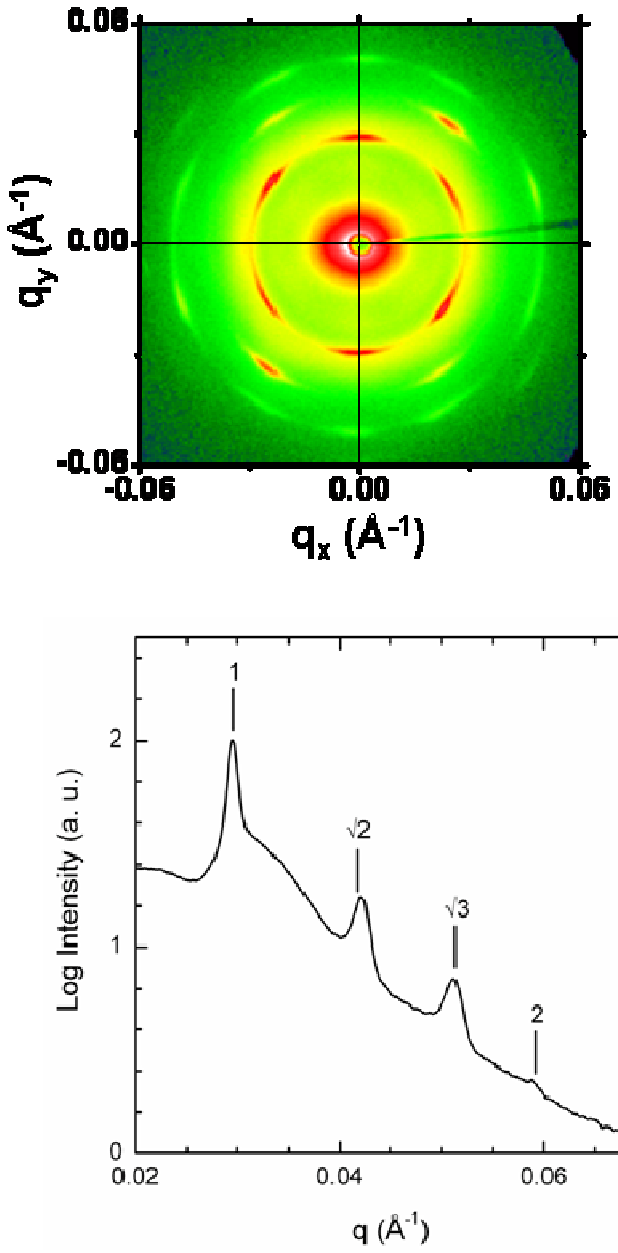

Figure 4.11: Two-dimensional SAXS pattern for CECD-7 obtained at 140 ºC after heating to 250 ºC (same data as Figure 4.10) and one-dimensional azimuthal integration plot. The diffraction spots occur at radial ratios q/q^* = 1, √2, √3, and 2, as indicated in the one-dimensional scattering profile.

Table 4.2: Extinction symbols associated with cubic space groups and observed reflection ratios multiplied by a factor of √2 for the high-temperature phase observed in CECD-7. X denotes experimentally observed reflections, while x denotes allowed reflections for a given extinction.

square of modulus[a]	Observed Reflection Ratios Multiplied by √2 Cubic Extinction Symbol																		observed
	P---[b]	*P*4$_2$--	*P*4$_1$--	*P*--*n*	*Pa*--	*Pn*--	*Pn*-*n*	*I*---[c]	*I*4$_1$--	*I*--*d*	*Ia*--	*Ia*-*d*[d]	*F*---[e]	*F*4$_1$--	*F*--*c*	*Fd*--	*Fd*-*c*		
1	x																		
2	X	X	X	X		X	X	X	X										X
3	x	x	x		x	x							x	x		x			
4	X	X		X	X	X	X	X			x		X		X				X
5	x	x	x	x	x														
6	X	X	X	X	X	X	X	X	X	X	X	X							X
8	X	X	X	X	X	X	X	X	X	X	X	X	X	X	X	X	X		X

[a]Modulus *m* is defined for the reflection (*hkl*) as $h^2 + k^2 + l^2 = m^2$.

[b]Simple cubic ($Pm\bar{3}m$) possesses this extinction symbol.

[c]Body-centered cubic ($Im\bar{3}m$) is the highest symmetry space group associated with this cubic extinction symbol.

[d]The gyroid network morphology is the only space group ($Ia\bar{3}d$) associated with this extinction symbol.

[e] Face-centered cubic ($Fm\bar{3}m$) is the highest symmetry lattice associated with this cubic extinction symbol.

$Pm\bar{3}m$ (simple cubic). Rescaling the primary peak position by √2 greatly increases the possible allowed space groups. Six of the 17 cubic extinction symbols can account for the reinterpreted √2, √4, √6, and √8 peak positions. These are *P*---, $P4_2$--, *P*—*n*, *Pn*--, *Pn*-*n*, and *I*---. Of these six, four (*P*---, $P4_2$--, *P*—*n*, and *Pn*--) have allowed reflections that do not appear in scattering data. However, these absences may be due to minima in the structure factor, and thus, does not *prove* that the structure can not be a given space group. The two remaining cubic extinction symbols are *Pn*-*n* and *I*---. Differentiating between these two symmetries would require a large number of higher order peaks. However, we note that the commonly found body-centered cubic morphology ($Im\bar{3}m$) is associated with *I*--- extinction symbol and to the best of our knowledge, $Pn\bar{3}n$ symmetry has not been observed in soft matter.

This analysis leads us to the conclusion that the morphology observed in the SAXS results presented in Figure 4.10 is likely cubic. The relative peak positions are consistent with $Im\bar{3}m$ symmetry, but can also be attributed to a large number of other cubic space groups. Additionally, we do not have an explanation for the observation or the mechanism that would lead to the transition from the tentatively identified spheres-in-lamellae low-temperature morphology to a cubic structure at elevated temperatures. However, we do note that the low-temperature phase is not recovered upon cooling, suggesting that the low-temperature morphology was stabilized by the large shear deformation applied prior to the SAXS experiment.

4.3.3 Region 3 – Spheres in Lamellae (S-LAM)

With a further increase in D volume fraction, there is another change in the observed CECD microstructure. The primary peaks for CECD-8 (16% D) and CECD-9 (19% D) shift to a much lower q and a number of well-developed higher order reflections are evident (see Figure 4.3). These SAXS results are clearly different from those obtained from CEC-2, CECD-6, and CECD-7. We have associated a spheres-in-lamellae (S-LAM) morphology with CECD-8 and CECD-9 by utilizing SAXS measurements on unoriented and aligned samples and TEM.

SAXS experiments were conducted to determine the ordered state symmetry of CECD-9 at various temperatures. Figure 4.12 presents these data for an unoriented CECD-9 sample that was annealed for 7 days at 200 ºC. The specimen was heated from 140 to 250 ºC and then cooled to 140 ºC. At 140 ºC during the initial heating, Bragg reflections are apparent at $q/q^* = 1, 2, 3, 4$, and 5 along with five additional peaks at $q/q^* = 1.44, 2.49, 3.80, 4.31$, and 4.98. Rescaling these second set of wavevectors by the first reflection in the group ($q_2 = 0.0227$ Å^{-1}) yields $q/q_2 = 1, \sqrt{3}, \sqrt{4}, \sqrt{7}, \sqrt{9}$, and $\sqrt{12}$; these are the first five allowed peak ratios for a two-dimensional hexagonal structure. Taking the two groups of reflections as evidence of two length scales in CECD-9, d_1 and d_2, the SAXS pattern at 140 ºC has been indexed to a two-dimensional hexagonal lattice, (hk0) reflections, superimposed on a one-dimensional lamellar structure, (00l) reflections, (see Figure 4.12). These results are consistent with hexagonally arranged D embedded within the C domain, which forms a lamellar structure with E. The repeat distance along the lamellar normal (d_1) corresponds to one E layer and one C layer containing the D

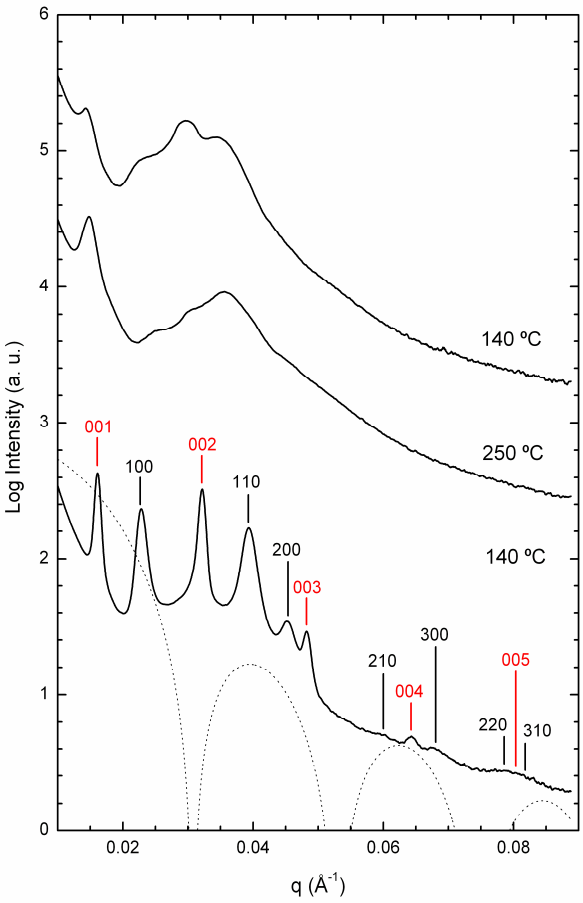

Figure 4.12: Azimuthally integrated SAXS data obtained from CECD-9 while heating from 140 ºC (bottom curve, same data as in Figure 4.3) to 250 ºC and then cooling to 140 ºC (top curve). The sample was annealed at 200 ºC for 7 days prior to data collection. The bottom trace has been indexed to a two-dimensional hexagonal lattice embedded in a layered structure. Broad, weaker peaks at 250 and 140 ºC (cooling) are consistent with the loss of long-range order in the two-dimensional hexagonal lattice that was present at 140 ºC upon heating. The dotted line corresponds to a spherical form factor with R = 14.6 nm: $P(q,R) = \left(3/(qR)^3\right)^2 \left(\sin(qR) - (qR)\cos(qR)\right)^2$. The upper two curves are shifted vertically for clarity.

domains. The lack of interlayer reflections, (101), (102), …, suggests that there is little or no correlation between D domains in adjacent C layers. A similar spheres-in-lamellae morphology has been previously documented by Shibayama *et al*. in a solvent-cast poly(styrene-*b*-(4-vinylbenzyl)dimethylamine-*b*-isoprene) (SAI) triblock terpolymer with 35% S, 39% A, and 26% I by volume.[36] TEM with selective staining revealed I domains dispersed in A lamellae in a regular two-dimensional array. SAXS results confirmed the presence of the secondary structure, but the authors were not able to determine the symmetry of the two-dimensional lattice due to a lack of higher order reflections. Additionally, when the sample was cast from another solvent, the I domains coalesced to form a three-domain lamellar morphology, suggesting the S-LAM microstructure may not be the equilibrium phase in this triblock terpolymer.

Further heating the sample to 250 ºC results in a significant broadening and weakening of the primary peak and higher order Bragg reflections, consistent with the loss of long-range order. The (100) reflection associated with the hexagonal lattice is nearly extinct and a broad maximum at $q \cong 0.036$ Å^{-1} (likely due to form factor scattering from D spheres, which is consistent with complementary TEM images discussed below) convoluted with weak (002) and (110) peaks is apparent. The D spheres likely undergo a lattice disordering process, which has been documented in sphere-forming AB diblock[66,67] and ABA triblock[68] copolymers. At 250 ºC CECD-9 is not disordered, but the D spheres possess only short-range, liquid-like order. Upon cooling to 140 ºC, the scattering results remain qualitatively similar, indicating that long-range order is not restored in the timeframe of the experiment (~5 min). We interpret this result as an effect

of slow sphere ordering kinetics[69,70] and approaching the glass transition of C ($T_g \cong 135$ ºC). The lattice dimensions, d_1 and d_2, for CECD-8 and CECD-9 determined at 140 ºC during heating are listed in Table 4.1.

A two-dimensional diffraction pattern ($\boldsymbol{q}_x$-$\boldsymbol{q}_y$ plane) generated from CECD-8 after large-amplitude oscillatory shear (T = 180 ºC) is presented in Figure 4.13. This image contains a number of well-defined diffraction spots, consistent with an anisotropic structure. Bragg reflections are located at q/q^* = 1, 1.44, 2, 2.49, 2.87, and 3, where q^* = 0.0173 Å^{-1}. Diffraction spots at q/q^* = 3.80, 4, 4.31, and 4.98 were also observed (not shown). These wavevectors agree quite well with the lattice dimensions measured from the unoriented, annealed CECD-8 sample (q^* = 0.0170 Å^{-1}, q_2/q^* = 1.45, see Figure 4.3). This suggests the shear alignment experiment has not disrupted or transformed the morphology observed in the undistorted sample. Like the reflections identified in the unoriented materials, the diffraction spots in Figure 4.13 can be divided into two categories: those arising from in-plane hexagonal scattering and those from a one-dimensional lamellar structure. The equatorial diffraction spots at q/q^* = 1, 2, and 3 ($3q^*$ reflections are partially cut off by cropping of image) are consistent with lamellae oriented parallel to the shear (x) direction[71] (see Figure 4.14a). Interlayer scattering from the two-dimensional hexagonal lattice is not observed, suggesting that the D domains remain uncorrelated between lamellae. However, strong diffraction spots are apparent at q/q_2 = 1, √3, √4, and √7. This scattering arises from a perpendicular orientation of the lamellar structure (lamellae normal perpendicular to shear (x) and velocity gradient (y)

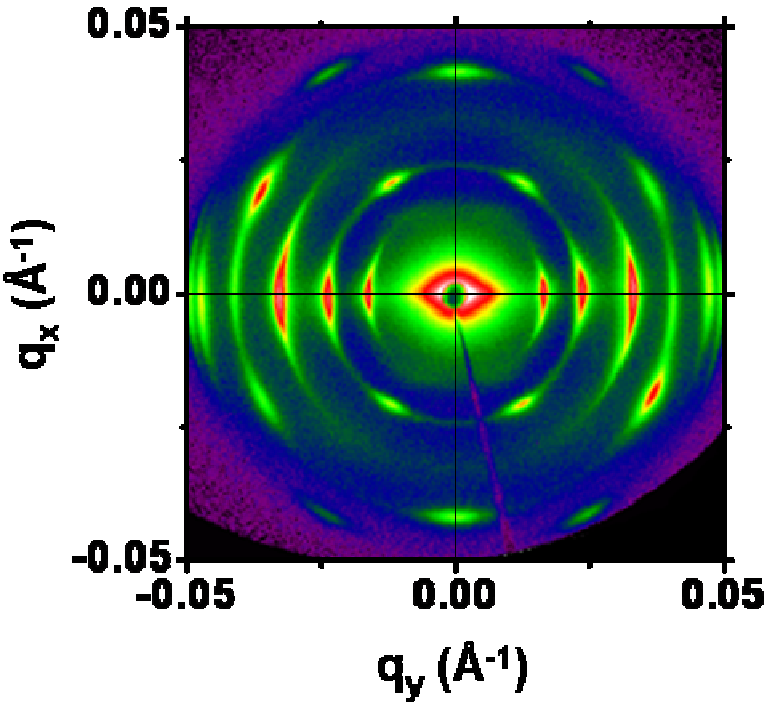

Figure 4.13: Two-dimensional SAXS pattern obtained from CECD-8 (16% D) at 140 ºC after large-amplitude ($|\gamma|$ = 200%, $\dot{\gamma}$ = 0.5 s^{-1}, T = 200 ºC) reciprocating shear. The scattering is consistent with a mixed orientation of parallel lamellae (lamellar normal parallel to shear gradient (y) direction) and perpendicular lamellae (lamellar normal parallel to vorticity (z) direction). The hexagonal reflections arise from the arrangement of D spheres within the C lamellae.

directions[71]) as shown in Figure 4.14b. The hexagonal diffraction spots are consistent with alignment of the (100) planes of the hexagonal lattice parallel to the shear plane.[72]

TEM micrographs presented in Figure 4.15 from CECD-8 and CECD-9 provide further evidence for this complex sphere-in-lamellae morphology. Hexagonally packed circular D domains are readily apparent in the unstained images (Figure 4.15a,

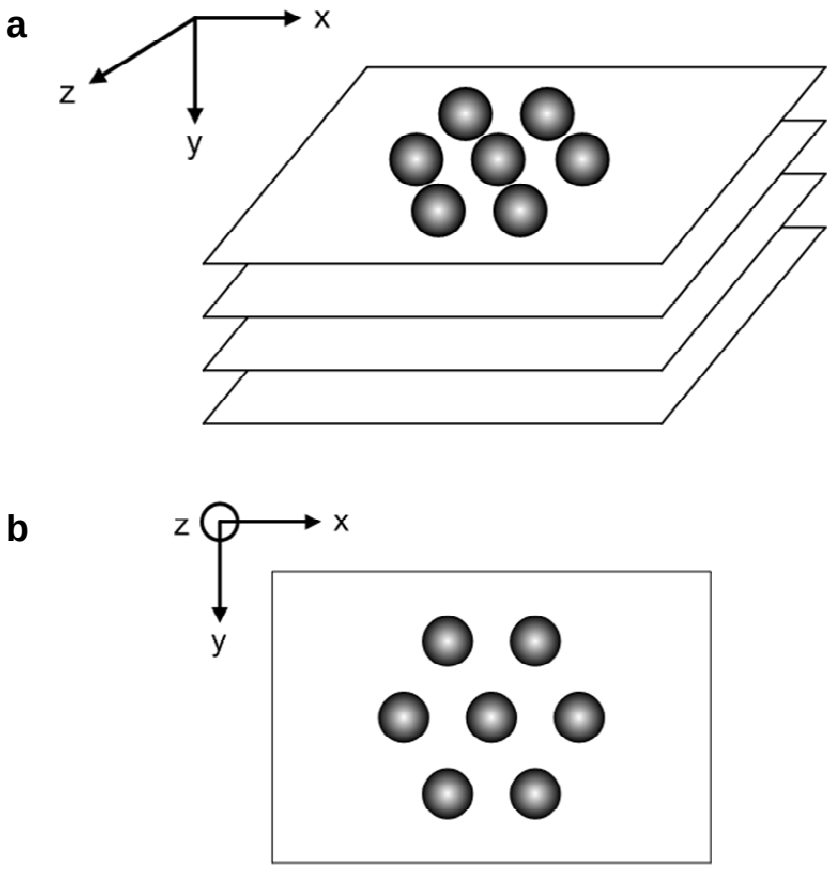

Figure 4.14: Schematic of the two observed orientations in the shear-aligned CECD-8 sample that generate the scattering pattern in Figure 4.13. D spheres possess in-plane long-range order, but do not exhibit correlations between adjacent planes. Adapted from Hamley *et al*.[73]

Figure 4.15b and Figure 4.15c). Also visible in Figure 4.15b are alternating dark (D) and light (C and E) layers. Close examination of the D layer reveals discontinuities and circular regions substantiating the D sphere in C/E lamellae microstructure. A micrograph recorded after staining with ruthenium tetroxide (Figure 4.15d, CECD-9) reveals light and dark layers composed of stained C + D and unstained E domains, respectively. This

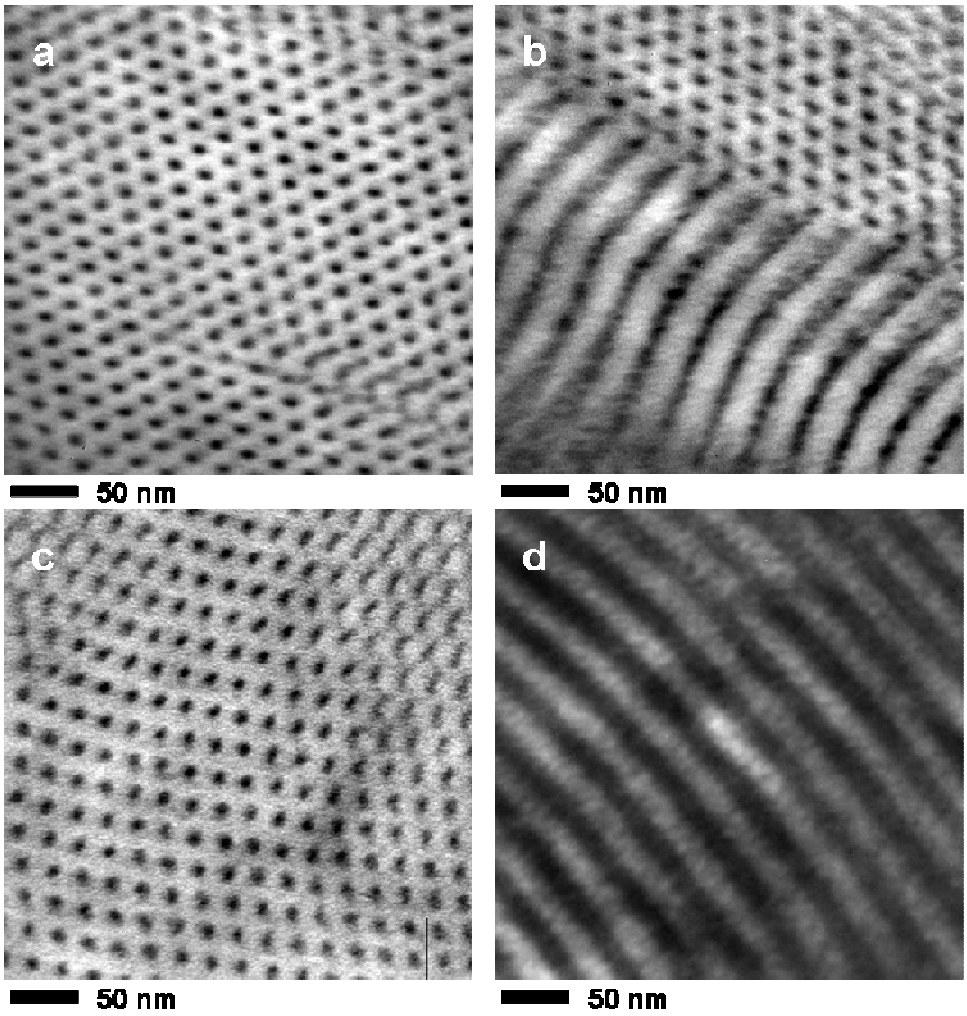

Figure 4.15: TEM micrographs obtained from (a), (b) CECD-8 (16% D) and (c), (d) CECD-9 (19% D) after large amplitude oscillatory shear ($|\gamma|$ = 200%, $\dot{\gamma}$ = 0.5 s^{-1}, T = 180 ºC). (a), (b), and (c) In these unstained images, the black regions correspond to D while the lighter areas are C and E. Six-fold symmetry of the D domains is apparent over a large portion of the micrographs. (b) Orthogonal view of D spheres in C/E layered structure is visible. (d) The sample has been stained with ruthenium tetroxide, which preferentially darkens the D and C blocks. These results are consistent with spheres of D embedded in the C domain of a C/E lamellar structure.

result is consistent with the previously observed preferential staining of D and C blocks relative to E.[51,74,75] Quantitative comparison of the TEM and SAXS results for the two structures yields $d_{100,\ TEM} \cong 0.8 d_{100,\ SAXS}$ and $d_{001,\ TEM} \cong (0.8 - 0.85) d_{001,\ SAXS}$. These discrepancies in domain spacings are similar to the previously discussed LAM_2 CECD-6 sample and have been noted previously in other semicrystalline block polymers.[1,2] Stained samples (Figure 4.15d) produced a slightly larger lamellar spacing (~10%), suggesting that beam damage at least contributes partially to this effect.

4.3.4 Region 4 – Three-domain Lamellae (LAM_3) with Coexisting Morphologies

In Figure 4.3, two tetrablocks, CECD-10 (24% D) and CECD-11 (33%D), were shown to exhibit qualitatively different scattering results from the S-LAM samples (CECD-8 and CECD-9). CECD-10 and CECD-11 have been determined to possess a coexistence of microstructures with three-domain lamellae (LAM_3) as the most common and likely equilibrium phase. These morphological assignments were made on the basis of SAXS and TEM results as discussed below.

SAXS patterns obtained from CECD-10 as a function of temperature are presented in Figure 4.16. At 140 ºC during heating, three sharp reflections consistent with a lamellar structure, $q/q^* = 1, 2$, and 3, are apparent. A less intense, more diffuse peak at $q/q^* = 1.36$ ($q \cong 0.023$ Å^{-1}) and a broad maximum centered at $q \cong 0.041$ Å^{-1} (likely due to form factor scattering from the secondary structure) are also evident. Heating to 250 ºC does not change the ratios of the three lamellar peaks, but greatly diminishes the reflection at q

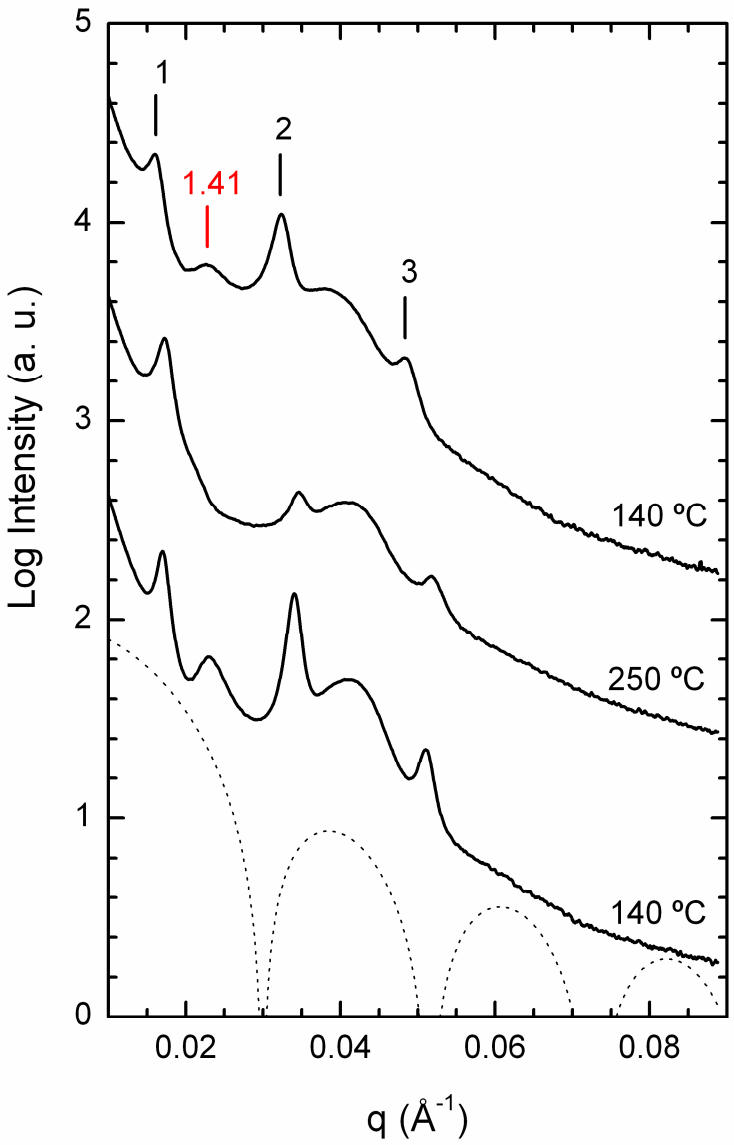

Figure 4.16: SAXS data collected from CECD-10 while the sample was heated from 140 ºC (bottom curve, same data as in Figure 4.3) to 250 ºC and then cooled to 140 ºC (top curve). The sample was annealed at 200 ºC for 7 days prior to data collection. The dotted line corresponds to a spherical form factor with R = 15.0 nm. The upper two curves are shifted vertically for clarity.

$\cong 0.023$ Å^{-1} (a high q shoulder in the primary peak is barely visible at 250 ºC). The broad feature at $q \cong 0.041$ Å^{-1} remains relatively unchanged. A decrease in temperature to 140 ºC causes a reappearance of the non-lamellar reflection at $q/q^* = 1.41$. The position of this secondary peak is qualitatively similar to the (100) reflection observed in the S-LAM samples (see Figure 4.3 and Figure 4.12), suggesting a similarity in microstructure. Scattering patterns obtained from CECD-11 upon heating and cooling were similar (not shown). We interpret these results as a coexistence of LAM_3, which yields the three lamellar reflections, and a secondary phase, which produces the weaker scattering. The long-range order associated with the LAM_3 structure is not lost when heated to 250 ºC, in contrast to the coexisting morphology and the previously identified S-LAM structure (Figure 4.12).

Two-dimensional scattering data obtained from the $\boldsymbol{q}_x$-$\boldsymbol{q}_y$ plane of a shear-oriented CECD-10 sample ($|\gamma|$ = 200%, $\dot{\gamma}$ = 0.5 s^{-1}, T = 200 ºC) are displayed in Figure 4.17. Strong equatorial diffraction arcs are evident at $q/q^* = 1$, 2, and 3, in agreement with the LAM_3 phase observed in the unoriented sample. The equatorial reflections are consistent with a layered microstructure aligned parallel to the shear (x) direction.[71] Weaker intensity scattering arcs are also apparent at $q/q^* = 1.28$, 2.22, and 2.56 (labeled red in one-dimensional scattering pattern in Figure 4.17), which can be attributed to a structure with hexagonal symmetry ($q/q_2 = 1$ and $\sqrt{3}$). Unlike the two-dimensional SAXS pattern collected from the sheared S-LAM sample (Figure 4.13), the hexagonal scattering is predominately limited to the q_y axis. We attribute this to formation of D cylinders aligned along the shear direction. Strong shear fields have been shown to orient a two-

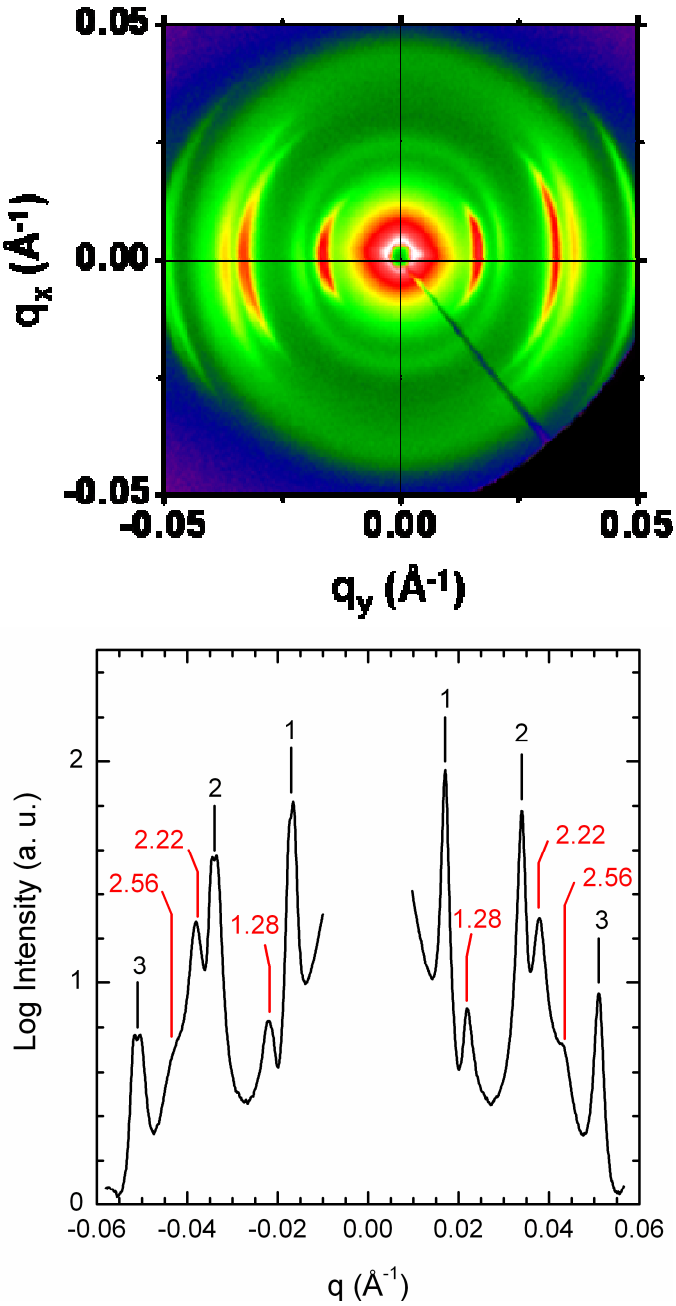

Figure 4.17: Two-dimensional SAXS pattern collected from CECD-10 (24% D) after large-amplitude reciprocating shear ($|\gamma|$ = 200%, $\dot{\gamma}$ = 0.5 s^{-1}, T = 200 ºC) and corresponding one-dimensional scattering profile along q_x = 0 (integrated over a 10º angle centered about the horizontal axis). The data were obtained at 140 ºC.

dimensional hexagonal lattice of spherical domains[76] or induce a sphere-to-cylinder transition along the shear direction.[77] Additionally, cylinders-in-lamellae phases have been documented in poly(ethylene-*alt*-propylene-*b*-ethylethylene-*b*-styrene),[37] poly(styrene-*b*-isoprene-*b*-methyl methacrylate),[38] and poly(styrene-*b*-2-vinylpyridine-*b*-tert-butyl methacrylate)[32] triblock terpolymers. The $\sqrt{3}q_2$ reflections in Figure 4.17 are approximately seven times as intense as the q_2 arcs, which have a weak underlying isotropic ring (see one-dimensional scattering profile in Figure 4.17). Lastly, the presence of an isotropic ring at q_2 may be the result of residual D spheres that have not coalesced into cylinders and have lost their translational order during the shear process.

TEM micrographs collected from unstained slices of CECD-10 and CECD-11 after shear-alignment (same sample as Figure 4.17) are displayed in Figure 4.18. Coexisting structures are apparent in Figure 4.18a (CECD-10) and Figure 4.18d (CECD-11), while alternating dark (D) and (C + E) layers in Figure 4.18b (CECD-10) and Figure 4.18c (CECD-11) are consistent with the LAM_3 phase assignment made on the basis of SAXS. The circular D domains in Figure 4.18a are consistent with kinetically trapped spheres or cylinders. Additionally, the domain spacing for the layered structure is ~35% larger than the secondary structure, in good agreement with the SAXS results. We attribute these results to a coexistence of morphologies. Figure 4.18d captures an undulating lamellar structure with a few discrete circular D defects. This morphology likely corresponds to an intermediate state during the transition from D domains consisting of spheres or cylinders to a continuous layer. Similar rippled lamellar structures have been observed by TEM for a cylinder to lamellae transition[78] and extensively modeled.[54,79,80]

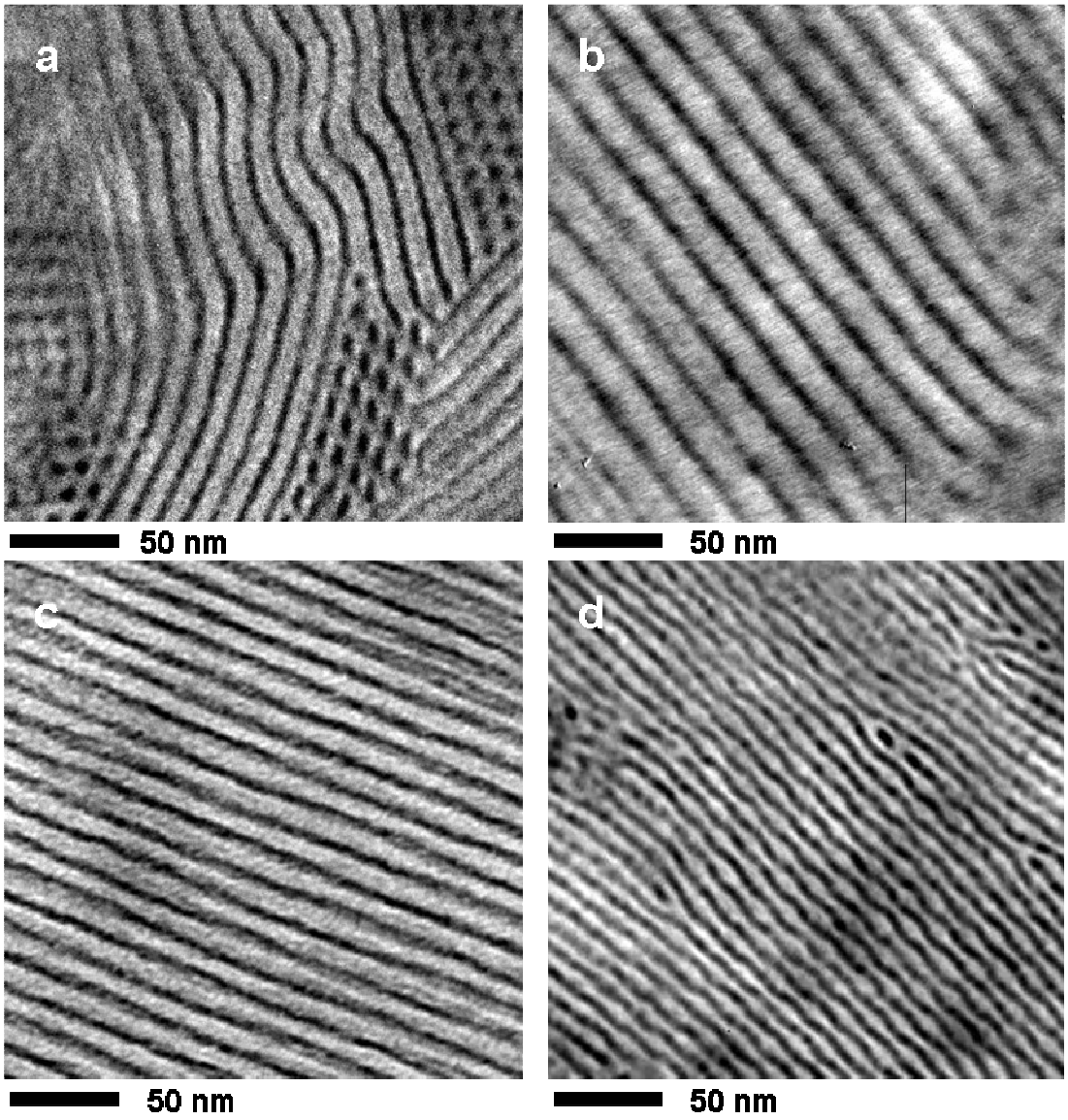

Figure 4.18: TEM micrographs generated from unstained (a), (b) CECD-10 (24% D) and (c), (d) CECD-11 (33% D) samples after reciprocating shear ($|\gamma|$ = 200%, $\dot{\gamma}$ = 0.5 s^{-1}, T = 200 ºC). In (b) and (c), alternating layers of D (dark areas) and C/E (light areas) are consistent with LAM_3 morphology. Coexisting microstructures are apparent in (a) and (d).

4.4 Discussion

We have presented morphological characterization data for a series of CECD terpolymers containing equal C and E content and D volume fractions ranging from 0 to 33%. Three phases have been conclusively identified (LAM_2, S-LAM, and LAM_3) in these tetrablocks, while a definitive structural assignment was not made for CECD-7 based on the current collection of data. In the discussion of these results, we invoke principles learned from previously studied "nonfrustrated"[81] ABC triblock terpolymers. These systems are identified by a sequencing of segment-segment interaction parameters in which A/B and B/C interfaces are preferred over creation of A/C contacts ($\chi_{AB} \cong \chi_{BC} < \chi_{AC}$). Extensive characterization of the morphological behavior of several nonfrustrated ABC terpolymer systems shows that these materials do not adopt phases that form enthalpically unfavorable A/C interfaces.[1-3,82-86] CECD tetrablocks are expected to follow this principle due to the block sequencing and the magnitudes of their interaction parameters ($\chi_{EC} \cong \chi_{CD} < \chi_{ED}$).[46,87,88] However, additional chain stretching in the central C block of the CECD molecular architecture undoubtedly complicates the delicate free energy balance that dictates self-assembly behavior.

The underlying structure that was observed in these CECD tetrablock terpolymers was a layered C/E morphology that included microphase-separated D domains as the volume fraction of D was increased. (The tentative cubic phase identified in CECD-7 does not follow this trend. This morphology may represent a core (D)-shell (C) spherical structure, which has been documented in poly(styrene-*b*-isoprene-*b*-styrene-*b*-ethylene oxide) tetrablocks (see Chapter 6). This exception likely exhibits the subtle differences in

free energies of different morphologies that are affected by variations in composition and molecular weight.) Addition of a short D chain to a symmetric, lamellae-forming CEC triblock does not affect the microstructure as the D block mixes into the C layers (CECD-6, 8% D). With increased D block length, mixing of the D and C blocks becomes energetically unfavorable, microphase separation occurs, and three-domain morphologies are observed. These three-domain structures include S-LAM (CECD-8 and CECD-9, 16 and 19%, respectively) and LAM_3 (CECD-10 and CECD-11, 24 and 33%, respectively) (Figure 4.19). The S-LAM morphology effectively shields enthalpically unfavorable E/D contacts while creating two interfaces with very different curvatures. The compositionally symmetric E and C blocks maintain a flat interface with zero curvature, while the D spheres possess positive Gauss curvature and are a result of the asymmetry between C and D domains. As the D chain length increases, the C/D interfacial curvature decreases and a flat surface is formed (i.e., the LAM_3 microstructure). (Cylinders, like flat sheets, possess zero Gauss curvature, but have a constant mean curvature that places it between spheres and lamellae.[89]) Thus, the addition of increasing D content could be accommodated by producing the "classical" AB diblock morphologies, spheres, cylinders, and lamellae, within the construct of the two-domain C/E lamellar microstructure.

Previously documented structure-in-structure phases in linear ABC triblocks include spheres-in-lamellae (S-LAM),[36] cylinders-in-lamellae (Cyl-LAM),[32,37,38] and the more common lamellae-in-lamellae (LAM_3).[1-3,24,30,83-85,90,91] In all cases, the minority C chains formed the spherical or cylindrical domains in the S-LAM and Cyl-LAM morphologies,

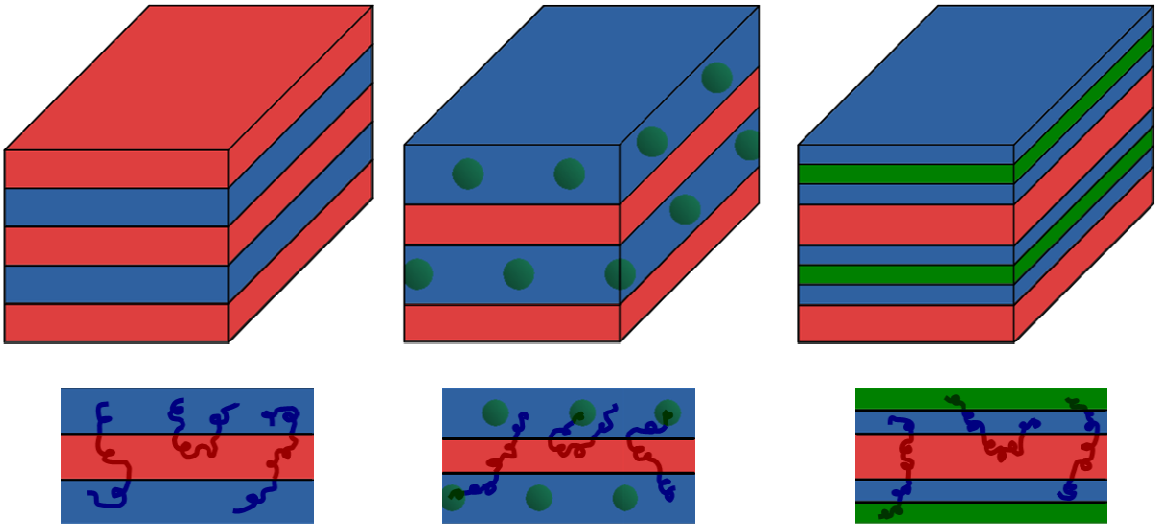

Figure 4.19: Illustrations of conclusively identified layered structures. Red, blue, and green represent E, C, and D, respectively. Two-domain lamellae, spheres in lamellae, and three-domain lamellae morphologies were observed with increasing D volume fraction. Tetrablock chains are sketched to illustrate molecular packing.

while the A and B block compositions were relatively symmetric. Self-consistent field theory (SCFT) calculations by Tang *et al.*,[92] using an adaptive, arbitrary two-dimensional unit cell, determined a "lamellae with beads inside" microstructure to be stable over a small region of composition space (C block less than 10% by volume). This microstructure represents a two-dimensional version of the S-LAM and Cyl-LAM morphologies. While the work of Tang *et al.* does not consider three-dimensional structures (such as core-shell double gyroid, alternating gyroid, O[70], and BCC), there is qualitative agreement between the SCFT calculations and the previously discussed experimental observations of structure-in-structure morphologies.

As stated at the outset of this chapter, differences in phase behavior due to chain architecture can be investigated by comparing CECD to the previously examined ECD triblock system (Chapter 3). The two-domain lamellae region extended to a much higher D content in the ECD system (21% versus 8%). However, this is likely due to the larger molecular weights employed in the CECD phase behavior study. Once segregation of the D domain occurs, spheres are formed in both architectures. As discussed previously, this highly curved structure accommodates the asymmetry in the C/D block compositions. Unlike ECD triblocks, half of the C chains in CECD are only tethered to one interface. This allows much greater freedom for the terminal C block to fill the volume between D spheres and stabilize the S-LAM phase. While LAM_3 was not observed in the ECD triblocks examined in Chapter 3, we anticipate this to be a common morphology between architectures. Characterization of ECD terpolymers with higher D content (the study was limited to 28% D) would likely identify LAM_3 samples. Lastly, the orthorhombic network morphology O^{70} was identified over a small region of temperature and composition space in ECD triblocks, while no network microstructures were identified in the CECD system. Epps *et al*.[2] postulated that this region of composition space would be rich with network morphologies in linear ABC triblock terpolymers due to the competing curvature requirements of the symmetric A/B and asymmetric B/C interfaces. This hypothesis was borne out by the expansive network region identified in poly(isoprene-*b*-styrene-*b*-ethylene oxide) triblocks. However, we have already observed that the network region in ECD terpolymers has shifted and/or is greatly diminished, likely due to the interaction parameters and statistical segment lengths inherent to the ECD system. In

addition, the chain architecture of the CECD terpolymer effectively creates one highly curved interface (C/D), while maintaining the preferred flat interface between A and B domains. Evidently, the hyperbolic (saddle) surfaces that are intrinsic to network morphologies are not energetically favorable.

We have utilized both long annealing times at elevated temperatures and large-amplitude oscillatory shear to aid in the morphological characterization of these CECD tetrablocks. In all cases there was good agreement between the two preparation methods in terms of domain spacings and morphological characteristics. However, the apparent presence of coexisting morphologies in the LAM_3 samples lead us to conclude that achieving equilibrium in these strongly-segregated materials is quite difficult. Additional characterization utilizing lower molecular weight tetrablocks would more conclusively determine the equilibrium morphologies in these tetrablocks. Nonetheless, CECD terpolymers represent an unexplored molecular architecture that has the possibility of producing morphologies that are inaccessible with ABC triblock terpolymers.

4.5 Conclusion

By utilizing SAXS, TEM, and DMS measurements, we have conclusively identified four microstructures in a sequence of CECD tetrablock terpolymers. These samples possess equal C and E content and vary in D block length from 0 to 33% by volume. Situated between two- and three-domain lamellar phases is a structure-in-structure

morphology (S-LAM) consisting of D spheres hexagonally packed within the C layers of C/E lamellae. This morphology was also observed in ECD triblocks with similar compositions (Chapter 3). We attribute the formation of the S-LAM microstructure to the sequencing of the χ parameters and the chain architecture of the CECD system.

Acknowledgement. I thank Dr. Steven Weigand and Dr. Denis Keane at the DuPont-Northwestern-Dow Synchrotron Research Center at the Advanced Photon Source for setting up the experimental equipment used to acquire the SAXS data presented in this chapter. I acknowledge the tremendous assistance provided by Dr. Guillaume Fleury in the synthesis of the CECD tetrablocks.

4.6 References

(1) Bailey, T. S.; Hardy, C. M.; Epps, T. H.,III; Bates, F. S. *Macromolecules* **2002**, *35*, 7007-7017.

(2) Epps, T. H.,III; Cochran, E. W.; Bailey, T. S.; Waletzko, R. S.; Hardy, C. M.; Bates, F. S. *Macromolecules* **2004**, *37*, 8325-8341.

(3) Chatterjee, J.; Jain, S.; Bates, F. S. *Macromolecules* **2007**, *40*, 2882-2896.

(4) Bates, F. S.; Fredrickson, G. H. *Phys. Today* **1999**, *52*, 32-38.

(5) Hadjichristidis, N.; Pitsikalis, M.; Iatrou, H. *Adv. Polym. Sci.* **2005**, *189*, 1-124.

(6) Hadjichristidis, N.; Pitsikalis, M.; Pispas, S.; Iatrou, H. *Chem. Rev.* **2001**, *101*, 3747-3792.

(7) Leibler, L. *Macromolecules* **1980**, *13*, 1602-1617.

(8) Bates, F. S. *Science* **1991**, *251*, 898-905.

(9) Bates, F. S.; Schulz, M. F.; Khandpur, A. K.; Foerster, S.; Rosedale, J. H. *Faraday Discuss.* **1995**, *98*, 7-18.

(10) Khandpur, A. K.; Förster, S.; Bates, F. S.; Hamley, I. W.; Ryan, A. J.; Bras, W.; Almdal, K.; Mortensen, K. *Macromolecules* **1995**, *28*, 8796-8806.

(11) Matsen, M. W.; Bates, F. S. *Macromolecules* **1996**, *29*, 1091-1098.

(12) Matsen, M. W.; Bates, F. S. *J. Chem. Phys.* **1997**, *106*, 2436-2448.

(13) Cochran, E. W.; Garcia-Cervera, C. J.; Fredrickson, G. H. *Macromolecules* **2006**, *39*, 2449-2451.

(14) Takenaka, M.; Wakada, T.; Akasaka, S.; Nishitsuji, S.; Saijo, K.; Shimizu, H.; Kim, M. I.; Hasegawa, H. *Macromolecules* **2007**, *40*, 4399-4402.

(15) Kim, M. I.; Wakada, T.; Akasaka, S.; Nishitsuji, S.; Saijo, K.; Hasegawa, H.; Ito, K.; Takenaka, M. *Macromolecules* **2008**, *41*, 7667-7670.

(16) Tyler, C. A.; Morse, D. C. *Phys. Rev. Lett.* **2005**, *94*, 208302.

(17) Yamada, K.; Nonomura, M.; Ohta, T. *J. Phys.: Condens. Matter* **2006**, *18*, L421-L427.

(18) Tyler, C. A.; Qin, J.; Bates, F. S.; Morse, D. C. *Macromolecules* **2007**, *40*, 4654-4668.

(19) Matsushita, Y.; Yamada, K.; Hattori, T.; Fujimoto, T.; Sawada, Y.; Nagasawa, M.; Matsui, C. *Macromolecules* **1983**, *16*, 10-13.

(20) Mogi, Y.; Kotsuji, H.; Kaneko, Y.; Mori, K.; Matsushita, Y.; Noda, I. *Macromolecules* **1992**, *25*, 5408-5411.

(21) Beckmann, J.; Auschra, C.; Stadler, R. *Macromol. Rapid Commun.* **1994**, *15*, 67-72.

(22) Krappe, U.; Stadler, R.; Voigt-Martin, I. *Macromolecules* **1995**, *28*, 4558-4561.

(23) Stadler, R.; Auschra, C.; Beckmann, J.; Krappe, U.; Voight-Martin, I.; Leibler, L. *Macromolecules* **1995**, *28*, 3080-3097.

(24) Breiner, U.; Krappe, U.; Stadler, R. *Macromol. Rapid Commun.* **1996**, *17*, 567-575.

(25) Breiner, U.; Krappe, U.; Abetz, V.; Stadler, R. *Macromol. Chem. Phys.* **1997**, *198*, 1051-1083.

(26) Breiner, U.; Krappe, U.; Jakob, T.; Abetz, V.; Stadler, R. *Polym. Bull.* **1998**, *40*, 219-226.

(27) Brinkmann, S.; Stadler, R.; Thomas, E. L. *Macromolecules* **1998**, *31*, 6566-6572.

(28) Matsushita, Y.; Suzuki, J.; Seki, M. *Phys. B* **1998**, *248*, 238-242.

(29) Shefelbine, T. A.; Vigild, M. E.; Matsen, M. W.; Hajduk, D. A.; Hillmyer, M. A.; Cussler, E. L.; Bates, F. S. *J. Am. Chem. Soc.* **1999**, *121*, 8457-8465.

(30) Bailey, T. S.; Pham, H. D.; Bates, F. S. *Macromolecules* **2001**, *34*, 6994-7008.

(31) Avgeropoulos, A.; Paraskeva, S.; Hadjichristidis, N.; Thomas, E. L. *Macromolecules* **2002**, *35*, 4030-4035.

(32) Ludwigs, S.; Boker, A.; Abetz, V.; Muller, A. H. E.; Krausch, G. *Polymer* **2003**, *44*, 6815-6823.

(33) Cochran, E. W.; Bates, F. S. *Phys. Rev. Lett.* **2004**, *93*, 087802/1-087802/4.

(34) Epps, T. H.,III; Cochran, E. W.; Hardy, C. M.; Bailey, T. S.; Waletzko, R. S.; Bates, F. S. *Macromolecules* **2004**, *37*, 7085-7088.

(35) Auschra, C.; Stadler, R. *Macromolecules* **1993**, *26*, 2171-2174.

(36) Shibayama, M.; Hasegawa, H.; Hashimoto, T.; Kawai, H. *Macromolecules* **1982**, *15*, 274-280.

(37) Neumann, C.; Loveday, D. R.; Abetz, V.; Stadler, R. *Macromolecules* **1998**, *31*, 2493-2500.

(38) Stangler, S.; Abetz, V. *Rheol. Acta* **2003**, *42*, 569-577.

(39) Bailey, T. S.; Rzayev, J.; Hillmyer, M. A. *Macromolecules* **2006**, *39*, 8772-8781.

(40) Epps, T. H.,III; Bailey, T. S.; Pham, H. D.; Bates, F. S. *Chem. Mater.* **2002**, *14*, 1706-1714.

(41) Epps, T. H.,III; Bailey, T. S.; Waletzko, R.; Bates, F. S. *Macromolecules* **2003**, *36*, 2873-2881.

(42) Mahanthappa, M. K.; Lim, L. S.; Hillmyer, M. A.; Bates, F. S. *Macromolecules* **2007**, *40*, 1585-1593.

(43) Meuler, A. J.; Fleury, G.; Hillmyer, M. A.; Bates, F. S. *Macromolecules* **2008**, *41*, 5809-5817.

(44) McKay, K. W.; Gros, W. A.; Diehl, C. F. *J. Appl. Polym. Sci.* **1995**, *56*, 947-958.

(45) Ndoni, S.; Papadakis, C. M.; Bates, F. S.; Almdal, K. *Rev. Sci. Instrum.* **1995**, *66*, 1090-1095.

(46) Maheshwari, S.; Tsapatsis, M.; Bates, F. S. *Macromolecules* **2007**, *40*, 6638-6646.

(47) Hucul, D. A.; Hahn, S. F. *Adv. Mater.* **2000**, *12*, 1855-1858.

(48) Fetters, L. J.; Lohse, D. J.; Richter, D.; Witten, T. A.; Zirkel, A. *Macromolecules* **1994**, *27*, 4639-4647.

(49) Mortensen, K.; Almdal, K.; Bates, F. S.; Koppi, K.; Tirrell, M.; Norden, B. *Phys. B* **1995**, *213&214*, 682-684.

(50) Brown, G. M.; Butler, J. H. *Polymer* **1997**, *38*, 3937-3945.

(51) Khandpur, A. K.; Macosko, C. W.; Bates, F. S. *J. Polym. Sci. Part B* **1995**, *33*, 247-252.

(52) Hermel, T. J.; Hahn, S. F.; Chaffin, K. A.; Gerberich, W. W.; Bates, F. S. *Macromolecules* **2003**, *36*, 2190-2193.

(53) Kossuth, M. B.; Morse, D. C.; Bates, F. S. *J. Rheol.* **1999**, *43*, 167-196.

(54) Hamley, I. W.; Koppi, K. A.; Rosedale, J. H.; Bates, F. S.; Almdal, K.; Mortensen, K. *Macromolecules* **1993**, *26*, 5959-5970.

(55) Vigild, M. E.; Almdal, K.; Mortensen, K.; Hamley, I. W.; Fairclough, J. P. A.; Ryan, A. J. *Macromolecules* **1998**, *31*, 5702-5716.

(56) Ahn, J. H.; Zin, W. C. *Macromolecules* **2000**, *33*, 641-644.

(57) Zhu, L.; Huang, P.; Cheng, S. Z. D.; Ge, Q.; Quirk, R. P.; Thomas, E. L.; Lotz, B.; Wittmann, J. C.; Hsiao, B. S.; Yeh, F.; Liu, L. *Phys. Rev. Lett.* **2001**, *86*, 6030-6033.

(58) Wang, C. Y.; Lodge, T. P. *Macromol. Rapid Commun.* **2002**, *23*, 49-54.

(59) Wang, C.; Lodge, T. P. *Macromolecules* **2002**, *35*, 6997-7006.

(60) Förster, S.; Khandpur, A. K.; Zhao, J.; Bates, F. S.; Hamley, I. W.; Ryan, A. J.; Bras, W. *Macromolecules* **1994**, *27*, 6922-6935.

(61) Hillmyer, M. A.; Bates, F. S.; Almdal, K.; Mortensen, K.; Ryan, A. J.; Fairclough, J. P. A. *Science* **1996**, *271*, 976.

(62) Hajduk, D. A.; Ho, R.; Hillmyer, M. A.; Bates, F. S.; Almdal, K. *J. Phys. Chem. B* **1998**, *102*, 1356-1363.

(63) Mortensen, K.; Vigild, M. E. *Macromolecules* **2009**, *42*, 1685-1690.

(64) Hamley, I. W.; Gehlsen, M. D.; Khandpur, A. K.; Koppi, K. A.; Rosedale, J. H.; Schulz, M. F.; Bates, F. S.; Almdal, K.; Mortensen, K. *J. Phys. II* **1994**, *4*, 2161-2186.

(65) Hajduk, D. A.; Gruner, S. M.; Rangarajan, P.; Register, R. A.; Fetters, L. J.; Honeker, C.; Albalak, R. J.; Thomas, E. L. *Macromolecules* **1994**, *27*, 490-501.

(66) Schwab, M.; Stühn, B. *Colloid Polym. Sci.* **1997**, *275*, 341-351.

(67) Han, C. D.; Vaidya, N. Y.; Kim, D.; Shin, G.; Yamaguchi, D.; Hashimoto, T. *Macromolecules* **2000**, *33*, 3767-3780.

(68) Sakamoto, N.; Hashimoto, T.; Han, C. D.; Kim, D.; Vaidya, N. Y. *Macromolecules* **1997**, *30*, 1621-1632.

(69) Adams, J. L.; Quiram, D. J.; Graessley, W. W.; Register, R. A.; Marchand, G. R. *Macromolecules* **1996**, *29*, 2929-2938.

(70) Cavicchi, K. A.; Lodge, T. P. *J. Polym. Sci., Part B: Polym. Phys.* **2003**, *41*, 715-724.

(71) Koppi, K. A.; Tirrell, M.; Bates, F. S.; Almdal, K.; Colby, R. H. *J. Phys. II* **1992**, *2*, 1941-1959.

(72) Tepe, T.; Schulz, M. F.; Zhao, J.; Tirrell, M.; Bates, F. S.; Mortensen, K.; Almdal, K. *Macromolecules* **1995**, *28*, 3008-3011.

(73) Hamley, I. W.; Pople, J. A.; Fairclough, J. P. A.; Terrill, N. J.; Ryan, A. J.; Booth, C.; Yu, G. E.; Diat, O.; Almdal, K.; Mortensen, K. *J. Chem. Phys.* **1998**, *108*, 6929.

(74) Hermel, T. J. *Ph.D. Dissertation*; University of Minnesota **2003**, 1-197.

(75) Bluemle, M. J.; Fleury, G.; Lodge, T. P.; Bates, F. S. *Soft Matter* **2009**, *5*, 1587-1590.

(76) Angelescu, D. E.; Waller, J. H.; Register, R. A.; Chaikin, P. M. *Adv. Mater.* **2005**, *17*, 1878-1880.

(77) Hong, Y.; Adamson, D. H.; Chaikin, P. M.; Register, R. A. *Soft Matter* **2009**, *5*, 1687-1691.

(78) Sakurai, S.; Momii, T.; Taie, K.; Shibayama, M.; Nomura, S.; Hashimoto, T. *Macromolecules* **1993**, *26*, 485-491.

(79) Liu, Y.; Li, M.; Bansil, R.; Steinhart, M. *Macromolecules* **2007**, *40*, 9482-9490.

(80) Qi, S.; Wang, Z. G. *Phys. Rev. E: Stat., Nonlinear, Soft Matter Phys.* **1997**, *55*, 1682-1697.

(81) Bailey, T. S. *Ph.D. Dissertation*; University of Minnesota **2001**, 1-211.

(82) Mogi, Y.; Mori, K.; Matsushita, Y.; Noda, I. *Macromolecules* **1992**, *25*, 5412-5415.

(83) Mogi, Y.; Mori, K.; Kotsuji, H.; Matsushita, Y.; Noda, I.; Han, C. C. *Macromolecules* **1993**, *26*, 5169-5173.

(84) Mogi, Y.; Nomura, M.; Kotsuji, H.; Ohnishi, K.; Matsushita, Y.; Noda, I. *Macromolecules* **1994**, *27*, 6755-6760.

(85) Hückstädt, H.; Göpfert, A.; Abetz, V. *Polymer* **2000**, *41*, 9089-9094.

(86) Sugiyama, M.; Shefelbine, T. A.; Vigild, M. E.; Bates, F. S. *J. Phys. Chem. B* **2001**, *105*, 12448-12460.

(87) Almdal, K.; Hillmyer, M. A.; Bates, F. S. *Macromolecules* **2002**, *35*, 7685-7691.

(88) Cochran, E. W.; Bates, F. S. *Macromolecules* **2002**, *35*, 7368-7374.

(89) Matsen, M. W.; Bates, F. S. *Macromolecules* **1996**, *29*, 7641-7644.

(90) Matsushita, Y.; Tamura, M.; Noda, I. *Macromolecules* **1994**, *27*, 3680-3682.

(91) Hardy, C. M.; Bates, F. S.; Kim, M.; Wignall, G. D. *Macromolecules* **2002**, *35*, 3189-3197.

(92) Tang, P.; Qiu, F.; Zhang, H.; Yang, Y. *Phys. Rev. E: Stat., Nonlinear, Soft Matter Phys.* **2004**, *69*, 031803/1-031803/8.

5

The O^{52} Network by Molecular Design: Poly(cyclohexylethylene-*b*-ethylene-*b*-cyclohexyl-ethylene-*b*-dimethylsiloxane) Tetrablock Terpolymers*

5.1 Introduction

The previous two chapters discussed the morphological investigations of poly(ethylene-*b*-cyclohexylethylene-*b*-dimethylsiloxane) (ECD) and CECD along the symmetric $f_C = f_E$ isopleth, where f_C and f_E are the volume fractions of C and E, respectively. In this chapter, we present the phase behavior of CECD tetrablocks with a constant asymmetric ratio of C to E content ($f_C/f_E = 3/7$) and D compositions that range from 0 to 20% D. As discussed previously in Chapter 4, the positioning of two separate C blocks in the tetrablock terpolymer architecture adds an additional degree of freedom in

*Reproduced in part with permission from Bluemle, M. J., Fleury, G., Lodge, T. P., Bates, F. S. *Soft Matter* **2009**, *5*, 1587-1590. Copyright 2009 The Royal Society of Chemistry (RSC).

the synthesis of block polymers and can produce qualitatively different morphological behavior.

While AB diblock copolymers form four equilibrium morphologies[1-3] and over thirty ordered phases have been documented in ABC triblock terpolymers,[4-21] multiply continuous network structures have earned a large amount attention from researchers. Block polymers that assemble into three-dimensionally continuous network structures represent an especially fascinating class of soft materials. These phases may be utilized as gas separation membranes,[14] photovoltaic media,[22] tough plastics,[23] or any other application where high internal surface area and a percolating pore structure would be beneficial. The double gyroid ($Ia\bar{3}d$ symmetry, Q^{230}), found in diblock copolymers,[24,25] is the most well-known of the network morphologies. Two other cubic gyroid phases have been identified in ABC triblock terpolymers: core-shell double gyroid (also $Ia\bar{3}d$ symmetry)[14,15,26,27] and alternating gyroid ($I4_132$, Q^{214}).[27,28] These structures are composed of a single set of symmetric three-fold junctions fitted with equal length connectors, that tile to form a connected net.[27,29] Using Wells' notation, Q^{214} is composed of one chiral (10,3)*a* net, whereas Q^{230} possesses two enantiomeric (10,3)*a* networks related by inversion.[30] Wells identified seven of these uniform (10,3) nets, where 10 and 3 denote the number of nodes and the connectivity of the nodes, respectively, in the net.

A second class of network morphologies with orthorhombic symmetry was recently reported by Bailey and coworkers[17] Like the cubic gyroid phases, the orthorhombic network morphologies are composed of trivalent connectors, but they are not three-fold symmetric as the overall symmetry is lower. Two orthorhombic network morphologies

have been identified to date: O^{70} (*Fddd* space group symmetry), in a poly(styrene-*b*-isoprene) (SI) diblock,[31] poly(isoprene-*b*-styrene-*b*-ethylene oxide) (ISO) triblocks,[17,21,27] a poly(cyclohexylethylene-*b*-ethylethylene-*b*-ethylene) (CE_EE) triblock,[19] and an OSISO pentablock,[23] and O^{52} (*Pnna* space group symmetry) as a metastable state in the CE_EE triblock after application of a strong shear field.[19] The topologies of these networks are classified as (10,3)*c* and (10,3)*d* for O^{70} and O^{52}, respectively.[30] A recent review by Meuler, *et al*.[32] summarizes the numerous block polymer systems in which multiply continuous phases have been documented.

In this chapter, the formation of the O^{52} network in a series of CECD tetrablock terpolymers is discussed. The morphological behavior of one CEC and five CECD tetrablock terpolymers, with a fixed C to E ratio of 3 to 7, was characterized with a combination of small-angle X-ray scattering (SAXS) and transmission electron microscopy (TEM). The multiply continuous O^{52} phase was found at an intermediate D composition, between two cylindrical phases. Additionally, the O^{52} topology was modeled to visualize the three-fold junctions and connectors. We attribute the formation of the orthorhombic network to the CECD block architecture.

5.2 Experimental Section

5.2.1 Block Polymer Synthesis

Five poly(cyclohexylethylene-*b*-ethylene-*b*-cylcohexylethylene-*b*-dimethylsiloxane) (CECD) tetrablock terpolymers with a fixed C to E ratio of 3 to 7 were synthesized by sequential anionic polymerization to generate the unsaturated precursor, poly(styrene-*b*-butadiene-*b*-styrene-*b*-dimethylsiloxane), followed by catalytic hydrogenation. A detailed description of this synthesis, purification, and molecular characterization can be found in Chapter 4. Table 5.1 provides a summary of the characterization data for the materials used in this study.

5.2.2 Thermal Analysis

Differential scanning calorimetry (DSC) experiments were conducted with a TA Instruments Q1000 DSC. A measured amount of polymer (5 – 10 mg) was heated to 170 ºC to erase the effects of thermal history prior to cooling to –150 ºC at 10 ºC/min. Data were acquired upon second heating at a temperature ramp rate of 10 ºC/min. The degree of crystallinity within the E domains was determined by the integration of the melting peak and referencing to the heat of fusion of bulk poly(ethylene) (277 J/g).[33]

5.2.3 Dynamic Mechanical Spectroscopy (DMS)

Samples used for DMS were prepared by compression-molding polymer powder into 25 mm ◈ 0.8 mm disks at 170 ºC using a pressure of 2000 psi for 5 – 6 min. A Rheometrics Scientific ARES strain-controlled rheometer fitted with 25 mm diameter

parallel plates was used to perform all rheological measurements. The dynamic elastic (G') and loss (G'') moduli were measured as a function of temperature at a constant frequency (typically ω = 0.05 rad/s unless otherwise noted) to probe for the order-disorder transition temperature (T_{ODT}). All measurements to determine T_{ODT}s were made from 140 ºC until 10 ºC beyond the point of disorder (or to 300 ºC if there was not an apparent T_{ODT}), defined by a large decrease in G'. The sample was then held at this temperature for 10 minutes and quickly cooled (20 ºC/min) to 140 ºC prior to a second isochronal heating ramp. Reported T_{ODT}s were measured on this second heating ramp. Isothermal frequency scans ($100 \leq \omega \leq 0.1$ rad/s) were also conducted to confirm the presence of the T_{ODT} and to characterize the viscoelastic response of the sample. All measurements were made under a constant blanket of nitrogen to mitigate polymer degradation at elevated temperatures. Experiments were conducted with strain amplitudes of 1 – 2.5%, which were within the linear viscoelastic regime of the block copolymers.

5.2.4 Small-angle X-ray Scattering (SAXS)

The reciprocating shear device described by Mortensen, *et al.*[34] was used to macroscopically orient specimens prior to interrogation by SAXS. 20 mm ◈ 20 mm ◈ 1 mm compression-molded samples were subjected to large amplitude reciprocating shear ($|\gamma|$ = 200% and $\dot{\gamma}$ = 0.5 s^{-1}) under an argon atmosphere at 250 ºC or 30 ºC below T_{ODT} for 2 hours. After shearing, the sample was cooled to room temperature over a two hour period leading to vitrification of the C domains ($T_{g,C}$ ~ 135 °C) followed by partial crystallization of the E blocks (T_m ~ 100 °C), which locked in the morphology developed

at the higher melt temperature. Small sections (3 mm x 2 mm) were cut from the macroscopically oriented specimen for investigation by SAXS along either the shear direction (x), the shear gradient direction (y), or vorticity direction (z) (see Figure 4.2 for deformation geometry).

SAXS experiments were conducted at the 5IDD beamline of the DuPont-Northwestern-Dow Synchrotron Research Center at the Advanced Photon Source using a sample-to-detector distance of 6.526 m and a wavelength (λ) of 0.89 Å. Two-dimensional SAXS patterns were acquired with a Mar CCD area detector. The sample temperature was controlled using a DSC chamber under a helium purge. Selected two-dimensional SAXS results are reported in the format $\boldsymbol{q}_x$-$\boldsymbol{q}_y$, $\boldsymbol{q}_x$-$\boldsymbol{q}_z$, and $\boldsymbol{q}_y$-$\boldsymbol{q}_z$, where $|\boldsymbol{q}_i| = q_i = 4\pi\lambda^{-1}\sin(\theta/2)$ is the magnitude of the scattering wavevector and θ is the scattering angle.

5.2.5 Transmission Electron Microscopy (TEM)

TEM micrographs were collected on a JEOL 1210 transmission electron microscope operating at 120 kV in the bright field mode at the University of Minnesota Institute of Technology Characterization Facility. Sections of the macroscopically oriented samples investigated by SAXS were also examined by TEM. Specimens were initially cryo-microtomed at –120 ºC on a Reichart ultramicrotome fitted with a Microstar diamond knife to create a flat surface. Some samples were stained with ruthenium tetroxide vapors for 1 – 4 hours to obtain sufficient electron mass density contrast between the different blocks.[35-37] Stained and unstained pieces were cryo-microtomed at –120 ºC to create thin

sections (70–90 nm thickness), which were collected on copper grids (Ted Pella) for subsequent TEM analysis. Unstained CECD specimens have natural contrast between D and the other polymer domains due to the higher electron density of silicon.

5.3 Results and Analysis

A CEC triblock and five CECD tetrablocks were used to investigate the phase behavior of the CECD system with a fixed C to E ratio of 3 to 7 and D content ranging from 0 to 20% by volume. The morphologies, lattice dimensions, and order-disorder transition temperatures of these polymers were obtained on the basis of SAXS, TEM, and DMS, and are summarized in Table 5.1. Three different ordered phases have been identified in this series of CECD tetrablock terpolymers: hexagonally packed cylinders (HEX), hexagonally packed core-shell cylinders (CSC), and an orthorhombic network phase, O^{52}. The O^{52} sample has an intermediate D content (9% D) compared to the CECD samples possessing HEX (0 and 6% D) and CSC (14, 19, and 20% D) morphologies. In the remainder of this section, the experimental data that were used to make these phase assignments are presented in detail, beginning with representative results from the HEX and CSC morphologies. Analysis of the orthorhombic, triply-periodic phase is presented last.

5.3.1 Hexagonally Packed Cylinders (HEX)

Hexagonally packed cylinder phase assignments have been made on the basis of SAXS and TEM results for the CEC-1 triblock (0% D) and CECD-1 (6% D) samples. Figure 5.1 depicts scattering data collected at 140 ºC from CEC-1 from all three principal directions after reciprocating shear. In the $\boldsymbol{q_y}$-$\boldsymbol{q_z}$ plane three orders of hexagonal scattering ((10), (11), and (20) planes) are visible and two-fold scattering is evident in the other two orthogonal directions. These scattering results are consistent with a parallel cylinder orientation,[38,39] where the (10) plane of the hexagonal unit cell is parallel to the shear plane (x-z plane). The asymmetry in the intensity distributions of these SAXS patterns is likely due to imperfect alignment of the specimens with respect to the X-ray beam. Similar scattering results were obtained for CECD-1. The domain spacings, $d_{10} = 2\pi/q^*$, collected from SAXS data at 140 ºC for HEX samples are listed in Table 5.1.

TEM micrographs of CEC-1, given in Figure 5.2, support the HEX morphology assignment. The dark regions correspond to C domains stained with RuO_4, while lighter areas are the semicrystalline E domains. In Figure 5.2a, the hexagonal symmetry of the C (black) cylinders within the E (white) matrix is apparent. Figure 5.2b provides direct visualization of an alternating black and white layered structure, consistent with the long axis of the HEX phase. Similar images were obtained from a RuO_4-stained CECD-1 sample (not shown).

Table 5.1: Characterization data for CEC triblock and CECD tetrablock copolymers.

Polymer	M_n, kDa	M_w/M_n	f_C[a]	f_E[a]	f_D[a]	X_c, E[b]	Phase[c]	d, nm[d,e]	T_{ODT}, °C[f]
CEC-1	22.9	1.06	0.31	0.69	0	0.31	HEX	23.9	180
CECD-1	26.3	1.06	0.28	0.66	0.06	0.26	HEX	23.7	190
CECD-2	36.8	1.06	0.27	0.64	0.09	0.27	O^{52}	1.75, 0.61, 61.0	>300
CECD-3	19.3	1.09	0.23	0.63	0.14	0.28	CSC	26.7	>300
CECD-4	25.0	1.08	0.23	0.58	0.19	0.25	CSC	30.4	>300
CECD-5	26.8	1.06	0.22	0.58	0.20	0.26	CSC	32.4	>300

[a]Volume fractions were calculated from melt density data at 140 °C (ρ_C = 0.920 g/cm^3, ρ_E = 0.784 g/cm^3, and ρ_D = 0.895 g/cm^3).[40]

[b]Fraction of crystallinity in the E domains as measured by DSC.

[c]HEX: hexagonally packed cylinders; O^{52}: orthorhombic network; CSC: core-shell HEX cylinders.

[d]Temperature is 140 °C.

[e]Lattice dimension listed for O^{52} corresponds to *a*/*c*, *b*/*c*, and *c*.

[f]Order-disorder transition temperature determined by DMS.

5.3.2 Hexagonally Packed Core-shell Cylinders (CSC)

Three CECD tetrablocks (CECD-3, CECD-4, and CECD-5) were determined to possess hexagonal symmetry with a core (D)-in-shell (C) structure. These samples represent a composition range of 14 – 20% D by volume. Two-dimensional SAXS data generated from CECD-5 after application of shear are presented in Figure 5.3. These results are similar in appearance to those shown in Figure 5.1 for CEC-1. We again interpret this as scattering from hexagonally packed cylinders of the minority components (C in CEC-1 and C and D in CECD-5) oriented parallel to the shear (x) direction. Along the shear direction ($\boldsymbol{q}_y$-$\boldsymbol{q}_z$ plane), a sharp spot pattern associated with scattering from the (10), (11), (20), (21), and (30) planes of a hexagonal lattice is apparent. The scattering from the other two principal directions, the shear gradient (y) and vorticity (z) directions, are less well-defined, but possess two-fold symmetry. In the $\boldsymbol{q}_x$-$\boldsymbol{q}_y$ plane equatorial scattering arcs corresponding to (10) and (20) diffractions can be readily seen. Along the shear gradient direction ($\boldsymbol{q}_x$-$\boldsymbol{q}_z$ plane), two orders of diffraction from (10) and (11) planes are evident. The (10) diffraction is about half as intense as the (11) diffraction and is attributed to misorientation of the hexagonal lattice about the shear (x) direction. Similar diffraction patterns were obtained for CECD-3 and CECD-4. The lattice constants ($d_{10} = 2\pi/q^*$) collected from SAXS data at 140 ºC are listed in Table 5.1 for all CSC samples.

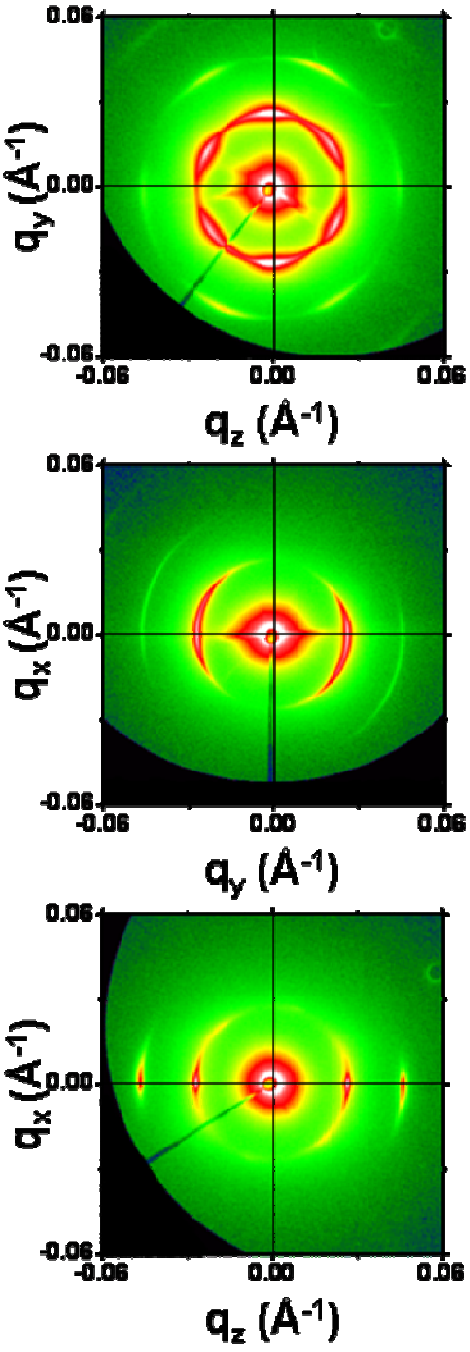

Figure 5.1: Two-dimensional SAXS data collected at 140 ºC from macroscopically-aligned CEC-1 triblock copolymer. These results are consistent with hexagonally packed cylinders oriented along the shear direction (x).

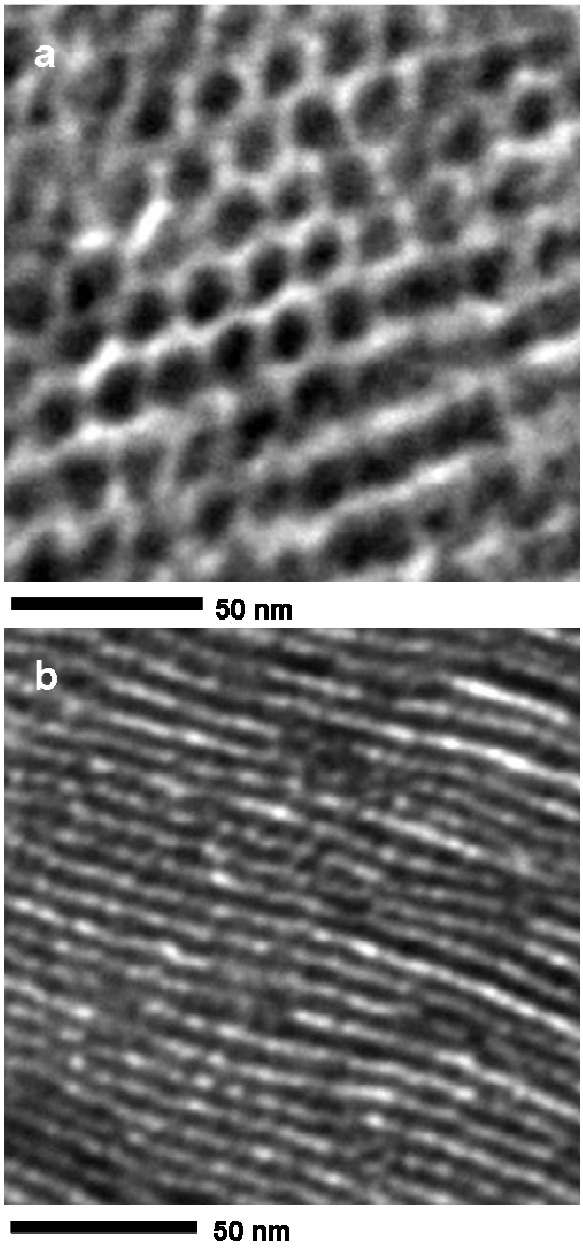

Figure 5.2: (a) TEM micrograph of the CEC-1 triblock copolymer displaying the six-fold axis of the hexagonally packed cylinders. (b) Image from the same material displaying the long axis of the cylinders. The samples have been stained with RuO_4, which preferentially interacts with C domains. These micrographs are consistent with the HEX phase assignment.

TEM micrographs generated from unstained CECD-4 and CECD-5 (Figure 5.4) provide visual evidence of the spatial arrangement of the terpolymer domains. Contrast in these images is provided by the natural mass density difference between D (black areas) and C or E (white areas). Figures 5.4a and 5.4c demonstrate that the D is clearly segregated from the C and E domains. A second view (Figures 5.4b and 5.4d) generated from the same materials displays alternating dark and light layers consistent with the long axis of hexagonally packed cylinders. The slight undulations in the cylinders in Figure 5.4b have been observed previously in shear-aligned block copolymers.[38,41] These results confirm the CSC morphology assignment with D as the core and C as the shell.

5.3.3 O^{52} (Orthorhombic Network)

CECD-2 produced strikingly different two-dimensional SAXS patterns compared to the HEX and CSC samples as shown in Figure 5.5. Numerous diffraction spots are visible in each sample orientation (annealing for five days at 220 °C did not change the positions of these reflections). Skewed intensities are likely due to misalignment between the specimen and X-ray beam. Using a least squares fit method, we have determined that the scattering data from all three orientations are best fit by an orthorhombic unit cell with *Pnna* (No. 52)[42] space group symmetry. The allowed reflections for *Pnna* with the unit cell parameters, $a = 1.75c$, $b = 0.61c$, and $c = 61.0$ nm, are displayed as the white circles in Figure 5.5. The observed diffraction spots and their associated *Pnna* reflections are summarized in Table 5.2. While there is good agreement between the calculated and experimentally observed scattering reflections, we can not account for several diffraction spots in the $\boldsymbol{q}_x$-$\boldsymbol{q}_y$ plane. We attribute these reflections to misoriented grains, which

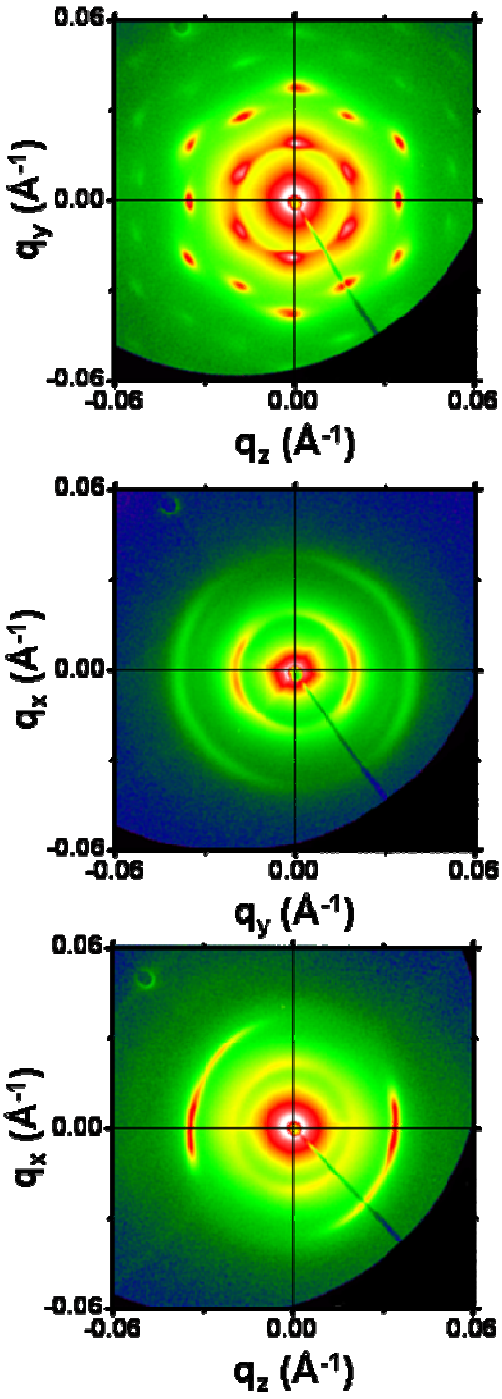

Figure 5.3: Two-dimensional SAXS data collected at 140 ºC from macroscopically-aligned CECD-5 tetrablock terpolymer. These results are consistent with hexagonally arranged cylinders oriented along the shear direction (x).

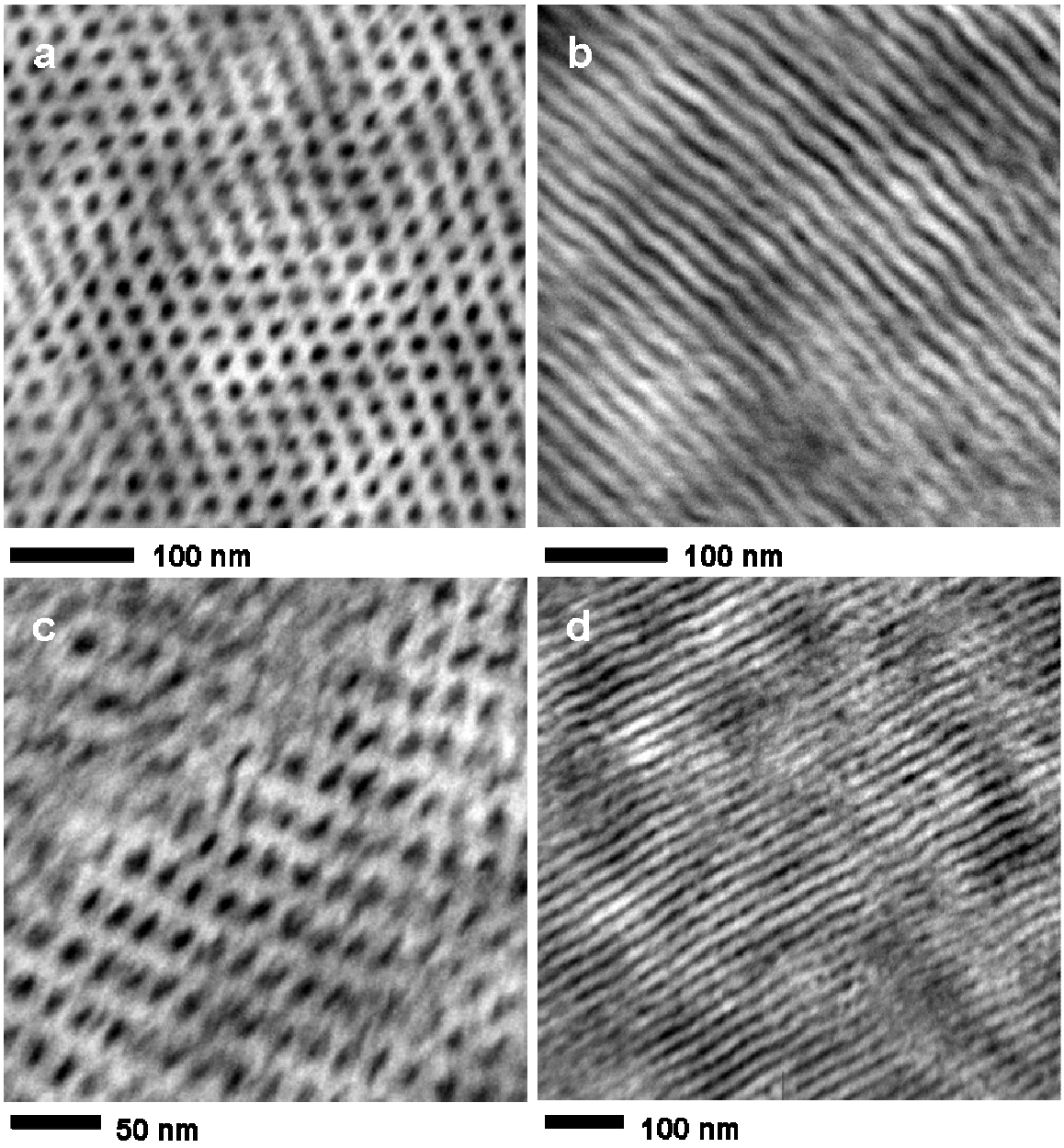

Figure 5.4: TEM micrographs obtained from (a), (b) CECD-4 and (c), (d) CECD-5 representative of the hexagonally packed core-shell cylindrical morphology. The dark regions are the result of the natural mass density contrast provided by the D domains. (a), (c) TEM images show six-fold axis of the hexagonally packed cylinders. (b), (d) View of long axis of cylinders.

Förster, *et al*.[43] have shown lead to secondary Bragg peaks in well-ordered and oriented soft materials. Attempted fits with other space groups, including *Fddd*, led to less satisfactory congruence between calculated and observed diffraction spots.

TEM micrographs were generated from CECD-2 using both unstained and stained samples. In Figure 5.6a, discrete, periodic D domains (black areas) are apparent, consistent with segregation of the D chains from C and E. After staining, the microstructure of CECD-2 is more complex (Figure 5.6b). Several grains with different orientations of light and dark structures are evident. Close examination of the dark circular regions (lower right portion of Figure 5.6b) reveals black dots, which we attribute to the rubbery D domains positioned in the glassy C. This topology of D surrounded by C within the semicrystalline E (white regions) is consistent with the chain architecture of the CECD tetrablock system.

5.4 Discussion

Based on the SAXS and TEM results generated from this series of CECD tetrablock terpolymers, we identified phase transitions from hexagonally packed cylinders to an orthorhombic network morphology (O^{52} with *Pnna* space group symmetry) to core-shell hexagonal cylinders with increasing D composition. The triply periodic O^{52} was previously observed by Cochran and Bates in a poly(cyclohexylethylene-*b*-ethylethylene-*b*-ethylene) (CE_EE) triblock terpolymer.[19] However, O^{52} was a metastable state induced by large-amplitude shear of the higher symmetry O^{70} phase (*Fddd* symmetry).

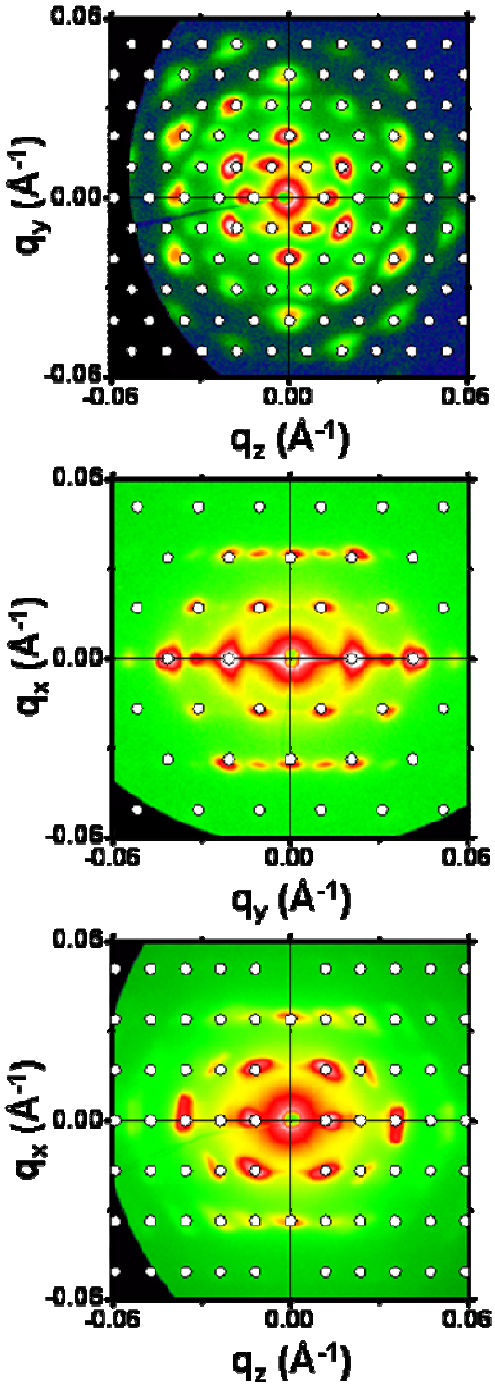

Figure 5.5: Two-dimensional SAXS patterns from macroscopically-oriented CECD-2 containing 9% D collected at 140 ºC. The white circles indicate the locations of allowed *Pnna* reflections with lattice parameters $a = 1.75c$, $b = 0.61c$, and $c = 61$ nm.

Table 5.2: Observed diffraction spot locations and associated Miller indices for *Pnna* assignment of the two-dimensional SAXS patterns shown in Figure 5.5 for CECD-2. The lattice parameters are $a = 1.75c$, $b = 0.61c$, and $c = 61.0$ nm.

	q_z, q_a, Å^{-1}	q_x, q_b, Å^{-1}	q_y, q_c, Å^{-1}	*hkl*
$\boldsymbol{q_y}$-$\boldsymbol{q_z}$ plane	0.0118	0	0	200
	0.0059	0	0.0103	101
	0.0177	0	0.0103	301
	0	0	0.0206	002
	0.0118	0	0.0206	202
	0.0295	0	0.0103	501
	0.0236	0	0.0206	402
	0.0059	0	0.0309	103
	0.0354	0	0	600
	0.0177	0	0.0309	303
	0.0354	0	0.0206	602
	0	0	0.0412	404
	0.0472	0	0.0206	802
	0.0354	0	0.0412	604
	0.0177	0	0.0515	305
$\boldsymbol{q_x}$-$\boldsymbol{q_y}$ plane	0	0.0169	0.0103	011
	0	0	0.0206	002
	0	0.0338	0	020
	0	0.0169	0.0309	013
	0	0.0338	0.0206	022
	0	0	0.0412	004
	0	0.0507	0.0103	031
	0	0.0507	0.0309	033
$\boldsymbol{q_x}$-$\boldsymbol{q_z}$ plane	0.0118	0	0	200
	0.0118	0.0169	0	210
	0.0236	0	0	400
	0.0236	0.0169	0	410
	0	0.0338	0	020
	0.0354	0	0	600
	0.0118	0.0338	0	220
	0.0354	0.0169	0	610
	0.0236	0.0338	0	420
	0.0354	0.0338	0	620
	0.0118	0.0507	0	230
	0.0236	0.0507	0	430

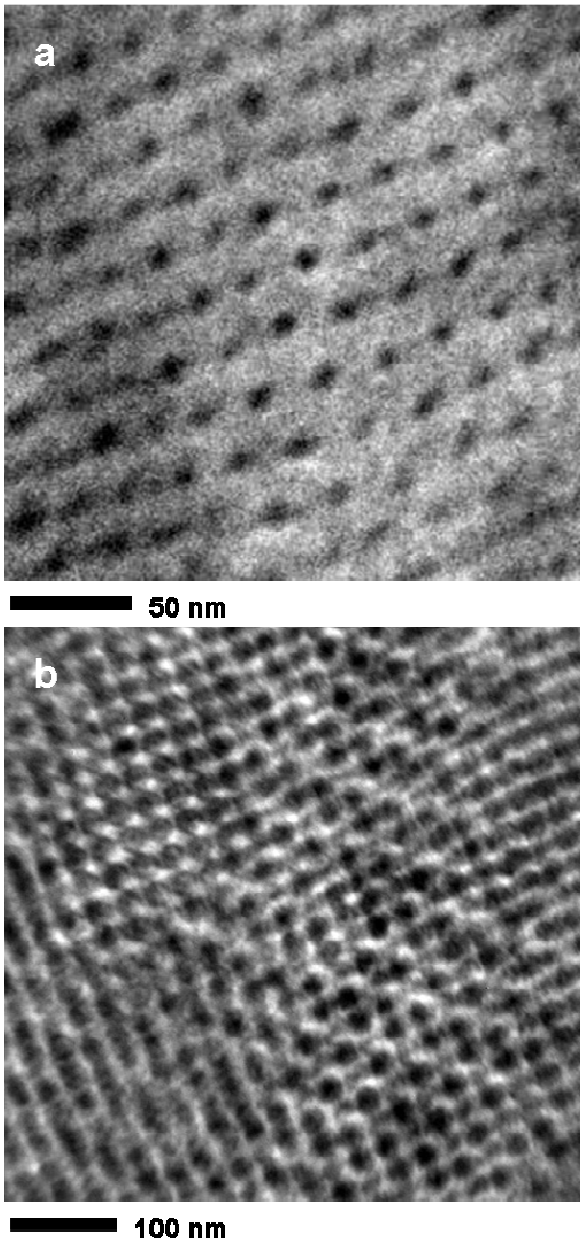

Figure 5.6: TEM micrographs generated from CECD-2 possessing *Pnna* (O^{52}) symmetry. The dark regions in (a) result from the natural contrast provided by the segregated D domains. The sample in (b) has been stained with RuO_4, which preferentially interacts with the C and D domains.

Additionally, the lattice parameters for CECD-2 (a = 1.75c, b = 0.61c) are quite different than those determined for the CE_EE example (a = 2.0c, b = 1.73c). The component volume fractions between CECD-2 (f_C = 0.27, f_E = 0.64, f_D = 0.09) and the CE_EE triblock (f_C = 0.25, f_{EE} = 0.50, f_E = 0.25) also differ significantly. In the CE_EE case, it was presumed that the O^{52} network contained three separate triply continuous domains, while in CECD-2 we have shown that the D domains are isolated (see Figure 5.6a).

To model the topology of the O^{52} structure, a procedure previously employed by Cochran[29] will be used to determine the lattice upon which this network phase is built. This method utilizes a Fourier synthesis technique previously used to model the triply-periodic Q^{230}, Q^{214}, O^{70}, and O^{52} morphologies[19,27,29] and is described by Wohlgemuth, *et al.*[44] A density field $S(\mathbf{x})$, which possesses the symmetry of the phase, is chosen to describe the intermaterial-dividing surface (IMDS) between block domains:

$$S(\mathbf{x}) = \sum_{hkl} f_{hkl} E_{hkl}$$
$$E_{hkl} = \sum_{\alpha} e^{2\pi i \mathbf{T}_\alpha(\mathbf{x})\cdot\mathbf{G}_{hkl}} \tag{0.47}$$

where f_{hkl} is a complex Fourier weight (analogous to the structure factor) for each Fourier mode $\mathbf{G}_{hkl}$ with basis functions E_{hkl}. $\mathbf{T}(\mathbf{x})$ defines the set of general positions unique to the space group symmetry (e.g., *Pnna* has eight equivalent positions). Setting $S(\mathbf{x})$ to a value s_{ij} creates an isosurface that models the IMDS between domains i and j. The s_{ij} of each IMDS can then be adjusted to match experimentally measured domain volume fractions.

In Figure 5.7a, a unit cell with a single block domain with an arbitrary composition of 0.25 has been constructed using the lattice constants and $S(x)$ given in Table 5.3. By changing the isovalue of the domain interface, the volume fractions of the block domain

have been decreased to 0.08 and 0.01 in Figures 5.7b and 5.7c, respectively. In Figure 5.7c, there is no longer three-dimensional connectivity within the block domain; the isosurface has collapsed to ellipsoidal particles located at the 8e Wyckoff setting of the *Pnna* unit cell. These positions identify the nodes of the eight three-fold connectors per unit cell that make up the O^{52} network. This is depicted by a ball-and-stick representation in Figure 5.7d. The 8e Wyckoff position also identifies the *Pnna* lattice as a (10,3)*d* net using Wells' classification scheme.[30] While the three-fold nodes in the (10,3)*a* net of the gyroid lattice are purely symmetric (120° angles and equal strut lengths), the (10,3)*d* network geometry is dependent upon lattice constants and three adjustable parameters, x, y, and z. The connectivity and coordinates of the *Pnna* lattice are listed in Table 5.4. Additional ball-and-stick representations of four unit cells of the O^{52} network are depicted in Figure 5.8 with x = 7/8, y = 5/12, and z = 3/8. In Figure 5.8a, the nodes and struts contained within one unit cell are highlighted, whereas a single (10,3)*d* loop is colored red for clarity in Figure 5.8b. A localized view of the trivalent connectors used in this construction is shown in Figure 5.9a.

We stress that we have not determined the exact positions and geometry of the nodes for the network structure reported here. This represents a very challenging task that may be aided with additional TEM or computational efforts such as self-consistent field theory (SCFT),[1,45] which can predict monomer density fields. Nevertheless, the overall network topology is established. Great flexibility is possible in modeling the O^{52} network lattice. *Pnna* symmetry does not require equal strut lengths, equal strut angles, mirror plane

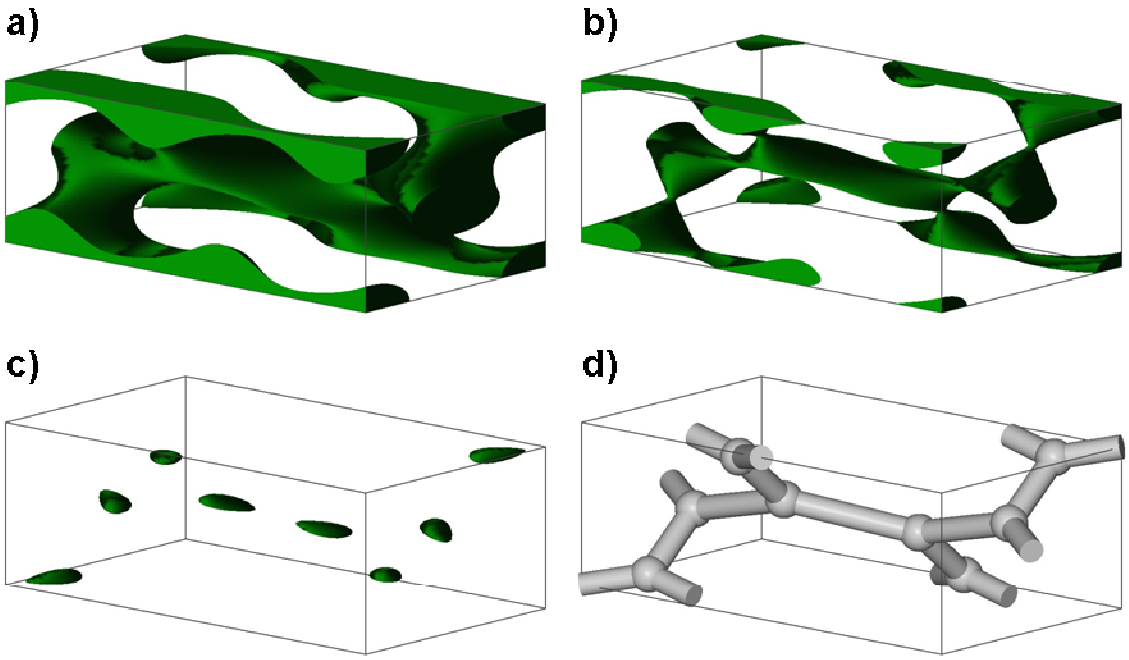

Figure 5.7: Visual representation of the construction method to generate the (10,3)*d* network lattice. (a) A domain with *Pnna* symmetry and a volume fraction of 0.25 generated using the level set model field and lattice parameters listed in Table 5.3. As the composition of the domain decreases (b and c), the isosurface condenses to the eight special (Wyckoff) positions that define the nodes of the connectors. (d) The isosurface is replaced with a ball-and-stick representation of the nodes and connectors of the (10,3)*d* network.

Table 5.3: Lattice parameters, field construction, and domain compositions used to generate the level set models in Figure 5.7.

Figure	Space Group	Lattice Constants	Density Field	Volume Fraction
5.7a 5.7b 5.7c	*Pnna* (O^{52})	$a = 1.75c$, $b = 0.61c$; $\alpha = \beta = \gamma = 90^{o}$	$S(\mathbf{x}) = 0.25E_{200} + E_{101} + E_{011} + 0.25E_{020} + E_{210}$	0.25 0.08 0.01

Table 5.4: Connectivity of (10,3)*d* net found within the O^{52} morphology. The coordinates correspond to the 8e Wyckoff position of the *Pnna* space group. The rows contain the fractional coordinates of each node and the three nodes to which they connect to form trivalent connectors within the orthorhombic unit cell.

Node	Coordinates	Connectivity		
1	(x, -y + ½, -z + ½)	2 – (0, 1, 0)	3 + (0, 0, 0)	8 + (1, -1, -1)
2	(-x + ½, y + ½, -z + ½)	1 + (0, 1, 0)	4 + (0, 0, 0)	7 + (0, 1, -1)
3	(x, y, z)	1 + (0, 0, 0)	4 + (0, 0, 0)	6 + (1, 0, 0)
4	(-x + ½, -y, z)	2 + (0, 0, 0)	3 + (0, 0, 0)	5 + (0, 0, 0)
5	(x + ½, y, -z)	4 + (0, 0, 0)	6 + (0, 0, 0)	7 + (0, 0, 0)
6	(-x, -y, -z)	3 – (1, 0, 0)	5 + (0, 0, 0)	8 + (0, 0, 0)
7	(x + ½, -y + ½, z + ½)	2 + (0, -1, 1)	5 + (0, 0, 0)	8 – (0, 1, 0)
8	(-x, y + ½, z + ½)	1 + (-1, 1, 1)	6 + (0, 0, 0)	7 + (0, 1, 0)

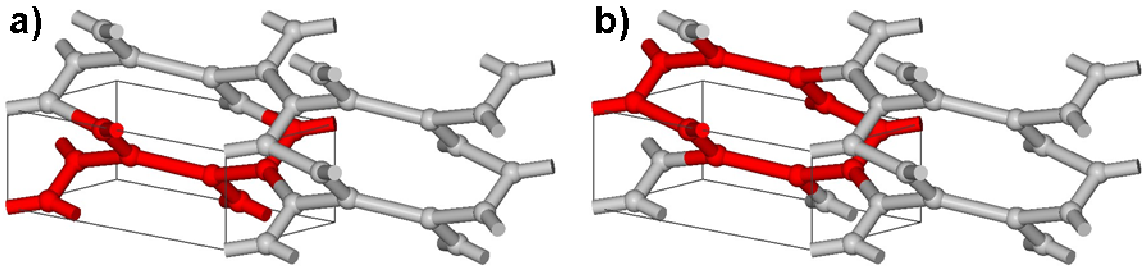

Figure 5.8: Ball-and-stick representations of the *Pnna* topology associated with CECD-2. (a) Four unit cells with one unit cell depicted in red. (b) Four unit cells with one (10,3)*d* loop highlighted in red. In both cases the wire-frame box denotes one unit cell with the lattice parameters $a = 1.75c$ and $b = 0.61c$.

symmetry, or a planar geometry. However, Wyckoff coordinates can be chosen to yield planar three-fold connectors with equal lengths (Figure 5.9b) or equal angles (Figure 5.9c).

We attribute the stabilization of three-fold junctions in the O^{52} network topology to the CECD chain architecture. In Figure 5.10 the local structure of the morphologies identified in this work are given. CEC-1 forms hexagonally packed cylinders of the minority C blocks in a matrix of E. Addition of short D chains to produce CECD-1 (6% D) does not alter the morphology, as the D mixes with the cylindrical C domains. Increasing the D content to 9% coupled with an increase in molecular weight (CECD-2) causes microphase separation of the D and C domains (see Figure 5.6a) to form a three-domain microstructure. To accommodate the large asymmetry in C and D compositions, D chains form spheres embedded in the C domain. These D spheres are located at the center of three-fold junctions that effectively insulate D from unfavorable contacts with

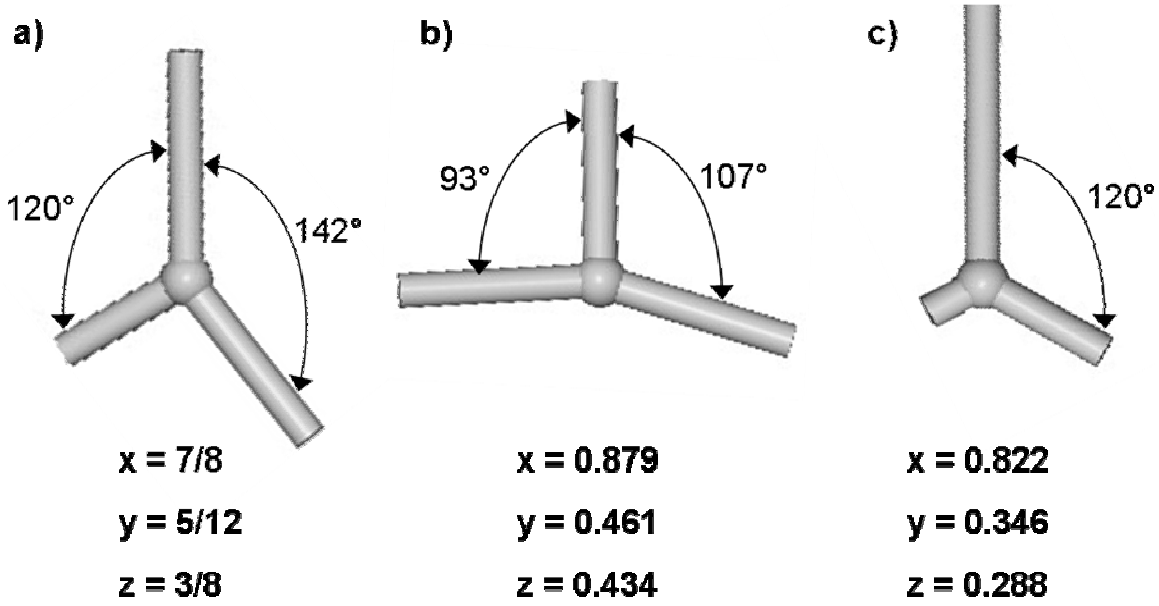

Figure 5.9: Planar trivalent connectors constructed using the *Pnna* Wyckoff 8e setting with the given parameters. (a) There are three unequal strut angles and lengths. (b) The strut lengths are equal, but the three strut angles differ. (c) In this case there are three unequal strut lengths with 120º strut angles.

E. Due to the CECD chain architecture, the terminal C chains are only bound to one interface. These chains can effectively fill the struts between junction points in the network topology (see Figure 5.10). With a further increase in D block length (CECD-3,CECD-4, and, CECD-5, 14%, 19%, and 20% D, respectively), the C/D interfacial curvature decreases and the isolated D domains become cylinders. This microstructure effectively embeds D cylinders in a shell of C, which are hexagonally arranged in the majority E matrix.

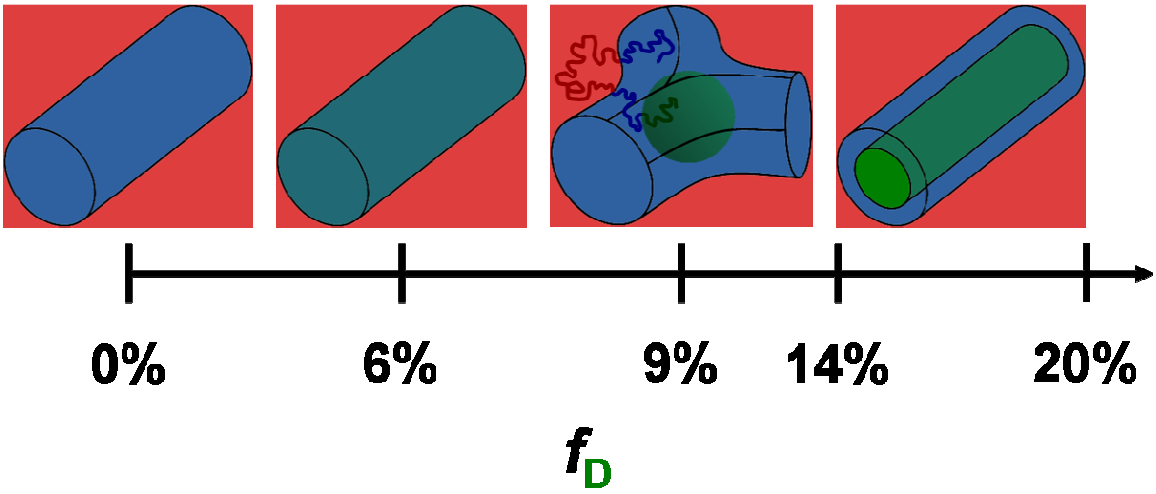

Figure 5.10: Local structure of CECD phases with increasing volume fraction of D. A three-dimensional O^{52} network phase is identified at f_D = 0.09. Network formation is associated with the combined effects of a spherical D domain and a tetrablock architecture, which accommodates placement of terminal C blocks in the strut region.

SCFT calculations by Tyler *et al.*[46] of nonfrustrated ABC triblock terpolymers indicate that O^{52} is not a stable morphology at any composition. We have relied on large shear deformations as a preparation method due to relatively strong segregation within the CECD terpolymers. This precludes us from making a definitive conclusion on whether O^{52} is an equilibrium morphology in these materials. Nonetheless, we believe the CECD tetrablock architecture represents a new design opportunity for the generation of network phases in block terpolymers.

5.5 Conclusion

We have shown by SAXS and TEM that varying the composition of D in asymmetric CECD block terpolymers between 0 and 20% produces the sequence of ordered phases: cylindrical-to-network-to-cylindrical. The two-dimensional SAXS patterns collected from the three orthogonal directions of the network specimen were consistent with a triply periodic structure with *Pnna* (O^{52}) space group symmetry. Stained and unstained TEM micrographs provided further evidence of a network morphology with segregated D domains. Ball-and-stick models were used to visualize the three-fold junctions and struts in the O^{52} topology. We suggest that these trivalent connectors are stabilized by the asymmetric CECD molecular architecture and the sequencing of the block interactions. These results establish a new design parameter for the generation of three-dimensional network structures soft materials.

Acknowledgement. I thank Dr. Steven Weigand and Dr. Denis Keane at the DuPont-Northwestern-Dow Synchrotron Research Center at the Advanced Photon Source for setting up the experimental equipment used to acquire the SAXS data presented in this chapter. I also thank Professor Eric W. Cochran for allowing me to use his level-set software, which was used to generate several of the figures in this chapter. Lastly, I acknowledge the tremendous assistance provided by Dr. Guillaume Fleury in the synthesis of the CECD tetrablocks.

5.6 References

(1) Matsen, M. W.; Bates, F. S. *Macromolecules* **1996**, *29*, 1091-1098.

(2) Matsen, M. W.; Bates, F. S. *J. Chem. Phys.* **1997**, *106*, 2436-2448.

(3) Cochran, E. W.; Garcia-Cervera, C. J.; Fredrickson, G. H. *Macromolecules* **2006**, *39*, 2449-2451.

(4) Matsushita, Y.; Yamada, K.; Hattori, T.; Fujimoto, T.; Sawada, Y.; Nagasawa, M.; Matsui, C. *Macromolecules* **1983**, *16*, 10-13.

(5) Mogi, Y.; Kotsuji, H.; Kaneko, Y.; Mori, K.; Matsushita, Y.; Noda, I. *Macromolecules* **1992**, *25*, 5408-5411.

(6) Beckmann, J.; Auschra, C.; Stadler, R. *Macromol. Rapid Commun.* **1994**, *15*, 67-72.

(7) Krappe, U.; Stadler, R.; Voigt-Martin, I. *Macromolecules* **1995**, *28*, 4558-4561.

(8) Stadler, R.; Auschra, C.; Beckmann, J.; Krappe, U.; Voight-Martin, I.; Leibler, L. *Macromolecules* **1995**, *28*, 3080-3097.

(9) Breiner, U.; Krappe, U.; Stadler, R. *Macromol. Rapid Commun.* **1996**, *17*, 567-575.

(10) Breiner, U.; Krappe, U.; Abetz, V.; Stadler, R. *Macromol. Chem. Phys.* **1997**, *198*, 1051-1083.

(11) Breiner, U.; Krappe, U.; Jakob, T.; Abetz, V.; Stadler, R. *Polym. Bull.* **1998**, *40*, 219-226.

(12) Brinkmann, S.; Stadler, R.; Thomas, E. L. *Macromolecules* **1998**, *31*, 6566-6572.

(13) Matsushita, Y.; Suzuki, J.; Seki, M. *Phys. B* **1998**, *248*, 238-242.

(14) Shefelbine, T. A.; Vigild, M. E.; Matsen, M. W.; Hajduk, D. A.; Hillmyer, M. A.; Cussler, E. L.; Bates, F. S. *J. Am. Chem. Soc.* **1999**, *121*, 8457-8465.

(15) Bailey, T. S.; Pham, H. D.; Bates, F. S. *Macromolecules* **2001**, *34*, 6994-7008.

(16) Avgeropoulos, A.; Paraskeva, S.; Hadjichristidis, N.; Thomas, E. L. *Macromolecules* **2002**, *35*, 4030-4035.

(17) Bailey, T. S.; Hardy, C. M.; Epps, T. H.,III; Bates, F. S. *Macromolecules* **2002**, *35*, 7007-7017.

(18) Ludwigs, S.; Boker, A.; Abetz, V.; Muller, A. H. E.; Krausch, G. *Polymer* **2003**, *44*, 6815-6823.

(19) Cochran, E. W.; Bates, F. S. *Phys. Rev. Lett.* **2004**, *93*, 087802/1-087802/4.

(20) Epps, T. H.,III; Cochran, E. W.; Hardy, C. M.; Bailey, T. S.; Waletzko, R. S.; Bates, F. S. *Macromolecules* **2004**, *37*, 7085-7088.

(21) Chatterjee, J.; Jain, S.; Bates, F. S. *Macromolecules* **2007**, *40*, 2882-2896.

(22) Urbas, A. M.; Maldovan, M.; DeRege, P.; Thomas, E. L. *Adv. Mater.* **2002**, *14*, 1850-1853.

(23) Meuler, A. J.; Fleury, G.; Hillmyer, M. A.; Bates, F. S. *Macromolecules* **2008**, *41*, 5809-5817.

(24) Hajduk, D. A.; Harper, P. E.; Gruner, S. M.; Honeker, C. C.; Kim, G.; Thomas, E. L.; Fetters, L. J. *Macromolecules* **1994**, *27*, 4063-4075.

(25) Schulz, M. F.; Bates, F. S.; Almdal, K.; Mortensen, K. *Phys. Rev. Lett.* **1994**, *73*, 86-89.

(26) Hueckstaedt, H.; Goldacker, T.; Goepfert, A.; Abetz, V. *Macromolecules* **2000**, *33*, 3757-3761.

(27) Epps, T. H.,III; Cochran, E. W.; Bailey, T. S.; Waletzko, R. S.; Hardy, C. M.; Bates, F. S. *Macromolecules* **2004**, *37*, 8325-8341.

(28) Mogi, Y.; Mori, K.; Matsushita, Y.; Noda, I. *Macromolecules* **1992**, *25*, 5412-5415.

(29) Cochran, E. W. *Ph.D. Dissertation*; University of Minnesota **2004**, 1-316.

(30) Wells, A. F. *Three Dimensional Nets and Polyhedra;* John Wiley & Sons: New York, NY 1977.

(31) Takenaka, M.; Wakada, T.; Akasaka, S.; Nishitsuji, S.; Saijo, K.; Shimizu, H.; Kim, M. I.; Hasegawa, H. *Macromolecules* **2007**, *40*, 4399-4402.

(32) Meuler, A. J.; Hillmyer, M. A.; Bates, F. S. *Macromolecules* **2009**, *42*, 7213-7216.

(33) Brandrup, J., Immergut, E. H. *Polymer Handbook*, Wiley: New York, 1989.

(34) Mortensen, K.; Almdal, K.; Bates, F. S.; Koppi, K.; Tirrell, M.; Norden, B. *Phys. B* **1995**, *213&214*, 682-684.

(35) Brown, G. M.; Butler, J. H. *Polymer* **1997**, *38*, 3937-3945.

(36) Khandpur, A. K.; Macosko, C. W.; Bates, F. S. *J. Polym. Sci. Part B* **1995**, *33*, 247-252.

(37) Hermel, T. J.; Hahn, S. F.; Chaffin, K. A.; Gerberich, W. W.; Bates, F. S. *Macromolecules* **2003**, *36*, 2190-2193.

(38) Winter, H. H.; Scott, D. B.; Gronski, W.; Okamoto, S.; Hashimoto, T. *Macromolecules* **1993**, *26*, 7236-7244.

(39) Fredrickson, G. H.; Bates, F. S. *Annu. Rev. Mater. Sci.* **1996**, *26*, 501-550.

(40) Fetters, L. J.; Lohse, D. J.; Richter, D.; Witten, T. A.; Zirkel, A. *Macromolecules* **1994**, *27*, 4639-4647.

(41) Handlin, D. L.; Thomas, E. L. *Macromolecules* **1983**, *16*, 1514-1525.

(42) Hahn, T., Ed. *International Tables for X-ray Crystallography;* Kluwer Academic Publishers: Boston, MA 1992.

(43) Förster, S.; Timmann, A.; Schellbach, C.; Fromsdorf, A.; Kornowski, A.; Weller, H.; Roth, S. V.; Lindner, P. *Nat. Mater.* **2007**, *6*, 888-893.

(44) Wohlgemuth, M.; Yufa, N.; Hoffman, J.; Thomas, E. L. *Macromolecules* **2001**, *34*, 6083-6089.

(45) Matsen, M. W.; Schick, M. *Phys. Rev. Lett.* **1994**, *72*, 2660-2663.

(46) Tyler, C. A.; Qin, J.; Bates, F. S.; Morse, D. C. *Macromolecules* **2007**, *40*, 4654-4668.

6

Inverted Phases Induced by Chain Architecture in Poly(styrene-*b*-isoprene-*b*-styrene-*b*-ethylene oxide) Tetrablock Terpolymers

6.1 Introduction

Self-assembly of block polymer melts into periodically ordered microstructures has proved attractive for generating materials with strict control over length scale and morphology.[1,2] The simplest class of linear block polymers, AB diblocks, generate only four stable phases. (Takenaka and coworkers[3,4] recently reported a fifth morphology, an orthorhombic network phase (O^{70}) with *Fddd* symmetry, in a poly(styrene-*b*-isoprene) diblock copolymer over a narrow slice of parameter space). At strong or intermediate segregation strength ($\chi_{AB}N$? 10, where χ_{AB} is the segment-segment interaction parameter and N is the overall degree of polymerization), these morphologies are dictated solely by the block volume fractions (f). Highly asymmetric diblocks (f ~ 0.1 – 0.15) produce spherical domains of the minority blocks, arranged with BCC order in a matrix

of the majority blocks. Hexagonally-packed cylinders occur when the molecular asymmetry decreases (f ~ 0.15 – 0.3), while alternating lamellae of A-rich and B-rich domains are most stable when the volume fractions of the blocks are comparable (f ~ 0.35 – 0.5). These "classical" phases are complemented by the bicontinuous double gyroid, which occurs over a narrow region of composition space between cylinders and lamellae (f ~ 0.3 – 0.35). While block conformational asymmetry[5] and modest polydispersity[6] can shift these morphology boundaries, the overall topology of the AB diblock phase portrait remains unchanged.

The number and geometrical complexity of morphologies increases dramatically with the addition of a third dissimilar block, as in ABC triblocks. The number of possible block interfaces (A/B, A/C, and B/C) triples, which complicates the free energy balance that determines self-assembly behavior. At this time, over thirty ordered morphologies have been reported for linear triblock terpolymers.[7-18] Among the ABC triblock microstructures are core-shell analogs of the sphere, cylinder, and double gyroid phases found in AB diblocks.[11,14,19] The core-shell cylindrical and gyroid phases are particularly attractive candidates for the creation of mechanically robust solid-state electrolytes,[20,21] nanoporous templates,[22-25] and semipermeable membranes.[14]

We are especially interested in using molecular architecture to produce new ordered morphologies, or to expand the range of block compositions that lead to a given microstructure. This has led us to explore the self-assembly behavior of ABAC tetrablock terpolymers. In Chapter 5, we discussed an unanticipated network structure (O^{52}) in a series of poly(cyclohexylethylene-*b*-ethylene-*b*-cyclohexylethylene-*b*-dimethylsiloxane)

tetrablocks.[26] In this chapter we describe the bulk morphological behavior of a sequence of poly(styrene-*b*-isoprene-*b*-styrene-*b*-ethylene oxide) SISO terpolymers with $f_S \cong f_I$ and f_O between 0 and 30% (the S is divided equally between the two S blocks, see Figure 6.1). Incorporation of O into a block polymer is appealing for two reasons: the growth of O can be initiated from a hydroxyl-terminated macromolecule,[27] and O containing block polymers have received widespread attention as electrolytes.[28] Additionally, SISO represents a variation of the well-studied ISO system,[16,18,29] making it ideal for examining differences in phase behavior that arise from chain architecture alone.

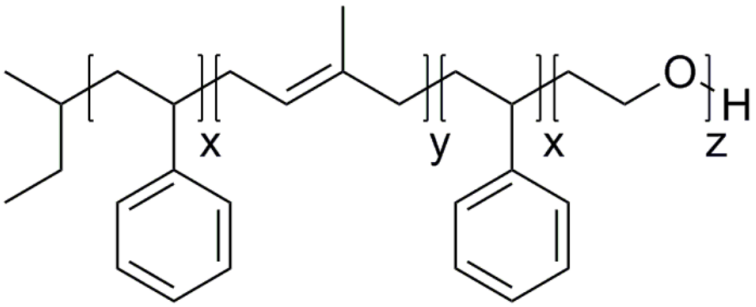

Figure 6.1: Molecular structure of SISO tetrablock terpolymers.

6.2 Experimental Section

6.2.1 Block Polymer Synthesis

Poly(styrene-*b*-isoprene-*b*-styrene-*b*-ethylene oxide) (SISO) tetrablock terpolymers were generated by the re-initiation and polymerization of ethylene oxide from a single

batch of hydroxyl-terminated SIS copolymer, using a previously published multi-step approach.[15,27] Sequential anionic polymerization of styrene, isoprene, and styrene was conducted at 40 ºC in cyclohexane under an argon atmosphere. The monomers and solvent were rigorously purified as described elsewhere.[30] Polymerization of the first block was initiated by *sec*-butyllithium. An aliquot of the styrene block was removed after 8 hours for analysis by size-exclusion chromatography (SEC) before proceeding with the sequential monomer addition sequence. A large excess (~10 times) of ethylene oxide was added to the reaction mixture, which functionalizes each triblock chain with a single $–CH_2CH_2O-$ unit.[31] Addition of excess degassed methanol produced the hydroxyl-terminated triblock copolymer. The precursor SIS triblock was recovered by precipitation into a 3:1 solution of methanol and isopropanol, followed by filtration and complete drying under dynamic vacuum.

Hydroxyl-terminated SIS triblock was dissolved in purified tetrahydrofuran at 45 ºC prior to polymerization of ethylene oxide with potassium naphthalenide as the initiator. The reaction was allowed to proceed for ~40 hours before terminating with excess degassed methanol. After removal of most of the solvent via rotary evaporation, the SISO polymers were redissolved in dichloromethane and washed with distilled water to remove excess salts following previously reported procedures.[15,27] The SISO tetrablocks were precipitated from dichloromethane into isopropanol and freeze-dried from benzene. During the freeze-drying process, 0.5 wt % of BHT antioxidant was added to the block polymers.

6.2.2 Molecular Characterization

Molecular weight distributions of the initial poly(styrene) block and the SIS triblock copolymer were obtained by SEC on a Waters 717 GPC equipped with three Polymer Labs Mixed-C columns and a Waters 410 differential refractometer. Samples were run at 30 ºC with a flow rate of 1.0 mL/min using tetrahydrofuran as the mobile phase. Polydispersities were calculated using ten poly(styrene) standards (Polymer Laboratories). The SISO tetrablocks were analyzed in chloroform, due to O interactions with the columns in tetrahydrofuran,[32] on a Hewlett-Packard 1100 liquid chromatography system equipped with a Hewlett-Packard 1047A RI detector and three Polymer Labs Mixed-C columns. The SEC traces of the poly(styrene) aliquot, hydroxyl-terminated SIS triblock, and a representative SISO tetrablock are given in Figure 6.2.

Quantitative compositions of the unsaturated SIS and SISO block polymers were determined using ^{1}H NMR spectroscopy on a Varian UNITY 300 spectrometer with a pulse repetition delay of 20 s. Samples were prepared by dissolving polymer in deuterated chloroform at room temperature. Volume fractions of poly(styrene), poly(isoprene), and poly(ethylene oxide) were determined from measured mole fractions using homopolymer densities at 140 ºC.[33] The ^{1}H NMR spectra for the hydroxyl-terminated SIS triblock and a representative SISO tetrablock are displayed in Figure 6.3. The molecular characterization data for the block copolymers utilized in this chapter are summarized in Table 6.1.

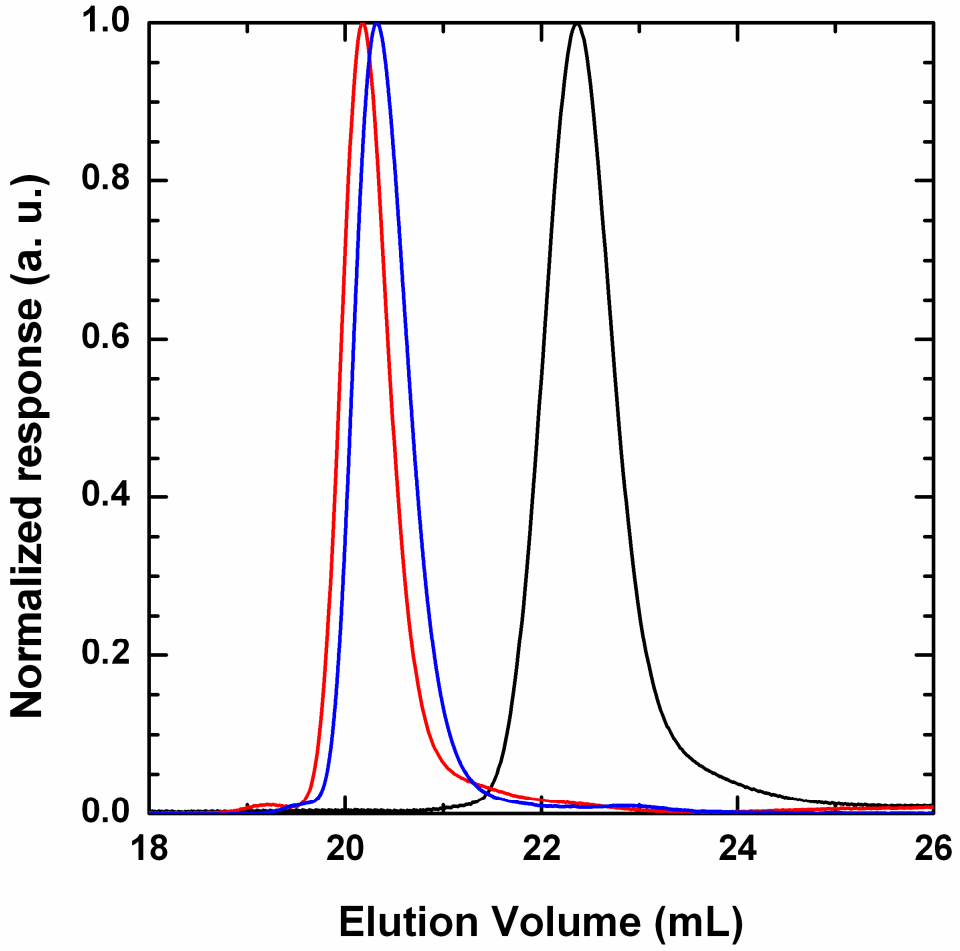

Figure 6.2: SEC traces for first poly(styrene) block (black line), hydroxyl-terminated SIS triblock (red line), and SISO-4 (f_O = 0.09) tetrablock terpolymer (blue line). The poly(styrene) and SIS data are from a GPC using tetrahydrofuran as the eluent, while SISO-4 was analyzed in chloroform due to O interactions with the columns in tetrahydrofuran.

6.2.3 Thermal Analysis

Differential scanning calorimetry (DSC) experiments were conducted on a TA Instruments Q1000 DSC. A measured amount of polymer (5–10 mg) was heated to 150

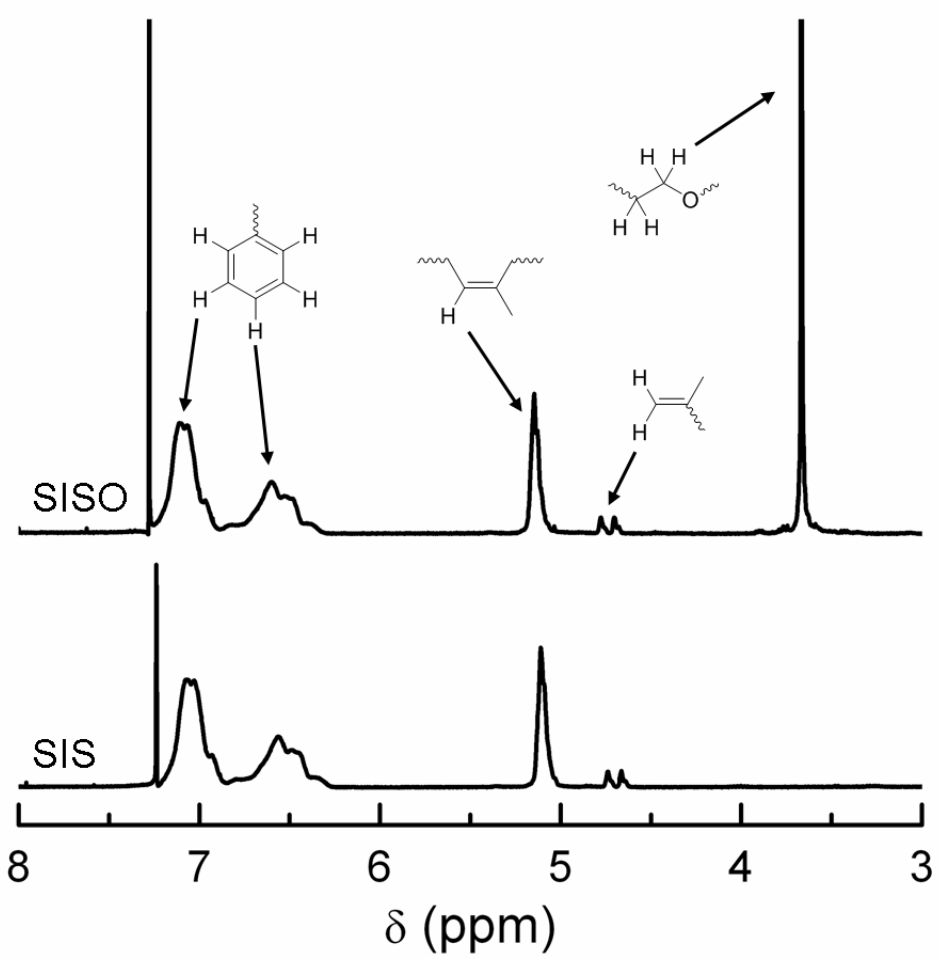

Figure 6.3: ^{1}H NMR spectra obtained from hydroxyl-terminated SIS and SISO-4 (f_O = 0.09) tetrablock. Peaks in both traces are consistent with five phenyl protons in S repeat unit, single proton in 1,4-microstructure of I, and two protons in 3,4-microstructure of I. The peak at 3.6 ppm in SISO is associated with the four protons in an O repeat unit.

ºC to erase the effects of thermal history prior to cooling to – 100 ºC at 10 ºC/min. Data were acquired upon second heating at a ramp rate of 10 ºC/min. The degree of crystallinity within the O domains was determined by the integration of the melting peaks

(see Figure 6.7) and referencing to the heat of fusion of bulk poly(ethylene oxide) (213 J/g).[34]

6.2.4 Dynamic Mechanical Spectroscopy (DMS)

Samples used for DMS were prepared by compression-molding polymer powder into 25 mm ◈ 0.8 mm disks at 100 ºC using a pressure of 2000 psi for 5 – 6 min. Two types of DMS experiments were conducted on a Rheometrics Scientific ARES strain-controlled rheometer with 25 mm diameter parallel plates between 80 and 250 ºC, well above the glass transition (T_g) and melting temperatures (T_m) of the S ($T_g \cong 60$ ºC) and O ($T_m < 60$ ºC) blocks. The samples were initially heated to 10 ºC above T_{ODT} or 250 ºC for 10 min to erase the thermal history of the sample. Isochronal (ω = 1 rad/s) measurements of the elastic (G') and loss (G'') moduli at a constant heating rate of 2 ºC/min yielded the T_{ODT} values listed in Table 6.1; no order-order transitions (discontinuities in G' or G'' prior to T_{ODT}) were recorded during these experiments. G' and G'' were also monitored during isothermal frequency scans ($100 \leq \omega \leq 0.1$ rad/s) to characterize the linear viscoelastic properties of the polymers. Experiments were conducted with a strain amplitude of 1%, which was within the linear viscoelastic regime of the block polymers.

6.2.5 Small-angle X-ray Scattering (SAXS)

Two-dimensional synchrotron SAXS data were collected at the Advanced Photon Source at Argonne National Laboratory on the 5IDD beamline of the DuPont-Northwestern-Dow Synchrotron Research Center. The sample-to-detector distance was 5.50 or 6.52 m and the radiation wavelength (λ) was 0.729 Å. The diffraction data were

acquired with a Mar CCD area detector, azimuthally averaged, and are presented as intensity as a function of scattering wave vector $|\boldsymbol{q}| = q = 4\pi\lambda^{-1}\sin(\theta/2)$, where θ is the scattering angle. Samples were annealed above the order-disorder transition temperature (T_{ODT}) for 5 min, or at 250 ºC for samples with T_{ODT} > 250 ºC in a DSC chamber under a helium purge.

6.2.6 Transmission Electron Microscopy (TEM)

TEM micrographs were collected on a JEOL 1210 transmission electron microscope operating at 120 kV at the University of Minnesota Institute of Technology Characterization Facility. Thin slices (~70 nm) of polymer were prepared by cryo-microtoming at –70 ºC on a Reichart ultramicrotome using a Microstar diamond knife and collected on copper grids (Ted Pella). Contrast was attained by exposing the polymer slices to the vapor from a 4% aqueous solution of osmium tetroxide (Ted Pella) for 10 min. The heavy metal oxide reacts preferentially with the poly(isoprene) domains providing electron mass density contrast within these materials. Samples were prepared for microtoming by annealing under vacuum for 3 days prior to quenching into liquid nitrogen to preserve the melt morphology.

6.3 Results and Analysis

Nine SISO tetrablocks were generated by the re-initiation and polymerization of ethylene oxide from a single batch of hydroxyl-terminated SIS copolymer with equal S and I content ($f_S = f_I$). The only variation within this series of SISO terpolymers is the O

block length (parameter z in Figure 6.1, $0 \leq f_O \leq 0.30$). The molecular, thermal, and structural characteristics of the parent SIS and SISO terpolymers are summarized in Table 6.1. Morphological assignments were made by utilizing a combination of small-angle X-ray scattering (SAXS), dynamic mechanical spectroscopy (DMS), and transmission electron microscopy (TEM). Two inverted phases, spheres with liquid-like packing and hexagonally-packed cylinders, have been identified in these materials. In the remainder of the section, we present the experimental results that led to the phase assignments.

6.3.1 Small-angle X-ray Scattering (SAXS)

Synchrotron SAXS powder patterns from the SIS triblock and nine SISO tetrablocks are presented in Figure 6.4. The SAXS data for SIS and SISO-1 (both collected at 80 ºC) show only a single, broad peak, which we associate with the disordered state. Increasing the O content to $0.07 \leq f_O \leq 0.09$ (specimens SISO-2 (140 ºC), SISO-3 (80 ºC), and SISO-4 (140 ºC)) leads to qualitatively different scattering behavior; an additional maximum at higher q is apparent, but the principal peak remains broad, implying limited long-range structural order. We attribute these results to liquid-like packed (LLP) spheres,[35-42] which were corroborated by TEM and DMS measurements (see below). If we assign the broad bump at $q \cong 0.058$ Å^{-1} (Figure 6.4, SISO-2) as the first maximum in the spherical form factor,[35,43] we obtain a sphere radius of 99 Å. Taking the primary peak

Table 6.1: Characterization data for SIS triblock and SISO tetrablock terpolymers.

Polymer	M_n, kDa	M_w/M_n	f_S[a]	f_I[a]	f_O[a]	X_c, O[b]	Phase[c]	T_{ODT}, °C[d]	d, nm[e]
SIS	20.8	1.03	0.51	0.49	0	–	DIS	<80	13.4 (80)
SISO-1	21.7	1.04	0.48	0.48	0.04	0	DIS	<80	15.4 (80)
SISO-2	22.7	1.07	0.46	0.47	0.07	30	LLP spheres	174	17.6
SISO-3	23.0	1.04	0.46	0.46	0.08	37	LLP spheres	196	18.7 (80)
SISO-4	23.2	1.07	0.45	0.46	0.09	41	LLP spheres	225	18.9
SISO-5	24.2	1.04	0.44	0.44	0.12	50	HEX	>250	21.0
SISO-6	24.6	1.10	0.43	0.43	0.14	54	HEX	>250	20.0
SISO-7	25.3	1.04	0.42	0.42	0.16	55	HEX	>250	20.9
SISO-8	26.4	1.12	0.40	0.41	0.19	53	HEX	>250	22.2
SISO-9	31.1	1.12	0.35	0.35	0.30	64	HEX	>250	28.1

[a]Volume fractions were calculated from published melt density data at 140 °C.[33]

[b]Fraction of crystallinity in the O domains as measured by DSC.

[c]DIS: disordered; LLP spheres: liquid-like packing of spheres; Hex: hexagonally packed cylinders.

[d]Order-disorder transition temperatures determined by DMS.

[e]Characteristic morphological length scale ($d = 2\pi/q^*$) at 140 °C unless noted in parentheses.

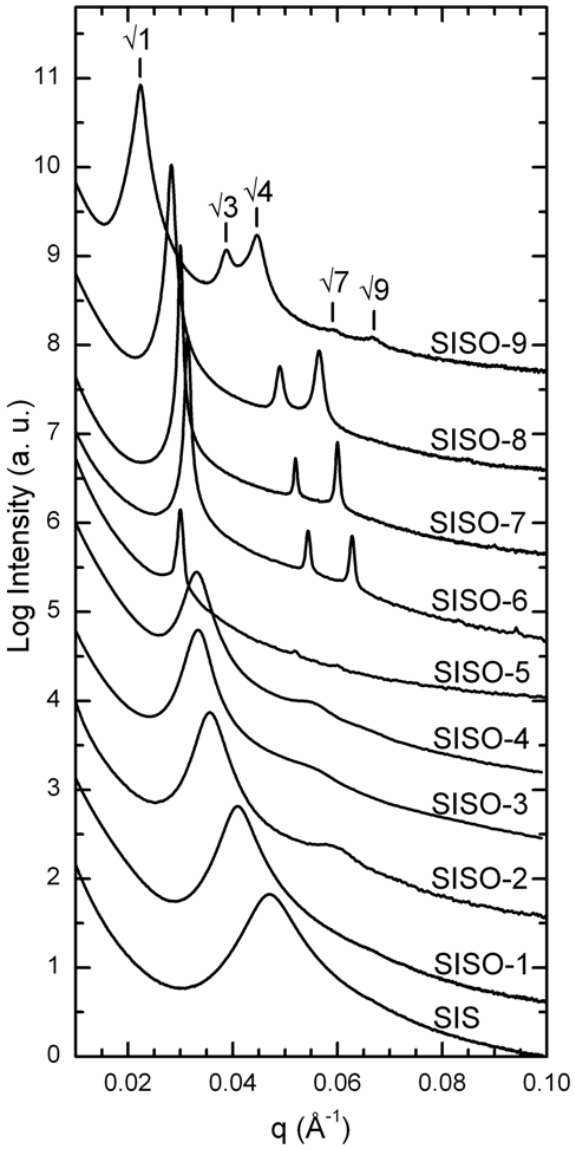

Figure 6.4: Synchrotron SAXS patterns obtained from SIS triblock and SISO tetrablock samples. Data were collected at 80 ºC (SIS, SISO-1, and -3) or 140 ºC (SISO-2, -4, -5, -6, -8, and -9). The broad primary peak and lack of higher order reflections for SIS and SISO-1 are consistent with a disordered melt. The patterns for SISO-2, -3, and -4 do not exhibit long-range structural order, but display a bump at higher *q* attributed to a maximum in the spherical form factor. The Bragg reflections for SISO-5, -6, -7, -8, and -9 are consistent with hexagonal symmetry, which have been indexed for SISO-9.

as the (110) reflection of a BCC lattice yields a core volume fraction of 0.53, which is equivalent to $f_S + f_O$ and suggests that the spheres consist of both S and O. The SAXS patterns produced by SISO tetrablocks with $f_O \geq 0.12$ (SISO-4, -5, -6, -7, -8, and -9 collected at 140 ºC) are strikingly different than the other samples, each containing at least three well-defined scattering peaks. The scattering pattern for SISO-9 displays peaks at $q/q^* = \sqrt{1}, \sqrt{3}, \sqrt{4}, \sqrt{7}$, and $\sqrt{9}$, where q^* is the principal peak location, consistent with hexagonal (HEX) symmetry. Characteristic structural length scales $d = 2\pi/q^*$ for the disordered, LLP spheres, and HEX samples are summarized in Table 6.1.

6.3.2 Transmission Electron Microscopy (TEM)

TEM was utilized to characterize the morphologies of the LLP sphere and HEX phases identified by SAXS. The images in Figures 6.5a and 6.5b were generated from SISO-2. Light circular regions associated with S and O appear to be dispersed without long ranged order in a dark matrix of I. However, careful examination reveals restricted regions of short ranged microdomain periodicity (Figure 6.5b). These TEM results are consistent with our interpretation of the SAXS results (Figure 6.4) as a spherical microstructure lacking long-range order. Micrographs recorded from SISO-6 are consistent with the HEX symmetry identified by SAXS (Figure 6.5c) and allow assignment of a cylindrical phase (Figure 6.5d). Like SISO-2, regions of S and O are arranged within the continuous I matrix, but are hexagonally-packed and display areas of long-range order in accordance with the relatively narrow diffraction peaks found in

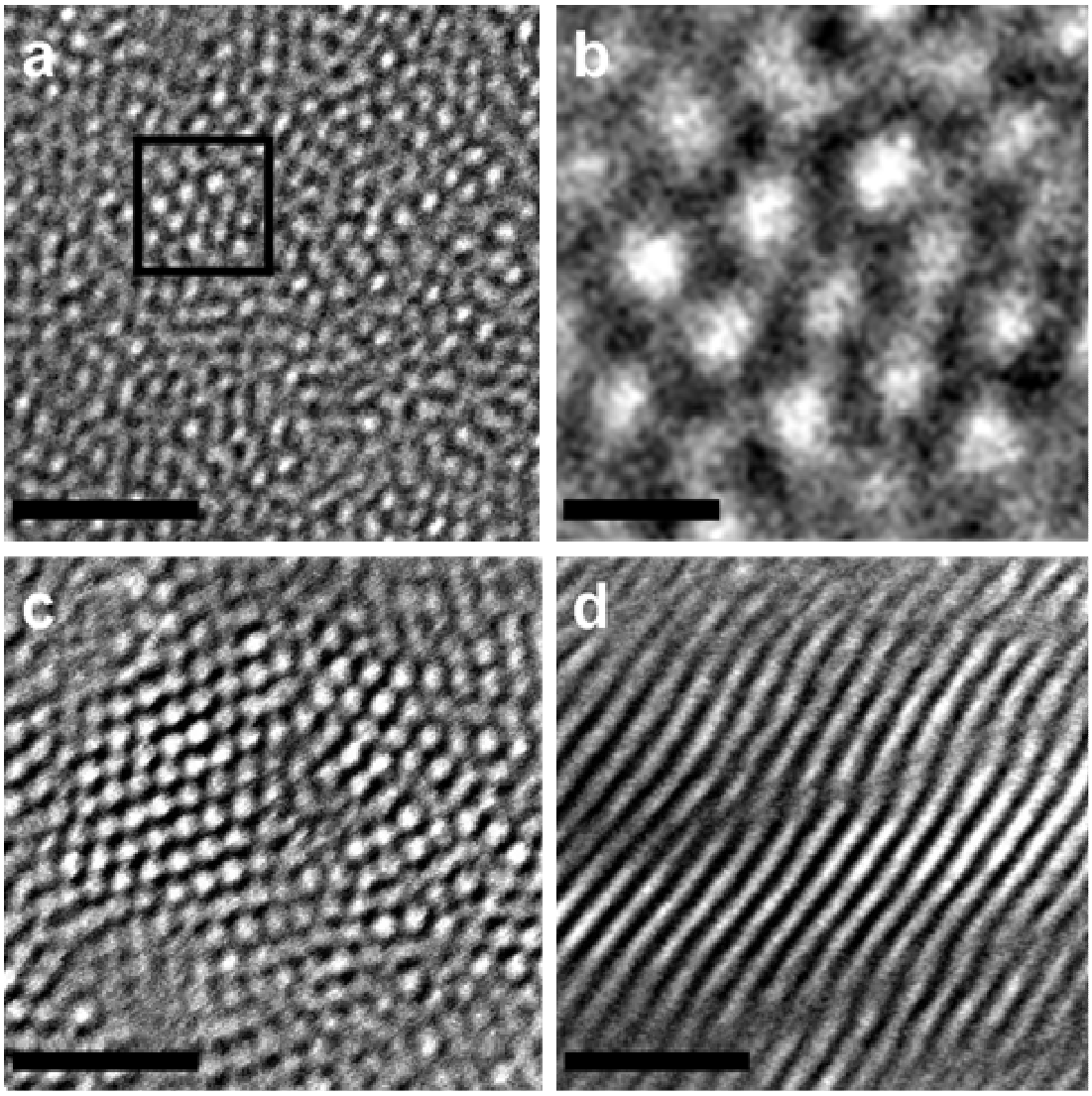

Figure 6.5: TEM micrographs generated from (a, b) SISO-2 ($f_O = 0.07$) and (c, d) SISO-6 ($f_O = 0.14$). The dark regions result from selective staining of the I domains with OsO_4. (a) I domains are microphase-separated from lighter S and O domains, but long-range order is lacking in the specimen. (b) Magnified view of the area marked with a square in (a) displaying short-range periodic order. (c) Hexagonal packing of unstained S and O domains within the I matrix is readily apparent. (d) Orthogonal view displaying the long axis of cylinders. The scale bars denote 100 nm except for 20 nm in (b).

Figure 6.4. The TEM results provide definitive evidence of inverted phases with the majority constituents (S and O) forming spheres and cylinders.

6.3.3 Dynamic Mechanical Spectroscopy (DMS)

Figure 6.6 displays the frequency-dependent rheological properties from three SISO tetrablocks, representative of the three phases identified on the basis of SAXS and TEM. These plots were constructed using time-temperature superposition (TTS) with a reference temperature (T_{ref}) of 80 ºC. (While TTS is not valid fundamentally for such rheologically complex materials it does facilitate comparison of data obtained at different temperatures). SISO-1 (f_O = 0.04, upper left panel in Figure 6.6) displays terminal linear viscoelastic behavior ($G' \sim \omega$ and $G'' \sim \omega^2$) over the investigated temperature range consistent with the disordered state and the SAXS results (Figure 6.4). The isothermal frequency results generated from SISO-4 (f_O = 0.09, upper right panel in Figure 6.6) are vastly different in appearance and are consistent with an ordered microstructure. The low frequency plateau in G' has been attributed to triply periodic morphologies[44] such as the three-dimensional sphere phase identified in this sample with SAXS and TEM. We associate the viscoelastic response of decreasing G' and G'' with decreasing ω (SISO-8, f_O = 0.19, bottom panel in Figure 6.6) to the HEX cylinder phase assigned by SAXS for SISO-5, -6, -7, -8, and -9.

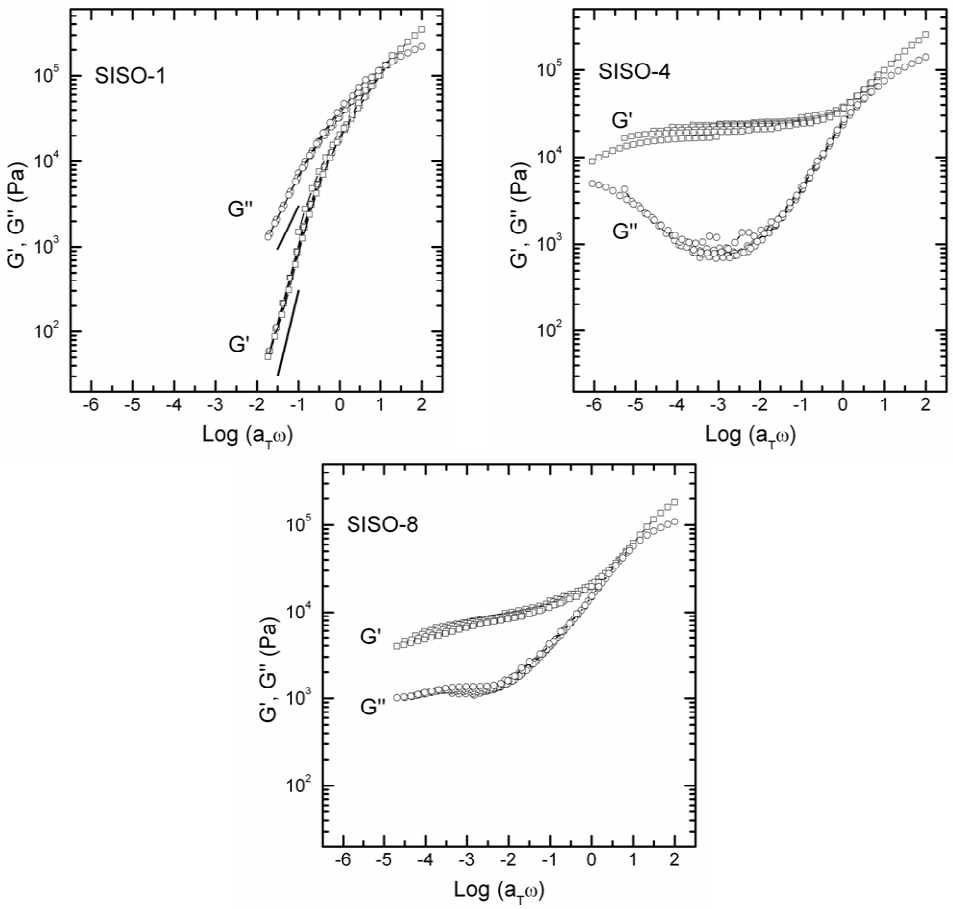

Figure 6.6: Isothermal frequency sweep data shifted according to time-temperature superposition (T_{ref} = 80 ºC) for samples possessing the three distinct microstructures discussed in this work. SISO-1 (80 ≤ T ≤ 110 ºC) exhibits liquid-like terminal behavior associated with the disordered phase ($G' \sim \omega^2$ and $G'' \sim \omega$). The solid black lines near G' and G'' indicate slopes of two and one, respectively. The data for SISO-4 (80 ≤ T ≤ 220 ºC) display a low-frequency plateau in G' consistent with the spherical microstructure determined on the basis of SAXS and TEM. SISO-8 (80 ≤ T ≤ 240 ºC) yield qualitatively different frequency results, with a weak dependence of G' and G'' on ω at low frequencies.

6.3.4 Differential Scanning Calorimetry (DSC)

Figure 6.7 displays DSC curves for the block polymers examined in this study. The LLP sphere and HEX samples exhibit an O melting peak and a corresponding melting temperature that increases with increasing f_O. Integration of the melting peaks normalized by the O weight fraction and heat of fusion of bulk poly(ethylene oxide) yielded the O block crystallinity values listed in Table 6.1. The observed crystallinities are consistent with the assigned morphologies as discussed below.

6.4 Discussion

On the basis of SAXS, TEM, and DMS characterization results, the sequence of phases associated with this series of SISO tetrablock terpolymers can be summarized as disordered to spheres with short-range order (liquid-like packing) to hexagonally-packed cylinders with increasing f_O. A lack of long-range microstructural order in SISO-2, SISO-3, and SISO-4 ($0.07 \leq f_O \leq 0.09$) may reflect slow equilibration kinetics likely exacerbated by the SISO chain architecture. Cavicchi and Lodge proposed that the development of well-ordered BCC arrays in sphere-forming block polymers is hindered by the expulsion and reinsertion of chains from one sphere to another during domain equilibration,[45] a restriction that will be amplified by the tetrablock architecture. Additional high-temperature annealing of these samples may yield microstructures with long-range, periodic order. While we can not visualize microphase separation of the O and S blocks with our TEM staining method, DSC experiments (see Figure 6.7) indicate

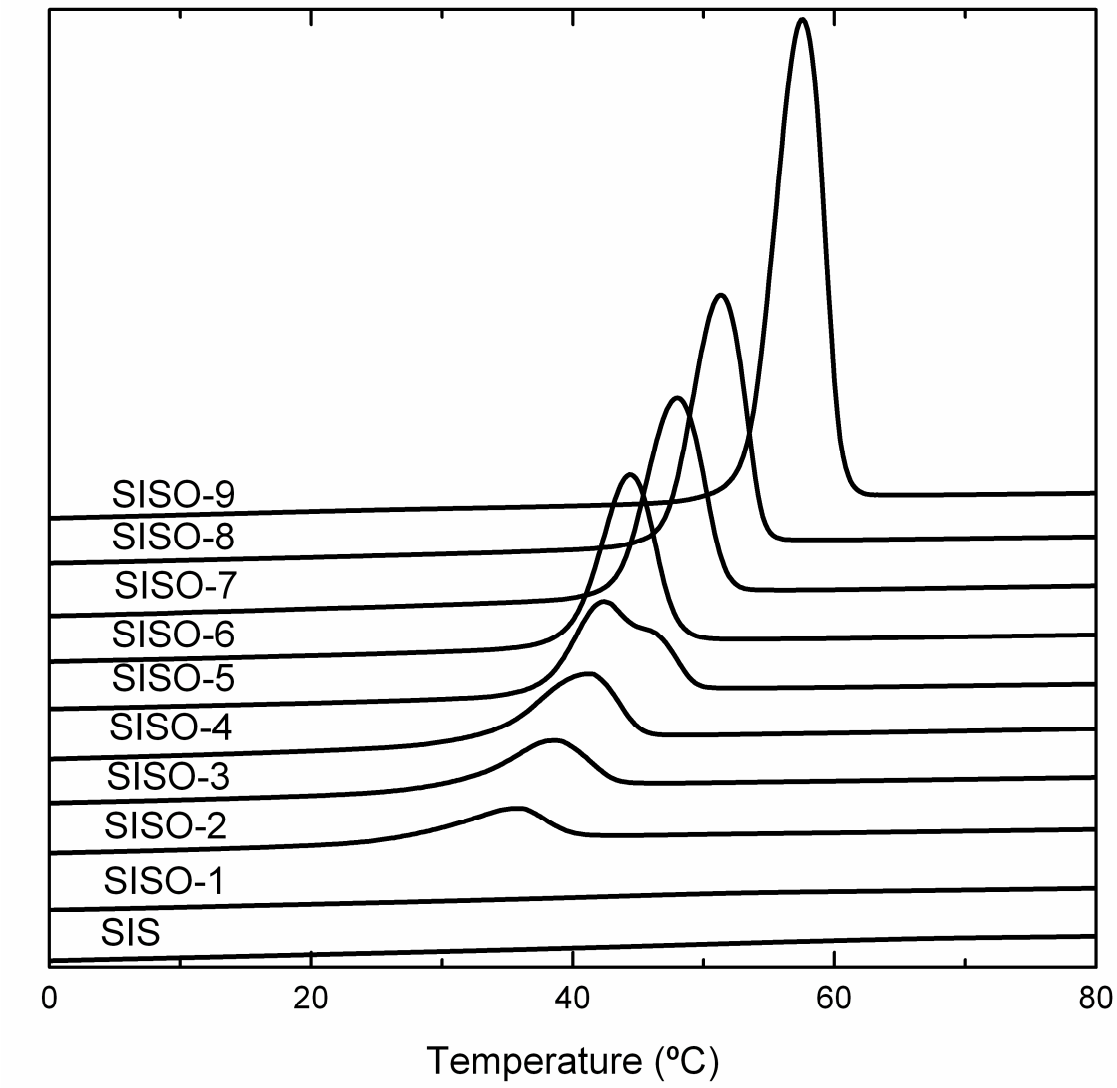

Figure 6.7: DSC endotherms near the melting point of O for the SIS triblock and SISO tetrablocks examined in this work. Tetrablocks possessing ordered microstructures display melting peaks of semicrystalline O block. Curves have been shifted vertically for clarity.

that core-shell structures are formed in the ordered samples (f_O > 0.07). Transition from the disordered state to the LLP sphere phase is associated with a significant increase in O crystallinity (from 0% in SISO-1 to 30% in SISO-2, Table 6.1) consistent with at least partial segregation of the S and O blocks. The amount of crystallinity increases with f_O up to a value of 50 to 64% in the HEX phase region. This level of crystallinity is similar to that reported by Bailey *et al*. in a series of ISO triblock terpolymers with well-segregated O domains.[16]

Core-shell structures are favorable due to the block sequence and segment-segment interactions ($\chi_{IO} > \chi_{IS} \cong \chi_{SO}$, see Figure 6.8) present in SISO. Addition of a short O chain to the SIS triblock (SISO-1, f_O = 0.04) does not disrupt the state of disorder above 80 ºC. Increasing the O block length (SISO-2, f_O = 0.07) induces microphase separation, driven primarily by unfavorable interactions between the I and O blocks, and to a lesser extent the S and I blocks. Core (O)-shell (S) microstructures are able to utilize S as an insulating barrier between highly unfavorable I/O contacts while maintaining the chain connectivity dictated by the SISO molecular architecture. For samples with lower O content (SISO-2, SISO-3, and SISO-4, f_O = 0.07 – 0.09), the observed core-shell particles are spheres (see Figure 6.9). Increasing the O chain length (f_O = 0.12 and higher) reduces the O domain curvature driving a transition to core-shell cylinders as depicted in Figure 6.9. The packing constraints of the asymmetric SISO molecules are satisfied by embedding the minority O within shells of S in a matrix of I. These core-shell phases minimize the chain stretching penalty associated with the S chains that must span the S/O and S/I interfaces

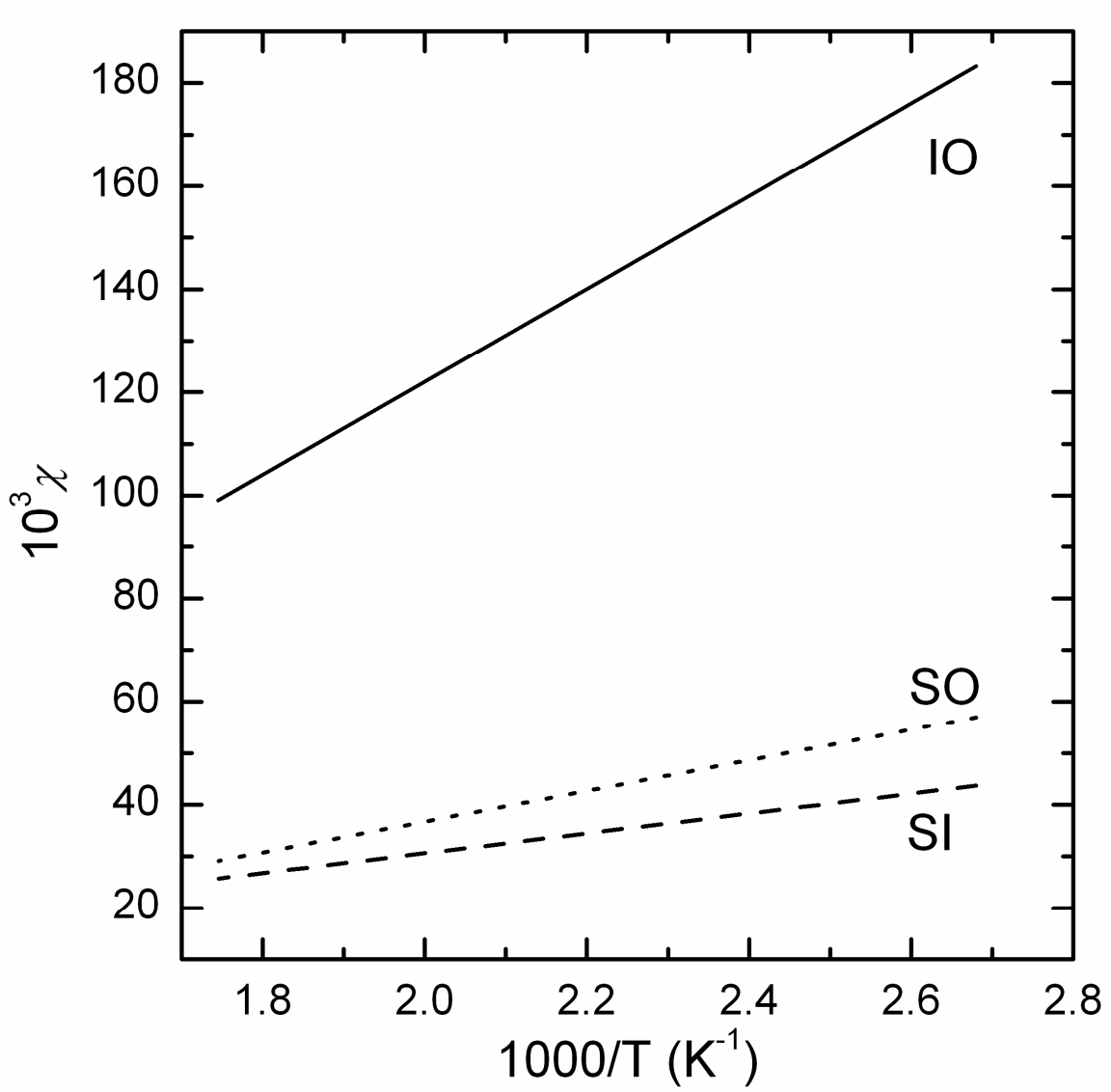

Figure 6.8: Comparison of binary interaction parameters as a function of temperature in the SISO system. Correlations are taken from previously published results.[46,47]

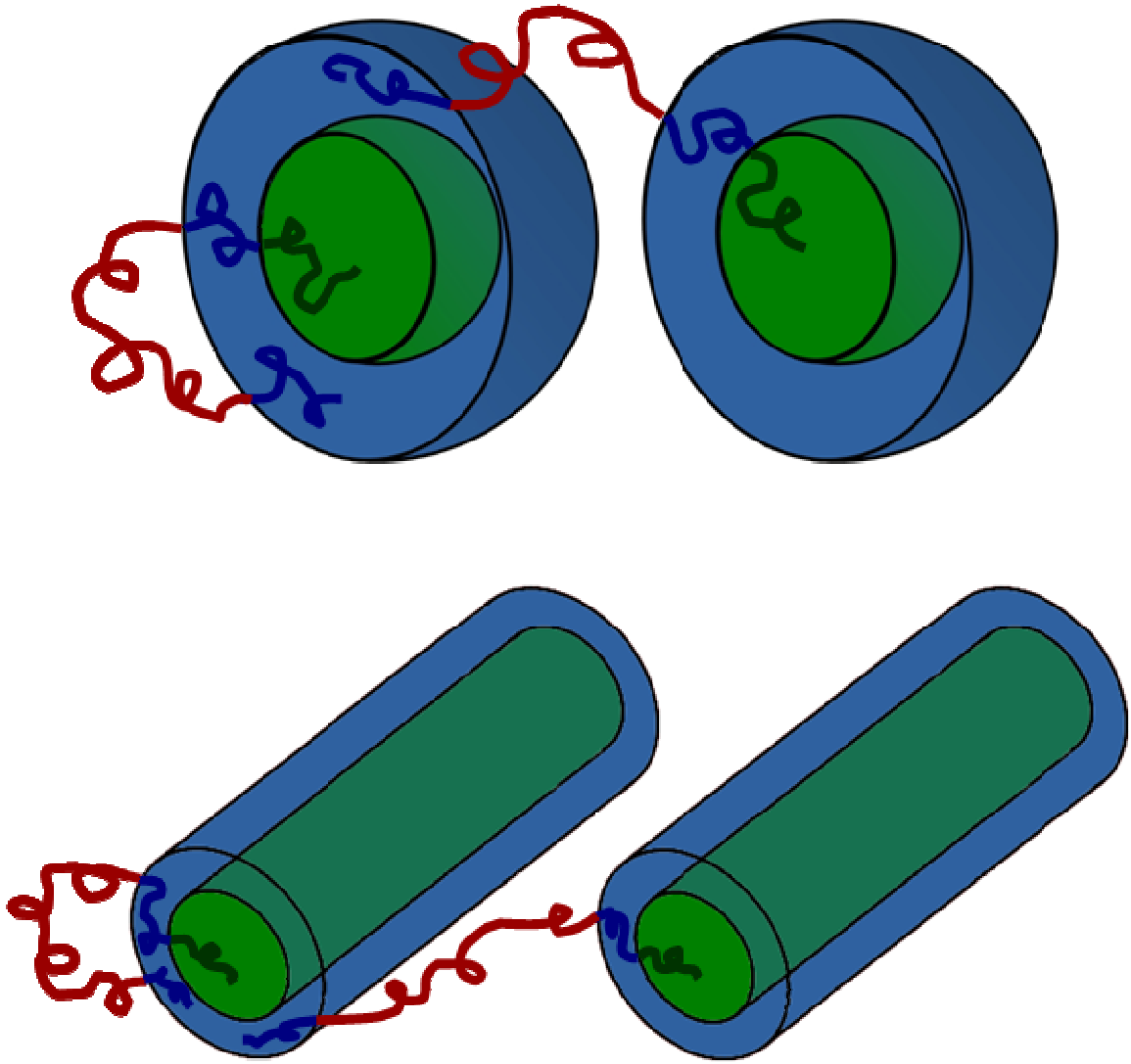

Figure 6.9: Schematic representations of inverted structures observed in this work. Red, blue, and green represent I, S, and O, respectively. With $0.07 \leq f_O \leq 0.09$, SISO self-assembles into core (O)-shell (S) spheres with the minority I forming the matrix. Increasing the O content ($0.12 \leq f_O \leq 0.30$) leads to core (O)-shell (S) cylinders.

(half of the S blocks) while I chains are free to adopt looping and bridging configurations (see Figure 6.9).

The core-shell morphologies documented in SISO differ dramatically from the equilibrium microstructures identified in ISO triblocks with comparable compositions. An orthorhombic network structure (O^{70}) possessing *Fddd* symmetry was found to be stable over a wide range of O content ($0.13 \leq f_O \leq 0.24$) along the $f_I = f_S$ isopleth. Like the double gyroid morphology, the O^{70} phase is constructed of trivalent connectors, but possesses lower symmetry. Two- and three-domain lamellae phases bracketed the multiply continuous O^{70} region at lower and higher f_O, respectively.[16,18] Changing the molecular architecture from ISO to SISO drives a preference from the hyperbolic interfaces inherent in network morphologies, like O^{70}, to the higher, and zero Gauss, curvature surfaces present in spheres and cylinders.

A core (O)-shell (S) cylinder microstructure is favored even when f_O approaches f_I and f_S, which is the case for SISO-9 ($f_O = 0.30$). A similar inverted cylindrical phase, where a minority component forms the continuous domain, has been identified in SIO,[15] poly(isoprene-*b*-styrene-*b*-dimethylsiloxane),[48] and diblock/triblock copolymer blends.[49] Extensive characterization of the phase behavior of ISO over a wide range of compositions has not yielded similar structures. In the previous examples of inverted cylindrical phases, the segment-segment interaction parameters are asymmetric ($\chi_{BC} > \chi_{AB} \cong \chi_{AC}$), whereas this is not the case for ISO ($\chi_{AC} > \chi_{AB} \cong \chi_{BC}$). Inverted phases have also been documented in block copolymer thin films as non-equilibrium morphologies generated by casting from solvents that were selective towards the minor component. He

and coworkers identified inverted spheres and cylinders in poly(styrene-*b*-butadiene) (SB), poly(styrene-*b*-methyl methacrylate) and SBS triblock copolymer films.[50-54] While the phase behavior of these systems is fascinating, the kinetically trapped morphologies are highly-dependent on the solvent, evaporation rate, and molecular weight of the block polymer making them impractical for many applications.

Modification of molecular architecture to produce ABAC tetrablocks has the potential to produce ordered morphologies in new areas of composition space. Determining the specific effects of the asymmetric placement of A blocks in the ABAC architecture will require further experimental and theoretical studies. We have shown that SISO has qualitatively different phase behavior compared to ISO at identical compositions and similar segregation strengths. While ISO samples formed a three-dimensional, orthorhombic network microstructure over a wide range of f_O, inverted spherical and cylindrical morphologies were discovered in SISO. An investigation of complementary asymmetric SISO isopleths is currently underway.

6.5 Conclusion

In this chapter we have described the synthesis and morphological characterization of a series of linear poly(styrene-*b*-isoprene-*b*-styrene-*b*-ethylene oxide) (SISO) tetrablock terpolymer melts. Growth of ethylene oxide from a single disordered, symmetric SIS yielded nine tetrablocks that varied only in the O chain length (0 to 30% O by volume). Addition of sufficient O ($0.07 \leq f_O \leq 0.09$) resulted in microphase separation into core

(O)-shell (S) spherical particles with short-range order in the minority I matrix. A further increase in the O block length led to hexagonally-packed core (O)-shell (S) cylinders. These structural assignments were made on the basis of small-angle X-ray scattering, transmission electron microscopy, and dynamic mechanical spectroscopy experiments. The development of these atypical, inverted morphologies is due to the molecular architecture and χ interaction parameter sequencing in the SISO system.

Acknowledgement. I greatly appreciate the assistance and guidance that Dr. Adam J. Meuler provided in synthesizing these materials. I also thank Dr. Steven Weigand and Dr. Denis Keane at DND-CAT at the Advanced Photon Source for setting up the experimental equipment used to acquire the SAXS data presented in this chapter.

6.6 References

(1) Bates, F. S.; Fredrickson, G. H. *Phys. Today* **1999**, *52*, 32-38.

(2) Lodge, T. P. *Macromol. Chem. Phys.* **2003**, *204*, 265-273.

(3) Takenaka, M.; Wakada, T.; Akasaka, S.; Nishitsuji, S.; Saijo, K.; Shimizu, H.; Kim, M. I.; Hasegawa, H. *Macromolecules* **2007**, *40*, 4399-4402.

(4) Kim, M. I.; Wakada, T.; Akasaka, S.; Nishitsuji, S.; Saijo, K.; Hasegawa, H.; Ito, K.; Takenaka, M. *Macromolecules* **2008**, *41*, 7667-7670.

(5) Matsen, M. W.; Bates, F. S. *J. Polym. Sci. Part B* **1997**, *35*, 945-952.

(6) Matsen, M. W. *Phys. Rev. Lett.* **2007**, *99*, 148304/1-148304/4.

(7) Mogi, Y.; Kotsuji, H.; Kaneko, Y.; Mori, K.; Matsushita, Y.; Noda, I. *Macromolecules* **1992**, *25*, 5408-5411.

(8) Gido, S. P.; Schwark, D. W.; Thomas, E. L.; do Carmo Goncalves, M. *Macromolecules* **1993**, *26*, 2636-2640.

(9) Mogi, Y.; Nomura, M.; Kotsuji, H.; Ohnishi, K.; Matsushita, Y.; Noda, I. *Macromolecules* **1994**, *27*, 6755-6760.

(10) Stadler, R.; Auschra, C.; Beckmann, J.; Krappe, U.; Voight-Martin, I.; Leibler, L. *Macromolecules* **1995**, *28*, 3080-3097.

(11) Breiner, U.; Krappe, U.; Abetz, V.; Stadler, R. *Macromol. Chem. Phys.* **1997**, *198*, 1051-1083.

(12) Breiner, U.; Krappe, U.; Thomas, E. L.; Stadler, R. *Macromolecules* **1998**, *31*, 135-141.

(13) Brinkmann, S.; Stadler, R.; Thomas, E. L. *Macromolecules* **1998**, *31*, 6566-6572.

(14) Shefelbine, T. A.; Vigild, M. E.; Matsen, M. W.; Hajduk, D. A.; Hillmyer, M. A.; Cussler, E. L.; Bates, F. S. *J. Am. Chem. Soc.* **1999**, *121*, 8457-8465.

(15) Bailey, T. S.; Pham, H. D.; Bates, F. S. *Macromolecules* **2001**, *34*, 6994-7008.

(16) Bailey, T. S.; Hardy, C. M.; Epps, T. H.,III; Bates, F. S. *Macromolecules* **2002**, *35*, 7007-7017.

(17) Avgeropoulos, A.; Paraskeva, S.; Hadjichristidis, N.; Thomas, E. L. *Macromolecules* **2002**, *35*, 4030-4035.

(18) Epps, T. H.,III; Cochran, E. W.; Bailey, T. S.; Waletzko, R. S.; Hardy, C. M.; Bates, F. S. *Macromolecules* **2004**, *37*, 8325-8341.

(19) Zheng, W.; Wang, Z. *Macromolecules* **1995**, *28*, 7215-7223.

(20) Epps, T. H.,III; Bailey, T. S.; Pham, H. D.; Bates, F. S. *Chem. Mater.* **2002**, *14*, 1706-1714.

(21) Epps, T. H.,III; Bailey, T. S.; Waletzko, R.; Bates, F. S. *Macromolecules* **2003**, *36*, 2873-2881.

(22) Bailey, T. S.; Rzayev, J.; Hillmyer, M. A. *Macromolecules* **2006**, *39*, 8772-8781.

(23) Phillip, W. A.; Rzayev, J.; Hillmyer, M. A.; Cussler, E. L. *J. Membr. Sci.* **2006**, *286*, 144-152.

(24) Rzayev, J.; Hillmyer, M. A. *J. Am. Chem. Soc.* **2005**, *127*, 13373–13379.

(25) Bang, J.; Kim, S. H.; Drockenmuller, E.; Misner, M. J.; Russell, T. P.; Hawker, C. J. *J. Am. Chem. Soc.* **2006**, *128*, 7622-7629.

(26) Bluemle, M. J.; Fleury, G.; Lodge, T. P.; Bates, F. S. *Soft Matter* **2009**, *5*, 1587-1590.

(27) Hillmyer, M. A.; Bates, F. S. *Macromolecules* **1996**, *29*, 6994-7002.

(28) Singh, M.; Odusanya, O.; Wilmes, G. M.; Eitouni, H. B.; Gomez, E. D.; Patel, A. J.; Chen, V. L.; Park, M. J.; Fragouli, P.; Iatrou, H.; Hadjichristidis, N.; Cookson, D.; Balsara, N. P. *Macromolecules* **2007**, *40*, 4578-4585.

(29) Chatterjee, J.; Jain, S.; Bates, F. S. *Macromolecules* **2007**, *40*, 2882-2896.

(30) Ndoni, S.; Papadakis, C. M.; Bates, F. S.; Almdal, K. *Rev. Sci. Instrum.* **1995**, *66*, 1090-1095.

(31) Quirk, R. P.; Ma, J. J. *J. Polym. Sci. Part A* **1988**, *26*, 2031-2037.

(32) Davis, K. P. *Ph.D. Dissertation*; University of Minnesota **2009**, 1-270.

(33) Fetters, L. J.; Lohse, D. J.; Richter, D.; Witten, T. A.; Zirkel, A. *Macromolecules* **1994**, *27*, 4639-4647.

(34) Brandrup, J., Immergut, E. H. *Polymer Handbook*, Wiley: New York, 1989.

(35) Kinning, D. J.; Thomas, E. L. *Macromolecules* **1984**, *17*, 1712-1718.

(36) Winey, K. I.; Thomas, E. L.; Fetters, L. J. *Macromolecules* **1992**, *25*, 2645-2650.

(37) Schwab, M.; Stuehn, B. *Phys. Rev. Lett.* **1996**, *76*, 924-927.

(38) Adams, J. L.; Quiram, D. J.; Graessley, W. W.; Register, R. A.; Marchand, G. R. *Macromolecules* **1996**, *29*, 2929-2938.

(39) Sakamoto, N.; Hashimoto, T.; Han, C. D.; Kim, D.; Vaidya, N. Y. *Macromolecules* **1997**, *30*, 1621-1632.

(40) Han, C. D.; Vaidya, N. Y.; Kim, D.; Shin, G.; Yamaguchi, D.; Hashimoto, T. *Macromolecules* **2000**, *33*, 3767-3780.

(41) Dormidontova, E. E.; Lodge, T. P. *Macromolecules* **2001**, *34*, 9143-9155.

(42) Wang, X.; Dormidontova, E. E.; Lodge, T. P. *Macromolecules* **2002**, *35*, 9687-9697.

(43) Bates, F. S.; Cohen, R. E.; Berney, C. V. *Macromolecules* **1982**, *15*, 589-592.

(44) Kossuth, M. B.; Morse, D. C.; Bates, F. S. *J. Rheol.* **1999**, *43*, 167-196.

(45) Cavicchi, K. A.; Lodge, T. P. *J. Polym. Sci., Part B: Polym. Phys.* **2003**, *41*, 715-724.

(46) Hashimoto, T.; Ijichi, Y.; Fetters, L. J. *J. Chem. Phys.* **1988**, *89*, 2463.

(47) Frielinghaus, H.; Hermsdorf, N.; Almdal, K.; Mortensen, K.; Messe, L.; Corvazier, L.; Fairclough, J. P. A.; Ryan, A. J.; Olmsted, P. D.; Hamley, I. W. *Europhys. Lett.* **2001**, *53*, 680-686.

(48) Hardy, C. M.; Bates, F. S.; Kim, M.; Wignall, G. D. *Macromolecules* **2002**, *35*, 3189-3197.

(49) Goldacker, T.; Abetz, V. *Macromolecules* **1999**, *32*, 5165-5167.

(50) Zhang, Q.; Tsui, O. K. C.; Du, B.; Zhang, F.; Tang, T.; He, T. *Macromolecules* **2000**, *33*, 9561-9567.

(51) Huang, H.; Zhang, F.; Hu, Z.; Du, B.; He, T.; Lee, F. K.; Wang, Y.; Tsui, O. K. C. *Macromolecules* **2003**, *36*, 4084-4092.

(52) Huang, H.; Hu, Z.; Chen, Y.; Zhang, F.; Gong, Y.; He, T.; Wu, C. *Macromolecules* **2004**, *37*, 6523-6530.

(53) Gong, Y.; Huang, H.; Hu, Z.; Chen, Y.; Chen, D.; Wang, Z.; He, T. *Macromolecules* **2006**, *39*, 3369-3376.

(54) Chen, Y.; Wang, Z.; Gong, Y.; Huang, H.; He, T. *J. Phys. Chem. B* **2006**, *110*, 1647-1655.

7

Conclusions

7.1 Summary of Results

The work presented in this thesis was focused on identifying the effects of molecular architecture on phase behavior in ABAC tetrablock terpolymers. Two tetrablock systems were synthesized and characterized: poly(cyclohexylethylene-*b*-ethylene-*b*-cyclohexyl-ethylene-*b*-dimethylsiloxane) (CECD) and poly(styrene-*b*-isoprene-*b*-styrene-*b*-ethylene oxide) (SISO). In all cases, the C (S) compositions were divided evenly between the two C (S) blocks, simulating the effect of splitting the middle block of a triblock terpolymer in half to produce a tetrablock terpolymer (see Figure 7.1). Varying the ratios of the first and third block compositions is an additional design parameter in ABAC tetrablock systems. Future work with a series of ABA′C terpolymers in which $\frac{f_A}{f_A + f_{A'}}$ was varied from 0 to 1 would help elucidate the subtle factors that influence phase behavior between a nonfrustrated BA′C triblock to a frustrated ABC terpolymer.

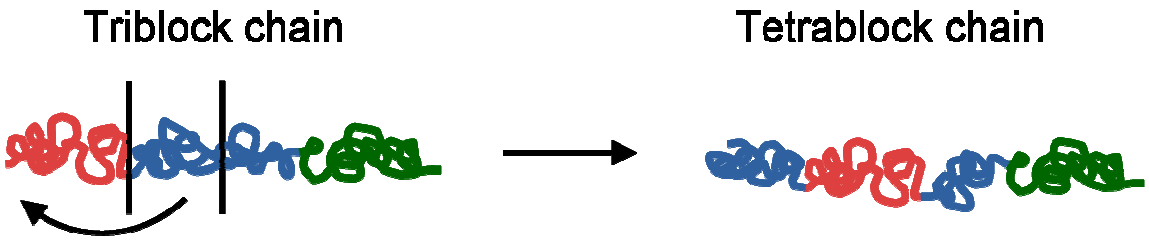

Figure 7.1: Illustration of cutting the middle block of a triblock terpolymer in half to produce a tetrablock terpolymer with the same composition.

Before investigating the morphological behavior of CECD tetrablock terpolymers, a series of ECD triblocks and binary blends were synthesized and characterized, as discussed in Chapter 3. The ECD system is "nonfrustrated" following the classification system developed by Bailey.[1] E/D interfaces are the most energetically unfavorable ($\chi_{EC} \cong \chi_{CD} < \chi_{ED}$), but are not required by the chain connectivity of the molecule. Extensive research with the nonfrustrated ISO system established an expansive window of network phases in these materials. Along the $f_I = f_S$ isopleth, the orthorhombic network O^{70}, possessing *Fddd* symmetry, was identified when $0.13 \leq f_O \leq 0.24$.[2,3] At lower and higher O content, two- and three-domain lamellar phases were observed. Prior to the observation of O^{70} in the ISO system, the only known network morphologies in block polymers were cubic, the alternating[4] and double gyroids,[5-8] which are composed of symmetric, three-fold connectors. The ISO triblock terpolymer system demonstrated that the lower symmetry O^{70} morphology could best accommodate the symmetric I/S and asymmetric S/O interfaces by creating interfaces with varying curvature. Altering the I to S composition ratio, produced the alternating gyroid (Q^{214}, $f_S > f_I$) and double gyroid (Q^{230},

$f_I > f_S$) morphologies at comparable O compositions. With the findings elucidated from the ISO system in mind, the phase behavior of ECD triblocks along the $f_E = f_C$ isopleth were characterized using small-angle X-ray scattering (SAXS), transmission electron microscopy (TEM), and dynamic mechanical spectroscopy (DMS). While O^{70} was identified in ECD, it was over a small range of temperature and composition space compared to ISO. This observation is discussed in more depth in the following section. In addition to O^{70} and lamellae, spheres-in-lamellae structures were observed in the ECD triblocks. These complex morphologies were induced by the microphase separation of D into spheres, which were embedded in the C lamellae. In two samples, order-order transitions were observed between hexagonally packed spheres-in-lamellae to O^{70} with increasing temperature.

In Chapter 4, the phase behavior of CECD tetrablock terpolymers along the symmetric $f_E = f_C$ isopleth was investigated. Along with LAM_2 and LAM_3, like the ECD triblocks, an ordered phase consisting of D spheres hexagonally packed within the C layers of the C/E lamellar structure was identified on the basis of SAXS and TEM. However, unlike the ECD triblocks, O^{70}, or any other network structure, was conclusively identified.

Chapter 5 also focused on the morphological behavior of CECD tetrablocks. A sequence of CECD terpolymers along an asymmetric isopleth (f_C/f_E = 3/7) was synthesized and characterized in a similar manner as the previous two chapters. Situated between hexagonally packed cylindrical phases (mixed C and D cylinders at low D content and core (D)-shell (C) cylinders at high D composition), an orthorhombic

network morphology, O^{52}, possessing *Pnna* symmetry was identified. This phase assignment was made largely on two-dimensional SAXS results obtained from a single crystal-like sample after large amplitude oscillatory shear. TEM micrographs of unstained samples displayed spherical domains of D, clearly segregated from the C and E blocks. After staining with ruthenium tetroxide, TEM images of the O^{52} morphology revealed an intricate microstructure consistent with D embedded in C domains, which were surrounded by E. We attributed the stability of the O^{52} network structure to the placement of the D spheres at the nodes of the three-fold junctions.

The phase behavior of a second tetrablock terpolymer system, SISO, was investigated in Chapter 6. SISO has a few inherent advantages over the CECD system. A series of SISO tetrablocks differing only in f_O can be efficiently generated by re-initiation and growth of O from a hydroxyl-terminated SIS triblock.[9,10] This procedure greatly reduces the laborious synthesis of multiblock polymers and eliminates differences in batch to batch molecular weight (besides the O block). Additionally, ISO is a well-studied system,[2,3,11] which makes SISO ideal for identifying differences in phase behavior due to chain architecture alone. A series of SISO tetrablocks along the symmetric $f_I = f_S$ isopleth was prepared. Two ordered morphologies were observed on the basis of SAXS and TEM: core (O)-shell (S) spheres with liquid-like packing ($0.07 \leq f_O \leq 0.09$) and core (O)-shell (S) hexagonally packed cylinders ($0.12 \leq f_O \leq 0.30$). These two inverted phases (the minority I forms the matrix) have not been identified in ISO at any composition. ISO samples with comparable compositions have been found to form LAM_2, O^{70}, or LAM_3.

The strikingly different morphological behavior in the ISO and SISO systems is a result of the SISO chain architecture.

7.2 Universality of ABC Triblock Terpolymer Phase Behavior

Epps *et al*. postulated that, like AB diblock copolymers, nonfrustrated ABC triblock terpolymers would display qualitatively similar phase behavior.[3] However, as Tyler *et al*. suggested with self-consistent field theory (SCFT) calculations,[12] phase boundaries are quite sensitive to variations in block statistical segment lengths and interaction parameters from one system to another. Thus, it is not surprising that when we map the two ECD samples from Chapter 3 in which O^{70} was observed, Blend D and ECD-5, onto the experimentally determined ISO phase portrait[3] (black diamonds in Figure 7.2), we do not find perfect agreement. ISO specimens with comparable compositions to the ECD triblocks formed LAM_3. This suggests that the stable O^{70} window is located at higher D compositions. In Table 7.1, the volume fractions, segment-segment segregation strengths (χN), and statistical segment lengths (b) for four O^{70} triblock terpolymers are listed. The segregation strength sequencing is similar for all four cases (these are nonfrustrated systems). However, the statistical segment length sequencing exhibits some differences. SID is nearly conformationally symmetric ($b_A \sim b_B \sim b_C$). For ISO and CE_EE, $b_A \sim b_B < b_C$. ECD switches this relationship, $b_A > b_B \sim b_C$, resulting in a different sequence of statistical lengths.

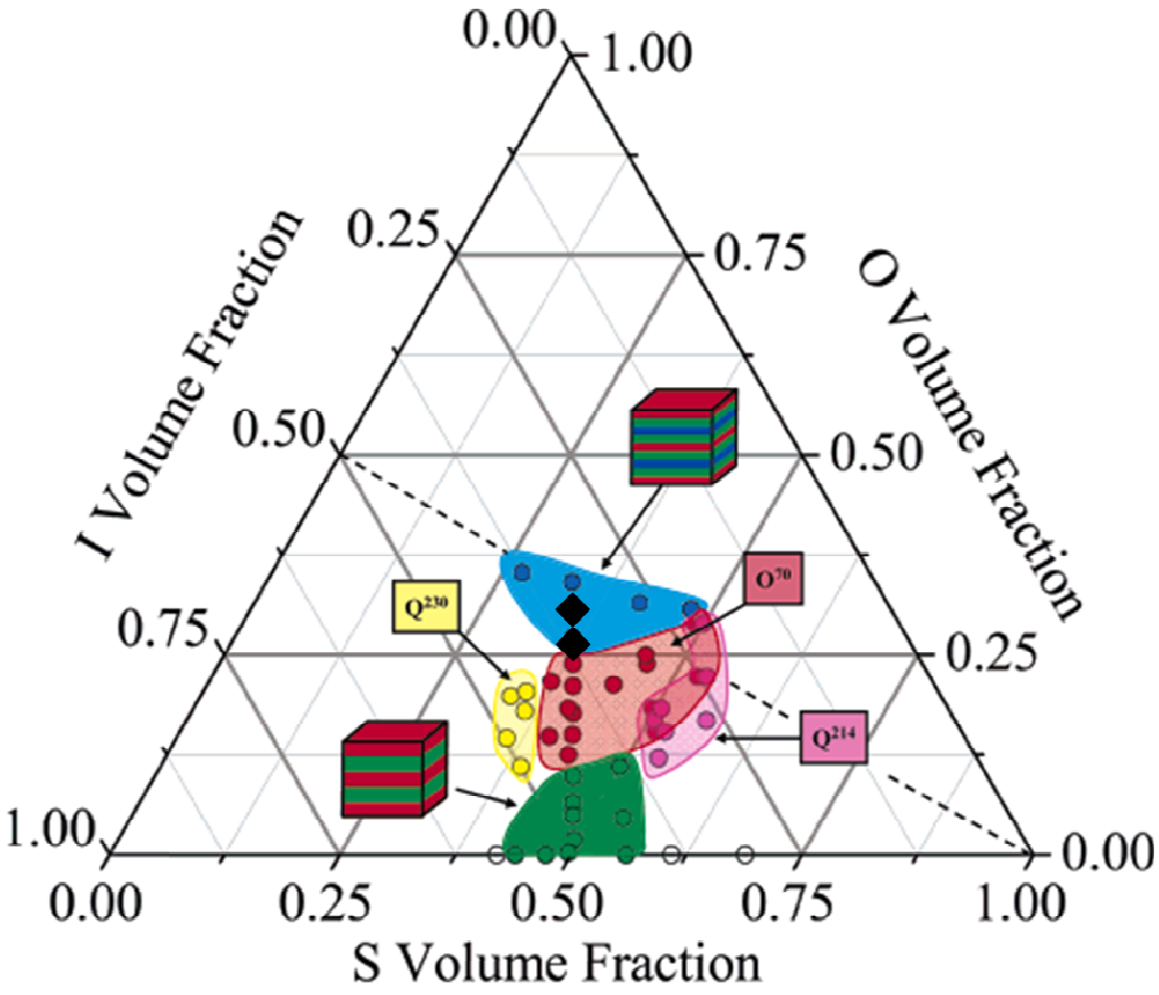

Figure 7.2: Poly(isoprene-*b*-styrene-*b*-ethylene oxide) phase portrait reproduced from Epps *et al*.[3] The two black diamonds represent Blend E and ECD-5 from Chapter 3.

Table 7.1: Comparison of molecular characteristics of O^{70}-forming ABC triblocks.

	f_A	f_B	f_C	$\chi_{AB}N^e$	$\chi_{BC}N^e$	$\chi_{AC}N^e$	$b_{A,}$ Å^f	$b_{B,}$ Å^f	$b_{C,}$ Å^f
ECD-5[a]	0.36	0.36	0.28	10.6	16.7	22.3	8.35	4.60	5.39
ISO-3h[b]	0.41	0.41	0.18	8.3	11.9	38.8	6.07	5.47	7.80
CE_EE-3[c]	0.25	0.50	0.25	8.3	11.4	24.7	4.60	5.39	8.35
SID-11[d]	0.31	0.40	0.29	4.4	13.3	29.3	5.47	6.07	5.39

[a]Poly(ethylene-*b*-cyclohexylethylene-*b*-dimethylsiloxane) discussed in Chapter 3 of this work.

[b]Poly(isoprene-*b*-styrene-*b*-ethylene oxide) published by Bailey *et al.*[2] and Epps *et al.*[3]

[c]Poly(cyclohexylethylene-*b*-ethylethylene-*b*-ethylene) published by Cochran and Bates.[13]

[d]Poly(styrene-*b*-isoprene-*b*-dimethylsiloxane) synthesized by Hardy[14] and characterized by Cochran.[15]

[e]Segregation strengths calculated at 220, 160, 178, and 200 ºC for ECD-5, ISO-3h, CE_EE-3, and SID-11, respectively.

[f]Obtained from Fetters *et al.*[16]

The experimental results generated from ECD triblock terpolymers, taken with the previously studied ISO system, indicate that the classification of ABC triblock terpolymers as nonfrustrated is sufficient to only broadly describe the type of phases that are stable. Only morphologies that do not form A/C interfaces have been observed in nonfrustrated triblock systems. However, from a geometric standpoint there are many ways to accomplish this. Over a wide range of composition space in the ISO system, network phases (Q^{230}, Q^{214}, and O^{70}) with hyperbolic interfacial surfaces have been identified as the most energetically favorable. The presence of the spheres-in-lamellae phases documented in ECD suggests another way to satisfy the competing symmetric E/C

and asymmetric C/D interfaces. Future SCFT calculations incorporating the block statistical segment lengths and interaction parameters of the ECD system may find the spheres-in-lamellae morphologies to be stable over some region of composition space. Isolating the effects of differences in statistical segment lengths or interaction parameters will require continued experimental and theoretical work.

7.3 Influence of ABAC Chain Architecture on Phase Behavior

As documented in Chapters 4, 5, and 6, the ABAC chain architecture induces qualitatively different phase behavior when compared to similar triblock terpolymers. Several similarities were identified in the two tetrablock terpolymer systems investigated in this work. D blocks formed spherical domains at moderate compositions, either embedded in C layers or at the nodes of three-fold connectors in the O^{52} network morphology. A core (O)-shell (S) spherical morphology was also observed in SISO samples when $0.07 \leq f_O \leq 0.09$. Spherical domains of the terminal chain (D or O) with a high degree of curvature are favorable due to the asymmetry in block compositions (C versus D or S versus O). With increased terminal block length, the asymmetry decreases resulting in core-shell cylinders with a smaller interfacial curvature in the SISO and the asymmetric CECD tetrablocks. Similar structures have not been observed in the extensively-studied ISO system or any other nonfrustrated triblock terpolymer. The hyperbolic (negative Gauss curvature) surfaces inherent to network morphologies appear to be a universal feature of nonfrustrated triblocks. The asymmetric positioning of the A

block in ABAC tetrablock terpolymers evidently disrupts the sensitive free energy balance that determines morphological behavior.

7.4 References

(1) Bailey, T. S. *Ph.D. Dissertation*; University of Minnesota **2001**, 1-211.

(2) Bailey, T. S.; Hardy, C. M.; Epps, T. H.,III; Bates, F. S. *Macromolecules* **2002**, *35*, 7007-7017.

(3) Epps, T. H.,III; Cochran, E. W.; Bailey, T. S.; Waletzko, R. S.; Hardy, C. M.; Bates, F. S. *Macromolecules* **2004**, *37*, 8325-8341.

(4) Mogi, Y.; Mori, K.; Matsushita, Y.; Noda, I. *Macromolecules* **1992**, *25*, 5412-5415.

(5) Hajduk, D. A.; Harper, P. E.; Gruner, S. M.; Honeker, C. C.; Kim, G.; Thomas, E. L.; Fetters, L. J. *Macromolecules* **1994**, *27*, 4063-4075.

(6) Schulz, M. F.; Bates, F. S.; Almdal, K.; Mortensen, K. *Phys. Rev. Lett.* **1994**, *73*, 86-89.

(7) Shefelbine, T. A.; Vigild, M. E.; Matsen, M. W.; Hajduk, D. A.; Hillmyer, M. A.; Cussler, E. L.; Bates, F. S. *J. Am. Chem. Soc.* **1999**, *121*, 8457-8465.

(8) Hueckstaedt, H.; Goldacker, T.; Goepfert, A.; Abetz, V. *Macromolecules* **2000**, *33*, 3757-3761.

(9) Hillmyer, M. A.; Bates, F. S. *Macromolecules* **1996**, *29*, 6994-7002.

(10) Bailey, T. S.; Pham, H. D.; Bates, F. S. *Macromolecules* **2001**, *34*, 6994-7008.

(11) Chatterjee, J.; Jain, S.; Bates, F. S. *Macromolecules* **2007**, *40*, 2882-2896.

(12) Tyler, C. A.; Qin, J.; Bates, F. S.; Morse, D. C. *Macromolecules* **2007**, *40*, 4654-4668.

(13) Cochran, E. W.; Bates, F. S. *Phys. Rev. Lett.* **2004**, *93*, 087802/1-087802/4.

(14) Hardy, C. M. *Ph.D. Dissertation*; University of Minnesota **2003**, 1-249.

(15) Cochran, E. W. *Ph.D. Dissertation*; University of Minnesota **2004**, 1-316.

(16) Fetters, L. J.; Lohse, D. J.; Richter, D.; Witten, T. A.; Zirkel, A. *Macromolecules* **1994**, *27*, 4639-4647.

Bibliography

Abetz, V.; Simon, P. F. W. *Adv. Polym. Sci.* **2005**, *189*, 125-212.

Adams, J. L.; Quiram, D. J.; Graessley, W. W.; Register, R. A.; Marchand, G. R. *Macromolecules* **1996**, *29*, 2929-2938.

Ahn, J. H.; Zin, W. C. *Macromolecules* **2000**, *33*, 641-644.

Almdal, K.; Bates, F. S.; Mortensen, K. *J. Chem. Phys.* **1992**, *96*, 9122-9132.

Almdal, K.; Hillmyer, M. A.; Bates, F. S. *Macromolecules* **2002**, *35*, 7685-7691.

Almdal, K.; Mortensen, K.; Koppi, K. A.; Tirrell, M.; Bates, F. S. *J. Phys. II* **1996**, *6*, 617-637.

Almdal, K.; Rosedale, J. H.; Bates, F. S. *Macromolecules* **1990**, *23*, 4336-4338.

Alward, D. B.; Kinning, D. J.; Thomas, E. L.; Fetters, L. J. *Macromolecules* **1986**, *19*, 215-224.

Angelescu, D. E.; Waller, J. H.; Register, R. A.; Chaikin, P. M. *Adv. Mater.* **2005**, *17*, 1878-1880.

Arai, K.; Kotaka, T.; Kitano, Y.; Yoshimura, K. *Macromolecules* **1980**, *13*, 455-457.

Arai, K.; Ueda-Mashima, C.; Kotaka, T.; Yoshimura, K.; Murayama, K. *Polymer* **1984**, *25*, 230-238.

Auschra, C.; Stadler, R. *Macromolecules* **1993**, *26*, 2171-2174.

Avgeropoulos, A.; Dair, B. J.; Hadjichristidis, N.; Thomas, E. L. *Macromolecules* **1997**, *30*, 5634-5642.

Avgeropoulos, A.; Paraskeva, S.; Hadjichristidis, N.; Thomas, E. L. *Macromolecules* **2002**, *35*, 4030-4035.

Bailey, T. S. *Ph.D. Dissertation*; University of Minnesota **2001**, 1-211.

Bailey, T. S.; Hardy, C. M.; Epps, T. H.,III; Bates, F. S. *Macromolecules* **2002**, *35*, 7007-7017.

Bailey, T. S.; Pham, H. D.; Bates, F. S. *Macromolecules* **2001**, *34*, 6994-7008.

Bailey, T. S.; Rzayev, J.; Hillmyer, M. A. *Macromolecules* **2006**, *39*, 8772-8781.

Balsamo, V.; Gil, G.; Urbina de Navarro, C.; Hamley, I. W.; Von Gyldenfeldt, F.; Abetz, V.; Canizales, E. *Macromolecules* **2003**, *36*, 4515-4525.

Balsamo, V.; von Gyldenfeldt, F.; Stadler, R. *Macromolecules* **1999**, *32*, 1226-1232.

Bang, J.; Kim, S. H.; Drockenmuller, E.; Misner, M. J.; Russell, T. P.; Hawker, C. J. *J. Am. Chem. Soc.* **2006**, *128*, 7622-7629.

Bates, F. S. *Science* **1991**, *251*, 898-905.

Bates, F. S.; Cohen, R. E.; Berney, C. V. *Macromolecules* **1982**, *15*, 589-592.

Bates, F. S.; Fredrickson, G. H. *Phys. Today* **1999**, *52*, 32-38.

Bates, F. S.; Rosedale, J. H.; Fredrickson, G. H. *J. Chem. Phys.* **1990**, *92*, 6255-6270.

Bates, F. S.; Schulz, M. F.; Khandpur, A. K.; Foerster, S.; Rosedale, J. H. *Faraday Discuss.* **1995**, *98*, 7-18.

Beckmann, J.; Auschra, C.; Stadler, R. *Macromol. Rapid Commun.* **1994**, *15*, 67-72.

Beletskaya, I. P.; Kashin, A. N.; Litvinov, A. E.; Tyurin, V. S.; Valetsky, P. M.; van Koten, G. *Organometallics* **2006**, *25*, 154-158.

Bluemle, M. J.; Fleury, G.; Lodge, T. P.; Bates, F. S. *Soft Matter* **2009**, *5*, 1587-1590.

Brandrup, J., Immergut, E. H. *Polymer Handbook*, Wiley: New York, 1989.

Breiner, U.; Krappe, U.; Abetz, V.; Stadler, R. *Macromol. Chem. Phys.* **1997**, *198*, 1051-1083.

Breiner, U.; Krappe, U.; Jakob, T.; Abetz, V.; Stadler, R. *Polym. Bull.* **1998**, *40*, 219-226.

Breiner, U.; Krappe, U.; Stadler, R. *Macromol. Rapid Commun.* **1996**, *17*, 567-575.

Breiner, U.; Krappe, U.; Thomas, E. L.; Stadler, R. *Macromolecules* **1998**, *31*, 135-141.

Brinkmann, S.; Stadler, R.; Thomas, E. L. *Macromolecules* **1998**, *31*, 6566-6572.

Brown, G. M.; Butler, J. H. *Polymer* **1997**, *38*, 3937-3945.

Campbell, D.; White, J. R. *Polymer Characterization: Physical Techniques;* Chapman and Hall: New York, 1989.

Cavicchi, K. A.; Lodge, T. P. *J. Polym. Sci. , Part B: Polym. Phys.* **2003**, *41*, 715-724.

Cavicchi, K. A.; Zalusky, A. S.; Hillmyer, M. A.; Lodge, T. P. *Macromol. Rapid Commun.* **2004**, *25*, 704-709.

Chatterjee, J.; Jain, S.; Bates, F. S. *Macromolecules* **2007**, *40*, 2882-2896.

Chen, J. C.; Feng, X.; Penlidis, A. *Sep. Sci. Technol.* **2004**, *39*, 149-164.

Chen, Y.; Wang, Z.; Gong, Y.; Huang, H.; He, T. *J. Phys. Chem. B* **2006**, *110*, 1647-1655.

Choi, Y.; Lee, S.; Lee, D.; Ishigami, Y.; Kajiuchi, T. *J. Membr. Sci.* **1998**, *148*, 185-194.

Cochran, E. W. *Ph.D. Dissertation*; University of Minnesota **2004**, 1-316.

Cochran, E. W.; Bates, F. S. *Macromolecules* **2002**, *35*, 7368-7374.

Cochran, E. W.; Bates, F. S. *Phys. Rev. Lett.* **2004**, *93*, 087802/1-087802/4.

Cochran, E. W.; Garcia-Cervera, C. J.; Fredrickson, G. H. *Macromolecules* **2006**, *39*, 2449-2451.

Dair, B. J.; Avgeropoulos, A.; Hadjichristidis, N.; Thomas, E. L. *J. Mater. Sci.* **2000**, *35*, 5207-5213.

Dair, B. J.; Honeker, C. C.; Alward, D. B.; Avgeropoulos, A.; Hadjichristidis, N.; Fetters, L. J.; Capel, M.; Thomas, E. L. *Macromolecules* **1999**, *32*, 8145-8152.

Daoulas, K. C.; Muller, M.; Stoykovich, M. P.; Park, S.; Papakonstantopoulos, Y. J.; de Pablo, J. J.; Nealey, P. F.; Solak, H. H. *Phys. Rev. Lett.* **2006**, *96*, 036104/1-036104/4.

Davis, K. P. *Ph.D. Dissertation*; University of Minnesota **2009**, 1-270.

De Gennes, P. G. *Faraday Discuss. Royal Soc. Chem.* **1979**, *68*, 96-102.

Dinnebier, R. E.; Billinge, S. J. L., Eds.; *Powder Diffraction: Theory and Practice;* The Royal Society of Chemistry: Cambridge, UK, 2008.

Dormidontova, E. E.; Lodge, T. P. *Macromolecules* **2001**, *34*, 9143-9155.

Edwards, E. W.; Stoykovich, M. P.; Muller, M.; Solak, H. H.; de Pablo, J. J.; Nealey, P. F. *J. Polym. Sci. Part B* **2005**, *43*, 3444-3459.

Epps, T. H.,III; Bailey, T. S.; Pham, H. D.; Bates, F. S. *Chem. Mater.* **2002**, *14*, 1706-1714.

Epps, T. H.,III; Bailey, T. S.; Waletzko, R.; Bates, F. S. *Macromolecules* **2003**, *36*, 2873-2881.

Epps, T. H.,III; Cochran, E. W.; Bailey, T. S.; Waletzko, R. S.; Hardy, C. M.; Bates, F. S. *Macromolecules* **2004**, *37*, 8325-8341.

Epps, T. H.,III; Cochran, E. W.; Hardy, C. M.; Bailey, T. S.; Waletzko, R. S.; Bates, F. S. *Macromolecules* **2004**, *37*, 7085-7088.

Fetters, L. J.; Lohse, D. J.; Richter, D.; Witten, T. A.; Zirkel, A. *Macromolecules* **1994**, *27*, 4639-4647.

Fielding-Russell, G. S.; Pillai, P. S. *Polymer* **1974**, *15*, 97-100.

Förster, S.; Khandpur, A. K.; Zhao, J.; Bates, F. S.; Hamley, I. W.; Ryan, A. J.; Bras, W. *Macromolecules* **1994**, *27*, 6922-6935.

Förster, S.; Timmann, A.; Schellbach, C.; Fromsdorf, A.; Kornowski, A.; Weller, H.; Roth, S. V.; Lindner, P. *Nat. Mater.* **2007**, *6*, 888-893.

Fredrickson, G. H.; Bates, F. S. *Annu. Rev. Mater. Sci.* **1996**, *26*, 501-550.

Fredrickson, G. H.; Helfand, E. *J. Chem. Phys.* **1987**, *87*, 697-705.

Frielinghaus, H.; Hermsdorf, N.; Almdal, K.; Mortensen, K.; Messe, L.; Corvazier, L.; Fairclough, J. P. A.; Ryan, A. J.; Olmsted, P. D.; Hamley, I. W. *Europhys. Lett.* **2001**, *53*, 680-686.

Gehlsen, M. D.; Almdal, K.; Bates, F. S. *Macromolecules* **1992**, *25*, 939-943.

Gido, S. P.; Schwark, D. W.; Thomas, E. L.; do Carmo Goncalves, M. *Macromolecules* **1993**, *26*, 2636-2640.

Goldacker, T.; Abetz, V. *Macromolecules* **1999**, *32*, 5165-5167.

Gong, Y.; Huang, H.; Hu, Z.; Chen, Y.; Chen, D.; Wang, Z.; He, T. *Macromolecules* **2006**, *39*, 3369-3376.

Gottlieb, H. E.; Kotlyar, V.; Nudelman, A. *J. Org. Chem.* **1997**, *62*, 7512-7515.

Hadjichristidis, N.; Iatrou, H.; Pispas, S.; Pitsikalis, M. *J. Polym. Sci. Part A* **2000**, *38*, 3211-3234.

Hadjichristidis, N.; Pitsikalis, M.; Iatrou, H. *Adv Polym Sci* **2005**, *189*, 1-124.

Hadjichristidis, N.; Pitsikalis, M.; Pispas, S.; Iatrou, H. *Chem. Rev.* **2001**, *101*, 3747-3792.

Hadziioannou, G.; Mathis, A.; Skoulios, A. *Colloid Polym. Sci.* **1979**, *257*, 136-139.

Hahn, T., Ed. *International Tables for X-ray Crystallography;* Kluwer Academic Publishers: Boston, MA 1992.

Hajduk, D. A.; Gruner, S. M.; Rangarajan, P.; Register, R. A.; Fetters, L. J.; Honeker, C.; Albalak, R. J.; Thomas, E. L. *Macromolecules* **1994**, *27*, 490-501.

Hajduk, D. A.; Harper, P. E.; Gruner, S. M.; Honeker, C. C.; Kim, G.; Thomas, E. L.; Fetters, L. J. *Macromolecules* **1994**, *27*, 4063-4075.

Hajduk, D. A.; Harper, P. E.; Gruner, S. M.; Honeker, C. C.; Thomas, E. L.; Fetters, L. J. *Macromolecules* **1995**, *28*, 2570-2573.

Hajduk, D. A.; Ho, R.; Hillmyer, M. A.; Bates, F. S.; Almdal, K. *J. Phys. Chem. B* **1998**, *102*, 1356-1363.

Hajduk, D. A.; Takenouchi, H.; Hillmyer, M. A.; Bates, F. S.; Vigild, M. E.; Almdal, K. *Macromolecules* **1997**, *30*, 3788-3795.

Hamley, I. W. *J. Phys: Condens. Matter* **2001**, *13*, R643-R671.

Hamley, I. W.; Gehlsen, M. D.; Khandpur, A. K.; Koppi, K. A.; Rosedale, J. H.; Schulz, M. F.; Bates, F. S.; Almdal, K.; Mortensen, K. *J. Phys. II* **1994**, *4*, 2161-2186.

Hamley, I. W.; Koppi, K. A.; Rosedale, J. H.; Bates, F. S.; Almdal, K.; Mortensen, K. *Macromolecules* **1993**, *26*, 5959-5970.

Hamley, I. W.; Pople, J. A.; Fairclough, J. P. A.; Terrill, N. J.; Ryan, A. J.; Booth, C.; Yu, G. E.; Diat, O.; Almdal, K.; Mortensen, K. *J. Chem. Phys.* **1998**, *108*, 6929.

Han, C. D.; Kim, J. K. *Polymer* **1993**, *34*, 2533-2539.

Han, C. D.; Vaidya, N. Y.; Kim, D.; Shin, G.; Yamaguchi, D.; Hashimoto, T. *Macromolecules* **2000**, *33*, 3767-3780.

Handlin, D. L.; Thomas, E. L. *Macromolecules* **1983**, *16*, 1514-1525.

Hardy, C. M. *Ph.D. Dissertation*; University of Minnesota **2003**, 1-249.

Hardy, C. M.; Bates, F. S.; Kim, M.; Wignall, G. D. *Macromolecules* **2002**, *35*, 3189-3197.

Harrison, W. L.; Hickner, M. A.; Kim, Y. S.; McGrath, J. E. *Fuel Cells* **2005**, *5*, 201-212.

Hasegawa, H.; Hashimoto, T.; Kawai, H.; Lodge, T. P.; Amis, E. J.; Glinka, C. J.; Han, C. C. *Macromolecules* **1985**, *18*, 67-78.

Hasegawa, H.; Tanaka, H.; Yamasaki, K.; Hashimoto, T. *Macromolecules* **1987**, *20*, 1651-1662.

Hashimoto, T.; Ijichi, Y.; Fetters, L. J. *J. Chem. Phys.* **1988**, *89*, 2463.

Helfand, E. *Macromolecules* **1975**, *8*, 552-556.

Helfand, E.; Tagami, Y. *J. Chem. Phys.* **1972**, *56*, 3592-3601.

Helfand, E.; Wasserman, Z. R. *Macromolecules* **1976**, *9*, 879-888.

Helfand, E.; Wasserman, Z. R. *Macromolecules* **1978**, *11*, 960-966.

Helfand, E.; Wasserman, Z. R. *Macromolecules* **1980**, *13*, 994-998.

Herman, D. S.; Kinning, D. J.; Thomas, E. L.; Fetters, L. J. *Macromolecules* **1987**, *20*, 2940-2942.

Hermel, T. J. *Ph.D. Dissertation;* University of Minnesota **2003**, 1-197.

Hermel, T. J.; Hahn, S. F.; Chaffin, K. A.; Gerberich, W. W.; Bates, F. S. *Macromolecules* **2003**, *36*, 2190-2193.

Hiemenz, P. C.; Lodge, T. P. *Polymer Chemistry*, 2nd Edition; CRC Press: Boca Raton, FL, 2007.

Hillmyer, M. A.; Bates, F. S. *Macromolecules* **1996**, *29*, 6994-7002.

Hillmyer, M. A.; Bates, F. S.; Almdal, K.; Mortensen, K.; Ryan, A. J.; Fairclough, J. P. A. *Science* **1996**, *271*, 976.

Holden, G.; Milkovich, R. (Shell Internationale Research Maatschappij NV, Netherlands). Rubberlike block copolymers.US Patent 3265765, August 8, 1966.

Hong, Y.; Adamson, D. H.; Chaikin, P. M.; Register, R. A. *Soft Matter* **2009**, *5*, 1687-1691.

Huang, H.; Hu, Z.; Chen, Y.; Zhang, F.; Gong, Y.; He, T.; Wu, C. *Macromolecules* **2004**, *37*, 6523-6530.

Huang, H.; Zhang, F.; Hu, Z.; Du, B.; He, T.; Lee, F. K.; Wang, Y.; Tsui, O. K. C.

Macromolecules **2003**, *36*, 4084-4092.

Hückstädt, H.; Göpfert, A.; Abetz, V. *Polymer* **2000**, *41*, 9089-9094.

Hucul, D. A.; Hahn, S. F. *Adv. Mater.* **2000**, *12*, 1855-1858.

Hueckstaedt, H.; Goldacker, T.; Goepfert, A.; Abetz, V. *Macromolecules* **2000**, *33*, 3757-3761.

Jerome, R. *Macromol. Eng.* 2007, *3*, 1753-1782.

Karatasos, K.; Anastasiadis, S. H.; Pakula, T.; Watanabe, H. *Macromolecules* **2000**, *33*, 523-541.

Kawasaki, K.; Onuki, A. *Phys. Rev. A: At., Mol., Opt. Phys.* **1990**, *42*, 3664-3666.

Kekicheff, P.; Cabane, B. *J. Phys.* **1987**, *48*, 1571-1583.

Kekicheff, P.; Tiddy, G. J. T. *J. Phys. Chem.* **1989**, *93*, 2520-2526.

Keller, A.; Pedemonte, E.; Willmouth, F. M. *Nature* **1970**, *225*, 538-539.

Khandpur, A. K.; Förster, S.; Bates, F. S.; Hamley, I. W.; Ryan, A. J.; Bras, W.; Almdal, K.; Mortensen, K. *Macromolecules* **1995**, *28*, 8796-8806.

Khandpur, A. K.; Macosko, C. W.; Bates, F. S. *J. Polym. Sci. Part B* **1995**, *33*, 247-252.

Kim, M. I.; Wakada, T.; Akasaka, S.; Nishitsuji, S.; Saijo, K.; Hasegawa, H.; Ito, K.; Takenaka, M. *Macromolecules* **2008**, *41*, 7667-7670.

Kim, W. G.; Chang, M. Y.; Garetz, B. A.; Newstein, M. C.; Balsara, N. P.; Lee, J. H.; Hahn, H.; Patel, S. S. *J. Chem. Phys.* **2001**, *114*, 10196-10211.

Kinning, D. J.; Thomas, E. L. *Macromolecules* **1984**, *17*, 1712-1718.

Koning, C.; Van Duin, M.; Pagnoulle, C.; Jerome, R. *Prog. Polym. Sci.* **1998**, *23*, 707-757.

Koppi, K. A.; Tirrell, M.; Bates, F. S.; Almdal, K.; Colby, R. H. *J. Phys. II* **1992**, *2*, 1941-1959.

Kossuth, M. B.; Morse, D. C.; Bates, F. S. *J. Rheol.* **1999**, *43*, 167-196.

Krappe, U.; Stadler, R.; Voigt-Martin, I. *Macromolecules* **1995**, *28*, 4558-4561.

Krause, S. *J. Polym. Sci., Part B: Polym. Phys.* **1969**, *7*, 249-252.

Kudose, I.; Kotaka, T. *Macromolecules* **1984**, *17*, 2325-2332.

Laurer, J. H.; Hajduk, D. A.; Fung, J. C.; Sedat, J. W.; Smith, S. D.; Gruner, S. M.; Agard, D. A.; Spontak, R. J. *Macromolecules* **1997**, *30*, 3938-3941.

Leary, D. F.; Williams, M. C. *J. Polym. Sci., Polym. Lett. Ed.* **1970**, *8*, 335-340.

Lee, M.; Cho, B.; Jang, Y.; Zin, W. *J. Am. Chem. Soc.* **2000**, *122*, 7449-7455.

Leibler, L. *Macromolecules* **1980**, *13*, 1602-1617.

Liu, Y.; Li, M.; Bansil, R.; Steinhart, M. *Macromolecules* **2007**, *40*, 9482-9490.

Lodge, T. P. *Macromol. Chem. Phys.* **2003**, *204*, 265-273.

Lodge, T. P.; Pudil, B.; Hanley, K. J. *Macromolecules* **2002**, *35*, 4707-4717.

Loo, Y. L.; Register, R. A.; Adamson, D. H.; Ryan, A. J. *Macromolecules* **2005**, *38*, 4947-4949.

Ludwigs, S.; Boker, A.; Abetz, V.; Muller, A. H. E.; Krausch, G. *Polymer* **2003**, *44*, 6815-6823.

Luzzati, V.; Tardieu, A.; Gulik-Krzywicki, T. *Nature* **1968**, *217*, 1028-1030.

Macosko, C. W. *Rheology: Principles, Measurements and Applications;* Advances in Interfacial Engineering; Wiley-VCH: New York, 1994.

Mahanthappa, M. K.; Lim, L. S.; Hillmyer, M. A.; Bates, F. S. *Macromolecules* **2007**, *40*, 1585-1593.

Maheshwari, S.; Tsapatsis, M.; Bates, F. S. *Macromolecules* **2007**, *40*, 6638-6646.

Mai, S.; Mingvanish, W.; Turner, S. C.; Chaibundit, C.; Fairclough, J. P. A.; Heatley, F.; Matsen, M. W.; Ryan, A. J.; Booth, C. *Macromolecules* **2000**, *33*, 5124-5130.

Matsen, M. W. *J. Chem. Phys.* **1995**, *102*, 3884-3887.

Matsen, M. W. *J. Chem. Phys.* **2000**, *113*, 5539-5544.

Matsen, M. W. *Phys. Rev. Lett.* **2007**, *99*, 148304/1-148304/4.

Matsen, M. W.; Bates, F. S. *J. Chem. Phys.* **1997**, *106*, 2436-2448.

Matsen, M. W.; Bates, F. S. *J. Polym. Sci. Part B* **1997**, *35*, 945-952.

Matsen, M. W.; Bates, F. S. *Macromolecules* **1996**, *29*, 1091-1098.

Matsen, M. W.; Schick, M. *Macromolecules* **1994**, *27*, 187-192.

Matsen, M. W.; Schick, M. *Macromolecules* **1994**, *27*, 7157-7163.

Matsen, M. W.; Schick, M. *Phys. Rev. Lett.* **1994**, *72*, 2660-2663.

Matsen, M. W.; Thompson, R. B. *J. Chem. Phys.* **1999**, *111*, 7139-7146.

Matsushita, Y.; Nomura, M.; Watanabe, J.; Mogi, Y.; Noda, I.; Imai, M. *Macromolecules* **1995**, *28*, 6007-6013.

Matsushita, Y.; Suzuki, J.; Seki, M. *Phys. B* **1998**, *248*, 238-242.

Matsushita, Y.; Tamura, M.; Noda, I. *Macromolecules* **1994**, *27*, 3680-3682.

Matsushita, Y.; Yamada, K.; Hattori, T.; Fujimoto, T.; Sawada, Y.; Nagasawa, M.; Matsui, C. *Macromolecules* **1983**, *16*, 10-13.

Mayes, A. M.; Olvera de la Cruz, M. *J. Chem. Phys.* **1989**, *91*, 7228-7235.

Mayes, A. M.; Olvera de la Cruz, M. *J. Chem. Phys.* **1991**, *95*, 4670-4677.

McKay, K. W.; Gros, W. A.; Diehl, C. F. *J. Appl. Polym. Sci.* **1995**, *56*, 947-958.

Meier, D. J. *J. Polym. Sci., Part C: Polym. Symp.* **1969**, *No. 26*, 81-98.

Meuler, A. J. *Ph.D. Dissertation*; University of Minnesota **2009**, 1-328.

Meuler, A. J.; Fleury, G.; Hillmyer, M. A.; Bates, F. S. *Macromolecules* **2008**, *41*, 5809-5817.

Meuler, A. J.; Hillmyer, M. A.; Bates, F. S. *Macromolecules* **2009**, *42*, 7213-7216.

Mogi, Y.; Kotsuji, H.; Kaneko, Y.; Mori, K.; Matsushita, Y.; Noda, I. *Macromolecules* **1992**, *25*, 5408-5411.

Mogi, Y.; Mori, K.; Kotsuji, H.; Matsushita, Y.; Noda, I.; Han, C. C. *Macromolecules* **1993**, *26*, 5169-5173.

Mogi, Y.; Mori, K.; Matsushita, Y.; Noda, I. *Macromolecules* **1992**, *25*, 5412-5415.

Mogi, Y.; Nomura, M.; Kotsuji, H.; Ohnishi, K.; Matsushita, Y.; Noda, I. *Macromolecules* **1994**, *27*, 6755-6760.

Morrison, F. A.; Winter, H. H.; Gronski, W.; Barnes, J. D. *Macromolecules* **1990**, *23*, 4200-4205.

Morrison, R. T.; Boyd, R. N. *Organic Chemistry*; Prentice Hall: Englewood Cliffs, NJ, 1992.

Mortensen, K.; Almdal, K.; Bates, F. S.; Koppi, K.; Tirrell, M.; Norden, B. *Phys. B* **1995**, *213&214*, 682-684.

Mortensen, K.; Vigild, M. E. *Macromolecules* **2009**, *42*, 1685-1690.

Ndoni, S.; Papadakis, C. M.; Bates, F. S.; Almdal, K. *Rev. Sci. Instrum.* **1995**, *66*, 1090-1095.

Ndoni, S.; Vigild, M. E.; Berg, R. H. *J. Am. Chem. Soc.* **2003**, *125*, 13366-13367.

Neumann, C.; Loveday, D. R.; Abetz, V.; Stadler, R. *Macromolecules* **1998**, *31*, 2493-2500.

Odian, G. *Principles of Polymerization*; Wiley-Interscience: Hoboken, NJ, 2004.

Oh, N. K.; Zin, W. C.; Im, J. H.; Lee, M. *Polymer* **2006**, *47*, 5275-5286.

Oh, N.; Zin, W.; Im, J.; Ryu, J.; Lee, M. *Chem. Commun.* **2004**, 1092-1093.

Pangborn, A. B.; Giardello, M. A.; Grubbs, R. H.; Rosen, R. K.; Timmers, F. J. *Organometallics* **1996**, *15*, 1518-1520.

Papadakis, C. M.; Almdal, K.; Mortensen, K.; Vigild, M. E.; Stepanek, P. *J. Chem. Phys.* **1999**, *111*, 4319-4326.

Patel, S. S.; Larson, R. G.; Winey, K. I.; Watanabe, H. *Macromolecules* **1995**, *28*, 4313-4318.

Phillip, W. A.; Rzayev, J.; Hillmyer, M. A.; Cussler, E. L. *J. Membr. Sci.* **2006**, *286*, 144-152.

Price, C.; Lally, T. P.; Stubbersfield, R. *Polymer* **1974**, *15*, 541-543.

Qi, S.; Wang, Z. G. *Phys. Rev. E: Stat., Nonlinear, Soft Matter Phys.* **1997**, *55*, 1682-1697.

Quirk, R. P.; Ma, J. J. *J. Polym. Sci. Part A* **1988**, *26*, 2031-2037.

Riise, B. L.; Fredrickson, G. H.; Larson, R. G.; Pearson, D. S. *Macromolecules* **1995**, *28*, 7653-7659.

Rosedale, J. H.; Bates, F. S. *Macromolecules* **1990**, *23*, 2329-2338.

Rouse, P. E., Jr. *J. Chem. Phys.* **1953**, *21*, 1272-1280.

Ryu, C. Y.; Lee, M. S.; Hajduk, D. A.; Lodge, T. P. *J. Polym. Sci. Part B* **1997**, *35*, 2811-2823.

Rzayev, J.; Hillmyer, M. A. *J. Am. Chem. Soc.* **2005**, *127*, 13373–13379.

Sakamoto, N.; Hashimoto, T.; Han, C. D.; Kim, D.; Vaidya, N. Y. *Macromolecules* **1997**, *30*, 1621-1632.

Sakurai, S.; Isobe, D.; Okamoto, S.; Yao, T.; Nomura, S. , *Phys. Rev. E: Stat., Nonlinear, Soft Matter Phys.* **2001**, *63*, 061803/1-061803/5.

Sakurai, S.; Momii, T.; Taie, K.; Shibayama, M.; Nomura, S.; Hashimoto, T. *Macromolecules* **1993**, *26*, 485-491.

Schulz, M. F.; Bates, F. S.; Almdal, K.; Mortensen, K. *Phys. Rev. Lett.* **1994**, *73*, 86-89.

Schulz, M. F.; Khandpur, A. K.; Bates, F. S.; Almdal, K.; Mortensen, K.; Hajduk, D. A.; Gruner, S. M. *Macromolecules* **1996**, *29*, 2857-2867.

Schwab, M.; Stuehn, B. *Phys. Rev. Lett.* **1996**, *76*, 924-927.

Schwab, M.; Stühn, B. *Colloid Polym. Sci.* **1997**, *275*, 341-351.

Shefelbine, T. A.; Vigild, M. E.; Matsen, M. W.; Hajduk, D. A.; Hillmyer, M. A.; Cussler, E. L.; Bates, F. S. *J. Am. Chem. Soc.* **1999**, *121*, 8457-8465.

Shibayama, M.; Hasegawa, H.; Hashimoto, T.; Kawai, H. *Macromolecules* **1982**, *15*, 274-280.

Silverstein, R. M.; Webster, F. X.; Kiemle, D. J. *Spectrometric Identification of Organic Compounds;* John Wiley & Sons, Inc.: Hoboken, NJ, 2005.

Singh, M.; Odusanya, O.; Wilmes, G. M.; Eitouni, H. B.; Gomez, E. D.; Patel, A. J.; Chen, V. L.; Park, M. J.; Fragouli, P.; Iatrou, H.; Hadjichristidis, N.; Cookson, D.; Balsara, N. P. *Macromolecules* **2007**, *40*, 4578-4585.

Stadler, R.; Auschra, C.; Beckmann, J.; Krappe, U.; Voight-Martin, I.; Leibler, L. *Macromolecules* **1995**, *28*, 3080-3097.

Stangler, S.; Abetz, V. *Rheol. Acta* **2003**, *42*, 569-577.

Stout, G. H.; Jensen, L. H. *X-Ray Structure Determination;* John Wiley & Sons: New York, 1989.

Stoykovich, M. P.; Mueller, M.; Kim, S. O.; Solak, H. H.; Edwards, E. W.; de Pablo, J. J.; Nealey, P. F. *Science* **2005**, *308*, 1442-1446.

Sugiyama, M.; Shefelbine, T. A.; Vigild, M. E.; Bates, F. S. *J. Phys. Chem. B* **2001**, *105*, 12448-12460.

Szwarc, M.; Levy, M.; Milkovich, R. *J. Am. Chem. Soc.* **1956**, *78*, 2656-2657.

Takenaka, M.; Wakada, T.; Akasaka, S.; Nishitsuji, S.; Saijo, K.; Shimizu, H.; Kim, M. I.; Hasegawa, H. *Macromolecules* **2007**, *40*, 4399-4402.

Tang, P.; Qiu, F.; Zhang, H.; Yang, Y. *Phys. Rev. E: Stat., Nonlinear, Soft Matter Phys.* **2004**, *69*, 031803/1-031803/8.

Tepe, T.; Schulz, M. F.; Zhao, J.; Tirrell, M.; Bates, F. S.; Mortensen, K.; Almdal, K. *Macromolecules* **1995**, *28*, 3008-3011.

Thomas, E. L.; Alward, D. B.; Kinning, D. J.; Martin, D. C.; Handlin, D. L., Jr.; Fetters, L. J. *Macromolecules* **1986**, *19*, 2197-2202.

Trent, J. S.; Scheinbeim, J. I.; Couchman, P. R. *Macromolecules* **1983**, *16*, 589-598.

Tyler, C. A.; Morse, D. C. *Phys. Rev. Lett.* **2005**, *94*, 208302.

Tyler, C. A.; Qin, J.; Bates, F. S.; Morse, D. C. *Macromolecules* **2007**, *40*, 4654-4668.

Urbas, A. M.; Maldovan, M.; DeRege, P.; Thomas, E. L. *Adv. Mater.* **2002**, *14*, 1850-1853.

Vigild, M. E.; Almdal, K.; Mortensen, K.; Hamley, I. W.; Fairclough, J. P. A.; Ryan, A. J. *Macromolecules* **1998**, *31*, 5702-5716.

Vigild, M. E.; Chu, C.; Sugiyama, M.; Chaffin, K. A.; Bates, F. S. *Macromolecules* **2001**, *34*, 951-964.

Wang, C. Y.; Lodge, T. P. *Macromol. Rapid Commun.* **2002**, *23*, 49-54.

Wang, C.; Lodge, T. P. *Macromolecules* **2002**, *35*, 6997-7006.

Wang, X.; Dormidontova, E. E.; Lodge, T. P. *Macromolecules* **2002**, *35*, 9687-9697.

Watanabe, H. *Macromolecules* **1995**, *28*, 5006-5011.

Weimann, P. A.; Jones, T. D.; Hillmyer, M. A.; Bates, F. S.; Londono, J. D.; Melnichenko, Y.; Wignall, G. D.; Almdal, K. *Macromolecules* **1997**, *30*, 3650-3657.

Wells, A. F. *Three Dimensional Nets and Polyhedra;* John Wiley & Sons: New York, NY 1977.

Wetton, R. E. *Polymer Characterisation;* Hunt, B. J., James, M. I., Eds.; Blackie Academic & Professional: New York, 1993.

Williams, D. B.; Carter, C. B. *Transmission Electron Microscopy: A Textbook for Materials Science;* Plenum Press: New York, 1996.

Williams, M. L.; Landel, R. F.; Ferry, J. D. *J. Am. Chem. Soc.* **1955**, *77*, 3701-3707.

Winey, K. I.; Thomas, E. L.; Fetters, L. J. *Macromolecules* **1992**, *25*, 2645-2650.

Winter, H. H.; Scott, D. B.; Gronski, W.; Okamoto, S.; Hashimoto, T. *Macromolecules* **1993**, *26*, 7236-7244.

Wohlgemuth, M.; Yufa, N.; Hoffman, J.; Thomas, E. L. *Macromolecules* **2001**, *34*, 6083-6089.

Wu, L.; Cochran, E. W.; Lodge, T. P.; Bates, F. S. *Macromolecules* **2004**, *37*, 3360-3368.

Xie, R.; Yang, B.; Jiang, B. *Macromolecules* **1993**, *26*, 7097-7099.

Yamada, K.; Nonomura, M.; Ohta, T. *J. Phys.: Condens. Matter* **2006**, *18*, L421-L427.

Zhang, Q.; Tsui, O. K. C.; Du, B.; Zhang, F.; Tang, T.; He, T. *Macromolecules* **2000**, *33*, 9561-9567.

Zhao, J.; Majumdar, B.; Schulz, M. F.; Bates, F. S.; Almdal, K.; Mortensen, K.; Hajduk, D. A.; Gruner, S. M. *Macromolecules* **1996**, *29*, 1204-1215.

Zheng, W.; Wang, Z. *Macromolecules* **1995**, *28*, 7215-7223.

Zhu, L.; Huang, P.; Chen, W. Y.; Weng, X.; Cheng, S. Z. D.; Ge, Q.; Quirk, R. P.; Senador, T.; Shaw, M. T.; Thomas, E. L. *Macromolecules* **2003**, *36*, 3180-3188.

Zhu, L.; Huang, P.; Cheng, S. Z. D.; Ge, Q.; Quirk, R. P.; Thomas, E. L.; Lotz, B.; Wittmann, J. C.; Hsiao, B. S.; Yeh, F.; Liu, L. *Phys. Rev. Lett.* **2001**, *86*, 6030-6033.

Appendix A

Morphological Characterization of Additional Poly(ethylene-*b*-cyclohexylethylene-*b*-dimethylsiloxane) Triblock Terpolymers

Three poly(ethylene-*b*-cyclohexylethylene-*b*-dimethylsiloxane) (ECD) triblock terpolymers were synthesized with a C to E ratio of approximately three to seven. The ECD triblocks were prepared in a similar manner as the CECD tetrablocks discussed in Chapters 4 and 5. The molecular characterization data from these terpolymers are summarized in Table A.1. Samples were characterized with small-angle X-ray scattering (SAXS), dynamic mechanical spectroscopy (DMS), and transmission electron microscopy (TEM). Due to the strong segregation within the triblocks (T_{ODT} > 300 ºC), reciprocating shear[1] was used to macroscopically align the samples and aid in morphological characterization.

Table A.1: Characterization data for ECD triblock terpolymers.

Polymer	M_n, kDa	M_w/M_n	f_E[a]	f_C[a]	f_D[a]	T_{ODT}, °C[b]	*Phase*[c]	*d*, nm[d]
ECD-6	35.0	1.05	0.69	0.28	0.03	>300	LAM/HEX	40.5/36.5 (140 °C)
ECD-7	27.3	1.08	0.66	0.28	0.06	>300	HEX	28.2 (250 °C)
ECD-8	31.6	1.07	0.65	0.27	0.08	>300	Q^{230}	77.2 (250 °C)

[a]Volume fractions were calculated from published melt density data at 140 °C (ρ_C = 0.920 g/cm^3, ρ_E = 0.784 g/cm^3, and ρ_D = 0.895 g/cm^3).[2]

[b]Order-disorder transition temperatures determined by DMS.

[c]Phase assignments based on SAXS and TEM obtained from shear-aligned samples. LAM: lamellae; HEX: hexagonally packed cylinder; Q^{230}: Gyroid with $Ia\bar{3}d$ symmetry.

[d]Lattice dimensions, *d*, calculated as $d = 2\pi/q^*$ are based on LAM [100], HEX [100], and Q^{230} [001] at the specified temperature.

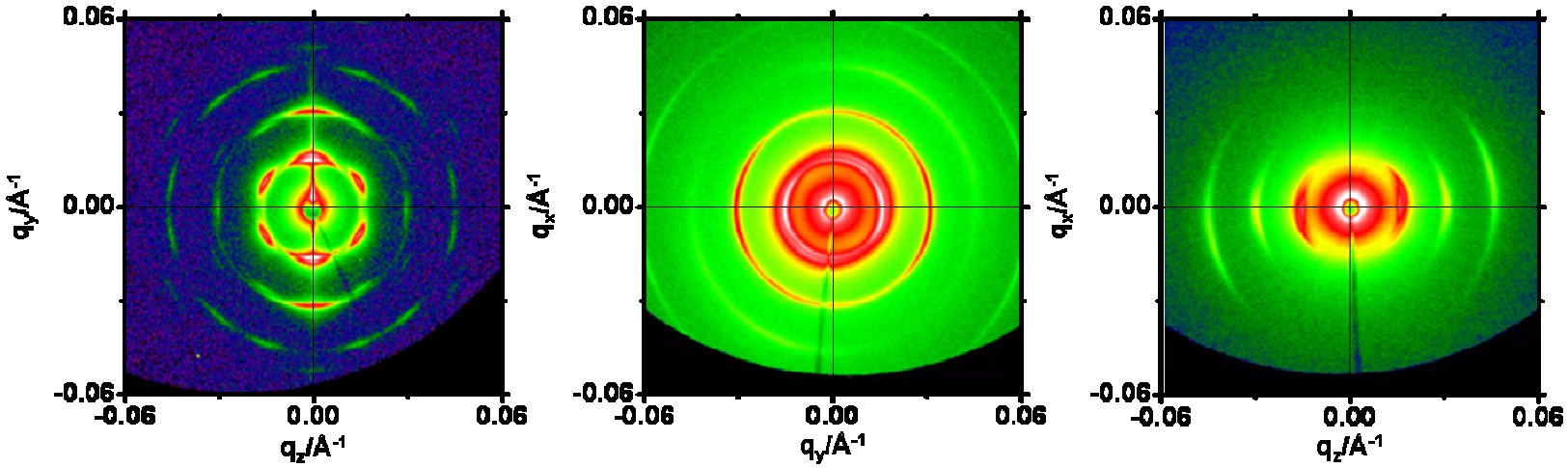

Figure A.8.1: Two-dimensional SAXS patterns obtained from ECD-6 after large-amplitude reciprocating shear ($|\gamma|$ = 200%, $\dot{\gamma}$ = 0.5 s^{-1}, T = 250 ºC). Data were obtained at 140 ºC. The scattering reflections are consistent with coexistence of lamellar and hexagonal structures. This is most apparent in the $\boldsymbol{q_y}$-$\boldsymbol{q_z}$ plane, where six-fold symmetry is superimposed onto two-fold reflections (strong meridional spots). The two-fold symmetry in the $\boldsymbol{q_x}$-$\boldsymbol{q_x}$ and $\boldsymbol{q_x}$-$\boldsymbol{q_z}$ planes is consistent with cylinders or lamellae oriented along the shear (x) direction. The domain spacings are 40.5 and 36.5 nm for the lamellar and hexagonal microstructures, respectively.

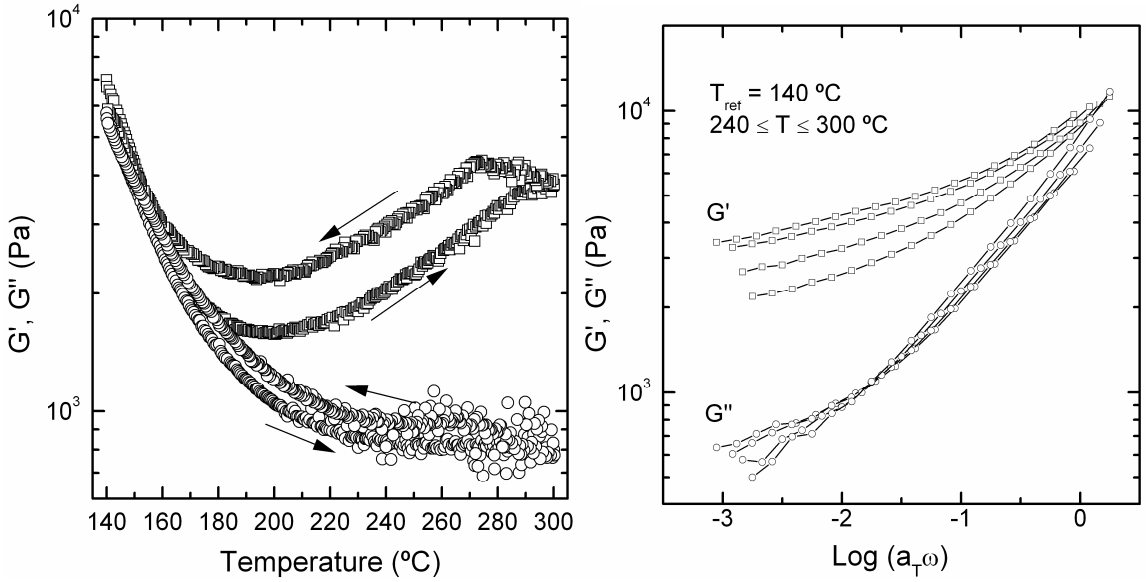

Figure A.8.2: (Left) Isochronal (ω = 1 rad/s) temperature scan of dynamic elastic (□) and loss (○) moduli for ECD-6 while heating and cooling at 2 ºC/min with a strain amplitude of 1%. Data were obtained after annealing at 300 ºC for 10 min and cooling (20 ºC/min) to 140 ºC. (Right) Isothermal frequency sweep data shifted according to time-temperature superposition (T_{ref} = 140 ºC) for ECD-6. Data were obtained at 240, 260, 280, and 300 ºC. The weak dependence of G' on ω is consistent with a singly- or doubly-periodic microstructure.

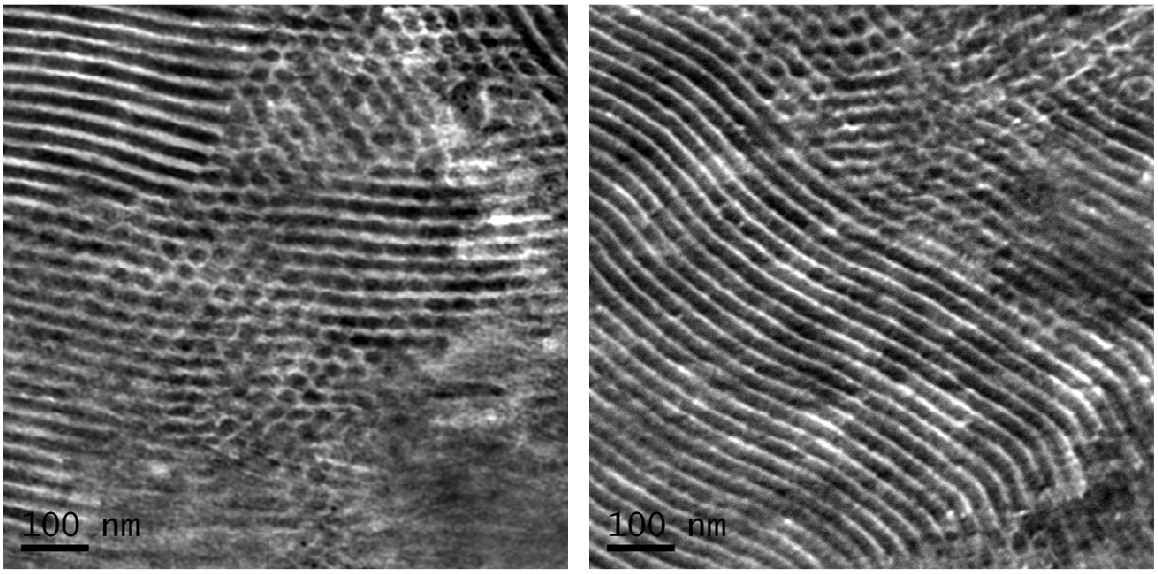

Figure A.8.3: TEM micrographs obtained from ECD-6. Sample was shear-oriented ($|\gamma|$ = 200%, $\dot{\gamma}$ = 0.5 s^{-1}, T = 250 ºC) prior to cryo-microtoming and staining with RuO_4. Dark areas correspond to C and D, while lighter regions are the semicrystalline E domains. Regions of six-fold symmetry are consistent with hexagonally packed cylinders. Alternating light and dark layers are consistent with lamellae or the long axis of cylinders.

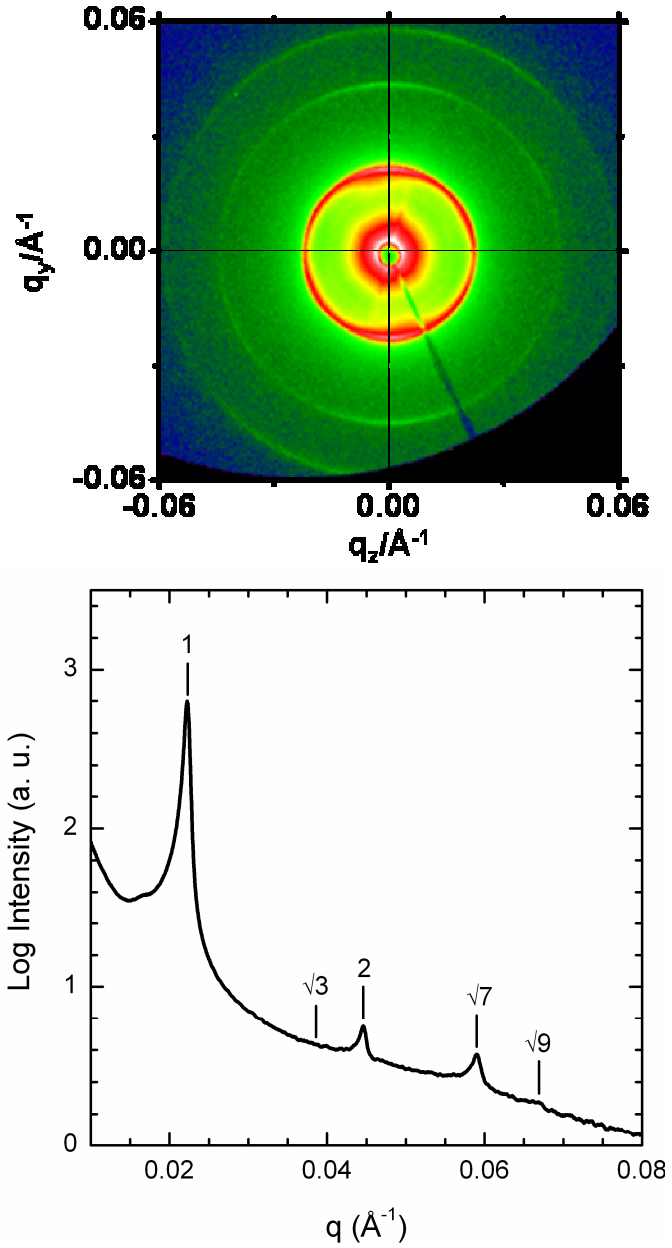

Figure A.8.4: (Top) Two-dimensional SAXS pattern along shear (x) direction obtained from ECD-7 after large-amplitude reciprocating shear ($|\gamma|$ = 200%, $\dot{\gamma}$ = 0.5 s^{-1}, T = 250 ºC). Data were obtained at 250 ºC. (Bottom) Azimuthal integration of two-dimensional pattern indexed to hexagonal symmetry.

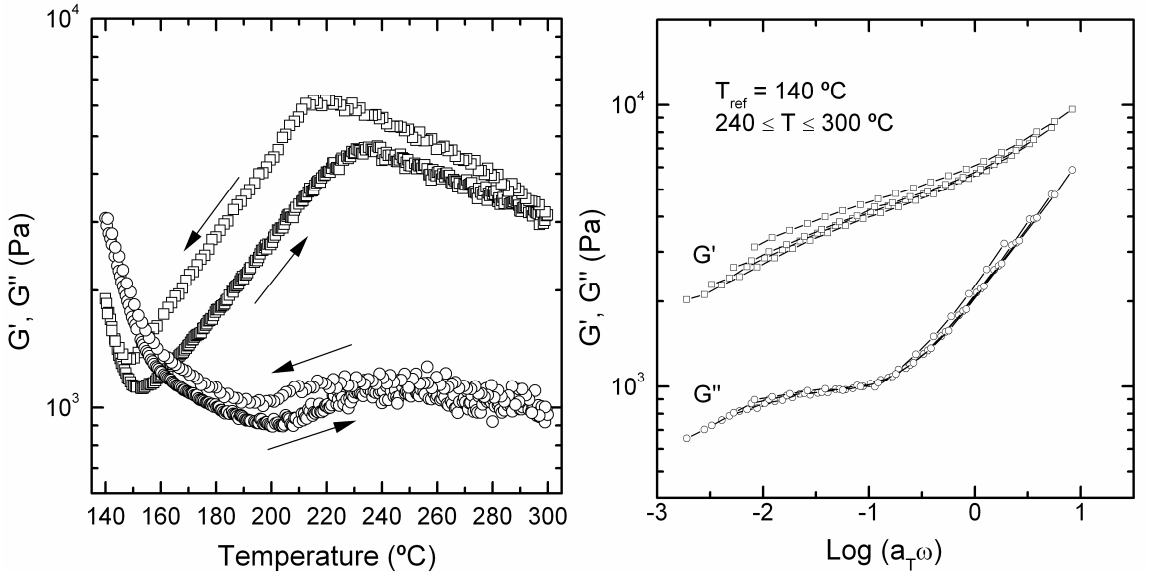

Figure A.8.5: (Left) Isochronal (ω = 1 rad/s) temperature scan of dynamic elastic (□) and loss (○) moduli for ECD-7 while heating at 2 ºC/min and cooling at 5 ºC/min with a strain amplitude of 1%. (Right) Isothermal frequency sweep data shifted according to time-temperature superposition (T_{ref} = 140 ºC) for ECD-7. Data were obtained at 240, 260, 280, and 300 ºC. The weak dependence of G' on ω is consistent with the phase assignment.

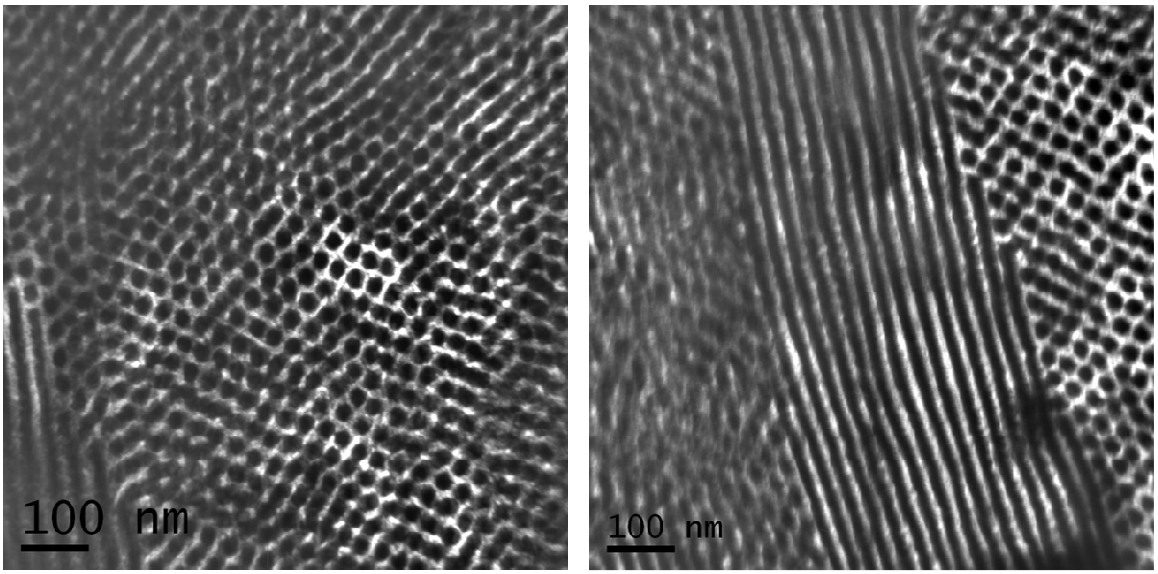

Figure A.8.6: TEM micrographs generated from ECD-7 after shear alignment ($|\gamma|$ = 200%, $\dot{\gamma}$ = 0.5 s^{-1}, T = 250 ºC). Sample was stained with RuO_4. Dark areas correspond to C and D, while lighter regions are the semicrystalline E domains. Regions of six-fold symmetry are consistent with hexagonally packed cylinders. Alternating light and dark layers are consistent with the long axis of cylinders.

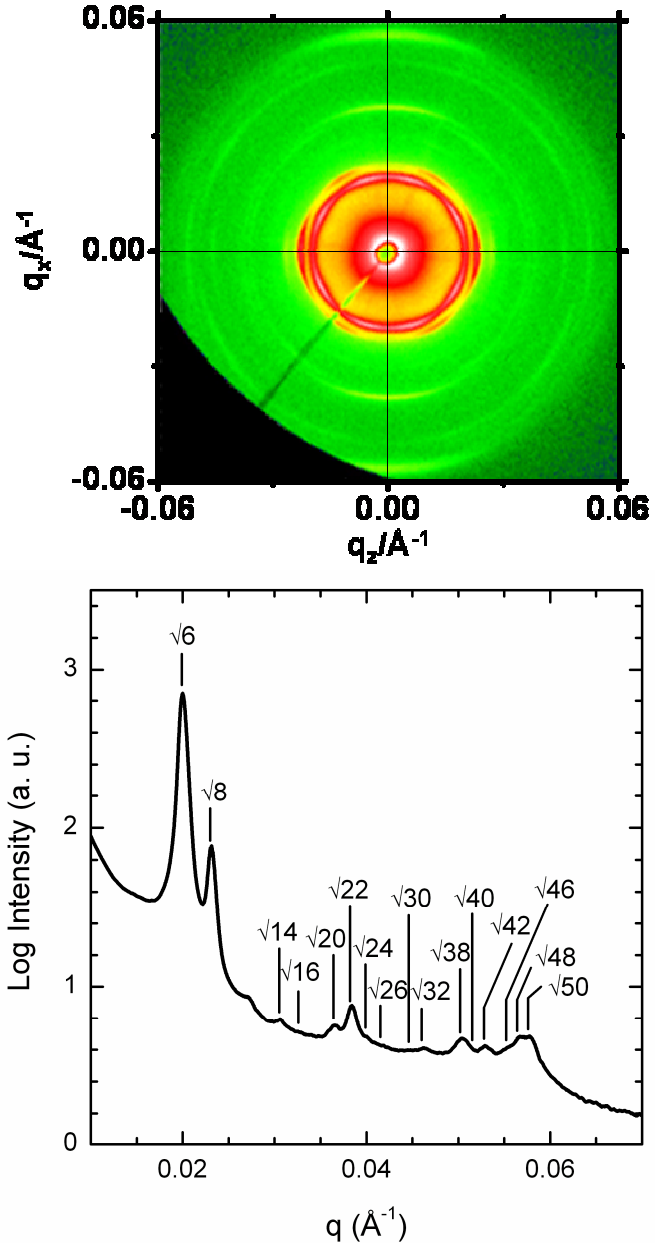

Figure A.8.7: (Top) Two-dimensional SAXS pattern along shear gradient (y) direction generated from ECD-8 after large-amplitude reciprocating shear ($|\gamma|$ = 200%, $\dot{\gamma}$ = 0.5 s^{-1}, T = 250 ºC). (Bottom) Azimuthal integration of two-dimensional pattern. The pattern has been indexed to Q^{230}. Data were obtained at 250 ºC.

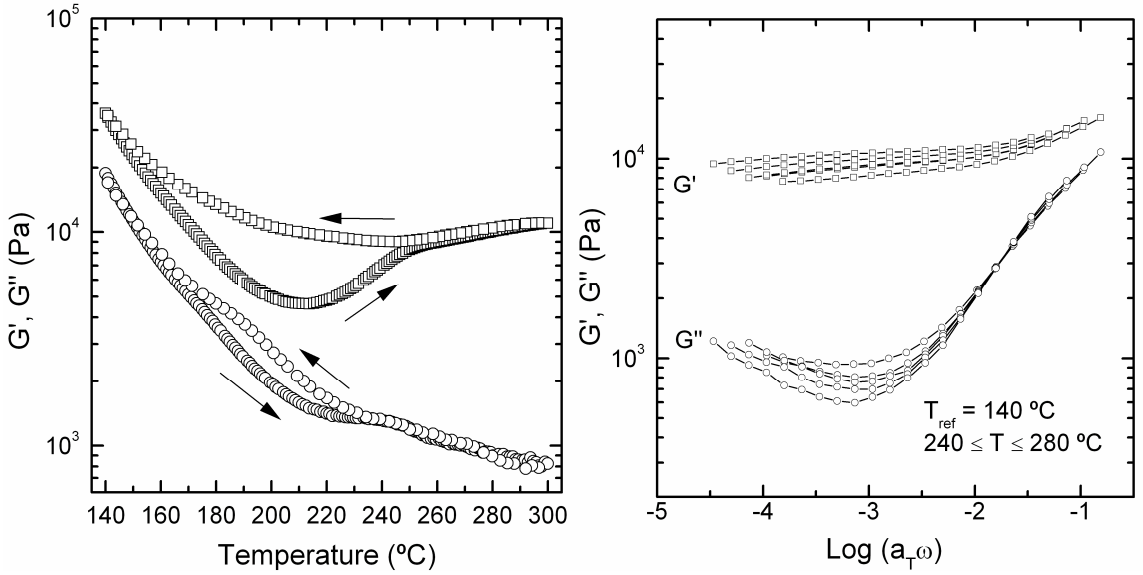

Figure A.8.8: (Left) Isochronal (ω = 1 rad/s) temperature scan of dynamic elastic (□) and loss (○) moduli for ECD-8 while heating at 2 ºC/min and cooling at 5 ºC/min with a strain amplitude of 1%. (Right) Isothermal frequency sweep data shifted according to time-temperature superposition (T_{ref} = 140 ºC) for ECD-8. Data were obtained at 240, 250, 260, 270, and 280 ºC. The plateau in G' **(**$G' \sim \omega^0$) is consistent with a triply-periodic microstructure, like Q^{230}.[3]

The morphological characterization of these three ECD triblocks was made more difficult by the large segregation strengths present in these materials. Samples with lower molecular weights and experimentally accessible T_{ODT}s would have been preferable. Additionally, there is evidence of order-order transitions in the temperature scans of all three materials. Thus, the observed phases may correspond to the shear-stable morphology rather than the equilibrium state.

ECD-8 proved especially interesting because it is similar in composition and molecular weight to the O^{52} CECD sample (CECD-2, 9% D) discussed in Chapter 5. ECD-8 and CECD-2 were prepared in identical manners (shear alignment at 250 ºC). Like CECD-2, ECD-8 forms a network structure, but the scattering data (Figure A.7) are consistent with the cubic gyroid (Q^{230}). This suggests that the CECD tetrablock architecture alters the energetically preferred morphology in these terpolymer systems. However, additional work is necessary to characterize this change in observed network structure.

References

(1) Mortensen, K.; Almdal, K.; Bates, F. S.; Koppi, K.; Tirrell, M.; Norden, B. *Phys. B: Condensed Matter* **1995**, *213&214*, 682-684.

(2) Fetters, L. J.; Lohse, D. J.; Richter, D.; Witten, T. A.; Zirkel, A. *Macromolecules* **1994**, *27*, 4639-4647.

(3) Kossuth, M. B.; Morse, D. C.; Bates, F. S. *J. Rheol.* **1999**, *43*, 167-196.

Appendix B

Tensile Properties of Poly(cyclohexylethylene-*b*-ethylene-*b*-cyclohexylethylene-*b*-dimethylsiloxane)

The stress-strain curves generated from three CECD tetrablocks and one ECD triblock are displayed in Figure B.0.1. Samples were prepared as 0.8 mm thick films by compression-molding at 170 ºC 2000 psi for 5 – 6 min. Prior to tensile testing the polymer sheets were annealed under vacuum at 200 ºC for 18 hours. Uniaxial deformation measurements were done at room temperature with a Rheometrics Scientific Minimat instrument equipped with a 200 N load cell operating with a crosshead speed of 8 mm/min. The initial gauge length was 8 mm. Results are presented as engineering stress (σ) versus nominal strain (ε), which are defined as

$$\sigma = \frac{F}{A_0} \tag{B.1}$$

$$\varepsilon = \frac{l - l_0}{l_0} \tag{B.2}$$

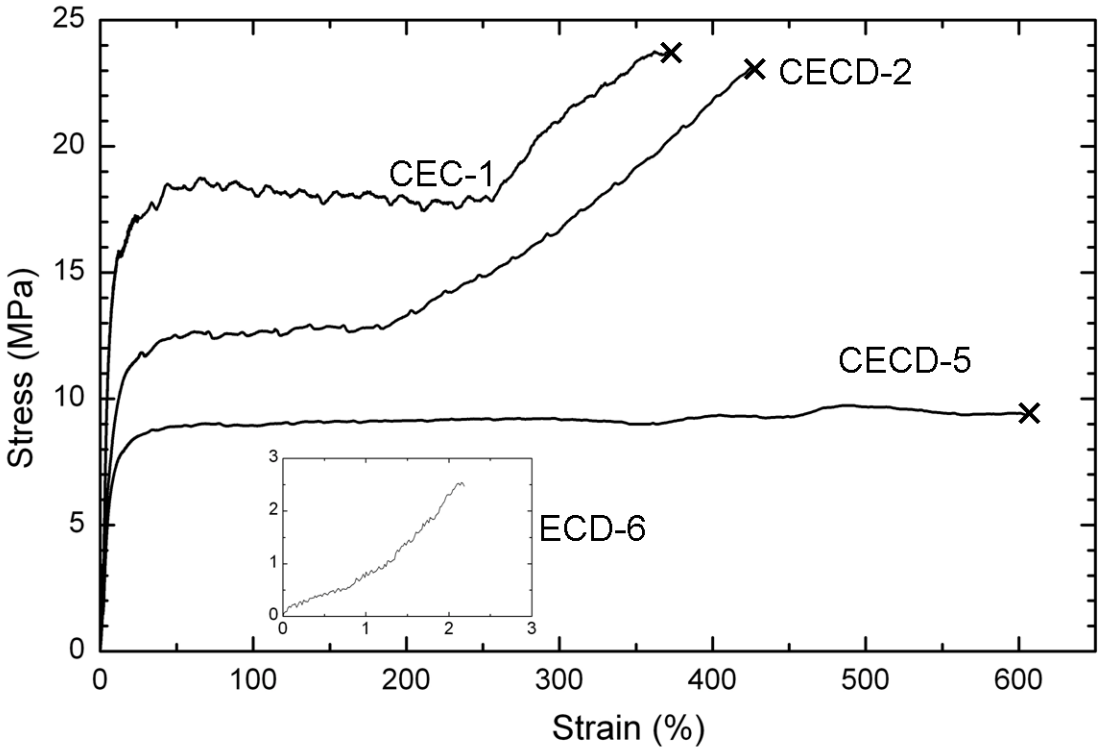

Figure B.0.1: Representative engineering stress versus nominal strain for CEC-1 (f_C = 0.31, f_E = 0.69), CECD-2 (f_C = 0.27, f_E = 0.64, f_D = 0.09), CECD-5 (f_C = 0.22, f_E = 0.58, f_D = 0.20), and ECD-6 (f_C = 0.28, f_E = 0.69, f_D = 0.03).

where F is the force of deformation, A_0 is the initial cross-sectional area and l and l_0 are the final and initial gauge lengths, respectively. At least five samples were tested for each block polymer.

The ultimate tensile properties (ε_{break} and σ_{break}) of the three CECD tetrablocks and one ECD triblock are listed in Table B.1. The increase in ε_{break} and the decrease in σ_{break} with increasing f_D among the CECD tetrablocks are consistent with the addition of a rubbery block (D) to a glassy/semicrystalline triblock. This simple analysis ignores

Table B.1: Summary of ultimate tensile properties of CECD tetrablocks and ECD triblock.

Polymer	f_D	ε_{break}	σ_{break} (MPa)
CEC-1	0	3.9 ± 0.2	22.7 ± 0.2
CECD-2	0.09	4.6 ± 0.6	24.7 ± 0.5
CECD-5	0.20	6.1 ± 0.4	9.3 ± 0.1
ECD-6	0.03	0.02 ± 0.01	2.4 ± 0.5

differences in molecular weight and microstructure among the three samples. The striking difference is between the CECD tetrablocks and the ECD triblock. The ECD triblock displays brittle failure at very small strains compared to plastic deformation in the CECD samples. These data are similar to the results obtained by Meuler *et al*.[1] when comparing the tensile properties of poly(isoprene-*b*-styrene-*b*-ethylene oxide) (ISO) to OSISO and support their hypothesis that a tough triblock core, in this case CEC, can provide superior mechanical properties.

Reference

(1) Meuler, A. J.; Fleury, G.; Hillmyer, M. A.; Bates, F. S. *Macromolecules* **2008**, *41*, 5809-5817.

Appendix C

Remarkable Small-angle X-ray Scattering Data Obtained from a Poly(styrene-*b*-isoprene-*b*-styrene-*b*-ethylene oxide) Tetrablock Terpolymer

In Chapter 6, the morphological behavior of a series of poly(styrene-*b*-isoprene-*b*-styrene-*b*-ethylene oxide) (SISO) tetrablock terpolymers along the $f_S = f_I$ isopleth were presented. SISO-3 ($f_O = 0.08$) was determined to possess a liquid-like packing of spheres microstructure when annealed well above its order-disorder transition temperature (T_{ODT}) and cooled to 140 ºC. In a separate experiment, a SISO-3 powder sample was heated to 205 ºC for 5 min using the DSC hot stage on the synchrotron small-angle X-ray scattering line at the Advanced Photon Source at Argonne National Laboratory (see Chapter 6 for details of the experimental setup). Scattering data were collected at 205 ºC and the sample was cooled to 140 ºC over the period of ~1 min. After 5 min, data were collected at this temperature. The SAXS data generated at 205 and 140 ºC are presented in Figure C.1. The two patterns are qualitatively similar with an increase in intensity apparent in

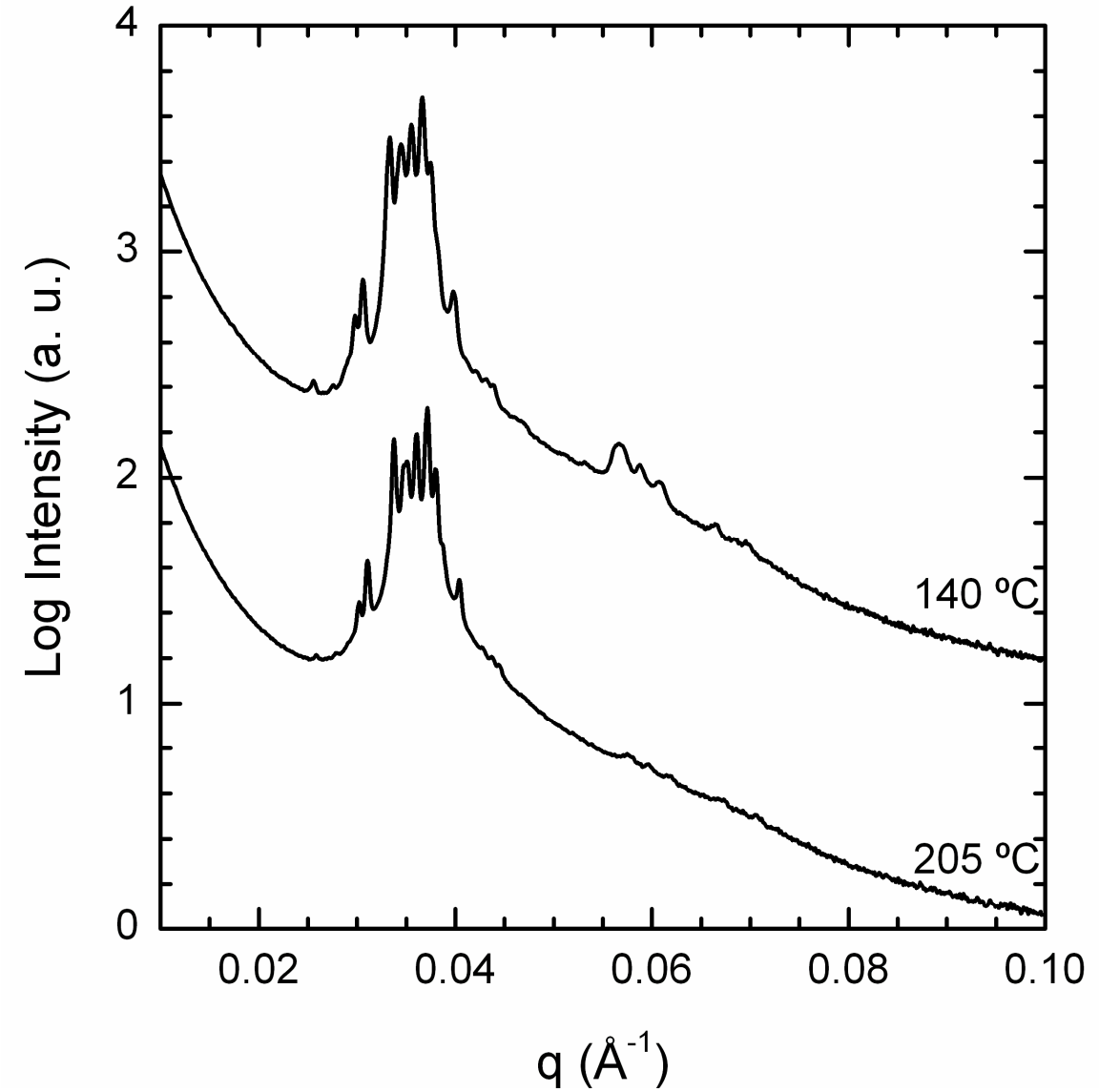

Figure C.1: SAXS patterns for SISO-3 collected at 205 and 140 ºC. The sample was prepared by heating polymer powder to 205 ºC for 5 min prior to data collection. The data at 140 ºC were generated after annealing for 5 min at 140 ºC.

Table C.1: Observed reflections for SISO-3 (f_O = 0.08) at 140 ºC (Figure C.1).

Peak Location ($Å^{-1}$)	Ratio	Peak Location ($Å^{-1}$)	Ratio
0.0256	1.00	0.0421	1.64
0.0275	1.07	0.0431	1.68
0.0298	1.16	0.0439	1.71
0.0306	1.19	0.0462	1.80
0.0333	1.30	0.0532	2.07
0.0345	1.35	0.0566	2.21
0.0355	1.39	0.0587	2.29
0.0367	1.43	0.0608	2.37
0.0374	1.46	0.0664	2.59
0.0398	1.55		

the higher *q* reflections at 140 ºC. Nineteen peaks have been identified and their positions have been listed in Table C.1 for the data collected at 140 ºC (some of the peaks likely consist of the superposition of reflections and several possible weak peaks have not been included). The ratios of the peak locations do not conform to a tetragonal, hexagonal, or cubic lattice. These positions also can not be accounted for by either of the two orthorhombic lattices identified in block polymer systems: *Fddd* (O^{70})[1-6] or *Pnna* (O^{52}).[5,7] Additionally, the "primary" peak at $q \cong 0.0256$ $Å^{-1}$ is significantly weaker than many of the higher *q* reflections suggesting that the scattering data are not generated from a "typical" block polymer microstructure. At this time, the morphology and process that led to the remarkable SAXS data presented in Figure C.1 is not well understood. However, strikingly similar SAXS data generated by Sangwoo Lee with a poly(isoprene-*b*-lactide) diblock copolymer[8] suggest that these results are not unique to this SISO tetrablock sample.

References

(1) Bailey, T. S.; Hardy, C. M.; Epps, T. H.,III; Bates, F. S. *Macromolecules* **2002**, *35*, 7007-7017.

(2) Epps, T. H.,III; Cochran, E. W.; Bailey, T. S.; Waletzko, R. S.; Hardy, C. M.; Bates, F. S. *Macromolecules* **2004**, *37*, 8325-8341.

(3) Chatterjee, J.; Jain, S.; Bates, F. S. *Macromolecules* **2007**, *40*, 2882-2896.

(4) Takenaka, M.; Wakada, T.; Akasaka, S.; Nishitsuji, S.; Saijo, K.; Shimizu, H.; Kim, M. I.; Hasegawa, H. *Macromolecules* **2007**, *40*, 4399-4402.

(5) Cochran, E. W.; Bates, F. S. *Phys. Rev. Lett.* **2004**, *93*, 087802/1-087802/4.

(6) Meuler, A. J.; Fleury, G.; Hillmyer, M. A.; Bates, F. S. *Macromolecules* **2008**, *41*, 5809-5817.

(7) Bluemle, M. J.; Fleury, G.; Lodge, T. P.; Bates, F. S. *Soft Matter* **2009**, *5*, 1587-1590.

(8) Lee, Sangwoo *Personal Communication*.